On semi-active inerters for improving machining productivity

Matt Tipuric

A thesis submitted in partial fulfilment of the requirements for the degree of

Doctor of Philosophy

The University of Sheffield

Faculty of Engineering

Department of Mechanical Engineering

Submission Date

August 18, 2022

Attribution

For the purpose of open access, the author has applied a Creative Commons Attribution (CC BY) licence to this work. You are free to:

Share – copy and redistribute the material in any medium or format; or

Adapt – remix, transform, and build upon the material; for any purpose, even commercially. The author cannot revoke these freedoms as long as you follow the license terms.

Acknowledgements

First and foremost, I would like to thank my supervisors Neil Sims and David Wagg for their advice, support and tyreless proofreading. Without them, this thesis would not have got written.

Next, I would like to thank my family -and most especially my parents, Mark and Janet, - for their love and (faintly baffled) support. Again, this whole endeavour would have failed without them.

I would like to thank all my colleagues in both the Dynamics Research Group and the Machining Science IDC for being the friendliest, sociable and knowledgeable research groups anyone could wish for. They made the last five years pass frighteningly quickly. I'd especially like to thank Max – for his long suffering answers to many inane questions – and to Chandy, for just being Chandy. I'd also like to thank both Chez and Clare, for helping me navigate many an admin related nightmare.

The technical staff in the Department of Mechanical Engineering deserve special recognition for their contributions to the experimental parts of this thesis. Mathew Hall, especially, has given me far too many hours of his life, as did Rob Abbott. I'd like to thank them both.

Outside of the Department, my thanks go to the members of Sheffield University Canoe Club and Peak Queer Adventures, for indulging me in my many hobbies. I'd separately like to thank both John and Jack, for being excellent friends and for helping me preserve my sanity throughout a pandemic.

Finally, and equally foremost, thank you to Fiona McBride. I thank her for her love and support, for not murdering me through these long months of writing up, and for her copyediting advice. I absolve her of all responsibility for any rogue commas or overzealous em-dashes – the fault for these lie with me and me alone.

Abstract

The inerter is a mechanical element, synthesised in 2002 as an analogue to the electrical capacitor. Originally used in Formula 1 racing as the 'J-damper', its potential has since been explored in other vehicles, as well as for vibration control of civil structures. In very recent years, some study has been given to the design and control of semi-active inerters. Such devices would be capable of varying their inertance in response to a control signal.

To date, no study has been made of the semi-active inerter in the context of machining chatter. This undesirable form of vibration, leading to poor surface finish on machined parts, is a major issue in machining. The growing requirements of high speed machining of lightweight, flexible parts mean that the need to develop new strategies to tackle chatter will only increase. This thesis seeks to fill this gap in the literature.

As a feasibility study, two chatter suppression strategies are developed using a simplified single degree of freedom chatter model. Both strategies assume the existence of an ideal semi-active inerter placed between the vibrating element and ground, allowing the natural frequency to be adjusted on-line. The first of these strategies, discrete inertance variation, is analogous to an existing lobe seeking strategy conducted by changing the spindle speed. It is shown that, with relatively modest ranges of inertance, this is an achievable strategy for high speed machining. The second strategy relies on cyclically adjusting the natural frequency to disrupt self-excited vibration. It is found that the amplitude of this variation is the important characteristic, rather than the ratio of the frequency of inertance variation to the tooth passing frequency. In both cases, the need to be able to rapidly control inertance is noted.

The design needs of a semi-active helical inerter are considered, with magnetorheological fluid providing the semi-active control. Three different layouts are studied using quasi-static models. The bypass valve type layout is selected as the most promising for future study. The design of the valve is considered and a new optimisation scheme is developed which better suits the need of the bypass valve than previous

schemes. The inerter model is extended into a quasi-dynamic model, which allows the varying inertance to be considered. This model would be key for developing any practical control scheme.

Prototype inerters were designed and tested. Initially an oil-based designed is built, followed by a design using magnetorheological fluid. The prototype was tested using a servo-hydraulic actuator, with the goal of validating the models developed in the previous chapter. Unfortunately, trapped air in both systems led to these results being inconclusive in both cases. The use of magnetorheological fluid for flow directional control in this way is unusual at this scale and this work is important for any future researchers who wish to work with the fluid in this way.

With this in mind, the issues encountered with the experimental rig are further analysed. Improvements to the design and filling method are proposed. Some more substantial design changes are also presented. Finally, some focus is given to the practical issues of implementing semi-active inerters in machining. The need to miniaturise the design to fit into modern machine tools is highlighted. Two areas in which this would be less of an issue – fixturing and robotic machining – are discussed. Notably, key challenges for robotic machining include the number and placement of the inerters, and whether new strategies would be needed to tackle mode-coupling chatter.

Nomenclature

This list contains the acronyms, variables and other relevant symbols used within this thesis, along with the units (where relevant) and the page number in which they are introduced. An effort has been made to use a clear, consistent terminology while also keeping this work consistent with those it builds on where possible. In respect of this, terminologies used for valve design and for self-adaptive differential evolution have been afforded their own sections.

Acronyms and initialisms

CIV	Continuous inertance variation
DC	Direct current
DDE	Delayed differential equation
DIV	Discrete inertance variation
DoF	Degree of Freedom
ER	Electrorheological fluid
ER	Electrorheological
FRF	Frequency response function
I/O	Input/output
IMR	Inertance to mass ratio
MR	Magnetorheological fluid
MR	Magnetorheological
MRR	Material removal rate

NMSE	Normalised mean square error	
OTF	Oriented transfer function	
PVID	Parallel viscous inerter damper	
RAAR	Relative acceleration absolute velocity	
RARV	Relative acceleration relative velocity	
SA	Simulated annealing	
SADE	Self adaptive differential evolution algorithm	
SDoF	Single degree of freedom	
SEUMURE	Space Exploration and UniModal Region Elimination	
SLD	Stability lobe diagram	
SLDRT	Simulink Desktop Real-time	
TID	Tuned inerter damper	
TMD	Tuned mass damper	
TMDI	Tuned mass damper inerter	

Greek alphabet

α	Linear fluid pressure coefficient	$\text{kgm}^{-2}\text{s}^{-1}$
β	Quadratic fluid pressure coef. (w.r.t. to fluid flow)	kgm^3
χ	A useful substitution	-
Δp	Pressure loss	Pa
ϵ	Phase difference	s
κ	Approximation parameter	-
μ	Dynamic viscosity	Pa s
Ω	Spindle speed	Hz
ω	Frequency	rads^{-1}

ϕ	Phase difference	s
ρ	Density	$\mathrm{kg\,m^{-3}}$
τ	Tooth passing period	m
θ	Angle of rotation of fluid	J
ζ	Damping ratio	-

Latin alphabet

A	Area	$\mathrm{m^2}$
B	Flux density	$\mathrm{kgA^{-1}s^{-2}}$
b	Inertance	kg
C	Valve Newtonian pressure coeffiecient	$\mathrm{kgm^{-2}s^{-1}}$
c	Damping coefficient	$\mathrm{N\,s/m}$
D	Linearised hydraulic resistance in the Helix	$\mathrm{Pasm^{-3}}$
F	Force	N
f_0	Natural frequency	Hz
f_c	Chatter frequency	Hz
f_t	Tooth passing frequency	Hz
$G(j\omega)$	Admittance (frequency domain)	-
$G(s)$	Transfer function of fluid system(Laplace domain)	
h	Chip thickness (w.r.t. machining dynamics)	m
h	Height of fluid gap (w.r.t. valve design)	m
$H(s)$	Transfer function of mechanical system (Laplace domain)	
I	Current (w.r.t. electromagnetics)	A
I	Inertia (w.r.t. fluid dynamics)	$\mathrm{kgm^2}$
j	Imaginary unit	-

k	Stiffness	$\mathrm{N\,m^{-1}}$
K_s	Specific cutting force	$\mathrm{Nmm^{-2}}$
l	Length of helix	m
m	Mass	kg
m_0	Static mass	kg
m_1	Variable mass	kg
N	Lobe number	-
n_{teeth}	Number of teeth	-
p	Frequency ratio	-
Q	Volumetric flow rate	$\mathrm{m^3\,s^{-1}}$
r	Radius	m
R_A	Amplitude ratio	-
R_M	Modulation ratio	-
T	Energy	J
t	Time	s
t_n	Time step	s
T_P	Principle period	s
u	Fluid velocity	$\mathrm{m\,s^{-1}}$
w	Depth of cut	m
$x(t)$	Displacement	m
Y	Tool displacement amplitude	m
$y(t)$	Tool displacement	m
`Np`	Number of passes to be simulated	-
`SR`	Time steps per revolution	-

General matrices

$\boldsymbol{\Phi}$	Transition matrix	-
$\boldsymbol{A}$	State matrix	-
$\boldsymbol{B}$	Input matrix matrix	-

Subscripts and diacritics

$\cdot_0$	Fundamental natural frequency ((w.r.t. frequency)
$\cdot_0$	Value in cylinder (w.r.t. fluid flow)
$\cdot_A$	Value in helix without a valve (w.r.t. fluid flow)
$\cdot_a$	Accelerance
$\cdot_B$	Value in helix containing a valve (w.r.t. fluid flow)
$\cdot_f$	Value in fluid
$\cdot_i$	Instantaneous quantity (w.r.t. system parameters)
$\cdot_s$	Value in steel
$\cdot_w$	At channel wall
$\cdot_x$	Admittance
$\cdot_1$	Measurement relating to piston rod
$\cdot_2$	Measurement relating to piston cylinder
$\cdot_3$	Measurement relating to helix pipe
$\cdot_4$	Measurement relating to helix
$\cdot_{hel}$	Property of fluid in the helix
$\cdot_H$	Relating to flow in a helix
$\cdot_{lin}$	Linear property or coefficient
$\cdot_{max}$	Maximum
$\cdot_{min}$	Minimum

$\cdot_{nom}$	Nominal value	
$\cdot_{off}$	Quantity with no current to valve	
$\cdot_{on}$	Quantity with current supplied to valve	
$\cdot_{quad}$	Relating to the square of the velocity	
$\cdot_{rot}$	Rotational	
$\cdot_{RPM}$	Measured in rotations per minute	
$\cdot_{sf}$	Quantity relating to secondary flows	
$\cdot_{v}$	Measurement or property relating to the valve	
$\cdot_{y}$	Yield (w.r.t. to fluid stress)	
$\hat{\cdot}$	Laplace transform	
$\tilde{\cdot}$	Nondimensional quantity	
$\cdot_{\text{fc}}$	Frictional	
$\cdot_{lim}$	Value at limit of stability	

Valve Design

δ	Plug width	m
ϱ	Ratio of outer radius to inner radius	-
τ_b	Bingham shear stress	m
τ_w	Shear stress at wall	m
A_a	Cross sectional area of core	m^2
A_b	Cross sectional area offlux return	m^2
A_c	Interior area at the flanges	m^2
B	Flux density	kgA^{-1}s^{-2}
d_w	Diameter of wire	m
H	Magnetic field strength	Am^{-1}

h	Height of fluid gap	m
h_c	Total length of wire	m
I	Current	A
l_v	Total length of valve	m
Q_{An}	Volumetric flow rate through annulus	$\mathrm{m^3s^{-1}}$
Q_{FP}	Volumetric flow rate between flat plates	$\mathrm{m^3s^{-1}}$
r_i	Radius of inner plate	m
r_o	Radius of outer plate	m
r_v	Total radius of valve	m
T	Number of turns	-
t_a	Radius of core	m
t_b	Length of flange	m
W	Number of wraps	-
w	Width of flat plates	m
w_c	Total height of wire	m
y	Displacement perpendicular to flow	m

SADE

C_r	Crossover parameter	-
f	Mutation factor	-
G	Number of generations	-
N	Size of generation	-

Chapter 1
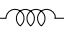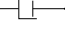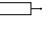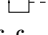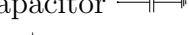
Introduction

1.1 The inerter

Compared to other elements used for passive vibration control – masses, springs, and dampers – the inerter is a recent addition to the literature. The (now standard) mechanical electrical analogy was established in 1933 by Firestone [1]. This draws a comparison between the force through a mechanical element with the current through its electrical counterpart. An example of this analogy is the fact that forces at a mechanical node and currents and an electrical junction must both sum to zero. Other equivalences are detailed in Table 1.1.

Under this analogy, a spring is considered to be equivalent to an inductor and a damper to a resistor. However, Firestone noted a gap in the analogy. Mass elements lack a second terminal and so it makes little sense to discuss the force 'across' the mass, in the way one can discuss the force across a spring or damper. Firestone's solution was to note that, if a force is applied to a mass, an equivalent force must be being applied elsewhere, as shown in Fig 1.1. This restriction means that mass can

Table 1.1: Summary of the electrical-mechanical analogy, as set out in Ref. [1].

Domain	Mechanical	Electrical
Through variable	Force	Current
Across variable	Velocity	Voltage
Proportional component	Spring -⋀⋀-	Inductor -⦚⦚⦚-
First derivative component	Damper -⊏-	Resistor -⊏⊐-
Second derivative component	Mass □--	Grounded capacitor -⊣⊢
Balanced at nodes	Sum of forces	Sum of currents
Balanced around loop	Sum of velocities	Sum of voltages

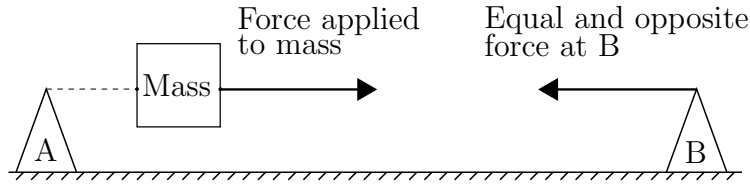only be considered equivalent to a *grounded* capacitor.

Figure 1.1: The way in which a mass is conceived of as a two terminal element in Ref. [1].

In a 2002 paper, Smith [2] proposed a new mechanical element, analogous to the ungrounded capacitor: the inerter[1]. This was defined as a mechanical device which fulfilled two necessary criteria:

1. the device possesses two terminals, and

2. the resistive force through the inerter must be proportional to the relative acceleration across it.

This coefficient of proportionality of this resistive force is referred to as *inertance*, is usually denoted with b and is measured in kg. The symbol for an inerter is ⊣⊢.

In order to ensure that physical realisations of the inerter would be useful, Smith imposed four further restrictions on designs:

1. they must have small mass compared to the inertance provided;

2. there must be no requirement for one of the terminals to be fixed to earth;

3. the device must be subject to reasonable dimensional constraints, including the region of linear travel; and

4. the device must be able to function in any spatial orientation and motion.

Smith suggested one possible implementation which met these criteria and three case studies for its use. This conception of the inerter was designed for use in Formula One cars and kept as a trade secret for some years. Since then, the field has grown in size, with novel designs and applications being proposed frequently.

While Smith published a formal definition for the inerter in 2002, related devices had been in use for some decades. Kuhnert [4] cites devices in existence as early as the sixties. Notably, in Japan the development of the inerter has followed a parallel track,

---

[1]Note that the term pre-exists this study [3].

leading to some established inerter-like devices. These include the hydraulic inerter damper [5], the tuned viscous mass damper [6] and the liquid type mass damper [7]. These devices are largely studied in the context of civil structures, especially earthquake and wind vibration of buildings.

Smith's initial study [2] concerned itself with a single implementation of the inerter, making use of a rack and pinion. A patent [8] filed the same year included four additional methods of implementation, using hydraulically powered flywheels, a lever arm and two possible uses of ball-screws. In subsequent years, a design making use of fluid forced through a meandering channel was proposed [9], as well as one using fluid rotating through a helical channel [10]. The fundamental layouts of these implementations are shown in Figure 1.2.

The parallel development of inerters is reflected in the use cases proposed in the literature. In the domain of civil engineering, as well as implementations for buildings, the potential for inerters to reduce vortex-induced vibration on bridges [11] and heave motion of oil platforms [12] have been investigated. Meanwhile, inerters have been proposed for automotive handling [13], train ride comfort [14] and motorcycle handling [15]. Any study of inerters outside of the areas of vehicle suspension and civil structures is extremely recent. This is especially true in the field of machining science.

1.2 Semi-active control

Classically, vibration control [16] was only possible using *passive* devices. Such devices operate without the need for a external power supply or control. For example, a spring stores mechanical energy without needing a control signal to tell it to do so. Such elements are foundational to control and are ubiquitous, being generally cheap to produce and run, as well as robust. However, they suffer from the requirement to be tuned to a specific problem. A passive suspension system, for example, might be optimised to mitigate vibration from asphalt roads but entirely inadequate for a rocky track. Some passive elements are designed in such a way that their properties can be adjusted in situ; such elements are *tunable*.

Active components, such as actuators, are defined by their ability to impart energy to a system, instead of just removing it. Such components require an external power source. They provide for significantly improved control which can react to changing conditions. Active control, however, tends to be more complex and expensive than passive and the energy costs associated with it are necessarily higher. In addition,
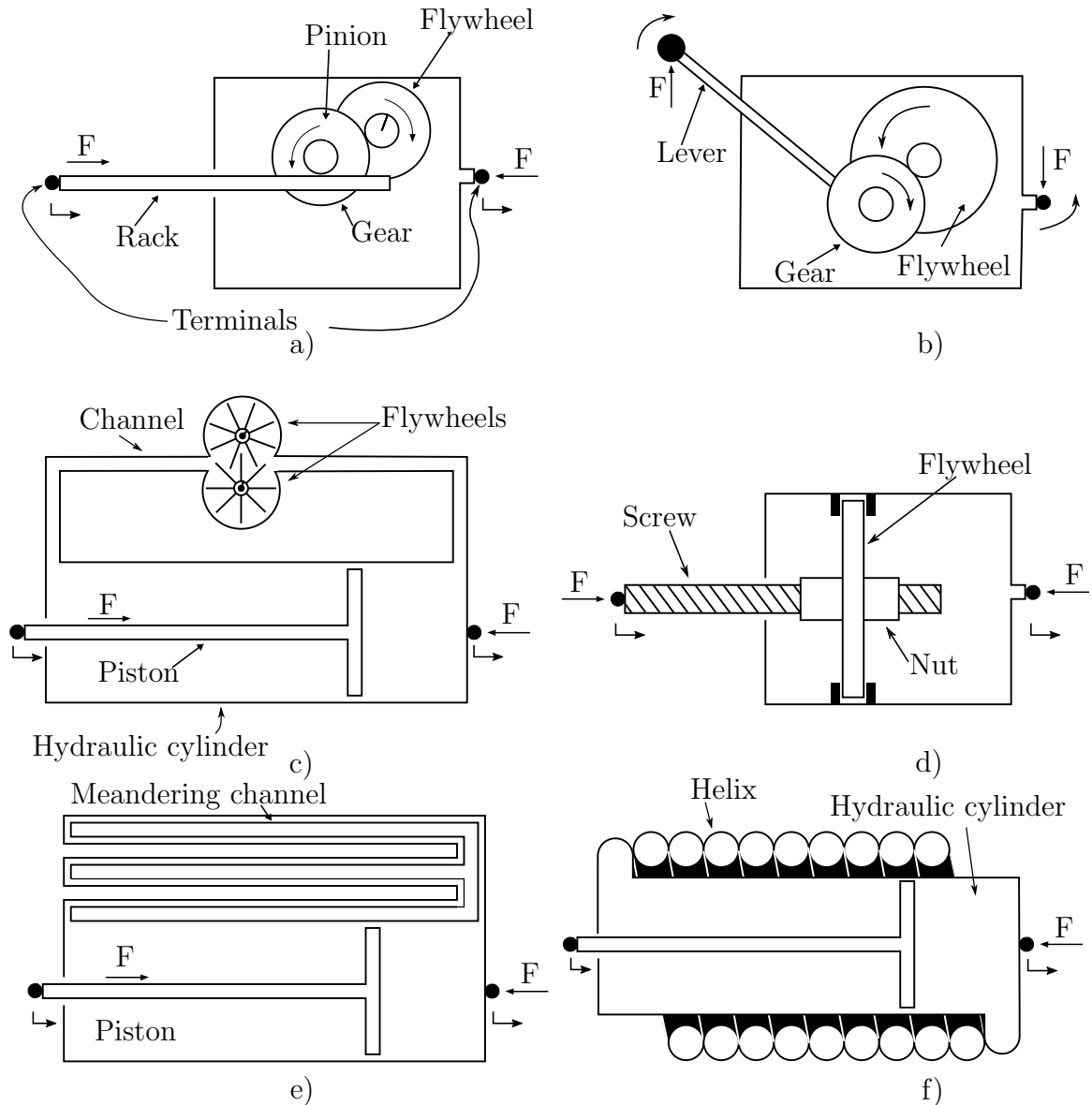
Figure 1.2: Sketch diagrams of a) rack and pinion, b) lever arm, c) hydraulic flywheel, d) ball screw, e) meandering channel and f) helical fluid inerter types.

the fact that active control can add energy to the system means that it is possible to introduce instability into a system in which there were none previously. Some systems combine both passive and active elements and known as *hybrid* systems.

A third class of component are known as *semi-active* components [17]. Semi-active components also require an external power source but cannot impart energy to the system they are controlling. Instead, the control logic is used to affect the parameters of an otherwise passive element. The difference between these elements and tunable elements is that a semi-active element can be controlled rapidly during

operation, following some kind of control logic. For example, a conventional dash-pot damper might be tuned by substituting the oil for one with different characteristics. However, doing so while the damper is in use would be relatively impractical. In contrast, magnetorheological shock absorbers are able to change their damping coefficient rapidly during use, through a change in the magnetic field which interacts with the fluid inside.

These three main classes of control can be seen as existing on a scale, in terms of costs and benefits. Passive components tend to be the cheapest and simplest but lack in performance and cannot easily adapt to changing conditions. Conversely, active methods offer high performance and versatility, at the cost of complexity, expense and high power draw. Semi-active control falls somewhere in the middle.

Semi-active control can be achieved through various means. One method is through the use of electrorheological or magnetorheological fluids [18]. Such fluids consist of a suspension of ferrous particles in oil, allowing the shear stress to be controlled using a magnetic field. The rapid response time and high forces available from MR fluid make it a popular candidate for semi-active systems.

1.3 Machining and chatter

Machining operations are a common part of many manufacturing processes. Such operations create parts from a work-piece by removing some of that material [19]. This can be contrasted with forging and casting, where material is melted and reshaped, and with additive manufacturing, where material is added. Many conventional machining methods, including turning and milling (Figure 1.3), involve the rotation of the part being machined or of the tool. This rotation imparts dynamic forces to the system, leading to inaccuracies and other issues. As such, machining dynamics is a major topic of research, with much historical and current research dedicated to it.

Within machining dynamics, a significant amount of research is dedicated to *chatter*: the appearance of wavy surface markings on the workpiece, first described in the literature by Frederik Taylor in 1907 [20]. Under normal operations, this waviness is accounted for. An acceptable tolerance is set and the machinist will achieve this through parameter selection, finishing passes at low depth of cut or some other method. However, under certain conditions, a feedback loop can occur, with oscillations during one pass interacting with the surface waviness from a previous pass. An (exaggerated) example of self-excited chatter during a turning operation is shown in Figure 1.4. The dotted line shows how the surface waviness created by the relative
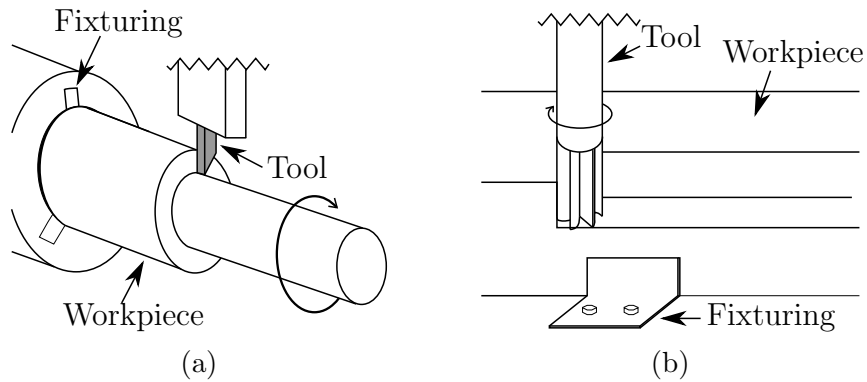
Figure 1.3: Examples of a) a turning operation and b) a face milling operation.

vibration of the tool during the second pass is additive with that from the first pass. The maximum amplitude (and so the cutting force required) of the vibration will then increase over time by a substantial amount. This leads to a poor surface finish and can damage the tool.
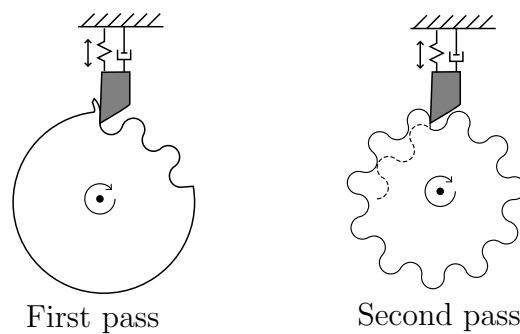

First pass   Second pass

Figure 1.4: The development of self-excited chatter in turning. The dashed line indicates the path the tool will follow during the second pass. Note that the amplitude of the waves has been exaggerate to demonstrate the effect.

A recent review [21] identified chatter as "one of the major limitations to productivity". Five reasons were identified as to why chatter is and will remain an on-going concern:

1. increasing material removal rate (MRR) available with higher-power machines and carbide tools;

2. inability to accurately model damping in the system;

3. low friction guiding systems reducing friction damping;

4. light weight machines which are susceptible to vibrations; and

5. manufacturing of flexible parts, e.g. in the aerospace sector.

While the basic theory of chatter is well established [19], the exact circumstances which will cause it depend on the speed of rotation (spindle speed), the depth of cut, the vibrating element (which might be a flexible tool or a lightweight work-piece), and on the dynamics of the specific system, which might change greatly over time. As such, a great many chatter mitigation techniques have been proposed, some broadly applicable, some narrowly tailored to specific circumstances. In recent years [22], the potential for passive inerters to mitigate chatter has been investigated but as of yet no study has been made into the possibilities that semi-active inerters might offer.

1.4 Aim and Objectives

The study of inerters is a relatively recent topic of study. The study of semi-active inerters is even more so. This is unsurprising, as few designs for such devices exist in the literature and the research field as a whole is extremely nascent.

The overall aim of this thesis is to explore potential for semi-active inerters within machining science.

This aim is supported by the following objectives:

O1. Explore the case for semi-active inerters in chatter mitigation, focusing on conventional machining operations. This is primarily the focus of Chapter 3, with further possibilities discussed in Chapter 6.

O2. Design a new semi-active inerter which uses magnetorheological fluid. This forms the first part of Chapter 4.

O3. Create models of the semi-active inerter, to both aid in design and to support future exploration of control schemes. This forms the second part of Chapter 4.

O4. Build and test a semi-active inerter, with the goal of validating the models. This process is documented in Chapter 5, with further discussion in 6.

Two further objectives were initially proposed but eventually rejected in favour of more time spent on the experimental work:

O5. Explore the possibilities of using semi-active inerters in aid of robotic machining. (Some brief discussion is given to this in Chapter 6).

O6. Develop control strategies for the semi-active inerter.

1.5   Summary of chapters

Chapter 2 contains a review of the relevant literature. The scope of this review includes literature concerning chatter (including models and mitigation techniques), inerters (including designs, uses, control and optimisation) and magnetorheological fluids (including formulations, 'modes', devices and models). Special focus is given to the literature surrounding helical inerters, the modelling of magnetorheological dampers and to the design of magnetorheological devices.

Chapter 3 presents a common, first order model of chatter. This model is then used to study the feasibility of two new proposed chatter mitigation techniques which could be enabled through the use of a semi-active inerter. The requirements of both strategies in terms of semi-active inerter design are discussed.

Chapter 4 covers the design and modelling of a semi-active helical inerter. Three general layouts are modelled using a quasi-static model and compared in terms of suitability. The magnetorheological valve design is also investigated, with a new optimisation scheme being proposed for this novel use. Finally, the quasi-static model is extended to a 'quasi-dynamic' model, which accounts for varying inertance, in aid of potential future control work.

In Chapter 5, the process of prototyping the semi-active inerter is documented. Two series of tests are described, starting with an oil-based design before moving on to using magnetorehological fluid. Test data is presented, and some of the potential issues - including trapped air and friction- are discussed.

In Chapter 6, these issues are revisited. Proposals are made for how the design might be improved. Some alternative methods for achieving a semi-active inerter are also proposed. The chapter also sets the overall context for the rest of the thesis by discussing the potential niches which semi-active inerters might find within different machining operations - in conventional tools, in fixturing, and in robotic machining- and the practical issues which will need to be overcome in each case.

Finally, in Chapter 7 the thesis is concluded and some recommendations for further work are suggested.

Chapter 2

Literature review

2.1 Introduction

This thesis brings together three largely disparate fields of study: machining science, inerters, and magnetorheological fluid. Each of these topics has a broad and evolving literature. This chapter provides an overview of the relevant historical and recent literature in each of these fields.

In Section 2.2, the issue of machining chatter is covered. The section commences with a broad overview of the field, before discussing some of the models which have been developed to describe it. A number of chatter mitigation techniques are described, commencing with lobe-based and passive strategies. The section concludes with a focus on active chatter control techniques, some of which a promising avenues of research for a semi-active inerter.

Section 2.3 covers inerters, starting with the historical background. This is followed by a description of some of the main types of inerter that have been developed, as well as the ways in which they have been used in both academia and industry. The section concludes with a focus on tunable and semi-active inerters and on optimisation and control. Both of these topics form the focus of this work.

Magnetorheological fluids are the focus of Section 2.4. After a brief overview and a discussion of fluid formulations, the different modes in which the fluid can be used are discussed. There is then a review of the main types of magnetorheological fluid devices which have been studied. The section- and chapter- conclude with a review of design methods, which feeds into the work presented in Chapter **??**.

2.2 Machining chatter

2.2.1 Chatter overview

Self excited vibrations in machining can arise in a variety of ways. It is common to refer to *primary* and *secondary* (or *regenerative*) chatter, although the former class can be split into *frictional*, *mode-coupling* and *thermo-mechanical* chatter. Quintana and Ciurana [23] provide a good overview of these categories in their review of chatter. Under either classification method, regenerative/secondary chatter is the most common form [24] and as such is the form that receives the most investigation (although mode-coupling chatter receives some attention within the bounds of robotic machining [25]) . A review of the most cited works on listed on Scopus shows this clearly, with works on self-excited chatter forming a vast majority, as seen in Figure 2.1. In addition, over half of these works gave no discussion of other forms of chatter, suggesting that it might be legitimate to say that chatter and self-excited chatter are near synonymous. In this work, unless otherwise specified, chatter should be assumed to be self-excited.
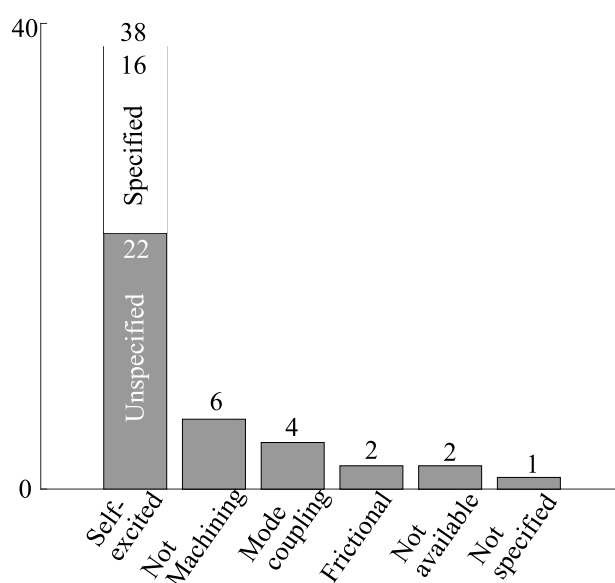
Figure 2.1: A review of the 50 highest cited papers on Scopus as of 08/10/2020, under the category of 'engineering' and containing 'chatter' in the keywords.

Topics within chatter include experimental detection, analytical prediction, and suppression or control. In their 2012 review of the field, Siddhpura and Paurobally [26] counted the number of papers they studied within each of these topics as being

80/43/31 split between detection/prediction/control. This was in no way an exhaustive list but does give some impression of the make-up of the field.

Early research into analytical chatter prediction was conducted by Arnold [27] but flaws in the experimental set-up, as noted by others (e.g. Stone [28]), led to the model developed being not particularly applicable. Tobias and Fishwick [29] and Tlusty and Poelack [30] (independently) had more success and can be credited with codifying the modern understanding of chatter. This work developed linear chatter analysis to create the stability lobe diagram (SLD), described in more detail and employed in Chapter 3. These diagrams can also be created using other methods, including Nyquist plots [31] and time domain finite element methods [32]. The former method is criticised for only being able to say whether a given set of parameters is or isn't stable [26], while the latter can have issues when modelling the damping introduced by joints [21], [26]. The Nyquist stability criterion is foundational for some analytical techniques, such as semi-discretisation [33].

2.2.2 Chatter models

The models developed by Tlusty [30], Tobias and Fishwick [29] and Atlintas and Weck [34] use a single degree of freedom (SDoF) approximation, with a linear relationship between cutting force and parameters, known as linear chatter analysis. The assumption of linearity is most applicable for turning, where (disregarding loss of contact caused by excessive vibrations) the single tool tip and constant depth of cut lend themselves to linear behaviour.

The analysis of chatter in milling can be more complex than in turning in various ways. Firstly, a milling tool system is inherently at least two-dimensional [35] and can require a 3-DoF[1] or even 4-DoF[2] system model. A good overview of these can be found in Figure 7 of Ref. [38]. Dombovari et al. [39] have shown, however, that it is possible to capture complex, chaotic, dynamics with a SDoF model.

This multidimensional behaviour leads to further complexities. The cutting force per tooth is not constant but instead increases from zero as each tooth enters the workpiece, to a maximum as it leaves. This, along with the fact that the number of teeth in contact with the workpiece may not be constant, leads to non-linear effects not observed in linear chatter analysis, including secondary Hopf bifurcation [40] and period doubling [41]. The practical effects of these are to lower the stability limit in some areas from that predicted by linear chatter analysis. Other non-linearities,

---

[1]for ball-nose mills, which can experience significant out of plane vibrations [36]

[2]to deal with two-dimensional vibration of both the tool and the workpiece [37]

such as unequal tooth pitch [42] and non-smooth ball bearings [43] can even lead to unstable islands with-in the stable zone.

A further complexity with milling is that the multiple teeth on the cutter mean that the forcing is now periodic at some integer multiple of the spindle speed. The appearance of significant stable lobes at lower spindle speeds means that lobe-based chatter mitigation strategies are more relevant [44]. As such, the accurate prediction of the shape of these lobes can be more important in milling.

These complexities not-withstanding, linear stability analysis is a good first order approximation for studying chatter in the abstract. It has been used consistently [22], [45], [46] by researchers to provide justification and physical understanding for their methods. While designing for implementation into real world systems may require these more complex effects to be taken into account, the simplicity and versatility offered by linear stability analysis should not be underestimated.

2.2.3 Chatter mitigation techniques

Quintana and Ciurana [23] divide chatter mitigation techniques into four categories: in-process lobe strategies, out-of-process lobe strategies, active system modification and passive system modification. In a more recent review, Munoa et al. [21] propose that techniques be evaluated based upon three criteria: machinability, the critical element[3], and the location in the SLD. Materials with poor machinability limit the range of available spindle speeds. Chatter arising from low frequency vibration caused by the machine structure may require different solutions or implementations to that arising from higher frequency chatter caused by spindle flexibility. This is especially true if the system is time-variant, such as when a large amount of material is removed [47].

The SLD is divided into four locations, as shown in Figure 2.2: zone A which is dominated by process damping, zone B in which there is little variation from the absolute stability limit, zone C which features large stability lobes and zone D, situated in the zeroth lobe. In zone D, the stability limit can increase with spindle speed up to limits set only by power availability and other such physical constraints. These zones are also referred to as the process damping, intermediate speed, high speed and ultra-high speed zones, respectively.

---

[3]i.e. which part of the system - workpiece, tool, fixture, spindle, etc.- is causing the chatter
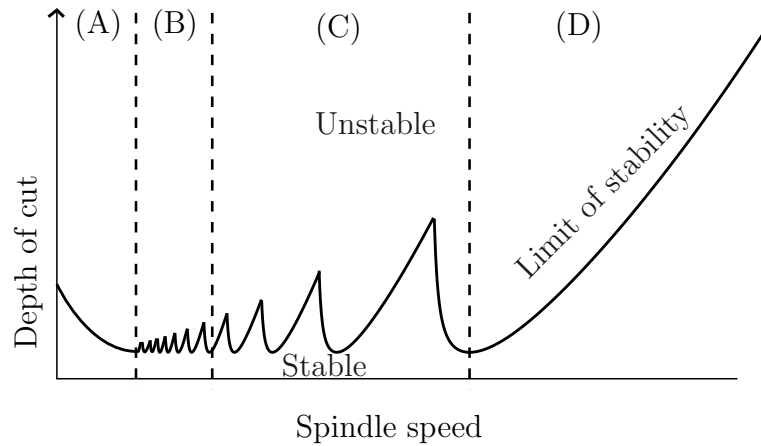
Figure 2.2: A simplified stability lobe diagram, featuring the four machining zones, as described by Ref. [21].

2.2.3.1 Lobe-based techniques

Under this framework, lobe-based strategies are most useful within zone C. Out-of-process lobe targeting, an aspect of parameter selection, requires accurate SLDs to be created, with a large amount of research being dedicated to achieving this goal [21]. In-process lobe targeting, achieved through discrete (or automatic [45]) spindle speed variation, requires some method of detecting chatter. Both active and passive system modification generally involve raising the absolute stability limit and so may be useful in any zone, depending on the exact strategy used.

With the number of factors involved in selecting a suitable chatter strategy and the great variety on machining operations, it is unsurprising that there are a number of chatter mitigation strategies within the literature. Many of these have little relevance to the current study but bear mentioning for completeness.

2.2.3.2 Passive techniques

A number of chatter mitigation techniques involve modifying the structure using passive components. The system damping can be improved using friction dampers [48] or impact dampers [49]. The stiffness can be increased through fixturing of thin-walled workpieces [50], use of sacrificial structures [51] or through use of high performance tool materials [52]. Meanwhile, milling tools with a helix [53], variable pitch [54] or serrated teeth [55] have been shown to perturb the regenerative effect in various ways.

Discrete spindle speed variation was first described by Smith and Tlusty [45]. The theory is described in detail in Chapter 3. For discrete spindle speed variation

to be implemented, it is necessary to be able to detect chatter as it occurs. This can be done using data from various signals, including detecting workpiece deflection [56], sound [57] or acoustic signals [58] or the torque of the spindle [59]. Tlusty and Andrews [60] provide a foundational review of sensors and Quintana and Ciurana [23] provide a more up to date review, including both sensors and signal processing methods. The main objectives in this field are the rapid identification of chatter and using sensors that can be deployed within the restrictive spaces offered by machines. For the present study, it is sufficient to be aware that these various methods exist, without being too constrained by the exact strengths and weaknesses of each.

Tuned mass dampers[4] (TMD), Figure 2.3a, have been present in the chatter literature for some time. In 1951, Hahn [62] presented a design of a Lanchester damper for a boring bar. This is a form of tuned mass damper with no stiffness element, as shown in Figure 2.3b; a mass is contained within a hollowed out boring bar, with an air gap providing damping. Hahn noted that this design could potentially be extended to other machine tools. More recent advances include a non-linear design for turning using friction damping [63], a magnetically tuned mass damper [64], a concentric design attached around thin-walled cylindrical parts [65] and a design and tuning methodology for a tunable clamping table [66].

The optimum tuning of vibration absorbers is a matter of some interest, as the standard method for tuned mass dampers elsewhere (Den Hartog tuning [67]) does not necessarily provide an optimal solution when applied to chatter [68], [49]. A tuning methodology for Hahn dampers was proposed by Rivin and Kang [68]. Sims [49] noted that this method requires either a graphical approach or numerical optimisation, as well as knowledge of the chatter frequency to employ. Sims proposed an alternative based on Den Hartog tuning but seeking to minimise the real part, rather than the absolute magnitude, of the frequency response function (FRF). The real part is the part relevant to the limiting depth of cut (see Chapter 3). Yang et al.[69] expanded this approach to multiple tuned mass dampers, a layout which has been shown to work better for dealing with multiple frequencies than using a single, larger tuned mass damper. Burtscher and Fleischer [70] used it as the basis for a tuning strategy for an adaptive tuned mass damper. Munoa et al. [21] note that, as real world chatter is affected by multiple modes, numerical optimisation is used in practice but that the use of an analytical strategy as a first guess increases the speed of convergence. They also note that difficulties associated with TMDs include lack of technician knowledge on the tuning methods, achieving a mass ratio of up to 20% within the limited space

---

[4]a class of tuned vibration absorber [61]- the terms are often used interchangeably in the literature

available and achieving automatic, in-process tuning. To deal with this third issue, Munoa et al. [46] proposed a controllable tuned mass damper with a rotary spring and the damping provided by eddy currents.

An alternative form of vibration absorber to the tuned mass damper is the tuned inerter damper (TID) [71]. These devices have a similar layout to tuned mass dampers, with the addition of an inerter, as shown in Figure 6.7. TIDs were first proposed for controlling structural vibration in civil structures, with the main advantage posed being the fact that the mass magnification effect offered by inerters allows for a greater effective mass ratio than in a tuned mass damper. Dogan et al. [22] investigated four candidate layouts, shown in Figure 2.4, based on those proposed by Hu and Chen [72]. They showed a 37% improvement performance over a tuned mass damper could be obtained with layouts C1 and C4. More recently, Dogan et al. [73] proposed a realisation of a modified version of layout C2, using a living hinge design.
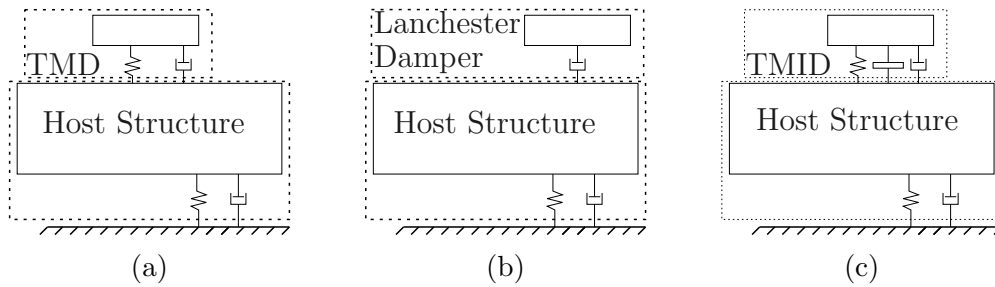
Figure 2.3: A diagram of (a) a tuned mass damper, (b) a Lanchester damper and (c) a tuned mass-inerter damper in situ.

The general effect of both TMDs [49] and TIDs [22] on the SLD is to increase the absolute stability limit, at the cost of the size of the stable lobes, as shown in Figure 2.5.

2.2.3.3 Active and semi-active techniques

Active techniques have the ability to introduce energy to the system. This contrasts with semi-active techniques, where parameters can be changed in process but the overall effect is to change the amount of energy removed from the system or the way that energy is converted. It should be noted, however, that not all researchers make this distinction [23], [21]. Active chatter reduction methods that appear in the literature include inertial actuators [74], piezoelectric actuators [75], active magnetic bearings [76] and active fixturing [77]. As is often the case with active control, the "economical and technical efforts are justified only when other simpler solutions cannot provide an
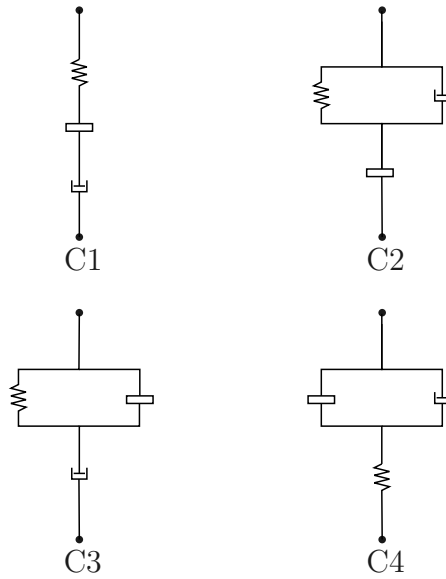
Figure 2.4: The four tuned inerter damper layouts investigated by Dogan et al. [22]. Layouts C1-3 correspond to layouts C3-5 in Ref. [72].

optimum response" [21]. Research challenges include sizing of actuators, suppression of high frequency chatter and the lack of industrialised designs.

Both magnetorheological and electrorheological fluids have been investigated for potential uses in chatter mitigation. Wang and Fei [78] presented a boring bar with variable stiffness provided by a layer of ER fluid. Mei et al. [79] followed this with a similar design, using MR fluid and showed that affecting the natural frequency in this way could suppress chatter, although doing so at higher spindle speeds required an impractical increase of stiffness. This was again built upon recently by Biju and Shunmugam [80], who created a design able to reduce vibration by 29-44%.

Sathianarayanan et al. [81] investigated the use of a magnetorheological damper with constant current for boring bars and showed increased damping. More recently, Pour and Behbahani [82] proposed a fuzzy-logic control scheme to use a magnetorheological damper for semi-active control and claimed a 50% improvement in the absolute stability limit, although this has yet to be confirmed experimentally. Paul et al. [83] designed a compact magnetorheological damper for end milling, investigating a wide range of parameters, including particle size and fluid composition. With thin walled parts, involving magnetorheological fluid in the fixturing to mitigate vibrations in the workpiece is an approach that has been shown to have some success in recent years [84], [85], [86].

One active technique which has received some interest is continuous spindle speed variation. Ref. [87] is an early paper in the english-speaking literature, although at
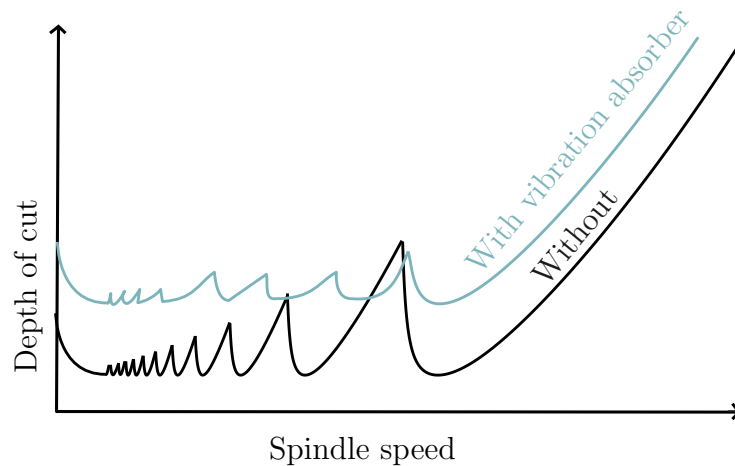
Figure 2.5: A sketch of the general effect of a tuned mass damper [49] or tuned inerter damper [22] on the SLD.

least one pre-existing work exists in Japanese [88]. If regenerative chatter is caused by interaction of the current vibration with that from the previous rotation, then varying the time delay between these rotations (by continuously varying the spindles speed) can disrupt chatter. One complexity lies in the fact that the system equation that comes about using this technique is a varying delay differential equation, as compared to the continuous delayed differential equation that occurs with a constant delay term. No closed-form solution exists to such equations [89] and so linear analysis is no longer appropriate. Instead, SLDs may be created using semi-discretisation [33], where the time dimension is divided into some number of discrete intervals, multi-frequency analysis [90] or using time-domain simulations. Due to the practicalities of accelerating and decelerating the spindle at high speeds, continuous spindle speed variation is restricted to machining in zones A and B [91].

Segalman and Redmond [92] proposed the use of a similar technique, christening it *impedance modulation*. Here, instead of varying the spindle speed, the natural frequency of the system was varied, using a boring bar containing a layer of magnetorheological fluid [93]. They showed a similar effect to continuous spindle speed variation. The ability of the fluid to vary its properties rapidly might allow this method to be used at higher spindle speeds than continuous spindle speed variation. Very recently, Defant and Albertelli [94] proposed a promising method for modelling systems of this type, using the harmonic solution and zero order harmonic solution.

2.3 Inerters

While various inerter-like devices have been developed in various fields for decades [4], the study of inerters *as inerters* is a thing of the 21st Century. As such, when compared to the study of chatter, advances in this field have been made extremely recently. Nevertheless, since its conception the inerter has been a very active area of research, with a variety of proposals both in terms of implementation and uses. After a brief overview, these topics form the early part of this section. This is followed by a focus on tunable and semi-active designs. Finally the state of the research surrounding optimisation and control of inerters is presented.

2.3.1 Background

Smith [2] proposed the inerter as a mechanical element analogous to an electrical capacitor. The definition provided is

> "a mechanical two-node (two-terminal), one-port[5] device with the property that the equal and opposite force applied at the nodes is proportional to the relative acceleration between the nodes."

Inerters are also required to have a low mass compared to the provided inertance (low parasitic mass), no requirement of being grounded, be subject to reasonable dimensional constraints and operate in any spatial orientation and motion.

More historical and international perspectives are offered by Kuhnert et al. [4] and by Wagg [95]. Both papers discuss a number of early devices which predate Smith's work, such as the dynamic antiresonant vibration isolator [96] and hydramounts [97]. The exact classification of devices which predate the term 'inerter' can become confused. There can be legitimate debate over whether a specific implementation could be considered a true inerter or simply an inerter-like device[6]. In the interests of not getting bogged down in semantics, this review will consider all such devices where relevant.

---

[5]This terminology is technically redundant as, as noted in Smith's paper, 'a port is a pair of nodes'.

[6]It should be reiterated that the inerter is an idealised fiction. Practical implementations exhibit non-linear behaviour and are often inseparably part of a vibration absorber. As such, one interpretation would be that *all* practical inerters are just inerter-like devices.

2.3.2 Types of inerter

In their recently published textbook [98], Chen and Hu propose two classification schemes for the existing realisations of the inerter: either the three categories of *rack-and-pinion*, *ball-screw* and *hydraulic* inerters or a binary classification, based on whether or not the inerter uses a flywheel. In a retrospective article [99], Smith uses the former schema but also introduces the categories of the *fluid pump* and *rotational inerters*. These last two categories can be considered to be special cases of the fluid and rack-and-pinion inerters, respectively. Introducing these categories raises questions as to why other special cases don't earn their own category, such as the meander-type inerter, while also leading to the possibility of every individual inerter implementation being a category in itself.

The rack-and-pinion inerter was first described by Smith in their seminal paper [2]. This design, as shown in Figure 2.6a, translates longitudinal motion into rotation of a flywheel, via a gear. The inertia is therefore provided by the flywheel and a magnification effect is created through the gears. Smith reported an inertance to mass ratio (IMR) of 300 for the initial prototype. In testing, Papageorgiou et al. [100] noted a non-linear spiking effect, caused by mechanical backlash (and friction at low frequencies).

While not discussed in Ref. [2], a design for a ball-screw inerter is included in the accompanying patent [8]. In this mechanical design, a lateral force is applied across the screw, causing it to rotate in the nut. The inertia of the attached flywheel creates the inertance. The non-linearities in rack-and-pinion are ball-screw inerters are similar, in that both theoretically susceptible to backlash and friction [100] (mainly between the teeth of the gears in the former and between the nut and bolt for the the latter). Wang and Su [101] note that friction can be large, due to preloading, while backlash is less of a concern.

Chen [98] considers the ball-screw inerter to be "the second generation of the inerter", replacing the rack-and-pinion inerter due to the reduced effect of friction and ability to eliminate backlash via pre-loading. However, Li and et al. [102] note that, when dealing with higher forces (such as in civil structures), rack-and-pinion designs become more cost-effective to produce.

Wang et al. [63] designed and tested a type of fluid inerter where the flow of fluid, caused by oscillation of a piston, rotates a motor attached to a flywheel. Smith [99] refers to this realisation as a *gear-pump* inerters. This design can provide high forces and avoids the backlash associated with mechanical designs, although friction can still be an issue and a parasitic damping force exists, caused by pipe losses. Nakaminami
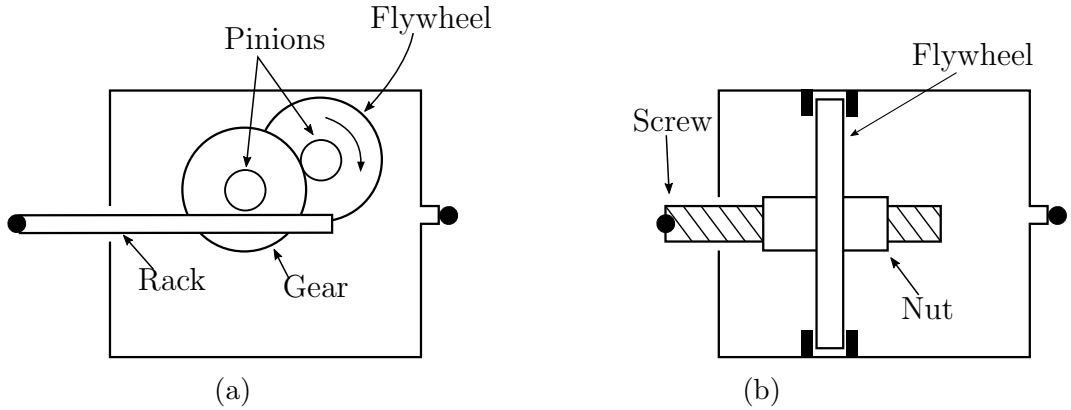
Figure 2.6: Sketch diagrams of a) a rack-and-pinion inerter and b) a ball-screw inerter.

et al. [5] developed and tested a full scale gear-pump inerter capable of producing an inertance of 10,000 tonnes. The total mass of the device goes unreported but a worst case assumption (that of a block of solid steel taking up the same volume) puts an upper bound at 1.45 tonnes. A sketch of a gear-pump inerter is shown in Figure 2.7a.

A potentially more elegant design of fluid inerter was proposed by Swift et al. [103]. Here, as shown in Figure 2.7b, instead of requiring a flywheel to provide inertia, the fluid itself acts as a flywheel as it is forced through a helical channel. As with the gear-pump inerter, a parasitic damping force is observed, although here it is dominated by secondary flows caused by centrifugal force on the fluid. These secondary flows can be characterised using the Dean number. The analysis shows that this leads to a quadratic pressure loss, which dominates other comparable phenomena, such as entry and exit losses and leakage. It should be noted that the model used by Swift et al. is only relevant for tightly wound helixes [104], however, as there is little benefit to not tightly winding the helix, this is a fair approximation.

Other examples of inerters making use of fluid exist. Titurus [105] proposed the meander-type fluid inerter, where the fluid is forced around a meandering path as shown in Figure 2.8a, rather than a helical channel. This might be realised by rearranging existing fluid lines in a system. Hwang [106] proposed increasing the resistive force of a ball-screw inerter by submerging the flywheel in a viscous fluid, as shown in Figure 2.8b. This idea was extended recently by Ma et al. [107], who proposed a novel design, using a turning plate. These designs may alternatively be referred to as *rotational inertia dampers*. Due to the inherent parasitic damping inherent to this kind of inerter, this terminology is equally valid and the choice of terms is a matter of preference.
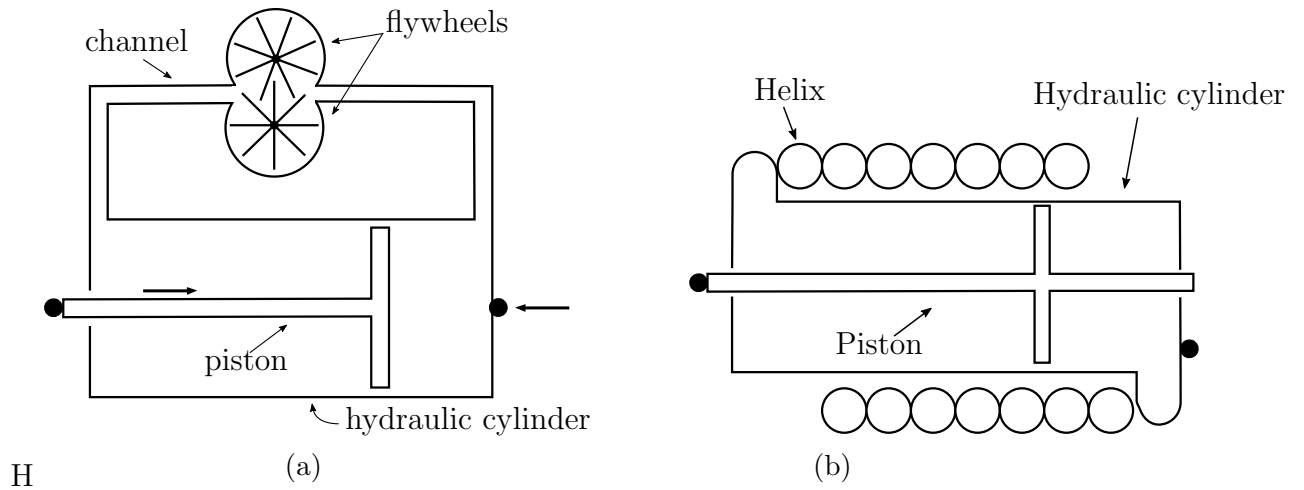
channel

flywheels

piston

hydraulic cylinder

H

(a)

Helix

Hydraulic cylinder

Piston

(b)

Figure 2.7: Sketch diagrams of a) a gear-pump inerter and b) a helical inerter.

Meandering channel

Piston

Hydraulic cylinder

(a)

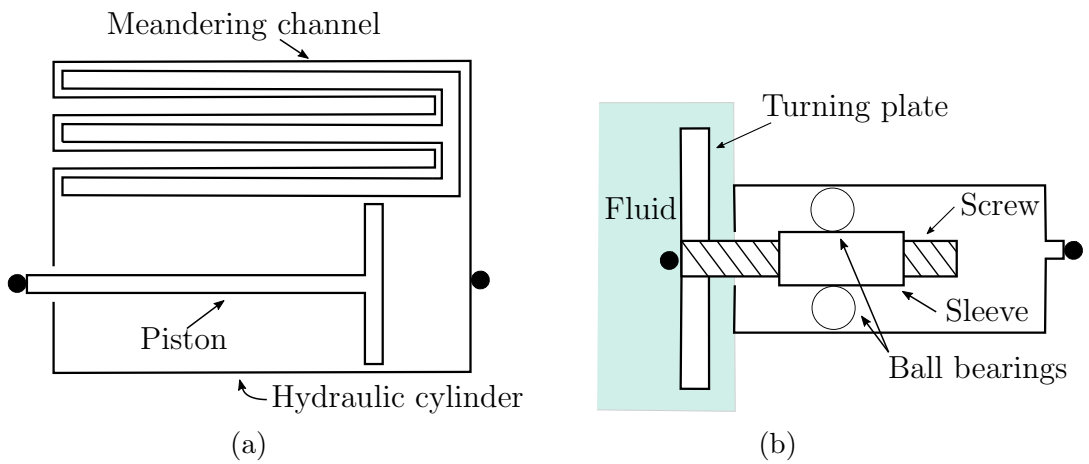Turning plate

Fluid

Screw

Sleeve

Ball bearings

(b)

Figure 2.8: Sketch diagrams of a) a meander inerter and b) a rotational inertia damper.

2.3.3 Uses

Inerters found commercial success in Formula One racing, where a ball-screw type was code-named the J-damper and deployed in 2005 by McLaren Racing [108], [109]. Smith [99] describes how the goal was to achieve a similar improvement in mechanical grip (ability of the suspension to maintain tyre contact with the road surface) to a mass damper device. Due to the secretive nature of elite motor racing and the fact that most of the limited reporting is from non-academic sources, it is hard to know how effective the inerter-based solution was.

Smith and Wang [110] numerically investigated how passive inerter systems could benefit vehicle suspension, looking at three different performance measures. These were J1 (ride comfort), J3 (mechanical grip) and J5 (ability to withstand dynamic loads), as well as a multi-oriented measure, based on J1 and J5. Improvements were reported of up to 9.26% in J1 and 6.53% in J3 over a conventional spring-damper suspension, depending on the layout. It should be noted that the optimal parameters for each of these measures are different to one another and that the results were not compared to a mass-damper solution. Scheibe and Smith [13] furthered this work, forming analytical equations, focusing on the J1 and J3 measures. This work validated Smith and Wang's numerical optimisation. Recently, Zhang et al. [111] noted that, despite these benefits, the inerter is still yet to be widely adopted in passenger vehicle suspensions. They ascribe this lack of adoption to previous optimisation solutions either ignoring some vital phenomena or leading to layouts with infeasible numbers of elements. To remedy this they conducted an optimisation study using using a structure-immitance approach [112]. This identified a different optimal layout to that found by Smith and Wang, with a 15% improvement in the J1 measure. Whether this is sufficient to lead to widespread adoption in passenger vehicles remains to be seen.

The use of inerters has been studied in other vehicle types, with Wang and Liao [14] conducting a feasibility analysis on the potential to increase the critical speed of trains, followed up with experimental testing by Wang et al. [113]. More recently, Lewis et al. [114] proposed a combined ball-screw inerter and 'Hall-bush' device, to improve passenger comfort and track wear. Evangelou et al. [115] proposed an inerter-based steering compensator for high-end motorcycles, a device which was then tested by Jiang et al. [15]. Patents have also been filed [116], [117] for mechanical inerter-based devices for managing flutter in aircraft.

The other major sector in which inerters have found use is in vibration control of structures. Such efforts include the 'Rotational Inertia Damper' proposed by Hwang

et al. [106], which is effectively a ball screw inerter with the flywheel submerged in fluid to provide a damping effect. The researchers note that increasing building mass, as required by a tuned mass damper, is not desirable in the case of earthquakes and potentially less economical for wind induced vibration. Lazar et al. [71] proposed the 'tuned inerter damper' to make clear the analogy with TMDs. They developed a tuning strategy and showed that the optimal location for such a device would be at the bottom of a building, as compared to the tuned mass damper, which is best located at the top. A hybrid device, the tuned mass damper inerter (TMDI), proposed by Marian and Giralis [118], consisting of a conventional tuned mass damper with an inerter included in parallel with the stiffness and damping elements, has also received some attention in this context in recent years [119].

Other uses of inerters for civil structure include TMDIs for reducing vortex-induced vibrations on bridges, which Xu et al. [11] concluded was slightly less effective than a tuned mass damper but more practical, as reduced stroke length means it would require a smaller space to work in. A similar use of the TMDI to control the vibration of wind turbine blades was investigated by Zhang and Fitzgerald, who also showed a slight decrease in performance compared to the tuned mass damper but reduced stroke length. Lazar et al. [120] proposed the use of TIDs to reduce cable vibration, where the mass magnification effect would make them a preferable option to TMDs on suspension bridges, for example. Ma et al. [12] proposed the 'Tuned Heave-Plate Inerter' to control heave motion induced on semi-submersible platforms by the surrounding water. More recently, a different kind of inerter-based vibration isolation system has been shown to be effective for this purpose [121].

The potential for inerters in machining science has only recently begun to be investigated in depth. Dogan et al. [22] conducted a numerical optimisation study for four different layouts of TMDI for chatter control. They employed a self-adaptive differential evolution algorithm to optimise the parameters, seeking to minimise the negative real part of the FRF, and then compared the improvements to the results from a closed-form analytical solution, which sort to minimise vibration amplitude. Using the numerical optimiser, an improvement in critical depth of cut of up to 37.19% was reported, compared to using a tuned mass damper alone. The numerical optimisation was shown to be better in this case than the closed form equations.

2.3.4 Tunable and semi-active inerters

In recent years, there has been an increasing amount of research dedicated to inerters with variable properties. It makes sense to refer to two main categories here: tunable

inerters, and semi-active inerters. Tunable inerters are passive inerters which can be adjusted off-line to vary the inertance. In contrast, with a semi-active inerter the inertance itself can be varied on-line, even if this also causes other properties to vary. Additionally, certain devices have been described as semi-active inerters but could more accurately be thought of as inerters with a semi-active damping component.

Tunable inerters include a helical inerter with an adjustable helix, proposed by Smith [122]. Here, the helix must be disconnected and replaced to adjust the inertance. Recently, Liu et al. [123] proposed a design of helical inerter which employs a bypass valve to provide a two-state device. While, making use of electromagnetic valves, it may be possible to employ this in a semi-active manner [124], most control schemes would require greater precision. There appears to be a gap in the research for more designs of tunable inerter, although this might be due to the fact that true semi-active inerters would also be able to be used as tunable inerters and are of greater interest in general. Nevertheless, it is possible to envisage the value of a low power or unpowered device with tunable inertance, to provide for greater flexibility at low cost.

Hu et al. [125] proposed a general model of the inerter through which to investigate controllability. In this model, the inertance is a product of two variables: the moment of inertia of the rotating element[7], and the transmission ratio between this element and the linear motion. Either (or presumably both) of these elements could be used for control. As discussed, the rotating elements are generally flywheels or rotating fluid. The transmission ratio depends on the gear ratios in a rack and pinion inerter, the pitch of the screw in a ball screw inerter, and the ratio the area of helix to piston in a helical inerter.

Devices which control the transmission ratio include a magnetic planetary gearbox design proposed and tested by Tsai and Huan [126]. Used in feed-forward control mode, varying the gear ratio allows the effective inertia of the device. While not a semi-active inerter in itself (the relative acceleration is rotational not linear), the planetary gear system could be employed within a mechanical inerter. Despite the fact that this was the authors' motivation, there is no record in the literature of this *variable inertia device* actually being employed in this way.

Brzeski et al. [127] proposed a device using a continuously variable transmission. This allows the inertance of the device to be steplessly varied. The motivation for this was ease of tuning and not semi-active control. Nevertheless, a continuously variable

---

[7]With one vaguely notable exception [105], the vast majority of inerters make use of a rotating element, for reasons of both functionality and practicality

transmission with a sufficiently low latency could be employed to achieve this. In testing a tuned mass damper using the variable inerter as part of its implementation [128], Brzeski et al. reported an inertance range of 2.4kg to 12.0kg.

Hu et al. [125] proposed a design of ball screw inerter, where the flywheel contains mass elements, the radial position of which can be adjusted using a linear actuator. A test device, with an inertance range of 99kg to 316kg was built and shown to be effective at 'perfect cancellation' control of single frequency vibration, using either frequency or phase tracking. The system was shown to be able to cope with a change in excitation frequency from 1Hz to 1.6Hz and (in a separate test) with a 43.6% change in the mass of the host structure. The linear actuator can move at 15mm/s, presenting a practical limit to the speed at which the inerter can be varied.

Zhang et al. [129] proposed a semi-active fluid inerter, using an internal helix with adjustable length. The design was modeled but does not appear to have been physically tested at the time of writing. A model was developed of this inerter as part of a car suspension to investigate the potential for skyhook control. The models revealed that this was effective at lower frequencies but that at some higher frequencies the system would offer worse performance than a passive suspension.

Zhong et al. [130] proposed a ball-screw design, where the flywheel contains magnetorheological fluid. The authors claim an "effective inertance", derived from the total force provided by the device divided by the acceleration. However, the inertance of the device is constant and the semi-active force is provided entirely by the magnetorheological fluid. Zhong et al. base their characterisation of the device on the Bingham fluid model and as such, the semi-active force is proportional to the velocity (making it a damping term). A compensator, consisting of a semi-active damper in series with a rack and pinion mechanism, in parallel with the 'semi-active inerter', causing the semi-active force to become in phase with acceleration. Whether or not this device counts as a true example of a semi-active inerter depends on definition.

Bonello [131] gives five attributes that designers of adaptive tuned vibration absorbers should aim for in their devices:

1. Low structural damping.

2. Minimal redundant mass from the actuation mechanism.

3. Ability to be retuned over a wide range of frequencies.

4. Rapid, low power retuning.

5. Cheap and simple to design and manufacture.

While these attributes are intended for vibration absorbers in general, there is no reason not to apply them to inerter-based vibration absorbers in particular. No comparison using these metrics has yet been made in the literature of the few designs of controllable and semi-active inerter currently available.

2.3.5   Optimisation and control of inerters

Optimal design of inerter-based vibration absorbers and isolators is an area of some interest, as the strategies are distinct from those for mass-based devices. Hu et al. [125] developed analytical solutions for different layouts of isolator, using fixed point theory. This theory states that, for lightly damped SDoF systems with an attached vibration absorber, there will be two peaks in the response function which are fixed, in that their frequency does not depend on the damping of the vibration absorber. Both H_2 optimisation (seeking to minimise total energy under white noise excitation) and H_∞ optimisation (minimising maximum displacement). Pietrosanti et al. [132] used numerical optimisation for a TMDI. As noted by Dogan et al. [22], these solutions are not appropriate for chatter control, as this requires minimising the negative real part of the transfer function only. In addition, the applicability of these to a semi-active system, where the properties can be changed online greatly depend on the type of vibration anticipated. For example, if random vibration is expected, then H_2 optimisation holds. However, if the vibration frequency is over a known range, then it may be possible to improve on the results given from fixed point theory for a passive device.

Hu et al. [125] investigated two control methods for their semi-active inerter based adaptive tuned vibration absorber. Frequency tracker based control uses the perfect cancellation condition to adjust the inertance, while phase detector based control seeks to adjust the inertance to achieve a 90° phase difference between the mass and the inerter connection point. The former method requires a single sensor, while the latter requires two. Testing showed that frequency tracker control performed better but was more sensitive to noise in the disturbance force. The authors did note that the experiments were designed to show that either method was possible and not to provide a systematic comparison.

Zhang et al. [129] used a skyhook control strategy using a continuously variable helical inerter. Using a quarter car model, they reported some improvements over a passive system, although said improvements appear to be small and limited to certain frequencies, with performance reductions at higher frequencies.

Wang et al. [124] proposed two strategies for a vibration absorber containing an inerter which could switch between a minimum and maximum value. These strategies were called relative acceleration relative velocity (RARV) and relative acceleration absolute velocity (RAAV). Analytical and numerical studies showed that, given equal inertance ranges, RARV achieved the best reductions in relative displacement, absolute displacement and absolute displacement transmissibility. However, if only a small inertance range is possible, then RAAV can achieve better results. Wang et al. [133] went on to further investigate the RARV control strategy, as applied to a quarter vehicle model. They differentiated the control scheme into two sub-schemes: $RARV_{+-}$ and $RARV_{-+}$, with the former achieving better dynamic tyre load and suspension stroke length, at the cost of relative acceleration, and the latter achieving the reverse.

2.4 Magnetorheological fluids

Magnetorheological fluids - and the closely related electrorheological fluids - were first studied in the mid 20th century. However, until more recently, using either in engineering applications were considered impractical. A recent revival of interest in the area has lead to magnetorheological dampers in particular becoming a well-established method of semi-active vibration control. Various formulations of magnetorheological fluid are available, some of which are compared in this section. This comparison is followed by a discussion of the different 'modes' of use, a useful concept for categorising the different devices available. An overview of some of these devices is presented, followed by a more detailed look at the models of dampers in particular. As this thesis is concerned with the design of a magnetorheological device, the section concludes with a look at some of the methods used by previous designers of such devices.

2.4.1 Overview

Magnetorheological (MR) materials are a class of smart material, where the viscosity can be controlled using a magnetic field [134]. They consist of non-colloidal, magnetically responsive particles (often iron or iron-carbide), suspended in a magnetically inert matrix material. When the magnetic particles encounter a magnetic field, they create chain-like structures, increasing the effective viscosity of the matrix.

The matrix material is most commonly [134] a fluid, with the resultant mixture called a magneto-rheological fluid (MRF). Elastomers can also be used as the matrix material, with the higher viscosity in the absence of the magnetic field aiding in

fail-safe devices [135]. Magnetorheological foams also exist, in which a MRF or MR elastomer is used to soak a spongy material, such as a metal foam [136].

MRFs sit alongside electro-rheological fluids (ERFs). Both were discovered nearly concurrently but separately, with MRFs being attributed to Rabinow in 1948 [137] and ERFs to Wimslow [138], who filed a patent in 1942 for it to be granted in 1947. Both materials are also very similar in the way they operate, with ERFs reacting to a electric, rather than magnetic field. Besides this technical distinction, ERFs also exhibit a more rapid response and simpler control, but also offer a lower yield stress than MRFs [139]. Olabi and Grünewald [140] summarised the key differences between ER and MR fluids, presented in Table 2.1.

For much of the previous century, there was a lack of research surrounding MRFs [134] and so much of the foundational literature and underlying models concentrate on ERFs.

2.4.2 Magnetorheological fluid formulations

The three main components of MRF are the magnetic particles, base fluids, and additives [141]. The magnetic particles are the magnetically active component, forming into chain-like structures when they encounter a magnetic field. The base fluid acts as a carrier and a lubricant, as well as providing damping in the conventional manner. Additives are included to improve various properties, including friction, corrosion, sedimentation, and viscosity. All three of these components affect the behaviour of the fluid in both its off- and on-state [140].

Carlson [134] gives the typical range of sizes for the magnetisable particles to be 10^{-7}-10^{-5}m. This size allows the fluid to be stable and highly magnetisable, in comparison to the ferrofluids, which use smaller particles. According to a recent review by Morillas and Vicente [142], the most common particle material is carbonyl iron powder. Other materials found in the literature include iron nano particles [143];

Table 2.1: MRF vs ERF, from Ref. [140].

Representative feature	MRF	ERF
Maximum yield stress	50-100kPa	2-5kPa
Power supply	2–24V, 1–2A	2–5 kV, 1–10 mA
Response time	Some millisecond	Some millisecond
Operational field	250 kA/m	4 kV/mm
Energy density	0.1 J/cm3	0.001 J/cm3
Stability	Good for most impurities	Poor for most impurities
Operational temperature	-40°C up to +150°C	-25°C up to +125°C

hexagonal, cobalt-nickel 'nanoplatelets' [144]; nickel 'nanowires' [145]; and magnetic carbon nanoparticles [146]. The common aim of developing these materials is to reduce particle mass, thereby reducing the reliance on additives which commonly reduce the shear stress.

Carrier fluids include petroleum-based oils, mineral oils, silicon oils, polyesters, polyethers, synthetic hydrocarbons, and water [134]. According to Olabi and Grünewald [140] "the viscosity of the fluid should be small and almost independent of temperature". Recently, Bigué et al. [147] have proposed that the choice of carrier fluid can also affect the durability of MRFs in clutches. Specifically, for fluids with a Mason number[8] higher than 1.0, the durability appears to relate to the carrier fluid, rather than the fatigue of the particles.

Additives are used in MRFs to prevent sedimentation, increase stability, enhance lubrication, and reduce the off-state viscosity [149]. Preventing the sedimentation of the dense particles is a popular topic of research. Additives which have been studied for this purpose include lauric acid and myristic acid [150], polyacryilic acid polymers [151], and polypropylene glycol [152].

To contextualise the effects of varying the composition of MRFs, Table 2.2 summarises the properties of the five MRF formulations commercially available from the Lord Corporation, and the two from Liquids Research Limited. Figure 2.9 shows the yield stress for the Lord fluids (data was not available for the Liquids Research fluids). These are estimated from technical data sheets and meant for comparison only. The exact compositions of these fluids are not given.

---

[8]a dimensionless quantity describing the breaking and reformation of the particle chains [148]

Table 2.2: Properties of commercially available MR fluids.

Formulation	Carrier fluid	Viscosity (Pas at 40°C)	Density (gcm^{-3})	Operating temperature (°C)
Lord MRF140CG	Hydrocarbon	0.28	3.64	-40 to +130
Lord MRF132DG	Hydrocarbon	0.11	3.05	-40 to +130
Lord MRF122EG	Hydrocarbon	0.04	2.38	-40 to +130
Lord MRF126LF	Hydrocarbon	0.07	2.74	-40 to +130
Lord MRF140BC	Hydrocarbon	0.11	3.85	-40 to +130
LR MRHCCS4-A	Hydrocarbon	Not given	2.49	-40 to +140
LR MRHCCS4-B	Hydrocarbon	Not given	3.08	-40 to +140
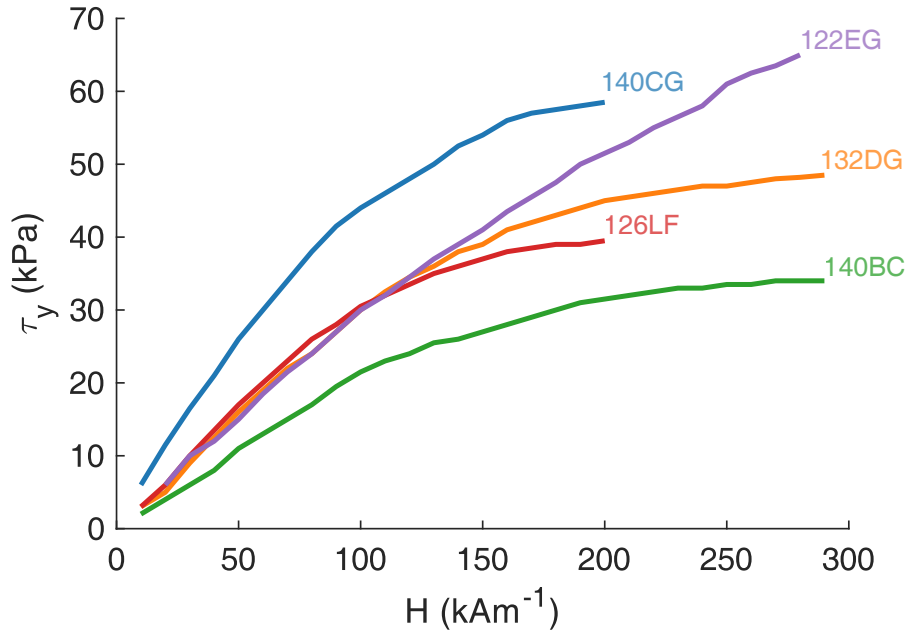
Figure 2.9: Yield stress against field strength for the commercially available Lord MRFs.

2.4.3 Magnetorheological fluid modes

The mechanism of MRF depends on both the orientation of the magnetic field with respect to the direction of the flow, and on the fluid-wall interaction. The different combinations of these effects are known as *modes* [153].

Conventionally [154], [134], [140], the main modes have been known as *flow mode*, *(direct) shear mode*, *squeeze mode* and *mixed mode*, in reference to based on the main practical uses of MR fluid in the automotive industry. In their recent review [142], Morillas and Vicente instead take a physics-based approach to categorisation. They use the categories of *shearing flow*, *elongational flow* and *mixed flows*, with various subcategories in each. These two categorisation schemes are mostly mutually compatible, as shown in Table 2.3 and so use of either is a matter of preference. Here, Morillas and Vicente's categories are broadly followed for completeness. However the terms 'flow' and 'shear' mode are retained, despite the semantic ambiguity, to maintain consistency with the majority of the literature.

Shearing flow involves the fluid travelling parallel to a surface, causing a shearing effect. This is a common condition in dampers. If the flow is relative to both channel walls of an annular valve [154] (or multiple walls in a porous channel [155], or the single wall of an orifice valve [156]) then this is known as *valve mode*. This kind of

30

Table 2.3: Comparison of the two categorisation schemes for flow modes.

Direction of movement	'Physics-based' category	'Physics-based' subcategory	'Use-based' category
Along surfaces	Shear	Capillary flow Drag	Valve mode Direct shear mode
With surface	Elongational	Slow squeeze Cyclic squeeze Extensional	Squeeze mode -
Both	Mixed flow	-	Mixed mode

flow is characterised by a flattened, curved flow profile, as shown in Figure 2.10a [154]. If, instead, the flow is only relative to one out of two surfaces (i.e. between a piston head and a cylinder wall [157]), the it is known as *shear mode*. Shear mode flow is characterised by a trapezoid profile, as shown in Figure 2.10b [134].

Figure 2.10: Examples of a) valve mode and b) shear mode flows.

If the fluid instead moves in tension or compression, the behaviour is very different. If the fluid undergoes quasi-static compression, under *slow squeeze mode*, an additional strengthening effect is observed [158]. Kordonski and Gorodkin [158] attribute this to enhanced elasticity of the fluid, while Ruiz-López et al. [159] have developed a micromechanical model which takes into account the local magnetic field around each particle. If the fluid is repeatedly compressed and relaxed in *cyclic squeeze mode*, increasing frequency is correlated with a small drop in the peak force experienced [160]. MRFs have also been investigated under *extensional mode*, to create a controllable adhesive [161].

Using a combination of other modes is known as *mixed mode*. Yazid [162] created a damper which employed both valve and squeeze modes, leading to a spike in force at the end of the piston travel. Mixed shear-squeeze mode has also been investigated [163].

2.4.4 Magnetorheological fluid devices

The renewed focus of MRF over ERF means the technology covers a range of readiness levels. In some areas, such as in automotive suspensions, MRF devices can be described as a widely available luxury [164]. In other areas, MRF has only been studied recently. To give a sense of the current areas of interest for MRF, Hua et al. [165] classified 104 articles on MRF which were published in the years 2018-20. The most popular area of study was dampers and mounts, covering 50% of papers studied. These were followed, in order from most to least popular, by brakes, clutches, medical rehabilitation devices, and medical haptic devices.

In the medical field, MRF is being studied for its use in haptic (sense of touch) sensors, and for 'smart orthoses' to rehabilitate limbs of patients who have suffered a stroke. Haptic devices are studied in the context of robotic surgery [166] or catheterisation [167]. These are areas in which the increased stability offered by the robot over a human is desirable but the loss of the sense of touch can increase the risk of injury to the patient. Force sensor signals from the operating robot are sent to MRF brakes or clutches by the controller, to simulate the resistance of tissue. Feedback can be purely haptic [168] or a mixture of haptic and visual [166]. Haptic devices require low off-state friction, constant force with constant input, and quick response even at low speeds [169].

Rehabilitation devices work to deliver resistive forces, to replace or supplement traditional physiotherapy [170]. As such, they are designed around the joints found in the body, namely rotary [171], and ball and socket [170]. MRF prostheses [172] and tremor-supressing exoskeletons [173] have also been studied.

The MRF clutch was designed [137] and patented [174] in the late 1940s by Rabinow. Here, the fluid is used in direct shear mode, to bind the two plates of the clutch together. The MRF clutch was noted for having a smooth action, having no discontinuities, and being easy to build due to its lack of axially moving parts. However, low quality MRFs and inability to accurately assess the magnetic field meant that MRF clutches did not find application for many years [175]. More recently, designs using permanent magnets have been studied [175]. A prototype MRF clutch has been developed for motorcycles, which uses 'slits' in the plate to generate a lift force [176].

MRF brakes are a more recent development, proposed by Li and Du in 2003 [177]. The design consists of a brake-disk submerged in MRF. This means the braking force can be controlled by the current to the electro-magnet, creating a 'brake-by-wire' design which can be more easily integrated with other electrical control systems in the vehicle [178]. Karakoc et al. [179] presented an optimisation scheme for MRF

brakes, making use of a 'simulated annealing' random search algorithm. Nguyen and Choi [180] expanded on this, using a finite element integrated optimisation method to take into account additional geometric parameters, as well as off-state friction and heat. They showed that a single disc design is insufficient for a medium sized car but a two disc design makes sense. Smaller MRF brakes for motorcycles [181] and miniature turbines [182] have also been proposed.

MRF has been used in the creation of various semi-active dampers, isolators, and engine mounts. These devices generally employ the fluid in similar ways, although differing in the exact design and usage. At least as far back as 1995, MRF devices were being designed for vehicle seat suspension and building seismic isolation [183]. Designs exist which employ the fluid in flow mode [184], squeeze mode [185], and mixed-mode [162]. In general flow mode devices are simpler to design but offers higher efficiency [186]. Pure squeeze mode is used for contexts involving small (mm level) scale vibration [187].

Yokata et al. [188] presented a pressure control valve for hydraulic systems, which uses MRF as the working fluid. This was different in design to the annular valves conventionally used in dampers, featuring a cylindrical flow channel between two magnetic poles. This can be contrasted to the similar 'orifice' valve evaluated by Grünewald and Olabi [156]. The orifice design was shown to have a strictly worse pressure-current relationship than a similarly dimensioned annular valve. It should, however, be noted that the valve designed by Yokata et al. was created with miniaturisation in mind and might have use at smaller scales. More recently, Salloom and Samad [189] built on prior work by Yoo and Wereley [190] to design a 4/3 MRF directional control valve, with a focus on simplicity and compactness.

2.4.5   Magnetorheological damper models

Various models have been developed over the years to characterise the behaviour of MRF and MRF devices. Of these, the simplest is based on a Bingham plastic model of the fluid. Bingham have a viscosity, which defines the ratio between flow rate and stress, in the same manner as a Newtonian fluid. However, Bingham fluids also exhibit a yield stress - a critical stress value, below which no flow occurs [191]. These leads to a stepwise behaviour, as shown compared to a Newtonian fluid in Figure 2.11.

Wereley and Pang [154] made use of the Bingham model in a nondimensional analysis of annular MR dampers. Approximating the annular channel as two flat plates, they characterised the dampers using three nondimensional measures:
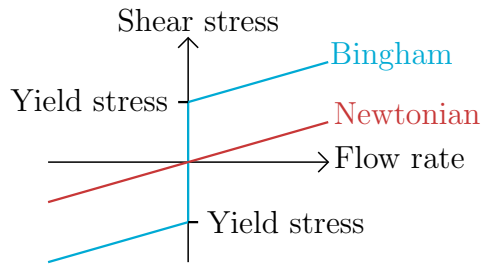
Figure 2.11: Comparison of the stress-flow relationship for a Bingham and Newtonian fluids.

- the proportion of the channels consisting of fluid in the pre-yield region, known as the *non-dimensional plug thickness*;

- the *Bingham number*, which describes the ratio of the yield stress to the viscosity; and

- the ratio of areas of the piston head and the channel.

For flow mode dampers, this scheme is functionally equivalent to a pre-existing one developed by Stanway et al. [153], which described the fluid in terms of the friction coefficient, Reynolds number, and the Hedstrom number. However, the Wereley and Pang scheme is more easily able to generalise to mixed-mode dampers.

A wide number of dynamic models of MR dampers have been developed over the years to improve on the accuracy of the quasi-static model. In their recent review, Rossi et al. [192] divide these models into three categories: dynamic parametric, dynamic non-parametric, and dynamic and inverse dynamic.

Commonly used dynamic parametric models include: the Herschel-Buckley model [193], which accounts for shear thinning in the post-yield regime; the Bouc-Wen model [194], modelling the hysteretic behaviour observed in some dampers; and a biviscous hysteretic model [195]. Good discussions of the advantages and disadvantages of each model have been written by Rossi et al. [192] and, more briefly, by Yang et al. [195].

Inverse dynamic models aim to directly relate the valve force to the input current, either by using neural networks [196] or by using an identification algorithm [197]. Dynamic non-parametric models, on the other hand, aim to use experimental data to fit a function or functions to the behaviour of the valve. Examples include polynomials [198], fuzzy [199], blackbox [200], and neural network [201] models. While these types of inverse and non-parametric models may successfully be used to control specific dampers, they don't seek to describe the physics involved and so are of little use in a priori predictions.

2.4.6 Design of magnetorheological devices

In the abstract, the design of magnetorheological devices is a matter of optimising the geometry to provide the best performance. As there are a number of parameters to be studied, and they have a non-linear relationship to the magnetic field strength, fully unconstrained optimisation can be costly. MR device design, therefore, is either a matter of constraining the parameters to limit the parameter space to be searched, using numerical optimisation techniques to efficiently search the parameter space, or often a mixture of both methods.

Rosenfeld and Wereley [202] used the Bingham model and parallel plate assumption to create an optimisation scheme for annular valves constrained in length, radius, and gap height. The scheme aimed to maximise the on-state damping coefficient of the valve. The authors showed that, given these constraints, the problem collapses down to a one dimensional, discrete optimisation curve as a function of the number of wire wraps used. The speed and simplicity of this method makes it useful for prototype valve design, although it is less useful when the design goals differ from those of damper design. The decision to limit the gap height to a fixed parameter also seems relatively arbitrary, given that this value has a cubic impact on the damping coefficient.

More advanced optimisation methods have been used in other cases. Naserimojarad et al. [203] provide a good, if brief, review in the introduction to their recent paper seeking to provide a comprehensive approach to MR damper optimisation.

For an MR brake, Park et al. [204] compared a simulated annealing (SA) algorithm to methods built into the Ansys computational finite element analysis suite: subproblem approximation and first order method. They showed that, while SA yielded some modest improvements, this came at the cost of a computing time of 100 hours, compared with 20 minutes and 4 hours for the other approaches, respectively.

Also studying an MR brake, Younis et al. [205] applied the Space Exploration and UniModal Region Elimination (SEUMRE) global optimization algorithm. The algorithm resulted in a maximum braking force c. 10% higher than that created by a genetic algorithm and c. 10% lower than the one supplied by SA. However, the run time of SEUMRE was around a third of the genetic algorithm and a quarter of that of SA.

2.5 Summary

In this chapter, the literature of three, largely disparate, areas are reviewed. In Section 2.2, the importance of controlling chatter in an effective manner is established. A selection of models are bpresented, some of which are revisited in Chapter 3. Following this, a review of existing chatter mitigation techniques are presented. The restriction of the (undeniably powerful) lobe-based techniques to certain speeds is discussed. Passive techniques which have been developed using inerter-based vibration absorbers are also discussed, as are the practical difficulties in tuning such devices. Finally, some active techniques are presented, with a focus on continuous spindle speed variation and impedance modulation. These techniques will be built upon in Chapter 3, where the concepts of discrete and continuous inertance variation are introduced. The wide variety of techniques discussed in this section underline the claim made by Munoa et al. [21] that chatter is a complex problem, which can be tackled from a variety of perspectives. As machinists seek to create increasingly complex parts, with ever greater efficiency, so they will require an ever expanding arsenal of tools with which to tackle chatter.

In Section 2.3, the research surrounding inerters is reviewed. The literature is still actively evolving in terms of both designs of and uses for inerters. In particular, the research of semi-active inerters is very recent, with all the relevant papers being published after the initiation of the current project. Of these, the best-established truly semi-active inerter is that presented by Hu et al. [125]. However, the use of electrical linear actuators inherently limits the rate at which inertance can be varied. It will be shown in Chapter 3 that a high rate of change would be required for continuous inertance variation. There is a clear gap in the literature for such a device. Much of this thesis is dedicated to the development of a candidate, which is modelled in Chapter 4 and designed and tested in Chapter 5.

The research on magnetorheological fluids presented in Section 2.4 is, in a way, more tangential to this work than the literature reviewed in Sections 2.2 and 2.3. Much of the research presented- especially the Bingham fluid model developed for valve flow [153], [154] and the MR valve design optimisation scheme [202] - is fundamental to the work in Chapters 4 and 5. However, unlike with chatter mitigation and inerters, it is not the goal of this thesis to contribute to this area of the literature. Nevertheless, some small contribution can be found in Chapter 4, in terms of an optimisation scheme for an flow control valve.

Chapter 3

Chatter suppression using discrete and continuous inertance variation

3.1 Introduction

In this chapter, two different ways in which a semi-active inerter could be employed are investigated. These methods are inspired by the discrete and continuous spindle speed variation, discussed in Chapter 2. A linear chatter model will be used and the existence of an ideal semi-active inerter will be assumed. Discussion of the requirements of practical implementations for machining systems can be found in Chapter 6.

The causes of chatter can be dived into two parts: the system equation of the vibrating element, and the time delay between one pass of a tooth and the next. It follows, then, that chatter can either be tackled by changing the system equation or by tackling the time delay term. The former can be done through either physically modifying the system or changing the cutting speed. The latter approach can be achieved through the use of cutters with a helix which varies along the length, for example.

In this context, two different strategies present themselves for using a semi-active inerter to mitigate chatter. Both strategies involve changing the system equation, through adjusting the natural frequency of the critical element. Beyond this, however, both approaches are very different. By analogy with similar spindle speed strategies [45], [87], these approaches have been named *discrete inertance variation* (DIV) and *continuous inertance variation* (CIV) .

DIV is inspired by discrete spindle speed variation, an approach detailed in Ref. [206]. With discrete spindle speed variation, stable lobes are targeted by changing the tooth passing frequency, aiming for resonance. The concept behind DIV is to achieve

the same result, using a semi-active inerter to change the natural frequency of the system while keeping cutting speed constant. The exact placement of the inerter is left for future work but it could conceivably form part of active fixturing or a support for longer tools, such as boring bars. One benefit of this approach is that inertance could potentially be varied almost instantaneously during operation. Discrete spindle speed variation requires the spindle motor to briefly power down and restart at the new target speed. DIV could also have a place in operations where cutting speed is limited in some way, such as when cutting temperature is of concern. In addition, it does not inherently affect the material removal rate or machining time, as discrete spindle speed variation does. A combined approach might offer even more versatility but that possibility is not explored here.

CIV, meanwhile, targets the time delay term in a similar way to continuous spindle speed variation. With continuous spindle speed variation, a continuously changing spindle speed mitigates the regeneration effect of chatter. Segalman and Butcher [93] took a similar approach, who looked at continuously varying the stiffness of a boring bar using MR fluid. Continuous spindle speed variation is necessarily limited by the ability of the spindle motor to accelerate and decelerate rapidly. This could be less of an issue for CIV, depending on the design of the inerter. In addition, using an external device instead of modifying the tool directly could allow for different methods of implementation. The so-called mass magnification effect increase the size of the effect over that achievable with impedance modulation.

The goal of this chapter is to act as a feasibility study for both of these possible implementations, with a mind to the design implications of a semi-active inerter intended for either use. To this end, a simple, SDoF model of chatter is used. As discussed in Section 3.2, this model can be modified in future work to cover either turning or milling in more specific contexts.

In Section 3.2, the underlying theory of chatter is discussed, including the construction of stability lobe diagrams using linear stability analysis. The general system model is developed. Section 3.3 takes this model and investigates DIV through linear stability analysis. A potential strategy is proposed and the design implications discussed. Section 3.4 looks at CIV. Semi-discretisation, a method used to investigate continuous spindle speed variation, is assessed for its applicability to CIV. A time domain model is used to investigate the potential parameter space and the design implications are again discussed. Conclusions are then drawn about both methods and further work discussed.

3.2 Linear stability analysis and the stability lobe diagram

Linear stability analysis is a useful, first-order model of chatter. As a physics-based model, it can offer important insight into the underlying causes of chatter and how it might be mitigated. This section aims to provide a basic summary of linear stability analysis and define the nomenclature used in the rest of the chapter. This summary is based heavily on the excellent machining dynamics textbook written by Schmitz [44], while the following non-dimensionalisation is based on analysis by Insperger and Stépán [33].

While linear stability analysis - based on the work of Tobias and Fishwick [29] - is a well established technique, it does have its limitations. A good knowledge of the system transfer function is required, which can become impractical when the dynamics becomes more complex. Additionally, as might be expected, linear stability analysis cannot account for certain non-linear effects experienced in multi degree of freedom systems - e.g. in milling - such as secondary Hopf bifurcation and period doubling. The practical effect of these phenomena is to reduce the size of the stability envelope for these systems. Linear stability analysis also cannot deal with systems containing time-varying parameters, as discussed in Section 3.4.

Despite these limitations, linear stability analysis is a robust first approximation. Its analytical nature lends itself to providing understanding of the underlying physics in a way that experimental or numerical methods cannot match. While it can be expanded to consider higher degree of freedom systems, for this work it is sufficient to consider only the SDoF system. The underlying physics remains unchanged and this leads to an overall clearer explanation.

Linear stability analysis of a single degree of freedom system is based on two simultaneous equations[1]:

$$w_{lim} = \frac{-1}{2K_s \text{Re}(G(j\omega))} \tag{3.1}$$

$$\frac{f_c}{f_t} = N + \frac{\epsilon}{2\pi}, \text{ where} \tag{3.2}$$

$$\epsilon = 2\pi - 2\tan^{-1}\left(\frac{\text{Re}(G(j\omega))}{\text{Im}(G(j\omega))}\right). \tag{3.3}$$

---

[1]For convenience, the second equation is often separated into two parts as it has been here

Equation 3.1 defines the depth of cut at the limit of stability, w_{lim}, while Equation 3.2 defines frequency of the chatter, f_c, as a ratio of the tooth passing frequency, f_t. Together, these equations define a stability lobe diagram (SLD), of the kind in Figure 3.1. The remaining terms are introduced below, at the points they are required to derive Equations 3.1 and 3.2.
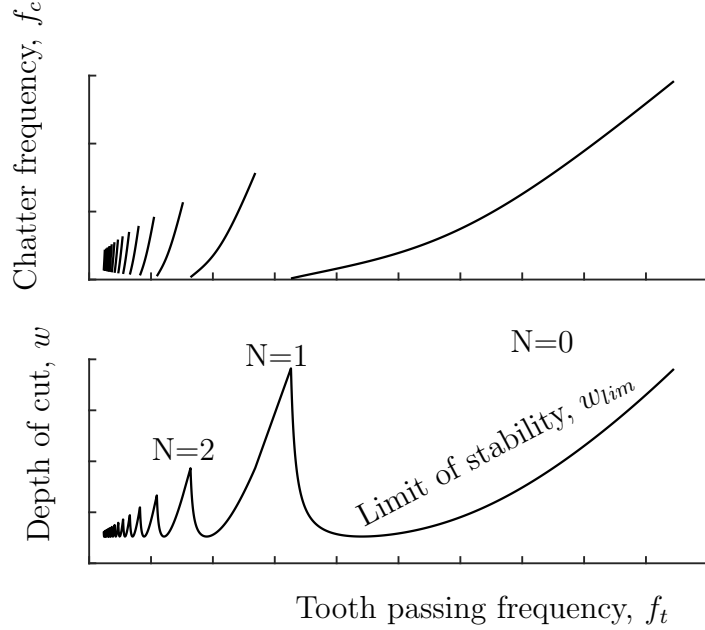
Figure 3.1: A demonstrative stability lobe diagram.

Equation 3.1 relates the transfer function to the limiting depth of cut, w_{lim}. The limiting depth of cut is the value above which the system becomes unstable. It depends on the specific cutting force, K_s, which is an empirical coefficient relating to material properties. Despite the name, the specific cutting force is measured in Nmm^{-2}. $Re(G(j\omega))$ and $Im(G(j\omega))$ are the real and imaginary components of the transfer function, $G(j\omega)$. The frequency ratio is $p = \frac{f_c}{f_0}$ and f_0 is the natural frequency.

Equation 3.2 is a standard way to describe the chatter frequency, as a proportion of the tooth passing frequency, $f_t = n_{teeth}\Omega$. This is the product of the number of teeth on the cutter, n_{teeth}, and the spindle speed, Ω, (here measured in Hz, although RPM is conventional in industry). This ratio is dependent on the *lobe number*, N, and the phase between one pass and the next, ϵ. The former corresponds to how many whole waves are left on the surface for during each rotation. The latter is described by Equation 3.3, again related to the transfer function.

From Equation 3.2, for a given lobe number there are a range of values the transfer function can take. Each of these corresponds to a unique pair of values of w_{lim} and

f_t. Plotting these pairs against one another creates the stability lobe diagram. What follows is a derivation of Equations 3.1-3.3, as well as a description of how they are used to create the SLD.

At any given point in time, the cutting force is proportional to the area of the chip being created. This is the product of the depth of cut, w, and the instantaneous chip thickness, $h(t)$. Although a nominal chip thickness, h_{nom}, is targeted, the difference in phase of the surface waves between one cut and the previous mean that this actually varies between maximum and minimum values, h_{max} and h_{min}, as shown in Figure 3.2. These depend on the current tool displacement, $y(t)$, and the displacement during the previous pass, $y(t-\tau)$, where $\tau = \frac{1}{f_t}$ denotes the tooth passing period. Thus, the cutting force has both a static and dynamic component

$$F = F_{static} + F_{dynamic} = K_s w h_{nom} + K_s w(y(t-\tau) - y(t)). \qquad (3.4)$$
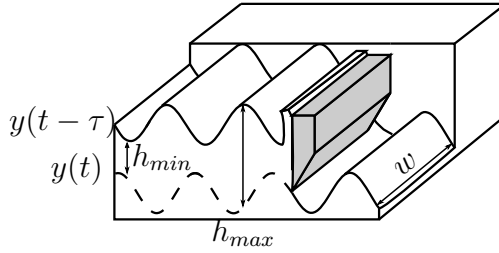
Figure 3.2: An example of how of the tool or work piece can cause chip thickness (h) to vary between a maximum at h_{max} and a minimum at h_{min}, while depth of cut (w) remains constant.

For the purpose of chatter analysis, only the dynamic force is of interest as, by definition, the static force is time invariant. The dynamic cutting force is counterbalanced by the dynamic forces of the system. These dynamic forces are described by

$$m\ddot{y}(t) + c\dot{y}(t) + ky(t) = K_s w(y(t-\tau) - y(t)), \qquad (3.5)$$

with m, c and k denoting the mass, viscous damping and stiffness of the system.

Equation 3.5 is a class of equation known as a delayed differential equation (DDE), due to the time delay term present on the right hand side. Assuming sinusoidal motion, $y(t) = Y \sin(2\pi f_c t)$ and $F(t) = |F| \sin(2\pi f_c t + \phi)$, with ϕ as the phase difference between the forcing, F, and displacement y. The amplitude of the displacement is Y. Taking the left hand side of Equation 3.5 in isolation and defining the natural

frequency $\omega_0 = \sqrt{\frac{k}{m}}$ and damping ratio $\zeta = \frac{c}{2\sqrt{km}}$ allows the admittance to be defined as

$$G(j\omega) = \frac{Y}{|F|} = \frac{1}{k(1 - p^2 + 2j\zeta p)}. \tag{3.6}$$

Here, j is the imaginary unit and ω is frequency in rads^{-1}. To simplify notation, the magnitude of the displacement at $t - \tau$ (i.e. at the same point during the prior pass) is denoted as $Y_{-\tau}$.

Equating the force term in Equations 3.5 and 3.6 returns

$$\frac{Y}{G(j\omega)} = K_s w(Y_{-\tau} - Y), \tag{3.7}$$

which with some rearrangement becomes

$$\frac{Y_{-\tau}}{Y} = \frac{\frac{1}{(K_s w)} + G(j\omega)}{G(j\omega)}. \tag{3.8}$$

The stability limit is defined as the depth of cut at which the amplitude of vibration is critically stable, i.e. neither increasing nor diminishing. This means that $\frac{|Y_{-\tau}|}{|Y|} = 1$ or

$$\left| \frac{1}{K_s w_{lim}} + G(j\omega) \right| = |G(j\omega)|. \tag{3.9}$$

Note that the depth of cut, w, has been replaced with the critical depth of cut, w_{lim}.

As both K_s and w_{lim} are real valued, the imaginary parts of both the left and right hand side of Equation 3.9 must be equal to one another. As such, there are only two possibilities: either $\frac{1}{K_s w_{lim}} = 0$, as shown in Figure 3.3a, or $\frac{1}{K_s w_{lim}} + \text{Re}(G(j\omega)) - \text{Im}(G(j\omega)) = -\text{Re}(G(j\omega)) - \text{Im}(G(j\omega))$, shown in Figure 3.3b. The first case implies that $w_{lim} = \infty$, which is incompatible with reality. The second, when rearranged, becomes

$$w_{lim} = \frac{-1}{2K_s \text{Re}(G(j\omega))}. \tag{3.1 revisited}$$

As shown in Figure 3.4, the displacement caused by the vibration during each period $\tau = \frac{1}{f_t}$ leads to some integer amount of surface waves, N, as well as a partial wave. By comparing the oscillation across one period to the previous period, it can be seen that this partial wave corresponds to the phase difference, ϵ, between y and $y_{-\tau}$, where

$$y = \sin(2\pi f_c) \tag{3.10}$$

$$y_{-\tau} = \sin(2\pi f_c + \epsilon). \tag{3.11}$$
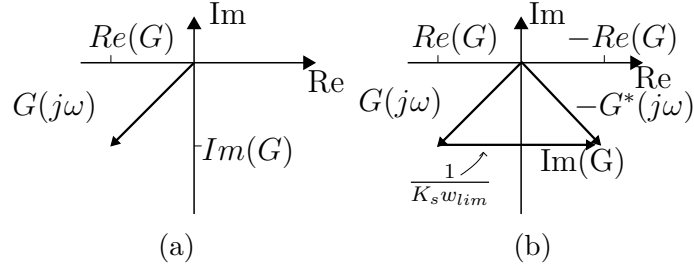
Figure 3.3: Vector diagram showing that, given $\frac{1}{K_s w_{lim}}$ must be real valued, the only possible solutions for any arbitrary transfer function is that it is (a) zero valued or (b) twice the value of the real part of the transfer function.

Thus

$$\frac{f_c}{f_t} = N + \frac{\epsilon}{2\pi}. \qquad \text{(3.2 revisited)}$$

This phase difference corresponds to the phase difference of the forces. It was previously shown that there is only one possible realisation of these vectors on the complex plane and so some trigonometry can be employed to show that

$$\epsilon = 2\pi - 2\tan^{-1}\left(\frac{\text{Re}(G(j\omega))}{\text{Im}(G(j\omega))}\right), \qquad \text{(3.3 revisited)}$$

as shown in Figure 3.5.

To construct the SLD, a range of frequency ratios are considered with a lower bound of $p = 1$, as only the negative part of the FRF is important. The upper limit is arbitrary, although it should be sufficient that the upper range of the first lobe intersects with the lower range of the zeroth lobe. From here, the FRF can be calculated and used in Equations 3.1 and 3.3 to find the limiting depth of cut and phase corresponding with each value. The tooth passing frequency corresponding to each value is found by using the definition of the frequency ratio in Equation 3.2

$$f_t = \frac{p f_0}{N + \frac{\epsilon}{2\pi}}, \qquad \text{(3.12)}$$

with a range of values for $N = 0, 1, 2....$

The limiting depth of cut is then plotted against the tooth passing frequency, as shown in Figure 3.6. Where this leads to two possible values for w_{lim}, the higher value is discarded. By convention and for the convenience of machinists, the tooth passing frequency is normally converted to the spindle speed in rotations per minute, $\Omega_{RPM} = \frac{60 f_t}{n_{teeth}}$.

An SdoF is generally sufficient for describing turning but to accurately capture milling two or more DoF models are required. Such models tend to lead to a reduction
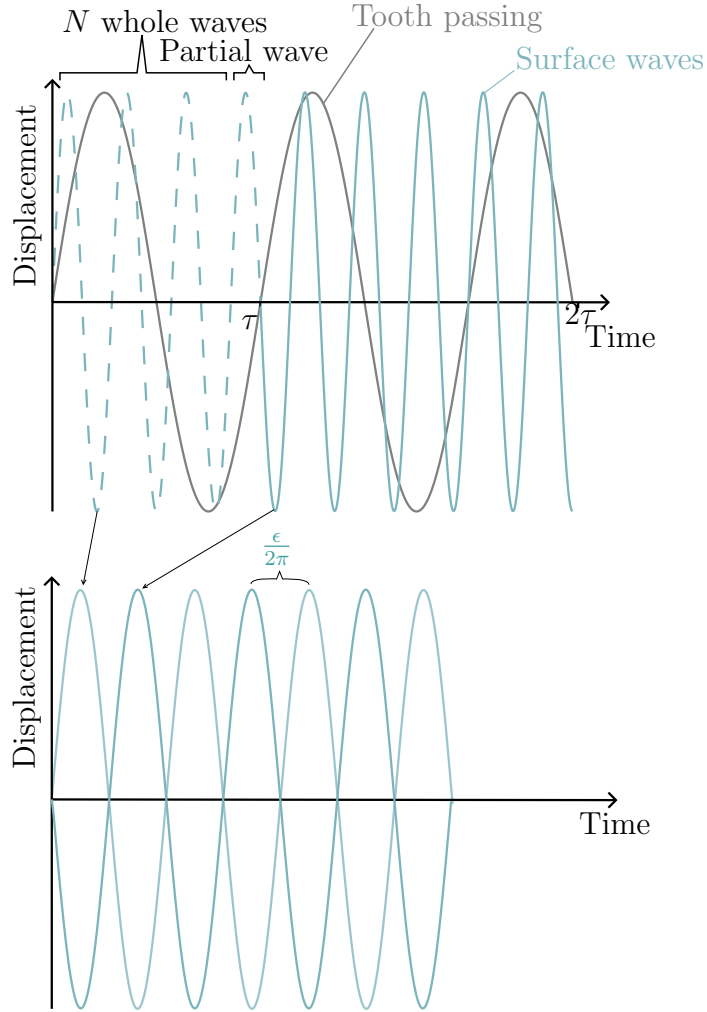
Figure 3.4: An example of how the vibration over one period and the previous period are out of phase by some amount, ϵ. This means that during each tooth passing period, τ, N whole waves and a partial wave are left on the surface. Transposing the vibration from one pass with that of the previous, as in the lower chart, shows how the length of this partial wave is proportional to the phase difference between them, ϵ.
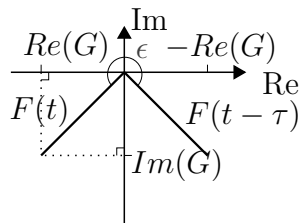
Figure 3.5: Vector diagram showing that the forces must be in phase with the vectors in Figure 3.3b. The phase angle is calculable using trigonometry.

44
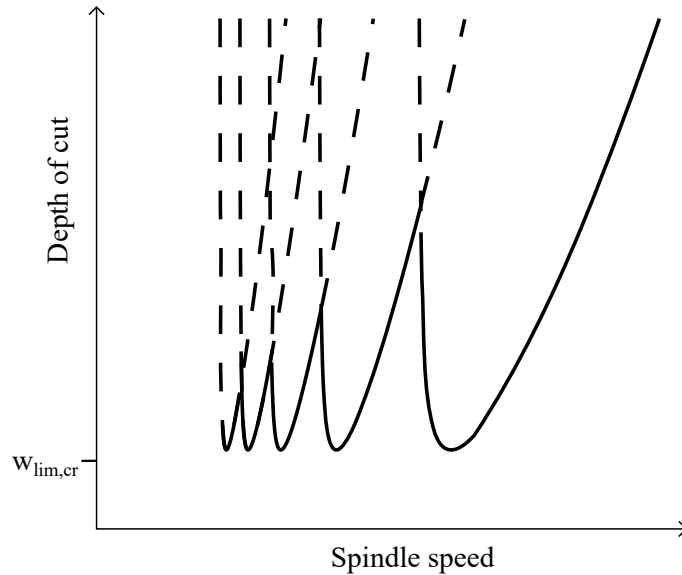
Figure 3.6: The construction of an SLD up to the fourth lobe. The dashed lines indicate values of w_{lim} to be discarded.

in the critical depth of cut but largely don't change the overall shape of the stability diagram.

This analysis can be extended to MDoF systems through choice of a different frequency response function. For milling, a common choice is a two dimensional *oriented transfer function* (OTF) [19], [44]. The OTF can be of an arbitrary degree of freedom as long as they are aligned into two perpendicular planes. This is the sum of two perpendicular transfer functions, orientated to the normal and tangential forces. As far as linear stability analysis is concerned, the rest of the analysis from Equation 3.6 is identical.

3.2.1 Non-dimensionalisation

Up until this point, everything has been defined in the conventional time domain. Transferring analysis to the non-dimensional time domain and introducing the non-dimensional depth of cut offers two advantages. The first advantage is greater generality, by describing systems in terms of their natural and tooth passing frequencies. The second reason to use the non-dimensional time domain has to do with the matrices used in semi-discretisation. Without non-dimensionalisation, the size of these matrices rapidly increases and overcome the available computational resources. The nomenclature is largely borrowed from that used by Insperger and Stépán, in their work on continuous spindle speed variation [33].

45

Non-dimensional time is defined by

$$\tilde{t} = \omega_0 t. \tag{3.13}$$

Maintaining the assumption of sinusoidal motion, $y(t) = Y\sin(\omega t) \implies y(\tilde{t}) = Y\sin\left(\frac{\omega}{\omega_0}\tilde{t}\right) = \sin(\omega\tilde{t})$ and introducing the non-dimensionalised delay term as $\tilde{\tau} = \omega_0\tau$, Equation 3.5 now becomes

$$\omega_0^2 m\ddot{y}(\tilde{t}) + \omega_0 c\dot{y}(\tilde{t}) + ky(\tilde{t}) = K_s w(y(\tilde{t} - \tilde{\tau}) - y(\tilde{t})). \tag{3.14}$$

Recalling the definitions of the natural frequency and damping ratio, it can be shown that $\omega_0^2 m = k$ and $\omega_0 c = 2\zeta k$. Using these substitutions and rearranging leads to

$$\ddot{y}(\tilde{t}) + 2\zeta\dot{y}(\tilde{t}) + y(\tilde{t}) = \tilde{w}(y(\tilde{t} - \tilde{\tau}) - y(\tilde{t})), \tag{3.15}$$

where $\tilde{w} = \frac{K_s w}{k}$ is the non-dimensional depth of cut.

For a hypothetical system with $k = K_s$ and $\omega_0 = 2\pi\mathrm{rads}^{-1}$, there is a one to one mapping between Equations 3.5 and 3.15 (i.e. $t = \tilde{t}$ and $w = \tilde{w}$). As there is no physical reason why a system that happens to have this specific set of parameters would operate differently to any other, the previous analysis holds. It should be noted that, under the new notation, Equation 3.1 now becomes

$$\tilde{w} = \frac{-1}{2\mathrm{Re}(G(j\omega))} \tag{3.16}$$

and that this cancellation of the stiffness term carries over to the admittance,

$$G(j\omega) = \frac{X}{\tilde{F}} = \frac{1}{1 - p^2 + 2j\zeta p}, \tag{3.17}$$

where $\tilde{F} = \frac{F}{k}$ is the scaled force term.

3.3 Discrete inertance variation

3.3.1 Discrete spindle speed variation

Creating accurate stability lobe diagrams is difficult, time consuming and requires good knowledge of the true dynamics of the system. Discrete spindle speed variation [45] removes this requirement by using a sensor to identify chatter and then targeting stable lobes using an algorithm. This does, however, require chatter to initiate so that the frequency can be identified. For this reason, it is more suitable for roughing

operations, where surface quality is less important, or for test pieces used to identify suitable system parameters. For discrete spindle speed variation to be effective, sizeable stable lobes need to be present. This means the operation needs to be in the high speed machining zone (zone C, as per Munoa et al. [21]). As such, the technique is more relevant for milling than turning [45], as the multiple cutting edges allow for larger lobes at lower spindle speeds.

The discrete spindle speed variation algorithm, summarised in Figure 3.7, uses as its inputs the depth of cut, w, spindle speed, Ω, and the chatter frequency, f_c. The first two are set by the operator and so can be assumed to be known. The chatter frequency can be identified through various means, such as accelerometers [207] or sound data [57]. New methods to rapidly identify and process the signal are a developing topic in the literature. The algorithm makes use of the twin facts that 1) there is a unique mapping between the chatter frequency and the stability limit for each lobe and 2) the most stable spindle speeds are around resonance.

Figure 3.8 shows an example of this. The SLD is shown on the lower chart, with the corresponding chatter frequencies shown above. The machine used has a maximum spindle speed such that the tooth passing frequency cannot be higher than 0.5. An operation is started at point a: $\tilde{w} = 0.5$, $\tilde{f}_t = 0.2$. This is unstable and so chatter at $f_c = 1.1$ is detected. The system stops and seeks to move the tooth passing frequency to this value but cannot, as it is above the maximum achievable. The second harmonic is also too high so $\tilde{f}_t = 0.37$ is selected, the third harmonic at point b. This is again unstable and chatter is now detected at $\tilde{f}_c = 1.3$. Again the system stops and moves the tooth passing frequency to the third harmonic, $\tilde{f}_t = 0.43$, point c. This value is stable and so the algorithm stops.

Wang and Fei [78] and Mei et al. [79] have proposed boring bars containing ER and MR fluid, respectively, which would be capable of an equivalent process by the natural frequency (via stiffness) of the system. This would be of interest for situations when varying spindle speed is not an option, such as with materials with low machinability. However, neither paper suggests an equivalent algorithm to discrete spindle speed variation.

It is proposed that a semi-active inerter set between the vibrating element and ground would also be able to modify the natural frequency of the system in this way. The implications of this idea are explored in this Section, with the goal of investigating the design requirements the method imposes. While a potential algorithm is proposed, no claims are made to its efficiency.
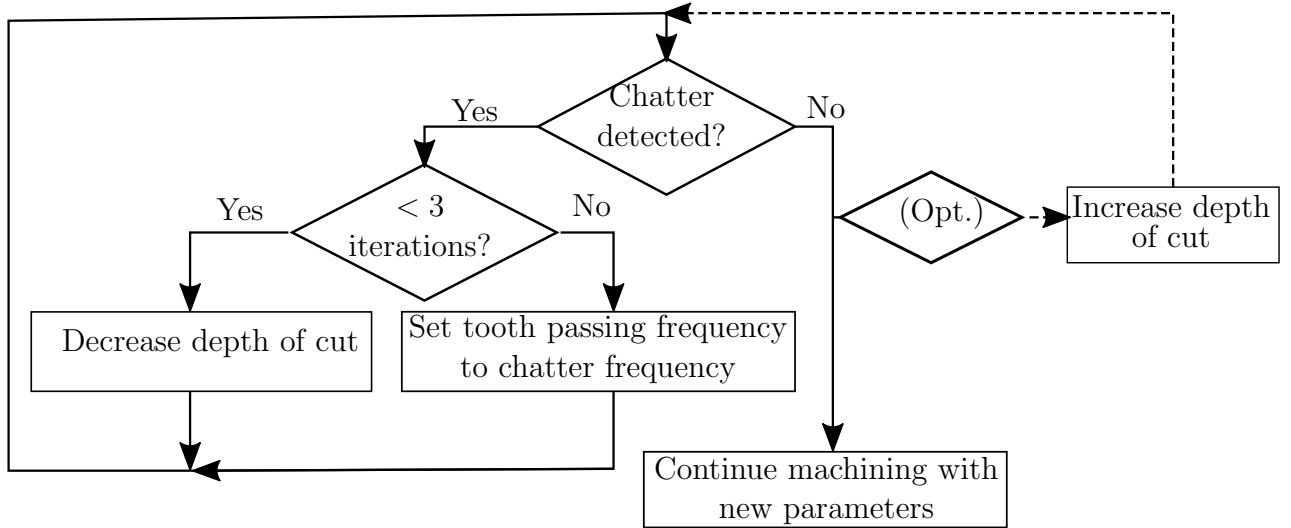
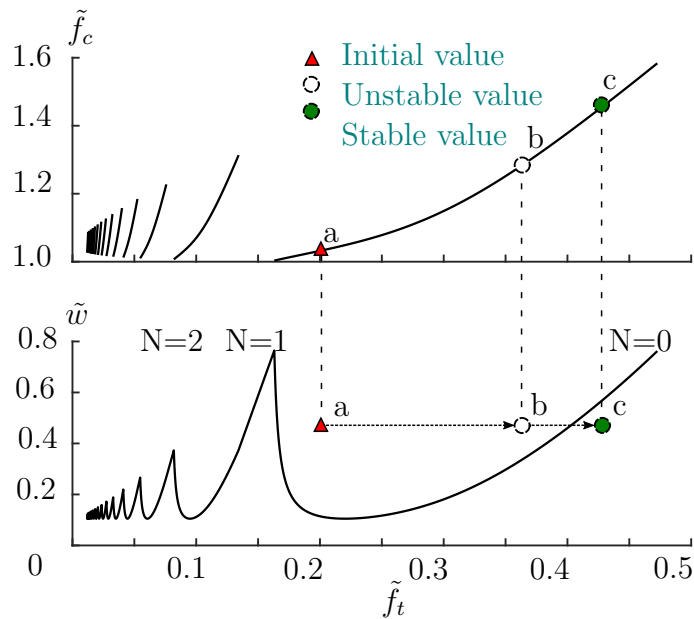Figure 3.7: The discrete spindle speed variation algorithm.

Figure 3.8: The SLD and related chatter frequency, showing the path of the discrete spindle speed variation algorithm. The values used here are for example only.

3.3.2 System model and problem constraints

A sketch comparison of the discrete spindle speed variation and DIV systems is shown in Figure 3.9. It is assumed that chatter frequency can be rapidly and accurately identified and that the new inertance can be set automatically during operation. While a model of the system dynamics is used in the derivation, the algorithm itself cannot require knowledge of the system dynamics.

The machine tool system is modelled by the SDoF system shown in Figure 3.10.
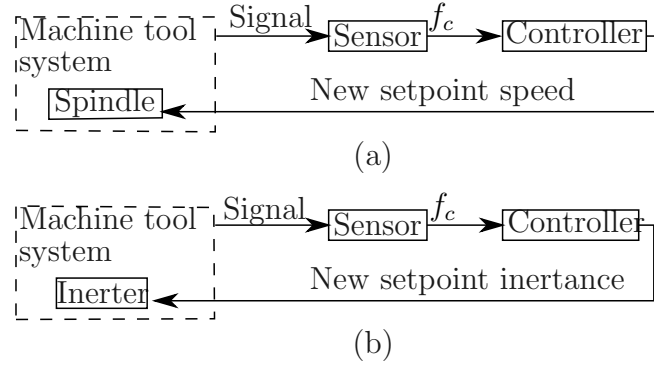
Figure 3.9: Comparison of the general control system for (a) discrete spindle speed variation and (b) discrete inertance variation.

The DDE of this system is

$$(m_0 + m_1)\ddot{y}(t) + c\dot{y}(t) + ky(t) = wK_s(y(t - \tau) - y(t)), \qquad (3.18)$$

which differs from Equation 3.5 in that the mass term has two parts. The static mass $m_0 = m + m_{inerter} + b_{min}$ consists of the system mass, the mass of the inerter and the minimum possible inertance, respectively. The variable mass $m_1 = b(t) - b_{min}$, consists of the the controllable part of the inertance and can be changed to a new set point value during operation.
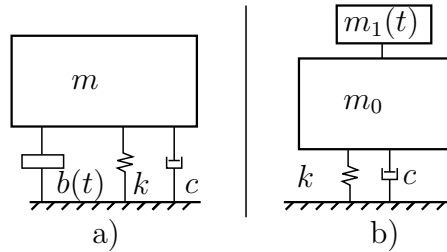
Figure 3.10: a) The SDoF system model and b)the equivalent system with mass terms.

The variable mass m_1 can be varied between b_{min} and some arbitrarily large value. Its is also assumed that the change in inertance can be achieved with sufficient speed that the change from one value to the next can be treated as instantaneous. Naturally, this last assumption is heavily dependent on the design of semi-active inerter.

3.3.3 Analysis

To use Equations 3.2, 3.3 and 3.16, it is first necessary to derive the system transfer function. Care must be taken, as the non-dimensional time domain is defined in terms

of the natural frequency, which is now no longer stationary. For this reason, the static natural frequency is redefined as $\omega_0 = \sqrt{\frac{k}{m_0}}$ and the instantaneous natural frequency is defined as $\omega_i = \sqrt{\frac{k}{m_0+m_1}}$. The definition of non-dimensional time remains $\tilde{t} = \omega_0 t$. So, in the non-dimensional time domain, Equation 3.18 becomes

$$\omega_0^2(m_0 + m_1)\ddot{y}(\tilde{t}) + \omega_0 c\dot{y}(\tilde{t}) + ky(\tilde{t}) = K_s w(y(\tilde{t} - \tilde{\tau}) - y(\tilde{t})). \qquad (3.19)$$

Defining the amplitude ratio, $R_A = \frac{m_1}{m_0}$, the scaled force term, $\tilde{F} = \frac{K_s w}{k}(y(\tilde{t} - \tilde{\tau}) - y(\tilde{t}))$ and adapting the definitions of the damping ratio, $\zeta = \frac{c}{2\sqrt{k(m_0+m_1)}}$, and frequency ratio, $p = \frac{\omega_c}{\omega_0}$, the transfer function of Equation 3.19 is derived in the normal way to be

$$G(j\omega) = \frac{Y}{\tilde{F}} = \frac{1}{1 - (1 + R_A)p^2 + 2\sqrt{1 + R_A}j\zeta p}. \qquad (3.20)$$

From this transfer function, it is possible to create SLDs of the kind in Figure 3.11. Here, the SLDs have been created for a range of values of R_A. The overlapping areas show the stable zones which can be targeted within the specified range. This visualisation is useful for demonstrating the the kind of value of mass ratio which might be required for a given speed. However, it does not offer much insight into the design. A different visualisation method is required to develop the algorithm.
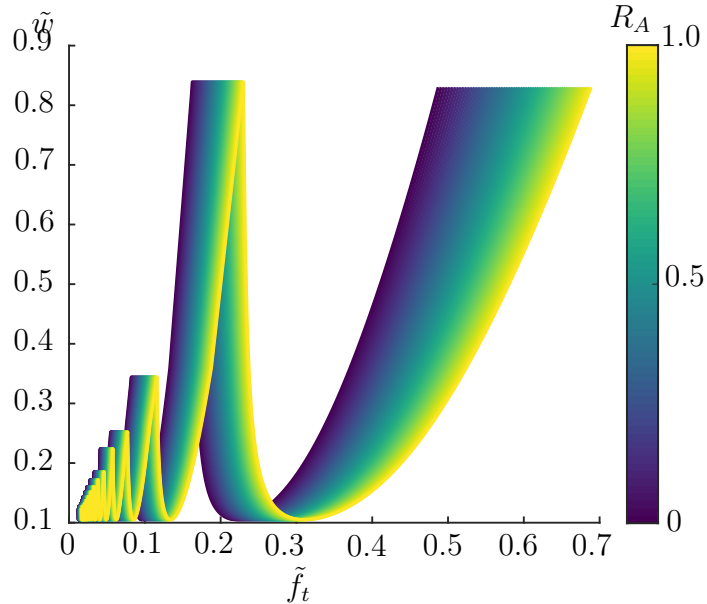
Figure 3.11: A composite SLD, showing the effects of varying R_A from 0-1.

Practically, Equation 3.20 is the same as Equation 3.17 but with the value of p scaled by $\frac{1}{\sqrt{1+R_A}}$, i.e. the system is evaluated with a natural frequency of $\omega_1 = \frac{\omega_0}{\sqrt{1+R_A}}$. Making this transform is more convenient as it allows Equations 3.16, 3.2 and 3.3 to

be used to find w_{lim} and f_c for a given tooth passing frequency at a range of values of p. The value of R_A required to create each frequency ratio can be calculated from

$$R_A = \left(\frac{p}{f_c}\right)^2 - 1. \tag{3.21}$$

This allows a stability lobe diagram to be created in the amplitude ratio domain, of the kind shown in Figure 3.12. This is similar in nature to the conventional SLD. However, rather than being unique to each system's natural frequency, this is unique to the tooth passing frequency. The R_A domain SLD allows for easier visualisation of the DIV algorithm.
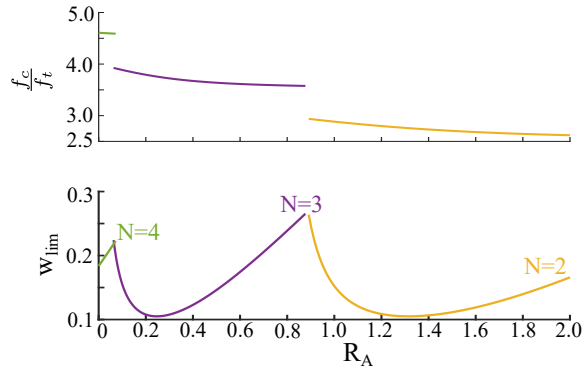
Figure 3.12: An R_A domain stability lobe diagram for a system with $\zeta = 0.05$ and $\frac{f_t}{f_0} = 0.25$.

The most noticeable feature of Figure 3.12 is the discontinuities in the frequency plot, approximately corresponding to integer values of $\frac{f_c}{f_t}$. Investigation of Equation 3.16 reveals that $\tilde{w} \to \infty$ as $\mathrm{Re}(G(j\omega)) \to 0$, only curtailed by intersection with the transfer function of the next lobe. It follows that, from Equation 3.3, as $\mathrm{Re}(G(j\omega)) \to 0$ then $\epsilon \to 1$ and so, from Equation 3.2, the maximal depth of cut is achieved near $\frac{f_c}{f_t} = N + 1$. This fact is the same reason that the discrete spindle speed variation algorithm counter-intuitively targets the system's natural frequency [45].

3.3.4 An example strategy

A simple DIV strategy can be realised using the bisection method. Recall that the goal here is to investigate the design implications and it is expected that this stategy will not necessarily be optimal. Nevertheless, it serves for illustration purposes.

An example of the process is shown in Figure 3.13. It is assumed that a machining operation has a non-dimensionalised tooth passing frequency $\tilde{f}_t = 0.24$, depth of cut

$\tilde{w} = 0.2$ and that the inerter can achieve a maximum amplitude ratio of $R_{A,max} = 1.2$. Chatter is detected at a frequency of $\frac{f_c}{f_t} = 4.67$, point a. The inerter switches to its maximum value, point b, where the new chatter frequency ratio is 2.87. There is at least an integer difference between this value and that at point a, which implies the existence of at least one stability lobe between these points. Whether that lobe is attainable at the current depth of cut is not known. The inerter is switched to its central value at point c, $R_A = 0.6$. The frequency ratio is now $\frac{f_c}{f_t} = 3.65$. Again, there has been a integer value change, so the lobe must lie between the previous two values. In this case, a shift to point d at $R_A = 0.9$, midway between points b and c, is sufficient to achieve stability. Otherwise, the operation can be repeated until either stability is achieved or it is decided that no stable point is achievable at this depth of cut.

It can be observed from the R_A domain SLD that the larger, lower order lobes are most attainable and so should be targeted.
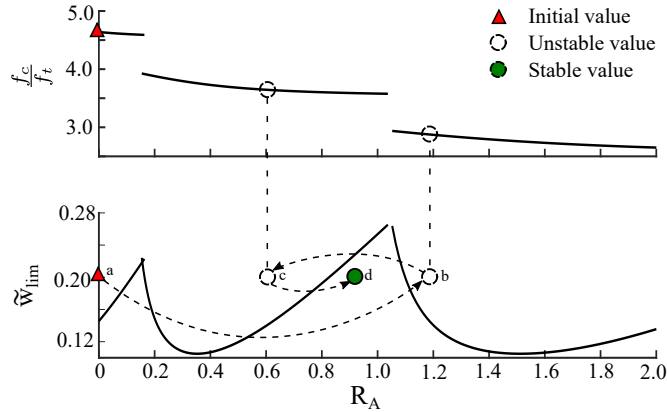
Figure 3.13: An example of a possible stategy, for a system with $\tilde{f}_t = 0.24$ and $R_{A,max} = 1.2$.

Note that at no point was it necessary to actually know the value of R_A, just that of $\frac{f_c}{f_t}$. This is useful, as R_A depends on the mass of the host structure, which may change during operation. However, for design purposes, it is useful to have a nominal value. As $R_A = \frac{m_1}{m_0}$, the removal of material can only increase the range of achievable values, i.e. as the operation progresses $R_{A,max}$ increases. If the critical element is the machine tool, then R_A will remain unchanged throughout operation.

3.3.5 Design implications

While the parallels between discrete spindle speed variation and DIV are clear, both techniques have different implications at the design stage. Discrete spindle speed

variation works with the existing machine and so must work within those constraints. For DIV a purpose built inerter needs to be designed, either to be retro-fitted or to be included in future machining systems. This would be designed with the control scheme in mind and so the requirements should be considered.

The challenges of designing inerters for this manner of control are best demonstrated by observing a couple of other potential cases. Figure 3.14 shows a system operating at the same depth of cut as that in Figure 3.13 but at just under half the tooth passing frequency (i.e. reduced cutting speed). It can be seen that although the lobes are closer together, the reduced height means that the system still needs to reach the fourth lobe to ensure stability. This requires a significantly larger maximum value of R_A to be achievable than for the previous case.

Conversely, Figure 3.15 shows the case for a non-dimensionalised tooth passing frequency of 1.2, significantly higher than that in Figure 3.13. Here, the fourth lobe has already been passed and the system is on its way to the zeroth lobe. This is the slowest of the lobes to grow and has the largest unstable gap. For this reason, it is necessary to have a value of $R_{A,max}$ of at least 1.8 to achieve stability.
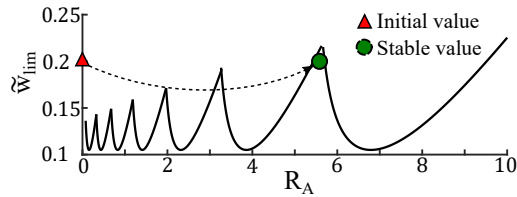
Figure 3.14: The best case paths for $\tilde{f}_t = 0.1$.

These three examples demonstrate that the relationship between the tooth passing frequency and the minimum amplitude ratio required to achieve stability is not simple. For operations at the same depth of cut, stability always occurs in the same lobe, or one of a lower order. However, the amplitude ratio required to reach this lobe depends on the tooth passing frequency. For higher spindle speeds the highest stable lobe has already been passed. Stability is achieved at the next lobe but, depending on the exact speed, this may require a higher or lower amplitude ratio.
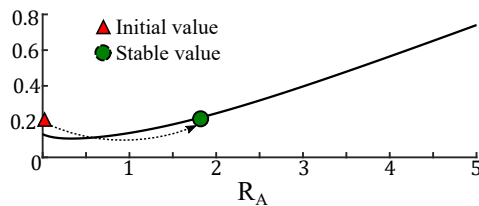
Figure 3.15: The best case paths for $\tilde{f}_t = 1.2$.

Figure 3.16 shows the minimum amplitude ratio, $R_{A,min}$, which would be required to achieve stability at $\tilde{w} = 0.2$ for a system with a damping ratio of $\zeta = 0.05$. At point A, the unmodified system is within the fourth lobe. This is the highest stable lobe for this depth of cut. It can be seen that the $R_{A,min}$ values required to achieve stability for tooth passing frequencies below this can be substantial. Conversely, values for higher tooth passing frequencies remain comparatively modest. The largest requirements occur immediately after the system leaves a lobe. This corresponds to the natural frequency needing to be shifted up to the next lobe, across the largest unstable gap. As has been previously noted, the gap between the first and zeroth (point B) lobes is the largest. Once the tooth passing frequency is above this point, the unmodified system is within the zeroth lobe and lobe-based strategies become irrelevant.
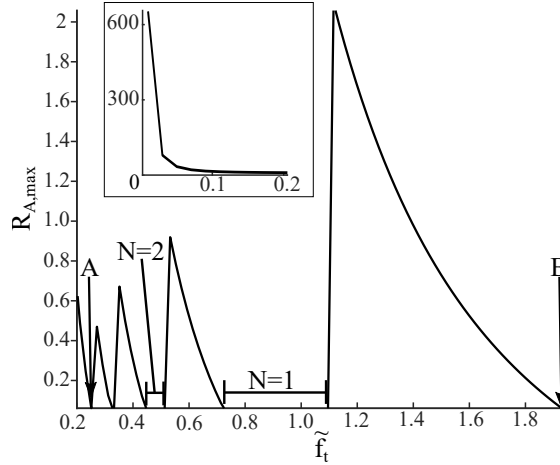
Figure 3.16: Maximum R_A required to achieve stability at a depth of cut $\tilde{w} = 0.2$ and damping ratio $\zeta = 0.05$, at a range of non-dimensional tooth passing frequencies.

Even for a higher depth of cut, as seen in Figure 3.17 which shows the case for $\tilde{w} = 0.6$, the required amplitude ratio is quite modest. Here, the desired depth of cut is only achievable in the zeroth and first lobes and so a large amplitude ratio is achievable. The utility of DIV in this case is debatable but it stands as a reasonable worst case scenario to consider. In design terms, this case would require the inertance range of the semi-active inerter to be six times the mass of the critical element. The case in Figure 3.16 would require a third of this and has utility at a wide range of tooth passing frequencies.

In designing an inerter for this method, then, it is important to consider both the depth of cut required and the mass of the critical element. This then allows charts like those in Figures 3.16 and 3.17 to be designed. It is proposed that the requirements of low speed machining be neglected and a suitable $R_{A,max}$ be designed with the
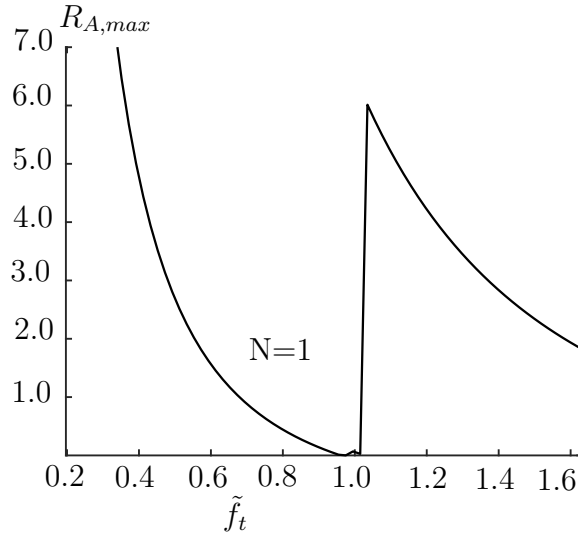
54

Figure 3.17: Maximum R_A required to achieve stability at a depth of cut $\tilde{w} = 0.6$ and damping ratio $\zeta = 0.05$.

requirements of the high speed machining zone in mind only. These requirements are relatively modest.

3.3.6 Conclusion

Discrete inertance variation is a promising avenue of investigation for the use of a semi-active inerter in machining. As with discrete spindle speed variation, this method has the most potential in the high speed machining zone, where the lobes are largest. For DIV to be achievable, the inerter should be able to vary the natural frequency of the critical element such that the next lobe is reached. It has been shown that this can be done with relatively modest inertance ranges.

3.4 Continuous inertance variation

3.4.1 Introduction

Mitigating chatter by continuously varying the spindle speed was first studied experimentally by Takemura [208]. The goal is to disturb the regenerative effect by having a non-constant delay between each pass. The advantage over variable pitch tools is that continuous spindle speed variation can be applied to a broad range of spindle speeds [209]. Analytical models of the effect have been developed by Inamara and Sata [88] and by Sexton et al. [87].

For mechanical reasons, continuous spindle speed variation becomes difficult at tooth passing frequencies. This is especially an issue for milling, as the tooth passing frequency is a multiple of the spindle speed. Segalman and Butcher [93] proposed an alternative way to vary the system's time delay. A boring bar containing a layer of magnetorheological fluid allows for continuously varying stiffness. The authors named this *impedance modulation*. They showed similar gains to continuous spindle speed variation by varying stiffness at half the frequency of the spindle speed. No further research has been published on this topic.

Continuously varying the inertance of a grounded inerter would be another method to realise this time delay variation. This section explores the potential of this method. The applicability of semi-discretisation is studied. Following this, a time domain simulation is developed. This is used to simulate continuous inertance variation (CIV) with different parameters. The results of these simulations are then discussed with regards to inerter design and conclusions are drawn.

3.4.2 System model

The system model is the same as that for DIV, shown in Figure 3.10. It is assumed that the inertance can be varied smoothly at a desired frequency. In the time domain, assuming sinusoidal inertance variation, the system equation is

$$(m_0 + m_1 \sin(\omega_M t + \phi))\ddot{y}(t) + c\dot{y}(t) + ky(t) = wK_s(y(t - \tau) - y(t)). \qquad (3.22)$$

This can be assumed to be zero valued without meaningfully changing the analysis. Defining the modulation ratio, $R_M = \frac{\tau_M}{\tau}$, with $\tau_M = \frac{2\pi}{\omega_M}$ and using the same non-dimensionalisation as used in Section 3.2.1 leads to the form

$$\frac{1}{\chi(\tilde{t})}\ddot{y}(\tilde{t}) + 2\zeta\dot{y}(\tilde{t}) + y(\tilde{t}) = \tilde{w}(y(\tilde{t} - \tilde{\tau}) - y(\tilde{t})), \qquad (3.23)$$

where the substitution $\chi(\tilde{t}) = \frac{1}{1 + R_A \sin\left(\frac{2\pi}{R_M \tilde{\tau}}\tilde{t}\right)}$. A full derivation is included in Appendix A.

3.4.3 Semi-discretisation

3.4.3.1 Introduction

The time-dependent term $\chi(\tilde{t})$ in Equation 3.23 means that linear chatter analysis is no longer possible: no closed form solution exists. Instead, more complex methods must be employed. One method used for efficiently investigating continuous spindle

speed variation is semi-discretisation. In this section, the semi-discretisation method proposed by Insperger and Stépán [33] is adapted for CIV and assessed for its suitability as a method of analysis. For consistency with this work, the nondimensional spindle speed $\tilde{\Omega} = 2\pi \tilde{f}_t$ is used in this section.

3.4.3.2 Semi-discretisation for CIV

Semi-discretisation is based on a method used in computational fluid dynamics. The name refers to the fact that the system equation is discretised along the spatial co-ordinates while the time co-ordinates remain unaltered. To apply this to a DDE, the idea is reversed so the discretisation is in the time dimension only.

Insperger and Stépán first developed the method for generic DDEs [89]. They then published a version of the strategy specifically designed for continuous spindle speed variation [33]. This second version is summarised here, before being applied to continuous inertance variation in the subsequent section.

The general equation is

$$\dot{\boldsymbol{y}} = \boldsymbol{A}(t)\boldsymbol{y}(t) + \boldsymbol{B}(t)\boldsymbol{y}(t - \tau), \tag{3.24}$$

where the state matrix, $\boldsymbol{A}(t)$, the input matrix, $\boldsymbol{B}(t)$, and τ are all periodic within the same principal period T^2. An approximation parameter, κ, is selected and T_P is divided into discrete time-steps of length $\Delta t = \frac{T_P}{\kappa}$. This allows Equation 3.24 to be written in its semi-discretised form, so that at any integer $i = 1, 2, ..., \kappa$

$$\dot{\boldsymbol{y}}(t) = \boldsymbol{A}_i \boldsymbol{y}(t) + \boldsymbol{B}_i \boldsymbol{y}(t - \tau), \tag{3.25}$$

where $\boldsymbol{A}_i = \frac{1}{\Delta t} \int_{t_i}^{t_{i+1}} \boldsymbol{A}(t)dt$ and $\boldsymbol{B}_i = \frac{1}{\Delta t} \int_{t_i}^{t_{i+1}} \boldsymbol{B}(t)dt$.

The instantaneous solution of Equation 3.25 is

$$\boldsymbol{y}_{i+1} = \boldsymbol{P}_i \boldsymbol{y}_i + \boldsymbol{R}_i \boldsymbol{y}_{i-N}, \tag{3.26}$$

where

$$\boldsymbol{P}_i = e^{\boldsymbol{A}_i \Delta t}, \tag{3.27}$$

$$\boldsymbol{R}_i = (e^{\boldsymbol{A}_i \Delta t} - \boldsymbol{I})\boldsymbol{A}_1^{-1}\boldsymbol{B}_i \tag{3.28}$$

and $N = \frac{\tau}{\Delta t}$.

If a vector

$$\boldsymbol{v}_i = \begin{bmatrix} \boldsymbol{y}_i & \boldsymbol{y}_{i-1} & \cdots & \boldsymbol{y}_{i-N} \end{bmatrix}^T \tag{3.29}$$

---

[2]i.e. T is the least common multiple of all the time-varying components

is defined, Equation 3.26 defines the map

$$\boldsymbol{v}_{i+1} = \boldsymbol{C}_i \boldsymbol{v}_i, \tag{3.30}$$

where the coefficient matrix is

$$\boldsymbol{C}_i = \begin{bmatrix} \boldsymbol{P_i} & \boldsymbol{0} & \boldsymbol{0} & \ldots & \boldsymbol{0} & \boldsymbol{R_i} \\ \boldsymbol{I} & \boldsymbol{0} & \boldsymbol{0} & \ldots & \boldsymbol{0} & \boldsymbol{0} \\ \boldsymbol{0} & \boldsymbol{I} & \boldsymbol{0} & \ldots & \boldsymbol{0} & \boldsymbol{0} \\ \vdots & \vdots & \vdots & \ddots & \vdots & \vdots \\ \boldsymbol{0} & \boldsymbol{0} & \boldsymbol{0} & \ldots & \boldsymbol{I} & \boldsymbol{0} \end{bmatrix}. \tag{3.31}$$

The final step is defining the transition matrix, $\boldsymbol{\Phi}$, over the principal period such that $\boldsymbol{y}_\kappa = \boldsymbol{\Phi}\boldsymbol{y}_0$. If the eigenvalues, or *characteristic multipliers*, of the transition matrix fit with in the unit circle, the system is known to be stable, otherwise it is unstable. From Equation 3.30, the transition matrix is

$$\boldsymbol{\Phi} = \boldsymbol{C}_{\kappa-1}\boldsymbol{C}_{\kappa-2}...\boldsymbol{C}_1\boldsymbol{C}_0. \tag{3.32}$$

For the system under investigation here, the time delay is constant and so can be replaced by $\tilde{\tau} = \frac{f_0}{f_t}$. This avoids some of the complexity involved in Insperger and Stépán's solution. Equation 3.23 can be rearranged to

$$\ddot{y}(\tilde{t}) = \chi(\tilde{t}) \left[2\zeta\dot{y}(\tilde{t}) - (1 + \tilde{w})y(\tilde{t}) + \tilde{w}y(\tilde{t} - \tilde{\tau}) \right], \tag{3.33}$$

so that

$$\boldsymbol{A}(\tilde{t}) = \begin{bmatrix} 0 & 1 \\ -(1 + \tilde{w})\chi(\tilde{t}) & -2\zeta\chi(\tilde{t}) \end{bmatrix} \text{ and } \boldsymbol{B}(\tilde{t}) + \begin{bmatrix} 0 & 0 \\ \tilde{w}\chi(\tilde{t}) & 0 \end{bmatrix}. \tag{3.34}$$

The second column of $\boldsymbol{B}(\tilde{t})$ is empty and therefore, from Equation 3.28, so is that of $\boldsymbol{R}(\tilde{t})$. This means the mapping from Equation 3.30 can be reduced to

$$\boldsymbol{z}_{i+1} = \boldsymbol{D}_i \boldsymbol{z}_i \tag{3.35}$$

where

$$\boldsymbol{z}_i = \begin{bmatrix} y_i & \dot{y}_i & y_{i-1} & y_{i-2} & \cdots & y_{i-N} \end{bmatrix}^T \tag{3.36}$$

and

$$\boldsymbol{D}_i = \begin{bmatrix} P_{i,11} & P_{i,12} & 0 & 0 & \ldots & R_{i,11} \\ P_{i,21} & P_{i,22} & 0 & 0 & \ldots & R_{i,21} \\ 1 & 0 & 0 & 0 & \ldots & 0 \\ 0 & 0 & 1 & 0 & \ldots & 0 \\ \vdots & \vdots & \vdots & \vdots & \ddots & \vdots \\ 0 & 0 & 0 & 0 & \ldots & 0 \end{bmatrix}, \tag{3.37}$$

with the transition matrix now defined as

$$\boldsymbol{\Phi} = \prod_{i=0}^{\kappa-1} \boldsymbol{D}_i. \tag{3.38}$$

The semi-discretisation stategy used here operates as shown in Figure 3.18. The eigenvalues over a given range of $\tilde{\Omega}$ and $\tilde{w}$ values are evaluated to find stable pairs.
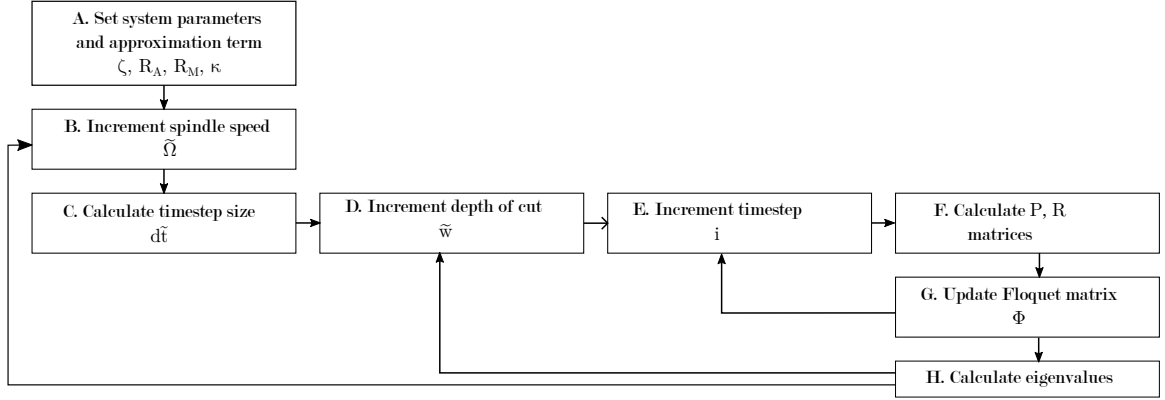

Figure 3.18: Summary of the semi-discretisation strategy.

3.4.3.3 Time-domain model

In order to verify the semi-discretisation results, a time domain model was created. The model takes the inputs of R_A, R_M, the number of passes to be simulated, Np, the number of time-steps per revolution, SR, damping ratio, ζ, and depth of cut, h_{nom}. As only the dynamic part of the model is of interest, the actual value of h_{nom} is arbitrary. For each time step, $t_n = n\Delta_t = \frac{n}{S_R \tilde{f}_t}$, the scaled force is found from

$$\tilde{F}_i = \tilde{w}(y_{n-S_R} - y_{i-1}). \tag{3.39}$$

The instantaneous value for χ is then calculated and the acceleration found from

$$\ddot{y}_n = \chi_{n-1}(\tilde{f}_n - 2\zeta\dot{y}_{n-1} - y_{n-1}). \tag{3.40}$$

The instantaneous velocity and displacement values are found by using the discrete first and second derivatives of Equation 3.40, $\dot{y}_n = \dot{y}_{n-1} + \ddot{y}_n\Delta t$ and $y_n = y_{n-1} + \dot{y}_n\Delta t$. The displacement is checked against the value for the previous pass and summed with the feed rate, $y_n = \min\{h_{nom} + y_n, h_{nom} + y_{n-S_R}\}$, where min denotes choosing the lowest value in a set. This is necessary, as it is possible to have a situation where the current displacement is higher than the surface left by the previous tooth.

If at any point during the simulation $\tilde{F}_i < 0$, then a loss of contact has occurred. For this to happen, the system must be unstable. In this case, the process halts, the $(\tilde{\Omega}, \tilde{w})$ pair marked as unstable and then the simulation iterates for the next pair. An example of stable and unstable simulations are shown in Figure 3.19a and 3.19b, respectively.

(a)   (b)
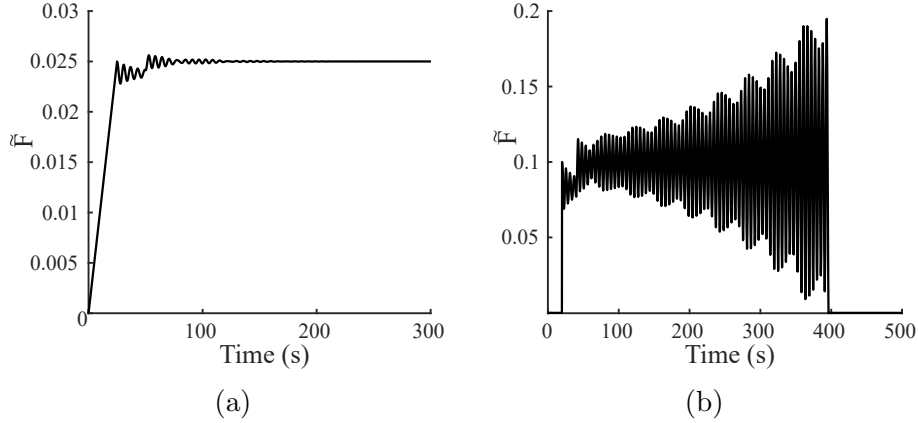
Figure 3.19: Time domain simulations of a) a stable system and b) an unstable system, where $\tilde{F} = 0$ is reached at 396s.

3.4.3.4   Convergence of the semi-discretisation method

A convergence study was conducted on the approximation parameter, κ. An example of the results is presented in Figure 3.20. It can be seen that convergence isn't achieved before $\kappa = 480$, especially for lower values of $\tilde{\Omega}$. This is a major issue, as if results are similar to those from impedance modulation [93], this is where any effect would be expected.

The simulation time for the three tests run in Figure 3.20 are presented in Table 3.1. It can be seen how, even at $\kappa = 240$, the simulation time becomes unfeasibly long. For this reason, and because it provides no additional understanding over time domain simulations, semi-discretisation was rejected as a method.

Table 3.1: Simulation time for the convergence study.

κ	Simulation time (s)
120	578.17
240	3289.42
480	34093.41
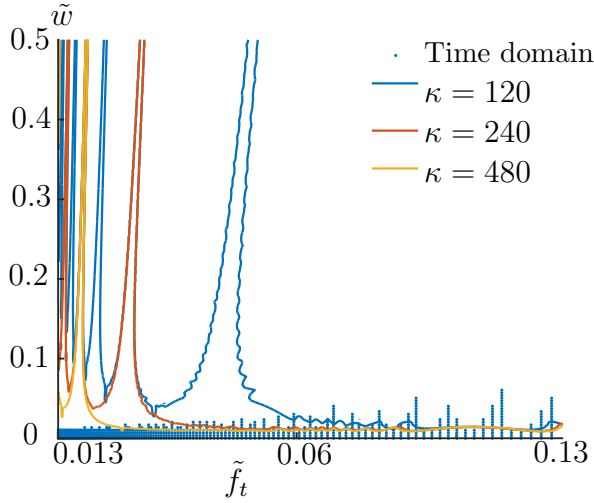
Figure 3.20: Convergence test of the semi-discretisation method.

3.4.4 Time-domain study

The time-domain model described in section 3.4.3.3 was used to investigate continuous inertance variation. The model contains two parameters which could affect the design of an inerter. The amplitude ratio, R_A is a product of the inertance range, the difference between b_{max} and b_{min}. This is a specific value, in that it would need to be matched to the mass of the critical element of the system. The modulation ratio, R_M, is dependent on the inerter's responsiveness, the speed with which it can switch states.

It was also observed that the research on impedance modulation [93] focused on a system with low damping. It is conventional to assume that any effects of damping simply increase stability. However, the effects shown were relatively small and located in the low speed machining and process damping zones. It was possible that the effect could be overcome by higher values of damping, to the point of becoming negligible. To reject this possibility, damping was also used as a variable parameter.

3.4.4.1 Model verification

Verifying the model consisted of three stages. Firstly, the results for the model without varying inertance (i.e. $\chi \equiv 1$) was compared to the analytical results from linear stability analysis. Secondly, the results of the model with the same parameters as that studied in Ref. [93] were compared to the results presented in that paper. Finally, a convergence study was run on the number of passes to be simulated, `Np`.

61

The first verification study is shown in Figure 3.21. The damping frequency ratio was 0.05 and up to 1000 revolutions were simulated for each $(\tilde{f}_t, \tilde{w})$ pair. A good correspondence can be seen in the limiting critical depth of cut and the position of lobes. The time domain model has a tendency to over-predict stability close to the limiting depth of cut. This is due to the slow growth of oscillations here, meaning loss of contact takes longer to occur.
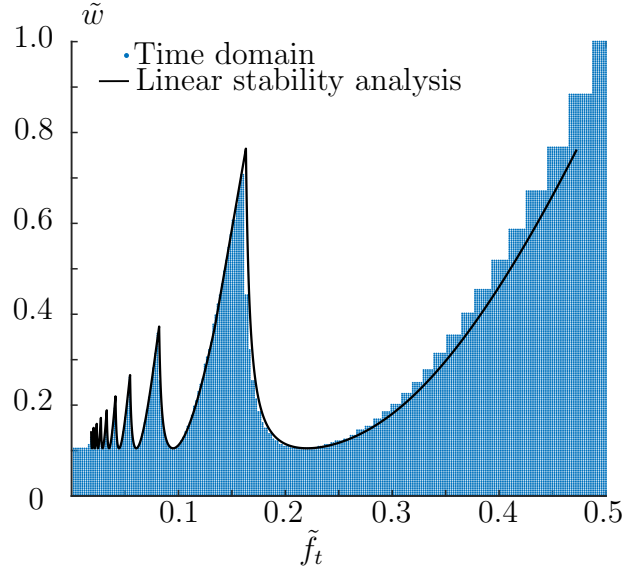
Figure 3.21: Comparison of the time domain simulation with linear stability analysis.

The second verification study is shown in Figure 3.22. The stability chart produced by the time domain simulation is shown in blue for the system with CIV and red for that without. This is compared to the limiting critical depth of cut given in Figure 2 of Ref. [93], shown with black squares. While the correlation is not perfect, a broadly similar pattern is followed.

This figure highlights a couple of limitations of the time domain simulation. At the low speeds shown the lobes are increasingly narrow and so the resolution is insufficient to capture the detail. The time domain simulations are also less reliable when systems are marginally stable, as the output can take longer to diverge than the simulation time. As such, the critical stability limit is consistently overestimated. Nevertheless, the overall trends can be taken to be accurate.

The third verification study was a convergence study on the `Np` parameter. This sets the maximum number of tooth passes simulated before declaring a system stable. Setting this value too low results in poor accuracy, while setting it too high increases simulation run time. From observation, this has the greatest effect in the low speed
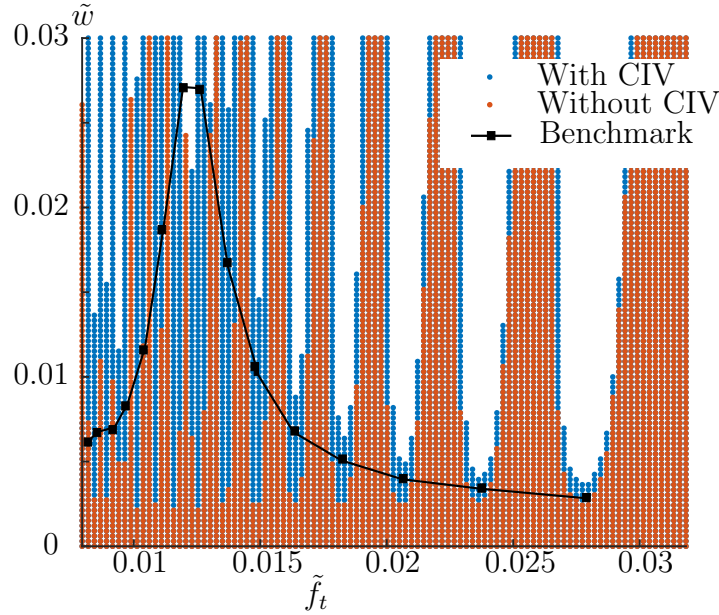
Figure 3.22: Results for CIV with $R_A = 0.1$, $R_M = 2$, $\zeta = 0.001$. The stability limit from Ref. [93], Figure 2, which uses the same parameters, is plotted with black squares.

machining zone. Simulations at low tooth passing frequencies have more time steps during each pass, so the total number of passes has a greater effect on simulation time.

Three values of $\tilde{f}_t$ in the low speed machining zone were selected. Simulations were run at twenty frequencies around these nominal tooth passing frequencies, with different values of Np. Convergence was measured from the mean stability limit of these values, shown in Figure 3.23. It can be seen that results largely converge by Np=500. This value was selected for the study.

3.4.4.2 Results

Simulations were run with different combinations of parameters as detailed in Table 3.2. Recall that $R_M = \frac{\tau_M}{\tau}$ and $R_A = \frac{m_1}{m_0}$, so that increasing R_A means larger magnitude of variation, while increasing R_M means a higher frequency variation. Four test were designed. Test A checked that the method was still effective with higher damping levels. Test B investigated the effects of increasing R_M. Test C investigated whether using a fractional value of R_M could have an effect. Test D investigated the effects of increasing R_A.

Instead of showing the result of each separately, as in Figure 3.22, the MATLAB
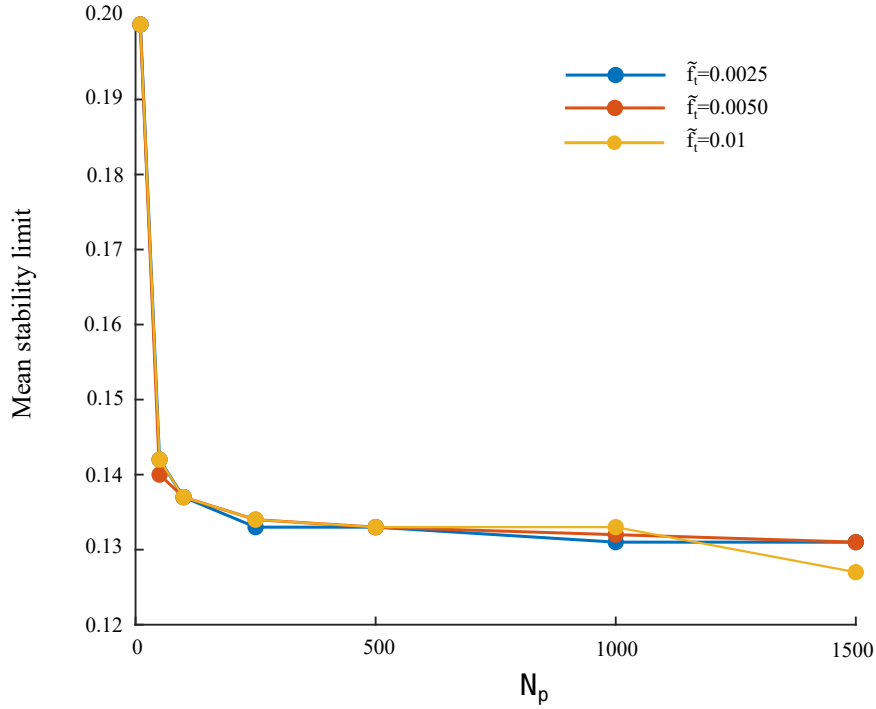
Figure 3.23: Convergence study of `Np` around three different values of $\tilde{f}_t$ in the low speed machining domain.

Table 3.2: Parameters used for each test.

Test	R_A	R_M	ζ	Figure
A	0.1	2	0.001	3.24a
	0.1	2	0.05	3.24b
B	0.1	2	0.05	3.24b
	0.1	3	0.05	3.25a
	0.1	4	0.05	3.25b
C	0.5	0.5	0.05	3.26
D	0.1	2	0.05	3.27a
	0.5	2	0.05	3.27b
	0.8	2	0.05	3.27c

function `contour` was used to create the SLD. In each figure, the results of the simulation without CIV are shown as a benchmark.

Figures 3.24a and 3.24b show the effect of changing damping from $\zeta = 0.001$ to $\zeta = 0.05$. It can also be seen that CIV offers larger stable depths of cut. The effects of increased damping are additive with CIV.

Figures 3.24b, 3.25a and 3.25b show the effect of increasing R_M. There is no noticeable change in the stability lobe diagram.
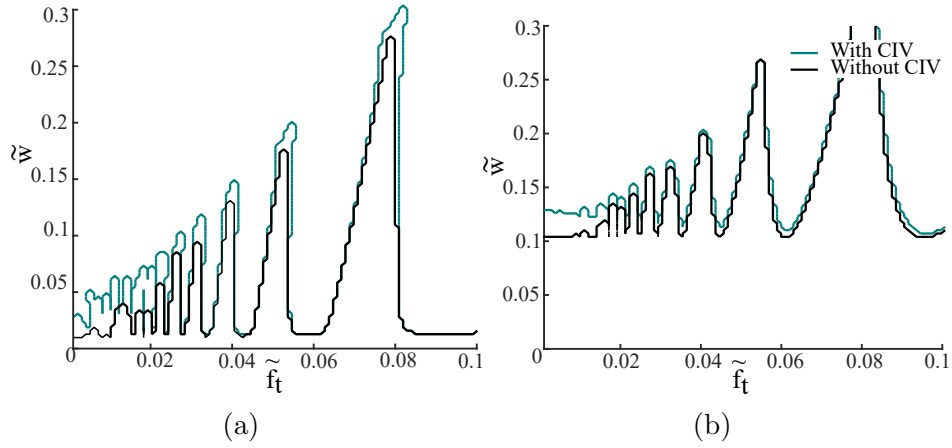
Figure 3.24: Comparison of CIV with $R_A = 0.1$ and $R_M = 2$ at a) $\zeta = 0.001$ and b) $\zeta = 0.05$.
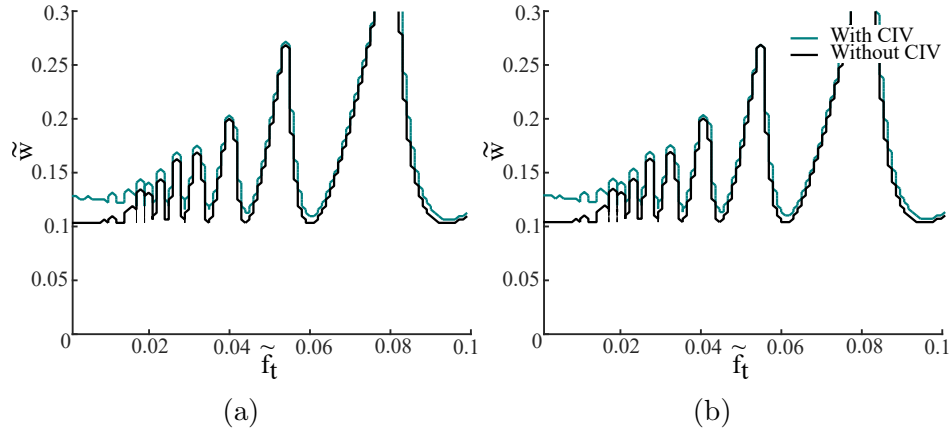
Figure 3.25: Comparison of CIV with $R_A = 0.1$ and $\zeta = 0.05$ for a) $R_M = 3$ and b) $R_M = 4$.

Figure 3.26 shows CIV with a fractional value of R_M. While the improvements are less pronounced than those in Figure 3.24b, there is an increase in the limiting critical depth of cut. The position of the stable lobes is also affected.

Figures 3.27a, 3.27b, 3.27c show the effect of increasing R_A. It can be seen that increasing this raises the stability limit. It also increases the range of spindle speeds over which the effect occurs significantly. It can be seen that substantially increasing R_A allows CIV to be used in the high speed machining domain. While the limiting critical depth of cut is raised consistently, in some locations CIV reduces the stability limit below that offered by lobe-based methods.
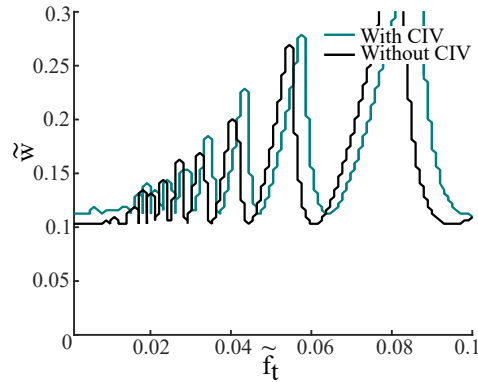
Figure 3.26: CIV with with $R_A = 0.5$, $R_M = 0.5$ and $\zeta = 0.05$.

(a)

(b)

(c)
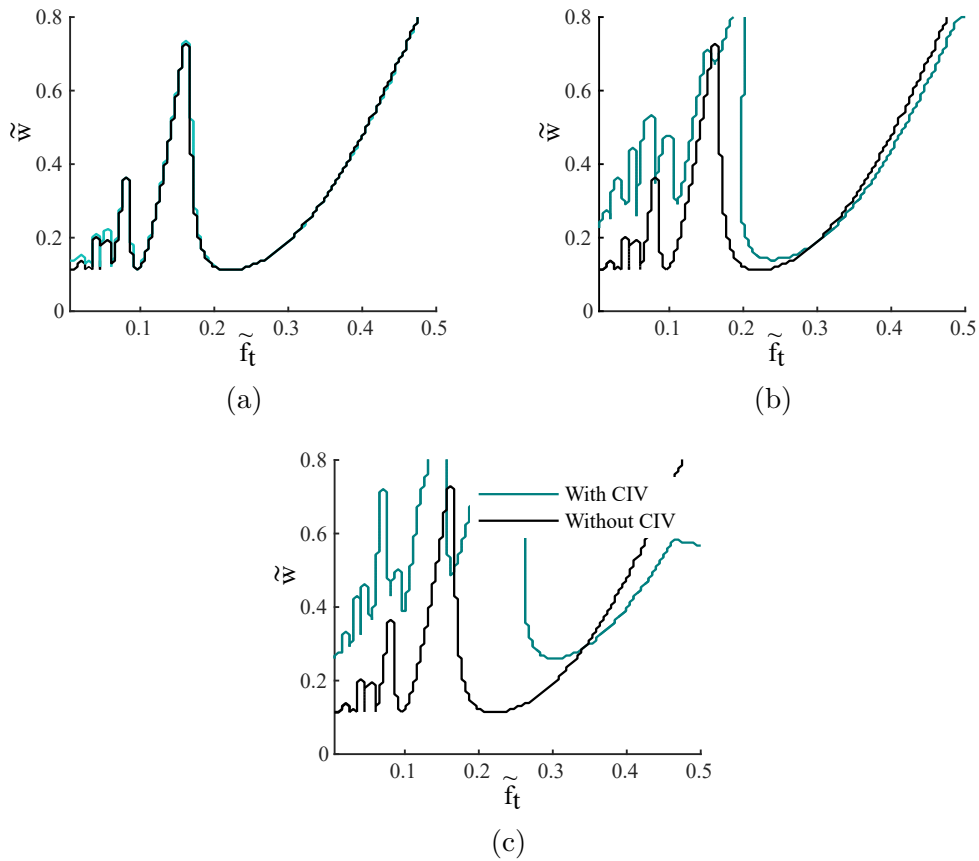
Figure 3.27: Comparison of CIV with $R_M = 2$ and $\zeta = 0.05$ for a) $R_A = 0.1$, b) $R_M = 0.5$ and $R_M = 0.8$.

3.4.4.3 Discussion

Figures 3.24a and 3.24b show that CIV is additive with the effects of damping. This is encouraging, as these effects can be quite substantial at low speeds. While this assumption of additional damping is common in chatter mitigation, it is useful to

verify it here.

Figures 3.24b-3.25b show that increasing the modulation ratio has little to no effect. This result is also encouraging, as increasing modulation frequency presents significant design challenges. However, it should be noted that keeping R_M constant as spindle speed increases still requires a corresponding increase in the modulation frequency. Figure 3.26 hints that this may not be strictly necessary. Being able to increase the limiting critical depth of cut by using CIV at lower frequencies than the tooth passing frequency would be extremely useful.

Figures 3.27a-3.27c show that the amplitude ratio has a significant effect on stability. Increasing this parameter increases the stable depth of cut both at lower and higher speeds. However, it should be noted that shifting of the stable lobes can lead to some previously stable processes becoming unstable.

In terms of inerter design, it is clear that the amplitude ratio should be the focus. This requires a large inertance range, which needs to be matched to the mass of the critical element and the inerter itself. The modulation frequency should be maximised, to allow the device to work at higher spindle speeds.

While the analysis conducted here is generalisable to impedance modulation and similar to continuous spindle speed variation, CIV offers improvements over both. The ability to vary inertance rapidly would be required for this technique to be of use. The 'mass magnification' effect of inerters would allow an inerter based device to more easily benefit from the performance improvements at higher amplitude ratios than impedance modulation.

These results should be taken as preliminary until validated against physical tests. Additionally, the assumption that sinusoidal variation would be possible is a major one.

3.4.4.4   Conclusion

Continuous inertance variation was studied as a potential method for mitigating chatter. Semi-discretisation was rejected as a method of study due to convergence issues. Using time domain simulations, it was shown that larger amplitude ratios increase the effectiveness of CIV. Increasing the modulation was shown to have no effect. There is some evidence that CIV would have some effect at modulation speeds below the tooth passing frequency.

3.5 Conclusion

Both discrete and continuous inertance variation are plausible use cases for semi-active inerter based devices in machining. With both methods, the range of inertance the device can provide is important. Designs should seek to maximise this quantity, while also aiming to be as responsive as possible.

The development of a more efficient stategy for DIV is left to future researchers, as is the possibility of achieving larger gains by using a hybrid approach, combining DIV and discrete spindle speed variation. This kind of multivariate optimisation might be an interesting area of future research.

The potential use of low frequency CIV, while small, are intriguing. Additionally, the possibilities for non-integer values of the modulation frequency merit investigation. The effects of using a more realistic models of inertance variation should be studied, once prototype devices are developed on which such models can be based.

The results in this chapter are presented as a feasibility study, to explore the space. Before than can be validated, a suitable semi-active inerter would need to be developed. The limited space available within machining systems - particularly modern multi-tool systems - presents a non-trivial issue in terms of design. This is discussed in more detail in Chapter 6, which also presents some alternative ways in which a semi-active inerter could be used within different machining operations.

In this chapter, the first objective from Chapter 1 has been achieved. The investigation of different use cases has highlighted some of the design needs which need to be considered. This consideration forms the basis of Chapter 4, in which different designs and models of a semi-active helical inerter are presented.

Chapter 4

Design considerations and models of a semi-active helical inerter

4.1 Introduction

In Chapter 3, the feasibility of chatter suppression using a semi-active inerter was analysed using the an idealised model. In the current chapter, a specific implementation of the semi-active inerter is explored. This implementation is based on the helical inerter and uses MR fluid to provide control.

It was demonstrated in Chapter 3 that the ability to control inertance at a high frequency would be very desirable, if not a fundamental requirement of a semi-active inerter. MR fluid has the potential to meet this requirement, with its millisecond response time translating to a theoretical bandwidth in the high hundreds of Hertz. Meanwhile, the helical inerter is the more well-established of the fluid-based inerters, with multiple versions presented in the literature (see Refs. [103], [122], [210], [123]). The combination of these two technologies therefore merit investigation.

In the first half of this chapter, three potential layouts are investigated. This investigation is undertaken using a quasi-static model. Designs using single double helices are investigated. This is followed by a look at the specific requirements of an MR valve designed for the semi-active inerter. The work in this part of the chapter is largely based on three papers presented at the 2018 [211] and 2019 [212] Smart Structures and Materials & Nondestructive Evaluation conferences and at the 2018 [213] conference on International Conference on Noise and Vibration Engineering.

Although the quasi-static model is sufficient for first order design and analysis, by its very nature it fails to capture a change in inertance. If more detailed design, as well as control logic, are to be considered, it is nessecary to have a model which captures this aspect of the inerter. The second half of the chapter focuses on developing such

a model. The approach takes the form of expanding the quasi-static model to include one dynamic parameter. As such, it is referred to as *quasi-dynamic* modelling, to distinguish it from a fully dynamic model such as fluid simulation.

4.2 Semi-active inerter layouts

4.2.1 Introduction

The first stage in creating a prototype device is the selection of a layout. Three layouts were considered. These are shown in Figure 4.1 and referred to as I1, I2 and I3. Design I1 features a single helix, as in existing inerter designs, with a MR valve in series. I2 includes a second helix and either one or two MR valves in series with the helices. I3 has a single helix, with a MR valve in parallel.

In this section, these three layouts are modelled analytically. The features and potential for each design are described.
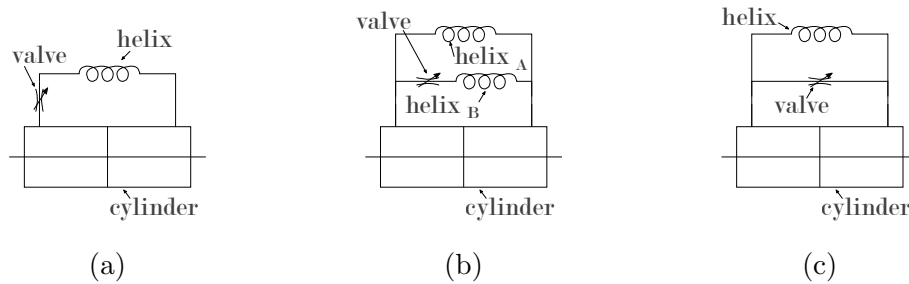
Figure 4.1: Layouts a) I1, b) I2 and c) I3.

4.2.2 Conversion from pressure and flow rate to force and velocity

The helical inerter is, at its core, a hydraulic device used for mechanical means. As such, it is useful to have models of the device in both the hydraulic and the mechanical domain, as well as to be able to easily convert between these domains. For reference and familiarity, the overall schemes used will now be briefly introduced - details, justifications,assumptions etc. will be included throughout the chapter, as and when they become relevant.

The general mechanical model, relates the force, F, device to the change in displacement, x, across the entire device

$$F = \begin{cases} b\ddot{x} + c_{lin}\dot{x} + c_{quad}\dot{x}^2, & \text{if } \dot{x} \geq 0 \\ b\ddot{x} + c_{lin}\dot{x} - c_{quad}\dot{x}^2, & \text{otherwise.} \end{cases} \qquad (4.1)$$

It can be seen that the force is modelled with three component parts: the force from inertance, proportional to acceleration; a linear damping force, proportional to velocity with coefficient c_{lin}; and quadratic damping force, proportional to the velocity squared with coefficient c_{quad}.

The general hydraulic model, relates the pressure drop across the helix, Δp_H, to the volumetric flow rate in the helix, $Q_H = u_H A_2$,

$$\Delta p_H = \begin{cases} I\dot{Q}_h + AQ_H + BQ_H^2, & \text{if } Q_H \geq 0 \\ I\dot{Q}_h + AQ_H - BQ_H^2, & \text{otherwise.} \end{cases} \qquad (4.2)$$

It is not particularly useful to consider the valve in the force domain in this context, as the valve is acting as a flow regulation device rather than as a damper. Pressure drop across a magnetorheological valves can be modelled using a Bingham fluid model:

$$\Delta p_v = \tau_y + CQ_v. \qquad \text{(?? revisited)}$$

The coefficient in Equations 4.1 and 4.2 are derived from Equations 4.5 and 4.11 and are collated in Table 4.1. For completeness, it is also useful to include the pressure drop coefficient for a cylindrical pipe, as this is used in Chapter 5. Some of the terms appearing in this table have not yet appeared. These terms will be defined when they are encountered in the text.

Table 4.1: Coefficients of the helix and valve equations in the mechanical and hydraulic domains.

Coefficient	Pressure/mass flow rate	Force/displacement
Through variable	Q	F
Across variable	Δp	x
Linear pressure drop/damping	$A = 44.67\frac{\mu l}{r_3^4}$	c_{lin}
Quadratic pressure drop/damping	$B = 4.91 \times 10^{-3}\frac{\rho l}{\sqrt{r_3 r_4} r_3^4}$	c_q
Inertia	$I = \frac{l\rho}{A2}$	b
Annular channel Newtonian pressure drop	$C = \frac{\mu l_v}{wh^3}$	-
Cylindrical pipe Newtonian pressure drop	$C = \frac{8\mu l_v}{\pi r_v^4}$	-

4.2.3 Quasi-static model

An analytical model for the helical inerter was created and validated by Swift et al. [103]. They considered the various pressure losses in the system and showed that the pressure drop caused by secondary flows were by far the largest cause of parasitic losses. The orders of magnitude were such that, in general, it is sufficient to describe a helical inerter in terms of these losses and its inertance. Losses from pipe entry and exit, as well as leakage, are negligible for example. This analysis does rely on the assumption that the helix is closely packed [104], so that the flow approximates circular flow. There are few practical reasons for this not to be the case in physical designs.

A typical helical inerter is shown in Figure 4.2. It consists of a two-way, constant volume hydraulic cylinder with cross-sectional area $A_2 = \pi(r_2^2 - r_1^2)$. Both ports of the cylinder are connected by a helix with a cross-sectional area of $A_3 = \pi r_3^2$. Linear motion of the the piston rod causes the fluid to flow round the helix. The rotational inertia of this spiralling body of fluid creates the inertance.
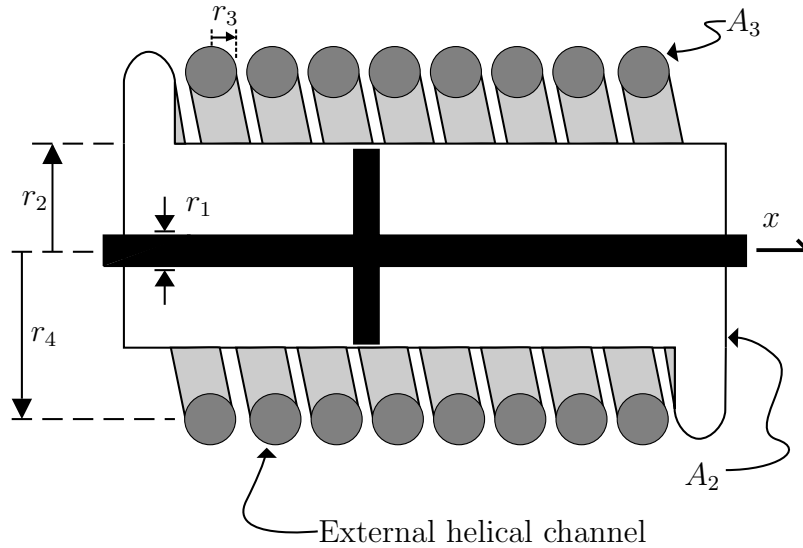
Figure 4.2: The key dimensions of a fluid inerter, as used in this section (not shown: helix length, L).

An ideal inerter, as defined by Smith [2] is described by the equation $F = b\ddot{x}$. Here b is the inertance and $\ddot{x}$ is the relative acceleration of the two terminals. Consider the fluid flowing through the helix, as shown in Figure 4.3. The rotational energy of this fluid is

$$T_{rot} = \frac{1}{2}J\dot{\theta}^2. \tag{4.3}$$

The moment of inertia of the fluid is approximately $J \approx m_{hel} r_4^2$ Here, $m_{hel} = \rho l A_3^2$ is the mass of the fluid, which has a density of ρ, in the helix of length l.
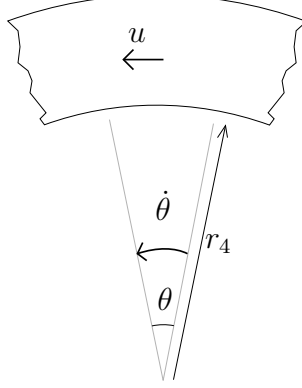

Figure 4.3: Angular velocity of a fluid element in the helix.

Considering the inerter under pure acceleration, the equivalent kinetic energy is

$$T_{lin} = \frac{1}{2} b \dot{x}^2. \tag{4.4}$$

Combining and rearranging Equations 4.3 and 4.4 gives the inertance to be

$$b = J \frac{\dot{\theta}}{\dot{x}} = m_{hel} \frac{u^2}{\dot{x}^2}. \tag{4.5}$$

For a passive device, continuity of flow means that $u = \frac{A_2}{A_3} \dot{x}$. This means that the inertance can be calculated from the geometry and fluid density to be

$$b = \rho l \left(\frac{A_2^2}{A_3} \right). \tag{4.6}$$

Flow in a curved channel will be faster (and so lower pressure) at the outer wall than the inner wall. In a curved pipe, this leads to secondary flows perpendicular to the main direction of flow. Swift et al. [103] calculated the pressure drop from these secondary flow pressure losses for a fluid with dynamic viscosity μ to be

$$\Delta p_{sf} = 0.04845 \frac{\rho l}{\sqrt{r_3 r_4}} u^2 + 8.77 \frac{\mu l}{r_3^2} u. \tag{4.7}$$

To simplify the notation, it is convenient to rewrite Equation 4.7 as

$$\Delta p_{sf} = \frac{\alpha}{r_3^2} u + \frac{\beta}{r_3^{0.5}} u^2, \tag{4.8}$$

where $\alpha = 8.77 \mu l$ and $\beta = 0.04845 \frac{\rho l}{\sqrt{r_4}}$.

The Resistive force from the MR valve is

$$F_{MR} + A_v\Delta p_v, \tag{4.9}$$

where A_v is the cross-sectional area of the channel in the valve and

$$\Delta p_v = \tau_y + CQ_v \tag{4.10}$$

is the pressure drop along the valve, modelling the fluid as a Bingham fluid. The yield stress, τ_y is created by the applied magnetic field. The second part of Equation 4.23 is the pressure drop across the valve of a newtonian fluid with a flow rate of Q_v. The coefficient C is the Newtonian pressure loss coefficient. Both τ_y and C are discussed in more detail in Section 4.3, which covers valve design. Equation 4.23 is sufficient to understand the models in the present section.

4.2.4 I1: series layout

Layout I1 could be realised by including an MR valve either in the helix or in the piston head. The latter is a method already used in some semi-active dampers [214] and would allow for a large valve size without increasing the footprint of the device.

From Equations 4.1 and 4.9, the expected force from the inerter would be

$$F = \begin{cases} b\ddot{x} + c_{lin}\dot{x} + c_{quad}\dot{x}^2 + F_{MR}, & \text{if } \dot{x} \geq 0 \\ b\ddot{x} + c_{lin}\dot{x} - c_{quad}\dot{x}^2 + F_{MR}, & \text{otherwise.} \end{cases} \tag{4.11}$$

The Newtonian valve damping constant is $c_v = C\frac{A_2}{A_v}$, where A_v is the cross sectional area of the valve annulus. The magnetorheological force is $\tau_y A_v$ and the linear damping coefficient is c_{lin}.

With this layout, the damping can be controlled but not the inertance. The device is equivalent to a passive inerter in parallel with a semi-active damper. This would provide for a compact semi-active device, similar in layout to the passive layout C3 as proposed by Hu et al. [72]. A similar device has recently been investigated by Zhong et al. [215].

A model of Layout I1 was programmed in `Matlab` [211], with geometry as described in Table 4.2. The effects of varying different parameters were assessed against inertance and 'controllability'. The highest and lowest damping coefficients achievable within the envelope of the non-linear damping-velocity curves over a given velocity range were calculated. The controllability was defined as the ratio of the minimum to maximum linear damping coefficient. As can be see in Figure 4.4, this is a worst-case

parameter, with a higher range of forces achievable at a low velocity. It was shown that increasing the helix radius and length improved inertance but reduced controllability. Controllability could be increased without impacting inertance by increasing the length of (and hence overall pressure drop along) the MR valve.
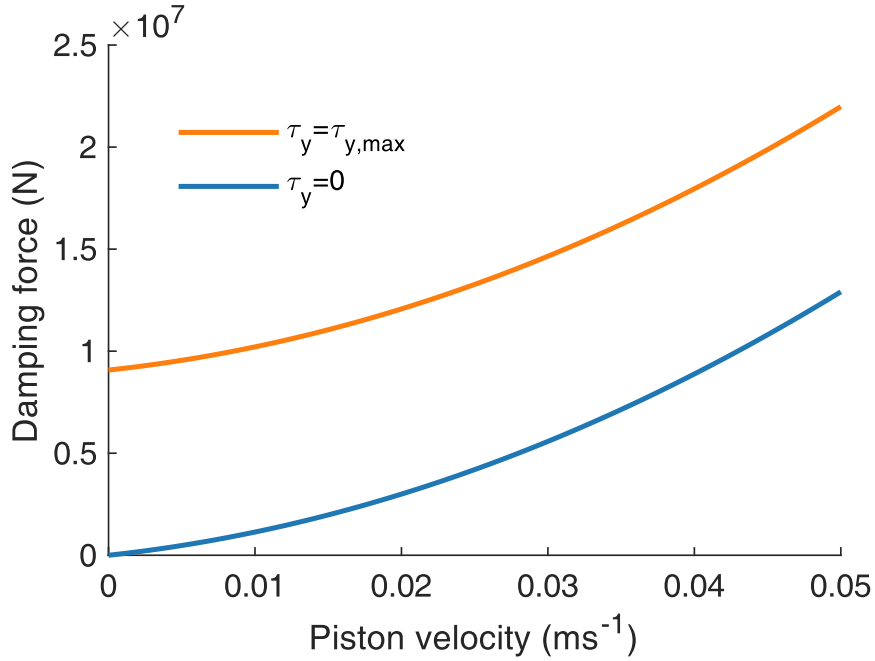

Figure 4.4: The control envelope of the I1 inerter design.

Table 4.2: Dimensions, in metres, of the inerter modelled in Figure. 4.7

r_1	r_2	r_3	r_4	L
0.12	0.30	0.01	0.13	0.6

Layout I1 was modelled as part of a parallel viscous inerter damper (PVID) [216], as shown in Figure 4.5a. The limits of the device were compared to a passive device, optimised using fixed point theory. It can be seen in Figure 4.5b that this allows for better control of frequencies close to the natural frequency of the host structure.

Layout I1 could have some uses. It could feasibly be sized similarly to semi-active dampers currently used in some modern cars. This would allow inerter-based vibration absorbers to be included without sacrificing the benefits of semi-active damping. Nevertheless, this layout does not allow for controllable inertance and cannot be called a semi-active inerter in any meaningful way.
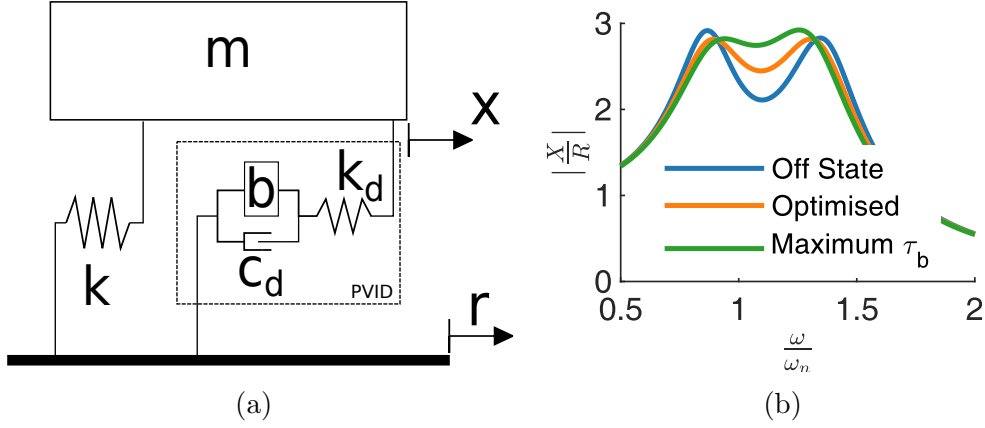
Figure 4.5: (a) Diagram of a PVID attached between a host structure and the ground and b) Control range offered by a semi-active PVID compared to an optimised passive PVID.

4.2.5 I2: dual-helix

If the inerter has two helices, it becomes necessary to consider the flow rates in each separately. This can be done by considering the flow diagram in Figure 4.1b. It is assumed for now that the flow is continuous and incompressible.

These assumptions simplify the problem to the simultaneous equations, for the flow rate and pressure drop equivalences

$$Q_0 = Q_A + Q_B \tag{4.12}$$

$$\Delta p_A = \Delta p_B + \Delta p_v. \tag{4.13}$$

Here subscript $_A$ denotes the helix without a valve and $_B$ denotes the other.

Consider the inerter with the valve powered such that τ_y is some arbitrary, non-zero value. Imagine the piston accelerating smoothly from rest. Initially, the entire flow travels through helix $_A$. The device operates as a conventional helical inerter, with inertance $b = \rho l \left(\frac{A_2^2}{A_A} \right)$. The pressure drop along the helix is $\Delta p_A = \frac{\alpha_A}{r_A^2} u_A + \frac{\beta_A}{r_A^{0.5}} u_A^2$.

As the piston accelerates, the pressure drop grows until $p_A > \tau_y$. At this point, the pressure overcomes the yield strength of the valve and so flow begins in helix $_B$. This is shown in Figure 4.7. From Equation 4.11 and continuity of flow, it can be shown that the flow in helix $_A$ must be a solution to

$$\left[\frac{\beta_B A_A^2}{r_B^0.5 A_B^2} - \frac{\beta_A}{r_A^0.5} \right] u_A^2 - \left[\frac{\alpha_B A_A}{r_B^2 A_B} + \alpha_A r_A^2 + 2\frac{\beta_B}{r_B^0.5} \frac{A_2}{A_B} \dot{x} \frac{A_A}{A_B} \right] u_A$$

$$+ \left[\left(\frac{\alpha_B A_2}{r_B^2 A_B} \dot{x} + \frac{\beta_B A_2^{2}}{r}_B^{0}.5 A_B^2 \right) \dot{x}^2 + \tau_y \right] = 0. \tag{4.14}$$

76

The derivation of Equation 4.14 can be found in Appendix B. For a given value of $\dot{x}$, u_A must be the positive solution to Equation 4.14, as the flow in the helix must be in the same direction as the piston movement. Flow velocity in helix $_B$ can then be found by $u_B = \frac{A_A}{A_B} u_A$. The total inertance is

$$b = b_A + b_B = m_{hel,A} \frac{u_A^2}{\dot{x}^2} + m_{hel,B} \frac{u_B^2}{\dot{x}^2}, \qquad (4.15)$$

while the total pressure drop is

$$\Delta p = \frac{\alpha_A}{r_A^2} u + \frac{\beta_A}{r_A^{0.5}} u^2. \qquad (4.16)$$

Equation 4.14 depends on the geometry of the inerter, material properties of the fluid, the velocity of the piston, and the yield stress of the valve. If the geometry is known, then the flow velocity can be calculated for ranges of different values of $\dot{x}$ and τ_y. These can then be used within Equation 4.15 to calculate the 'control envelope', i.e. the velocity-dependent range of inertance values which can be achieved. An example is shown in Figure 4.7 for demonstration purposes. The geometry of the inerter is given in Table 4.3. Here, both helices are dimensionally identical.

Table 4.3: Dimensions, in metres, of the inerter modeled in Figure 4.7.

r_1	r_2	r_A, r_B	r_4	L
0.12	0.30	0.01	0.13	0.6

Some important features, annotated in Figure 4.7, are

a the *on-state* limit, the inertance provided when the valve is 'fully on', such that no flow occurs in helix $_B$;

b the asymptotic *off-state* limit, the inertance when the valve is switched off, neglecting pressure drop along the valve;

c the actual off-state limit, the inertance when the valve is switched off, taking into account the drop along the valve; and

d the points at which the inertance begins to drop, set by τ_y.

The on-state limit is set by dimensions of the non-valved helix. In this case, it corresponds to the upper bound of the control envelope. It is the inertance achieved if the other helix is fully shut off, i.e. the inerter working as a conventional inerter with a single helix.
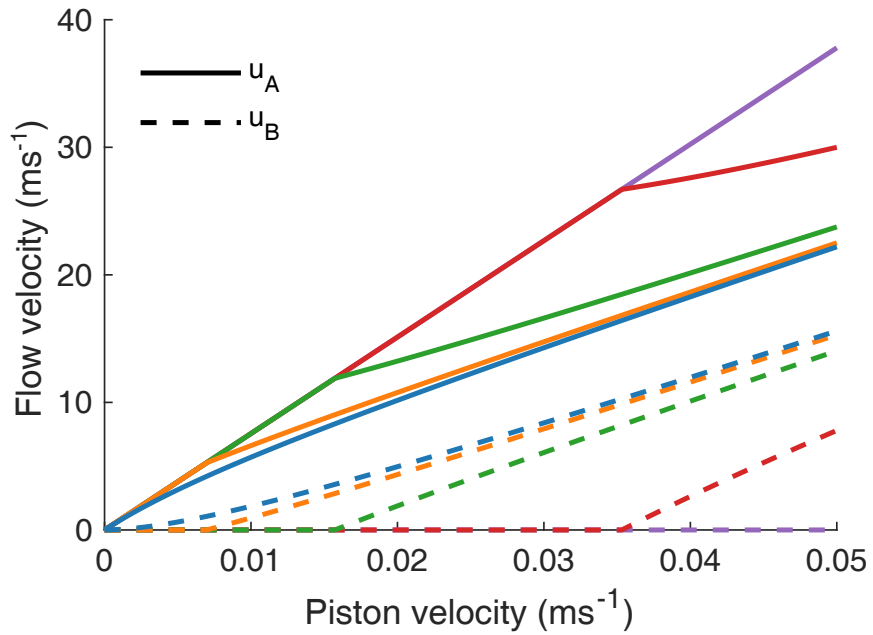
Figure 4.6: u_A accelerates in proportion to $\dot{x}$ until $\Delta p_A > \tau_y$. From this point, u_A and u_B accelerate non-linearly to some average value. The line colours correspond to the legend in Figure 4.7.
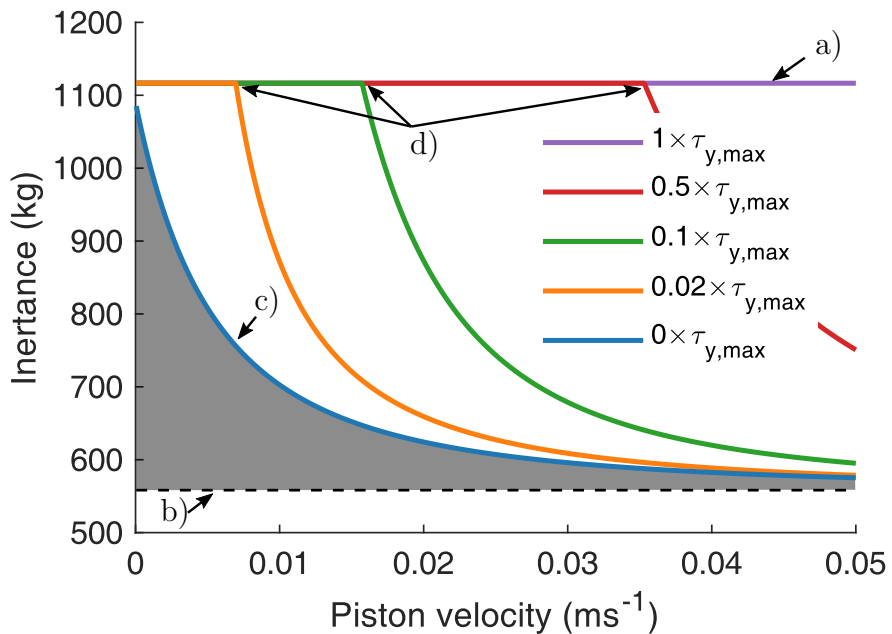

Figure 4.7: An example of an inertance envelope, created using the geometric values in Table 4.3. $\tau_{y,max}$ refers to the yield stress required to prevent any flow in helix B at the maximum velocity of the inerter. The area marked in grey is unreachable.

The asymptotic off-state limit can be found by considering the case without the valve. Equation 4.14 then simplifies to

$$\left(\frac{\beta_A}{r_A^{0.5}} - \frac{\beta_B}{r_B^{0.5}}\frac{A_A^2}{A_B^2}\right)u_A^2 + \left(\frac{\alpha_A}{r_A^2} + \frac{\alpha_B}{r_B^2}\frac{A_A}{A_B} + 2\frac{A_2 A_A}{A_B^2}\dot{x}\right)u_A - \left(\frac{\alpha_B}{r_B^2}\frac{A_2}{A_B}\dot{x} + \frac{\beta_B}{r_B^{0.5}}\frac{A_2^2}{A_B^2}\dot{x}^2\right),$$

(4.17)

and the inertance can be calculated from Equation 4.15. In this case, with geometrically identical helices, as $A_A + A_B$

$$u_A = u_B = \frac{A_0}{A_A}\dot{x},$$

(4.18)

so that the asymptotic off-state limit is exactly half of the on-state limit.

The pressure drop along the valve causes the actual off-state limit to differ from the asymptotic value. With the annular valve, this pressure drop increases proportionally with the flow rate. As the pressure drop along the helix is proportional to the square of the flow rate, this effect is larger at lower velocities.

Once the pressure in helix $_A$ is larger than the yield stress provided by the valve, flow commences in helix $_B$ and the flow begins to drop. This happens at a piston velocity of

$$\dot{x}^* = \frac{A_A}{A_0}\frac{\sqrt{\frac{\alpha^2}{r_A^4} + 4\frac{\beta}{r_A^{0.5}}\tau_y} - \frac{\alpha^2}{r_A^2}}{2\frac{\beta}{r_A^{0.5}}},$$

(4.19)

assumin $x > 0$.

If the helices are different sizes, the behaviour of the control envelope differs depending on the whether the valve is in the larger or smaller helix. Figure 4.8 shows the control envelope for two double helix inerters, with the one in Figure 4.8a having $r_B = \frac{1}{2}r_A$ and the one in Figure 4.8b having $r_B = 2r_A$. The dimensions are otherwise as given in Table 4.3. The pressure loss along the valves has been neglected for simplicity, meaning that the actual and asymptotic off-state limits are the same.

With the valve in the narrower helix, as in Figure 4.8a, the inerter operates in the same way as that in Figure 4.7. Reducing the radius of the helix causes the off-state limit to be higher, reducing the area of the control envelope.

If the valve is placed instead in the wider helix, the minimum inertance can undershoot the off-state limit, as shown in Figure 4.8b. It then gradually returns towards the off-state limit. The reason for this can be understood using Figure 4.9, which shows the contributions to inertance from each helix at $\tau_y = 0.02\tau_{y,max}$. Once flow commences in helix $_B$, the contribution from helix $_A$ drops steeply. The wider diameter in helix $_B$ allows for a higher flow rate at the same pressure but this creates less
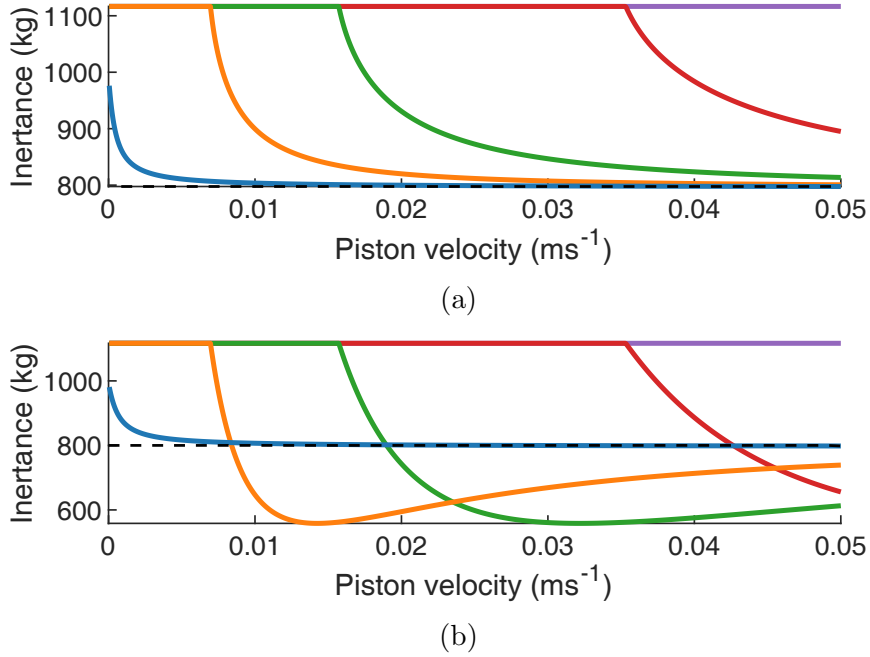
Figure 4.8: Control envelope for dual-helix inerters, with dimensions as given in Table 4.3, with a) $r_B = 0.005$m and b) $r_B = 0.02$m. Legend as in Figure 4.7.

inertance overall. The total inertance is simply the superposition of both of these effects.It should be noted that, practically, this effect is damped by the flow losses through the valve.

Figure 4.10 shows the profile of the damping force created by the inerter from Figure 4.7. It can be seen that the force is piecewise. Once the valve pressure is overcome, the rate of increase is shallower than it is before.

In general, the double-helix design may make sense in use cases where it is critical that inertance not drop below a certain value. However, care should be taken in designing the helices, especially if the valve is in the larger one. Equally, it should be kept in mind that pressure losses along the valve mean that the south-east corner of the control envelope (low inertance at low piston velocity) will be unreachable.

4.2.6   I3: bypass valve

A second feasible design for controlling inertance is to only use a single helix, with the valve connected in parallel. This configuration is shown in Figure 4.1c. As with design I2, the flow velocity in the helix is piecewise,
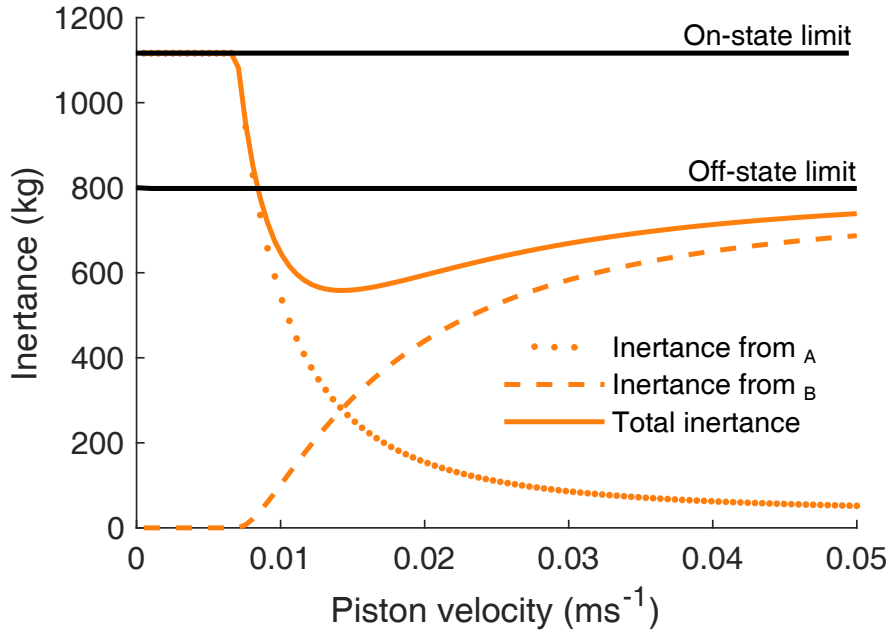
Figure 4.9: The contributions to the total inertance from helices $_A$ and $_B$, at $\tau_y = 0.02\tau_{y,max}$ for the inerter in Figure 4.8b.
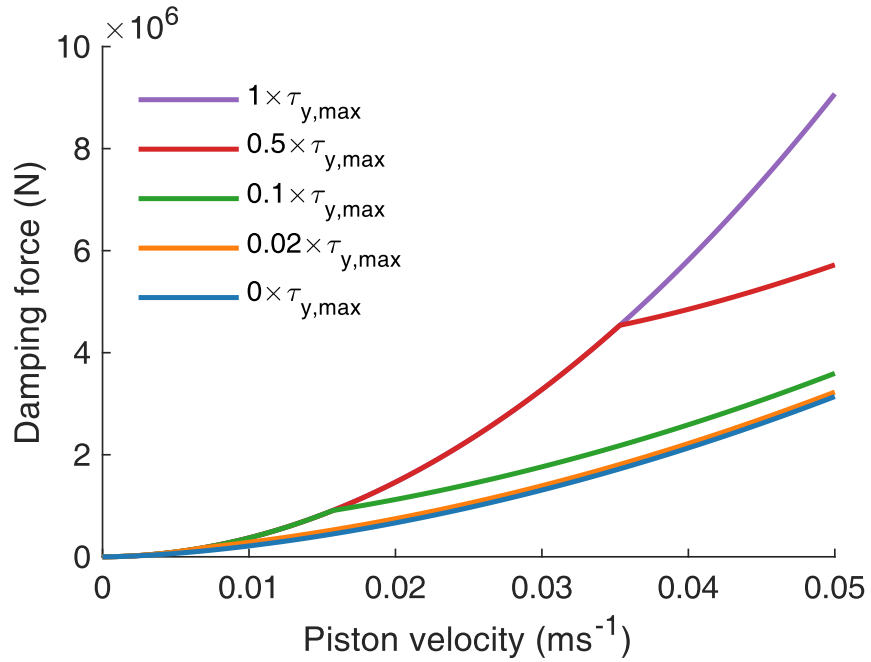

Figure 4.10: The damping force exhibited by the Inerter from Figure 4.8b.

$$
u = \begin{cases}
\dfrac{A_2 \dot{x}}{A_3} & \text{if } \dot{x} \leq \dot{x}^* \\[2em]
\dfrac{\sqrt{\left(\frac{\alpha}{r_3^2}+CA_3\right)^2+4\frac{\beta}{r_3^{0.5}}(\tau_y+CA_2\dot{x})}}{2\frac{\beta}{r_3^{0.5}}} & \text{if } \dot{x} > \dot{x}^*.
\end{cases}
\tag{4.20}
$$

The inertance can then be calculated from Equation 4.5.

The inertance and damping force for a bypass valve inerter are shown in Figure 4.11. The dimensions are the same as the device described in Table 4.2. It can be seen that, qualitatively, I3 and I2 have similar characteristics. The main difference is that the asymptotic off-state limit for the I3 device is at zero. I3 is, in some ways, an extension of the I2 design with $r_B \to \infty$.
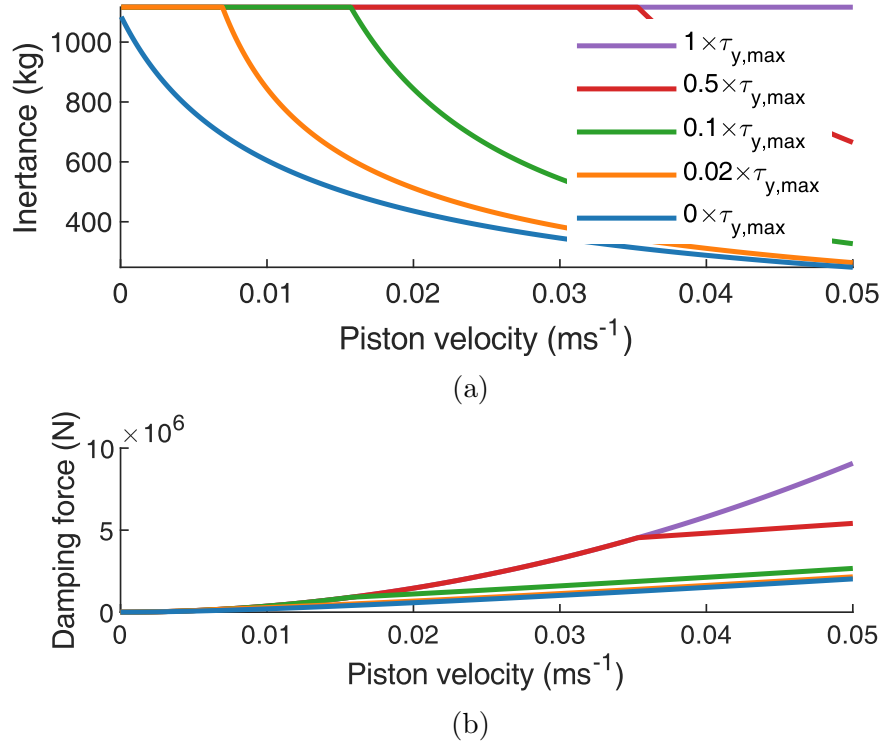
Figure 4.11: a) Inertance control envelope and b) damping force for an I3 type inerter, with dimensions as given in Table 4.3.

Using a bypass valve, instead of a second inerter, maximises the size of the control envelope. This layout also has some practical benefits, in terms of reducing the space required. However, this does come at the cost of having an off-state limit. The South-East corner of the control envelope is still inaccessible. This is an inherent characteristic but it can be minimised through careful valve design.

4.3 Valve design

4.3.1 Introduction

Much of the literature on the design of MR valves is based around design for dampers, which commonly use annular valves. While the underlying principles of designing these valves for damping and for direction control are the same, the design goals differ. This means that, while conventional MR valve design makes sense for layout I1, an adapted approach is needed to create valves for designs I2 and I3.

This section commences by describing the conventional optimisation method, developed by Rosenfeld and Wereley [202] for valves in MR dampers. This then forms the basis of a new optimisation scheme which considers the context of the bypass valve in designs I2 and I2.

4.3.2 Valve optimisation for MR dampers

This Section describes the optimisation scheme created by Rosenfeld and Wereley for MR dampers. At its simplest, an annular MR valve consists of four parts:

1. a magnetically conductive core, cylindrical in shape, with a central slot to contain the magnetic coils;

2. magnetic coils of electrical wire, wrapped tightly around the core;

3. a valve gap of height h, through which the MR fluid flows; and

4. a magnetically conductive flux return, annular in shape, which completes the magnetic circuit.

A cross section of an MR valve is shown in Figure 4.12, with these parts marked and the path of the magnetic field shown.

Rosenfeld and Wereley [202] considered an MR valve, designed for a controllable dashpot damper. The design constraints were that

1. a fixed, cylindrical volume was available for the valve;

2. the valve gap could not be varied;

3. a minimum off-state damping was required; and

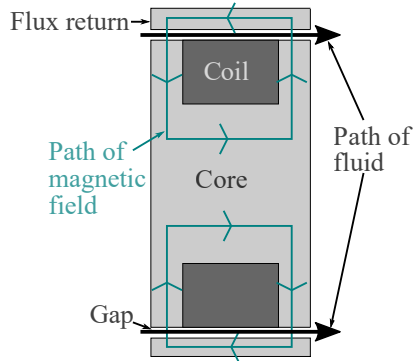4. the wire used to produce the magnetic field had a fixed diameter, d_w.

Figure 4.12: Cross-section of an MR valve, with parts labelled and the paths of the fluid and magnetic field marked.

The optimisation goal was to produce the maximum on-state damping. This optimisation method is detailed here.

So as to prevent bottlenecks in the magnetic field, it is nessecary to keep three 'critical areas' equal in size. These areas are highlighted in Figure 4.13a and are

- A_a, the cross section of the core, shown in red;

- A_b, the cross section of the flux return, shown in yellow; and

- A_c, the interior area at the flanges, shown in green.

Using the dimensions shown in Figure 4.13b, the critical areas are defined by

$$A_a = \pi t_a^2 \tag{4.21}$$

$$A_b = 2\pi t_a t_b. \tag{4.22}$$

$$A_c = \pi(r_v^2 - (t_a + w_c + h)^2) \tag{4.23}$$
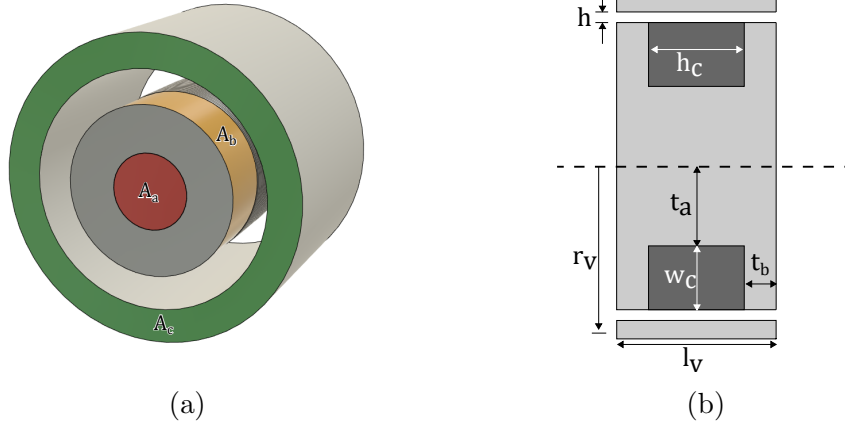
Figure 4.13: a) The critical areas of the valve and b) dimensions used in this optimisation.

Setting Equation 4.21 equal to 4.22 shows that

$$t_b = \frac{1}{2}t_a, \tag{4.24}$$

while Equations 4.21 and 4.23 can be equated and rearranged to get

$$t_a = \frac{\sqrt{2r_v^2 - (w_c + h)^2} - (w_c + h)}{2}. \tag{4.25}$$

As r_v and l_v are set by Constraint 1 and h is set by Constraint 2, Equations 4.24 and 4.25 are sufficient to fully constrain the valve geometry for a given value of w_c. As, from Constraint 4, the wire has a fixed thickness, it is only possible to achieve discrete values for h_c. For convenience, 'wrap numbers' are used, referring to the ratio $\frac{h_c}{d_w}$ (i.e. for a 12-wrap coil, $h_c = 12d_w$).

The minimum off-state damping, Constraint 3, can now be calculated by modelling the MR fluid as Newtonian. As long as $r_v >> h$, the annular channel can be approximated as two flat plates, with a width $w = 2\pi(t_a + w_c + \frac{h}{2})$. The pressure drop for a Newtonian fluid along a rectangular channel is [191]

$$\Delta p_{v,off} = CQ_v = 12\frac{\mu l_v}{wh^3}Q_v, \tag{4.26}$$

where C is the Newtonian pressure drop coefficient, used elsewhere in this section. If the piston area, A_2, is known, the off-state damping coefficient can then be calculated by

$$c_{off} = \frac{12\mu l_v}{wh}A_2. \tag{4.27}$$

To calculate the on-state damping force, the MR fluid can be modelled as a Bingham fluid. This is a class of non-Newtonian fluid, characterised by a shear stress profile of

$$\tau = \mu\frac{\mathrm{d}u}{\mathrm{d}y} + \tau_y\,\mathrm{sgn}\left(\frac{\mathrm{d}u}{\mathrm{d}y}\right), \tag{4.28}$$

where u is the flow velocity perpendicular to y, as defined in Figure 4.14.

Again, the channel can be approximated as two flat plates. The two-dimensional flow profile is then as shown in Figure 4.14, with a central plug of non-dimensional width $\tilde{\delta} = \frac{\delta}{h}$ where no shear exists. The size of this plug can be found by balancing the force from the Bingham stress on the plug with the wall stress, $\tau_w = \frac{\Delta p_a h}{2l_a}$:

$$\tilde{\delta} = \frac{\tau_b}{\tau_w} = \frac{t_a\tau_b}{\Delta p_a h}. \tag{4.29}$$

Wereley and Pang [154] have shown that the flow rate and pressure drop of a Bingham fluid between parallel plates of length l_v can be related by

$$Q = \frac{wh^3}{12\mu l_v}(1-\tilde{\delta})^2(1+\frac{1}{2}\tilde{\delta})\Delta p. \tag{4.30}$$

This Bingham flow only occurs along the section of the channel which is subject to the magnetic field, the so-called *active length*. As $2t_b = t_a$, the total pressure drop over the active length is

$$\Delta p_{v,a} = \frac{12\mu t_a}{bh^3}\frac{1}{(1-\tilde{\delta})^2(1+\frac{1}{2}\tilde{\delta})}Q_v. \tag{4.31}$$

As the flow rate in the active length must be the same as in the rest of the valve (the *passive length*), the total pressure drop along the valve in its on state is

$$\Delta p_{v,on} = \frac{12\mu Q_v}{bh^3}\left(w_c + \frac{t_a}{(1-\tilde{\delta})^2(1+\frac{1}{2}\tilde{\delta})}\right). \tag{4.32}$$

The exact value of the damping term depends on the cylinder cross-sectional area but is proportional to the pressure drop along the valve, $c \propto \Delta p_v$. It is therefore
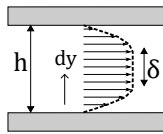

Figure 4.14: Stress profile of Bingham flow between two flat plates.

possible to calculate the ratio of the on-state to off-state damping terms from the valve geometry alone. From Equations 4.32 and 4.33, and recalling that $w_c = l_v - t_a$,

$$\frac{c_{on}}{c_{off}} = 1 + \frac{t_a}{l_v} \left(\frac{1}{(1 - \tilde{\delta})^2(1 + \frac{1}{2}\tilde{\delta})} - 1 \right). \qquad (4.33)$$

The optimisation process for a constrained MR valve for damping can be summarised as:

1. From the wire diameter, d_w, use Equation 4.25 to calculate candidate geometries for different amounts of wraps.

2. Discount any geometries which result in w larger than calculated in Step 1.

3. Find the geometry which maximises the value in Equation 4.33.

4.3.3 Valve optimisation for bypass valves

The scheme detailed in Section 4.3.2 is a well established optimisation scheme for valves within an MR damper. However, the needs and constraints of a bypass valve - as used in designs I2 and I3 - differ from those of a damper. The needs of such a valve have not previously been considered and so a new optimisation scheme is required.

With the damping control valve, a minimum off-state pressure loss is set and then the goal is to maximise the on-state pressure loss. For the bypass valve, this is reversed. A minimum value for the maximum achievable yield stress in the on-state is required. This value is based on the pressure loss in the helix at the maximum required velocity, $\dot{x}_{max}$, and can be found by

$$\tau_{y,max} = \frac{\alpha}{r_3^2} \frac{A_2}{A_3} \dot{x} + \frac{\beta}{r_3^{0.5}} \left(\frac{A_2}{A_3} \dot{x} \right)^2. \qquad (4.34)$$

This corresponds to the value required to achieve the North-East corner of Figure 4.11a.

Once $\tau_{y,max}$ is set, the goal is to design a valve which can achieve this, while having the minimum value for $\Delta p_{v,off}$. This then maximises the size of the control envelope of the device.

The fact that the valve must be in parallel with the cylinder makes it possible to relax some of the constraints used by Rosenfeld and Wereley. The maximum length of the valve is now unconstrained. While for a physical design, some practical constraints do exist on length, the fact that $\Delta p_{v,off} \propto l_v$ means that shorter valves will be inherently favoured. The minimum length of the valve is constrained by

$l_v > d_w + 2t_a$ (i.e. the valve must be long enough to contain both at least a single coil of wire and the active length). The maximum valve radius remains constrained, as this is inversely proportional to $\Delta p_{v,off}$ and so leaving it unconstrained would lead to an optimisation scheme which favours $r_v \to \infty$.

The constraint on the gap height is also removed, $\Delta p_{v,off} \propto \frac{1}{h^3}$. While relaxing this parameter does lead to a more complexity in the optimisation problem, it cannot be neglected in this case.

The equal areas requirement, used to prevent a bottleneck, is also relaxed. In its place, a *minimum area* requirement is used. Here, instead of requiring that $A_2 = A_3 = A_3$, it is simply required that all three areas are larger than the minimum required to deliver sufficient flux.

Different formulations of MRF have different curves relating yield stress and magnetic flux density, B. These relations are found experimentally and provided with the fluid. For the case of this optimisation, it is assumed that the curve is known. This means that, to achieve $\tau_y = \tau_{y,max}$, the valve must be designed to deliver sufficient maximum flux density, B_{max}.

4.3.3.1 Maximum gap height

Wereley and Pang's analysis relies on the parallel plate approximation. No reference is made to the physical requirements for this to be valid, it is simply assumed that $r_1 \cong r_2$. Relaxing this constraint by allowing the gap height to change, we require some metric to let us know at which point the parallel plate approximation stops being valid. Here we use the behaviours of Newtonian flow, under the assumption that these will carry over to Bingham flow.

The flow rate for Newtonian flow through an annular channel of length l is known to be [217]

$$Q_{An} = \frac{\pi \Delta p}{8\mu l}(r_2^2 - r_1^2)\left(r_2^2 + r_1^2 - \frac{r_2^2 - r_1^2}{\ln(\frac{r_2}{r_1})}\right),$$ (4.35)

where r_2 is the outer radius of the channel and r_1 is the inner radius. The Newtonian flow rate between two flat plates of width w and gap height h is

$$Q_{FP} = \frac{wh^3\Delta p}{12\mu l}.$$ (4.36)

If we use the outer radius of the annulus to approximate the flat plates, so that $w = 2\pi r_o$, $h = r_o - r_i$ then this becomes

$$\frac{\pi r_o(r_o - r_i)^3\Delta p}{6\mu l}.$$ (4.37)

We can now introduce the quotient $\varrho^1 \in (0,1)$ so that $r_i = \varrho r_o$. Equation 4.35 now becomes

$$Q_{An} = \frac{\pi \Delta p}{8\mu l} r_o^4 (1 - \varrho^2) \left(1 + \varrho^2 + \frac{1 - \varrho^2}{\ln(\varrho)} \right), \qquad (4.38)$$

and equation 4.37 becomes

$$Q_{FP} = \frac{\pi \Delta p}{6\mu l} r_o^4 (1 - \varrho)^3. \qquad (4.39)$$

The difference between these models can now be calculated from

$$|Q_{An} - Q_{FP}| = \frac{\pi \Delta p r_o^4}{2\mu l} \left(\frac{1}{4}(1 - \varrho^2)(1 + \varrho^2 + \frac{1 - \varrho^2}{\ln(\varrho)}) - \frac{1}{3}(1 - \varrho)^3 \right). \qquad (4.40)$$

Evaluating Equation 4.40 at the limits shows that the difference between the models tends towards zero as $\varrho \to 1$, although it is undefined at $\varrho = 0$. Both of these facts make physical sense, as the closer together the walls get, the better the parallel plate approximation becomes. However, at $\varrho = 0$, $r_i = r_o$ and so the gap becomes zero height. At the other limit, $\varrho \to 0$, the difference tends to $\frac{1}{6}Q_{An}$.

Equation 4.40 allows us to use judgement to set a reasonable limit on the parallel plate approximation. Figure 4.15 shows how the accuracy of the parallel plate assumption increases as $r_i \to r_o$. It can be seen that accuracy of 1% requires $\varrho = 0.98$, an accuracy of 5% requires $\varrho = 0.90$.

4.3.3.2 General method

From Equation 4.26,

$$\Delta p_{v,off} \propto \frac{h_c + 2t_b}{(t_a + w_c))h^3}. \qquad (4.41)$$

This represents our objective function, which we wish to optimise within our constraints. As an optimisation problem, this presents some complexities.

Firstly, the coil cannot be varied continuously but can only be defined in integer values of the number of wraps, W, and turns, T. This means that the objective function is inherently discontinuous and stepwise.

Secondly, the H-B curves which relate magnetic flux density and field intensity non-linear. Generally, look-up tables are used. This adds to the computational requirements.

Thirdly, the practicalities of machining must be accounted for. This means that the final design can't contain impossibly thin geometries. The flux return is especially
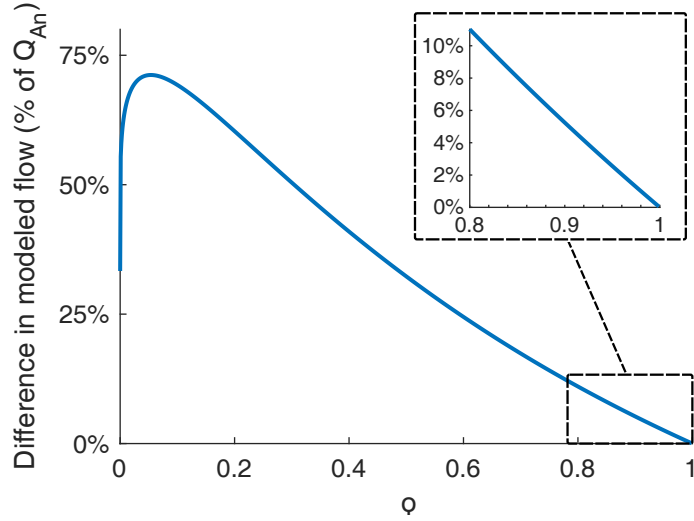
---

[1]pronounced *qoppa* or *koppa*

Figure 4.15: Relationship between accuracy of the parallel plate assumption and the quotient $\varrho = \frac{r_i}{r_o}$.

vulnerable to this with a naive approach. Additionally, we must also be mindful of the tolerances involved.

The approach taken here is two-step. First we consider the problem where the inner and outer radii of the gap are constrained. This causes the issue to become that finding the best layout of the coils of wire. Once an optimal solution can be found for this, we can iterate of the possible design space comprised of different gap heights and radii.

4.3.3.3 Optimisation criteria

As previously mentioned, we assume that r_v and $l_{v,max}$ are constrained. We also assume some maximum current, I, with a corresponding flux density and field strength in the fluid, B_f and H_f. It is convenient to describe the gap in terms of its inner and outer radii, r_1 and r_2, respectively. Initially, for clarity of explanation, we shall assume these to be fixed at some suitable value. This also fixes the cross-sectional area of the flux return, A_c.

As the flux is constrained on the minimum area along its route, we also need to ensure the other critical areas, A_a and A_b, are also at least as large as A_c. In fact, it can be shown from Equation 4.41 that the for the optimal design $A_b = A_c$. This is due to the fact that the only independent variable in A_b is t_b, which appears in the numerator of Equation 4.41. In other words, increasing the area of the flanges above the minimum required only serves to lengthen the valve unnecessarily. Thus,

the candidate geometries is constrained by $A_a \geq A_c$, $A_b = A_c$, so that

$$t_a \geq \sqrt{(r_v^2 - r_2^2)} \tag{4.42}$$

$$t_b = \frac{r_v^2 - r_1^2}{2t_a}. \tag{4.43}$$

It is now convenient to rephrase the geometry in terms of wraps, W, and turns, T. For a wired of diameter d_w, $t_a = r_1 - Wd_w$. The largest possible number of wraps is

$$W_{max} = \lfloor \frac{r_1 - \sqrt{r_v^2 - r_1^2}}{dw} \rfloor. \tag{4.44}$$

Here $\lfloor \cdot \rfloor$ denotes the floor function, i.e. the greatest integer smaller than the number contained within. As the maximum length of the valve, $l_{v,max}$ is constrained, the maximum number of turns occurs at $t_{a,max} \implies W = 1$, so that

$$T_{max} = \lfloor \frac{l_{v,max} - \frac{r_v^2 - r_1^2}{r_1 - Wd_w}}{d_w} \rfloor. \tag{4.45}$$

The zone of candidate functions is thus bounded by

$$W \in (1, W_{max}) \tag{4.46}$$

$$T \in (1, T_{max}). \tag{4.47}$$

From Ohm's law for magnetic circuits

$$NI = \sum H_i l_i, \tag{4.48}$$

where $_i$ refers to a length around the circuit and the number of turns around the circuit $N = WT$. For the circuit in question, Equation 4.48 expands to

$$WTI = 2H_f(r_2 - r_1) + H_s(2t_b + 2h_c + w_c + r_v). \tag{4.49}$$

H_s, the magnetic field intensity in the valve material can be found from the material's H-B curve for $B_s = \frac{A_f B_f}{A_c}$. Here, to ensure a sufficient H_f throughout the channel, the channel area is defined as $A_f = 2\pi r_2 t_b$.

With some rearrangement, it can be shown that to achieve sufficient field strength in the fluid, we require that

$$WTI - 2H_s d_w(W + T) \geq 2H_f(r_2 - r_1) + H_s(ta + tb + r_v - r_2). \tag{4.50}$$

Any geometry which fails to satisfy this condition can be rejected. For the remaining geometries, the solution to Equation 4.41 can be calculated and the geometry with

91

the minimum value selected as the optimum for that (r_1, r_2) pair. Any appropriate optimisation algorithm can be used for this.

This process can then be iterated for different pairs of (r_1, r_2) to maximise the denominator of Equation 4.41. Again, any suitable optimisation method can be used. From observation of Equation 4.41, larger values of both will be preferred and so maximising both r_1 and r_2 can be a useful initial guess.

4.3.3.4 Example

The criteria described in Section 4.3.3.3 were used to optimise an annular valve. The dimensions, detailed in Table 4.4 were based on the valve designed for the prototype rig, as described in Chapter 5. A grid-search function was coded in `Matlab` to find the best value of Equation 4.41 for fixed values of r_1 and r_2. This function was then called by a second grid-search, which iterated across different values of r_1 and r_2. Grid sizes of d_w and 0.1mm were used for the inner and outer functions, respectively. d_w represents the finest inner grid with physical meaning, being the diameter of the wire, while 0.1mm was selected as a suitable manufacturing tolerance. ρ was 0.95.

Table 4.4: Valve dimensions (mm) for $H_f = 190\text{kAm}^{-1}$ for the valves designed using A) the damping valve scheme and B) the bypass valve optimisation scheme

Valve	t_a	w_c	h	r_v	t_b	h_c	l_v	N
A)	5.67	2.06	0.50	10.00	2.85	14.30	20.00	111
B)	5.00	3.6	0.40	10.00	1.90	5.70	9.50	77

Low carbon steel was selected as the valve material, with a H-B curve sourced from Ref. [218]. Lord MRF-132DG was selected as the MR fluid, with magnetic properties as detailed on the data sheet [219].

The control envelopes offered by each valve on the prototype rig are shown in Figure 4.16. It can be seen that using the bypass valve optimisation scheme increases the area of the control window by 40.9%.

The valve design was validated with a finite element analysis in `Finite Elements Method Magnetics` ??, an open source Finite Element solver. The results of this validation are shown in Figures 4.17 and 4.18. It can be seen that the required value of $H_f = 190\text{kAm}^{-1}$ is, at the centreline, achieved along the entire active length.

4.3.3.5 Discussion

A grid search was used to achieve the results presented in Section 4.3.3.4. This was to ensure completeness of results and to enable sanity checks during the creation of the
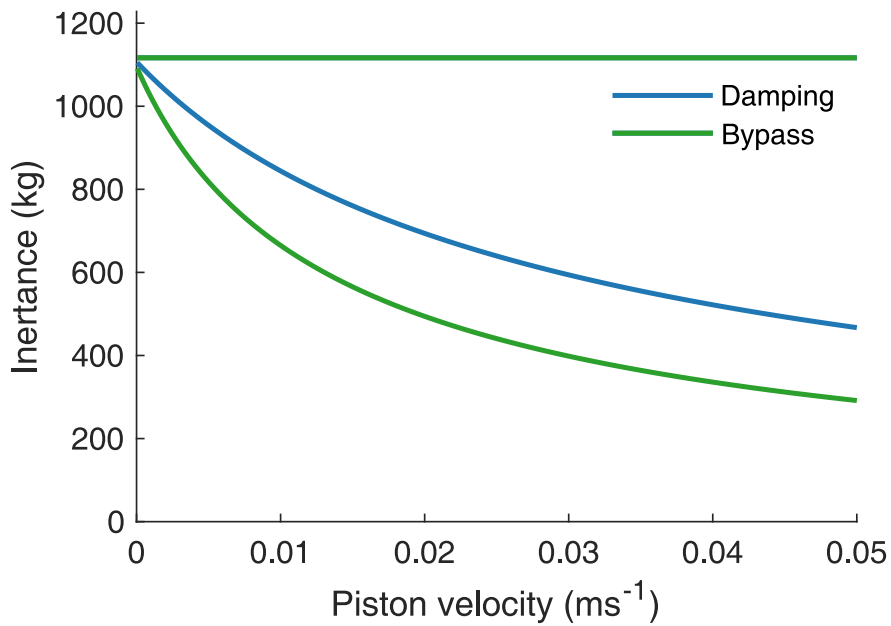
Figure 4.16: Comparison of the control envelopes for a bypass inerter with dimensions as in Table 4.4, with a valve designed using the damping and bypass optimisation schemes.
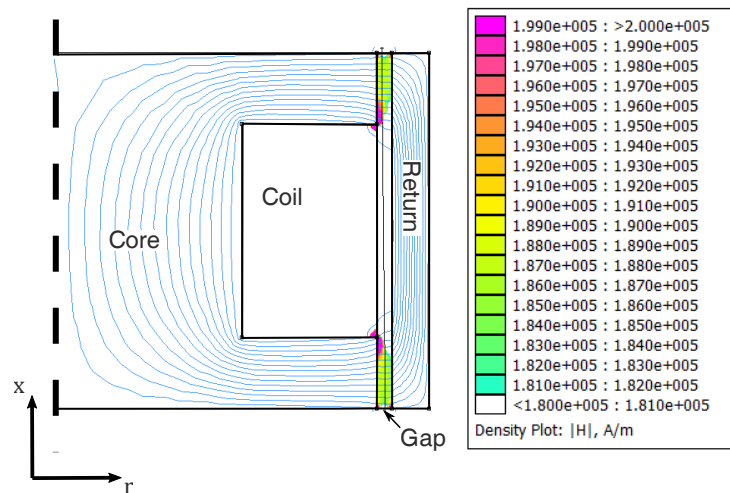

Figure 4.17: Finite element analysis of the optimised valve, showing H in the range 180-200kAm^{-1}, with the path of the magnetic field shown in blue.

scheme. The small maximum size of the valve led to a limited number of candidate geometries. This small search space meant that, despite the relative slowness of this approach, the code had a run time of around five minutes on a mid-high range laptop computer. It is conceivable that, for larger designs, the computational requirements

93
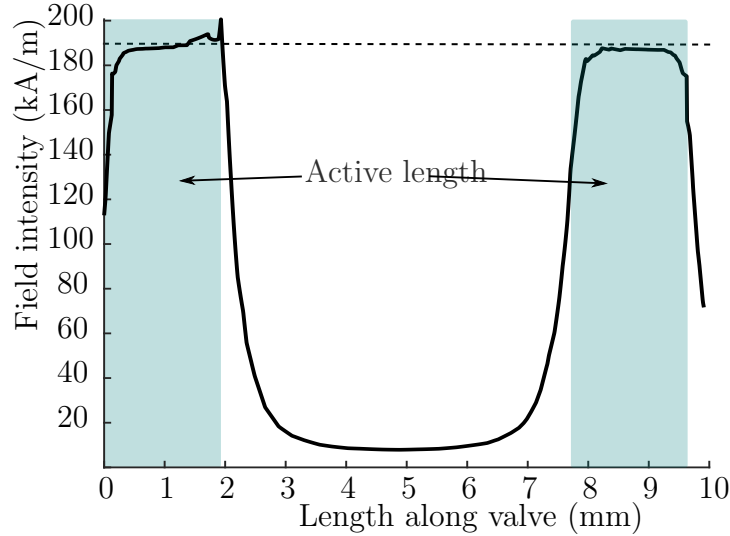
Figure 4.18: Magnetic field strength, H, along the centreline of the valve gap of the optimised valve design. The target value of 190kAm^{-1} is marked and the locations of the active length is highlighted.

could increase and different optimisation methods could be required. Those dealing with such a case should look at the methods used by other researchers dealing with MRF design, such as the SEUMRE algorithm [205].

The optimisation scheme was run multiple times, with r_v, l_v, I, and H_f all being varied. In this process, no design was observed which didn't maximise r_2 and ρ (i.e. selecting for the largest gap height at the largest gap radius). It is very easy to imagine how invalid geometries could be reached in certain cases, for example if $N_{max}I < 2B_f h$. However, it is hypothesised that, *provided a valid solution results* maximising both of these parameters will result in the optimal solution. Proving this statement is left for further work. In the interim following this heuristic greatly reduces the computational requirements of the optimisation scheme. Equally, for those using probabilistic methods, maximising both parameters would be a sensible initial guess.

While the scheme was verified using finite element analysis, no experimental validation was performed. One major area of uncertainty is the definition of ρ, which is based on the assumption that the parallel plate hypothesis generalises the same way for both Newtonian and Bingham fluids. Notably, attempts to run the optimisation with $\rho = 0.9$ ran into issues with flux leakage in the coil drastically reducing the field strength in the flux. As recent valve designs contain variable height gaps, further investigation into both the applicability of the parallel plate hypothesis and other issues surrounding larger gaps in MR valves may have some value.

94

Here, the maximising the size of the control window has been used as the basis of the optimisation scheme. For practical designs, other criteria might need to be considered either instead or as well. In some situations, material considerations and cost might need to be controlled for. For designs for high performance vehicles, weight might need to be considered. These are common criteria in design engineering, and multi-objective optimisation with these kinds of constraints possesses its own body of research, not touched upon here. One potentially interesting issue for future research is 'design for control' [220]. This involves designing to maximise 'controllability' (ability to cope with change of states). This is an important consideration when designing control hardware which we wish to be employed practically.

4.4   Quasi-dynamic models

The quasi-static models developed so far are sufficient for initial design work. However, if the control of dynamic systems is to be analysed, then clearly the dynamic behaviour of the device cannot be ignored.

The approach taken in this section is based on the hydraulic network analysis employed by Liu et al. [210]. The quasi-dynamic models are expanded by taking into consideration the changes in flow-rate in the valve and helix. The term *quasi-dynamic* has been borrowed from other fields to avoid the implication that he goal is to model the dynamics of the flow fully. The quasi-dynamic models are still an approximation, just ones involving first order differential terms.

Three models quasi-dynamic models are presented here. These are based on design I3, as described in Section 4.2.6. In the first model the bypass valve is represented by a Newtonian fluid in a cylindrical pipe, with a simple on-off valve. Additionally, the quadratic pressure loss from the secondary flows in the helix are approximated by a linear term. In the second model, this linear approximation is dropped, with the pressure loss being modelled using the quadratic, secondary damping-based model.

In the third model, the valve has an annular cross section and a Bingham model of MR fluid is used, to provide greater control. Again, quadratic pressure drop terms used in the helix. These latter two models represent the physical test rigs developed, described in Chapters 5 and 6, respectively.

4.4.1   Linear model

Approximating a non-linear system with a linear model allows for a number of analytical techniques to be applied. Analysing the linear system in this way provides for

a baseline against which the non-linear system can be compared; any discrepancies must be explainable as an effect of the non-linearities. This model is similar to the "complex damping" model employed by Deastra [221], although the route taken is different and allows for extension to a non-linear model. The value of this linear model is in the underlying trends, rather than any precise values.

The hydraulic network diagram of the model is shown in Figure 4.19. The volumetric flow rate of the flow in the cylinder is $Q_0 = A_0 \dot{x}$. Flow in the helix, Q_h is parametrised by a hydraulic resistance, D. Flow in the valve, Q_v, experiences a resistance C.
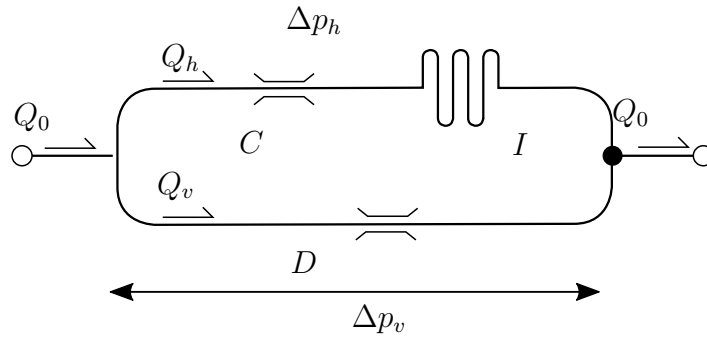
Figure 4.19: Hydraulic network diagram of the linear model.

At any given instant, flow must be conserved and that pressures must be equal. That is

$$Q_0 = Q_h + Q_v \text{ and} \tag{4.51}$$

$$\Delta p_h = \Delta p_v, \tag{4.52}$$

where $\Delta p_h = DQ_h + I\dot{Q}_h$ and $\Delta p_v = CQ_v$. Substituting these into Equations 4.51 and 4.52 leads to the form

$$DQ_h + I\dot{Q}_h = C(Q_0 - Q_h), \tag{4.53}$$

which can be rearranged to the ordinary differential equation (ODE)

$$\dot{Q}_h = \frac{D}{I}Q_0 - \frac{C+D}{I}Q_h. \tag{4.54}$$

Alternatively, a block diagram representation can be used, as shown in Figure 4.20a. Here, the forward transfer function represents the valve pressure (i.e. the right hand side of Equation 4.53). The feedback term is the calculation for the helix flow rate. The resulting transfer function can be calculated to be

$$G(s) = \frac{\Delta \hat{p}_h}{\hat{Q}_0} = \frac{C(Is + D)}{Is + (D + C)}, \tag{4.55}$$

where $\hat{\ }$ denotes the Laplace transform of a variable. The relations $\Delta\hat{p}_h = A_3\hat{F}$, $\hat{Q}_0 = A_0\hat{\dot{x}} = A_2\hat{x}s$ and $\hat{\ddot{x}} = \hat{x}s^2$ can be used. The transfer function for the admittance of the system can be shown to be

$$H_x(s) = A_2A_3sG(s), \tag{4.56}$$

while that for the accelerance is
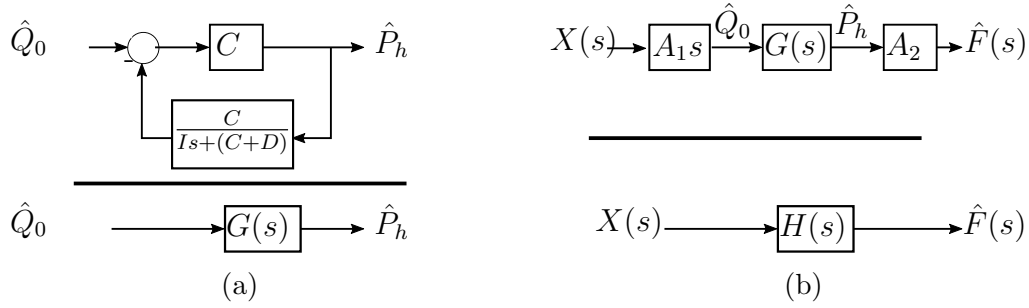
$$H_a(s) = \frac{A_2A_3}{s}G(s), \tag{4.57}$$

Figure 4.20: Block diagrams of the linear model quasi-dynamic models relating a) pressure to flow rate in the cylinder and b) force to piston displacement.

Values for the coefficients were based on an early design of the oil-based inerter developed in Chapter 5[2]. These values are given in Table 4.5. The linear pressure drop term was derived from the quadratic values according to the formula $D = A + B \cdot 2.8 \times 10^{-4}$. This corresponds to drawing a slope of a line connecting the intercept to a flow rate of $D = A + B \cdot 2.8 \times 10^{-4}\text{m}^s\text{s}^{-1}$, the equivalent of Q_0 at $\dot{x} = 0.1\text{ms}^{-1}$. This is a relatively arbitrary approach but does return a value of the correct order of magnitude. This is further discussed in Section 4.4.2.

Table 4.5: Representative coefficients for the linear quasi-dynamic model.

A_0 (m^2)	A_h (m^2)	C (kgs^{-1}m^{-4})	D (kgs^{-1}m^{-4})	I (kgm^{-4})
2.8×10^{-3}	2.0×10^{-3}	3.94×10^7	9.06×10^7	1.43×10^6

Using these values a representative Bode diagram can be constructed for the pressure-flow transfer function, $G(s)$ (Equation 4.55). This diagram is shown in Figure 4.21. The corresponding Bode diagrams for the admittance and accelerance

---

[2]As the design evolved throughout the design process, these values ended up differing from those used in the final design. This does not change any of the underlying analysis - the values still represent a realistic design of semi-active inerter

(Equations 4.56 and 4.57) are shown in Figures 4.22 and 4.23, respectively. For comparison, the equivalent Bode diagrams for the system without the bypass valve is also shown [3].
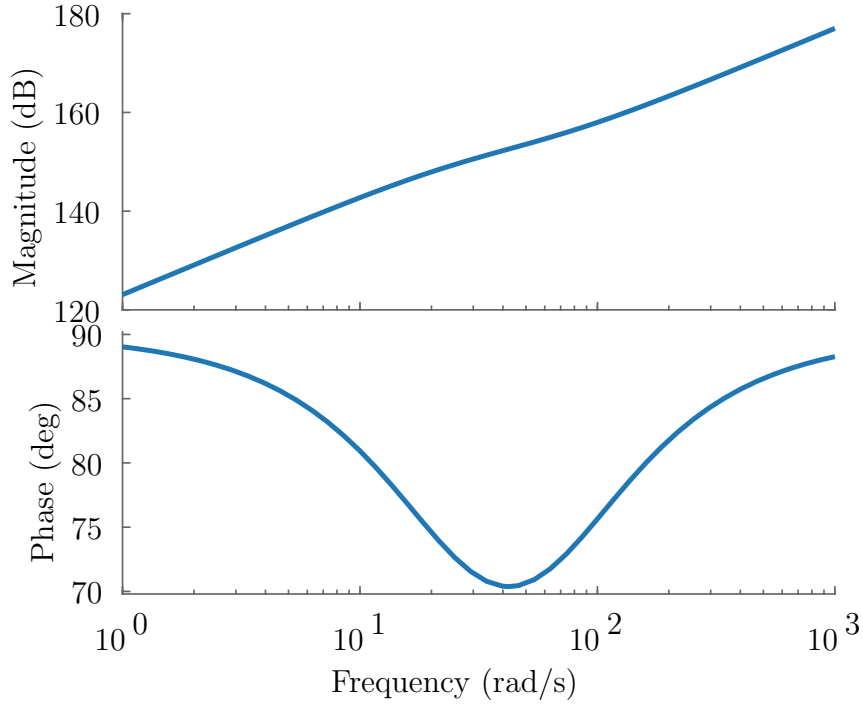

Figure 4.21: Bode diagram of pressure-flow transfer function of the linear system.

Equation 4.54 was solved in Matlab using the ODE-45 solver. The solution assumed a sinusoidally varying input such that $Q_0 = -2\pi A_2 f \sin(2\pi ft)$, where $f =$5Hz, calculated over a time vector of t from 0s to $\frac{3}{f}$s (i.e. three oscillations). The first oscillation was then discarded to account for transient effects from an imprecise initial solution. The results for Q_0, Q_h, $\dot{Q}_0$ and $\dot{Q}_h$ are shown in figure 4.24.

The resistive force from the flow in the helix was then calculated using $F = A_h(DQ_h + I\dot{Q}_h)$. This is plotted against the piston displacement Figure 4.25. The corresponding plot for the figure without the valve is included for comparison.

The clearest prediction from this model lies within the change in behaviour of the inerter with increasing frequency. This is most clearly seen in Figure 4.23. An ideal inerter would be expected to have a constant (i.e. horizontal) magnitude, representing the inertance, and a phase of $0°$. The inerter with the bypass valve closed is effectively an ideal inerter with a damper in parallel. At high frequencies the acceleration component of the force dominates and the behaviour of the ideal inerter

---

[3]The pressure-flow transfer function for this system is $G(s) = Is + D$
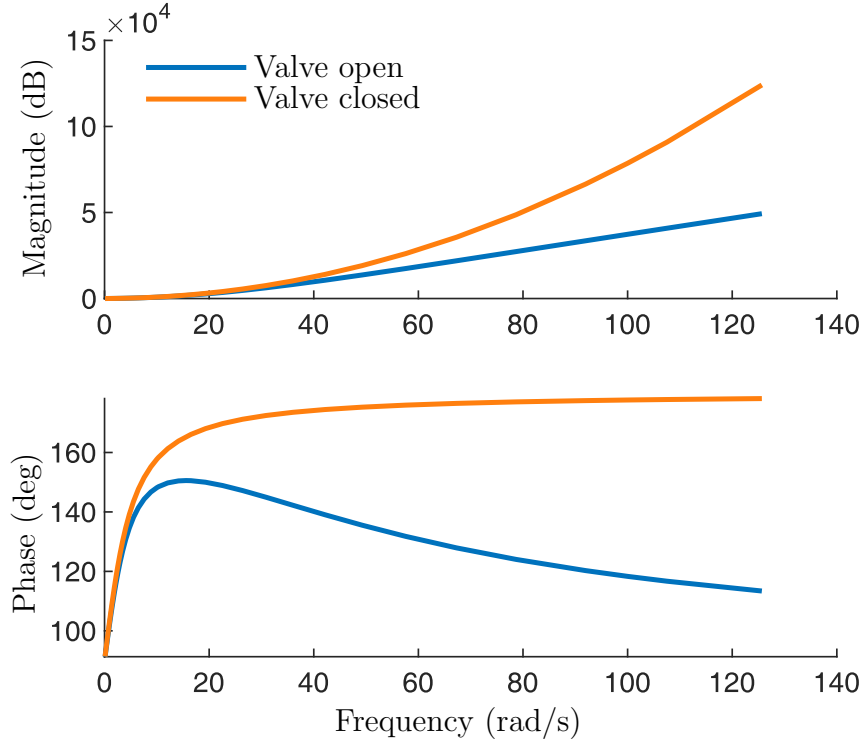
Figure 4.22: Bode diagrams of the admittance of the linear system with the valve open and closed.

is approached. At lower frequencies - where the velocity component dominates - the valve-closed inerter acts more similarly to a damper.

This behaviour can be contrasted with that of the inerter with the valve open. With the valve open, the phase of the admittance is closer to $90°$ than $180°$, i.e. the device is more like a damper than inerter, especially at higher frequencies. This difference is further highlighted by Figure 4.25, showing the force displacement behaviour of the model at 5Hz ($\approx 30\text{rads}^{-1}$). Here the change in gradient of the hysteretic loop is striking. With the valve open, the gradient is near to the $45°$ observed for other helical inerters (e.g. in Ref. [221]), while with the valve open the gradient is close to $0°$.

4.4.2   Quadratic model

The quadratic model acts as an extension of the linear model. The linearised secondary flow coefficient, D, is replaced by the linear and quadratic secondary hydraulic resistance terms, A and C respectively. Thus Equation 4.53 becomes

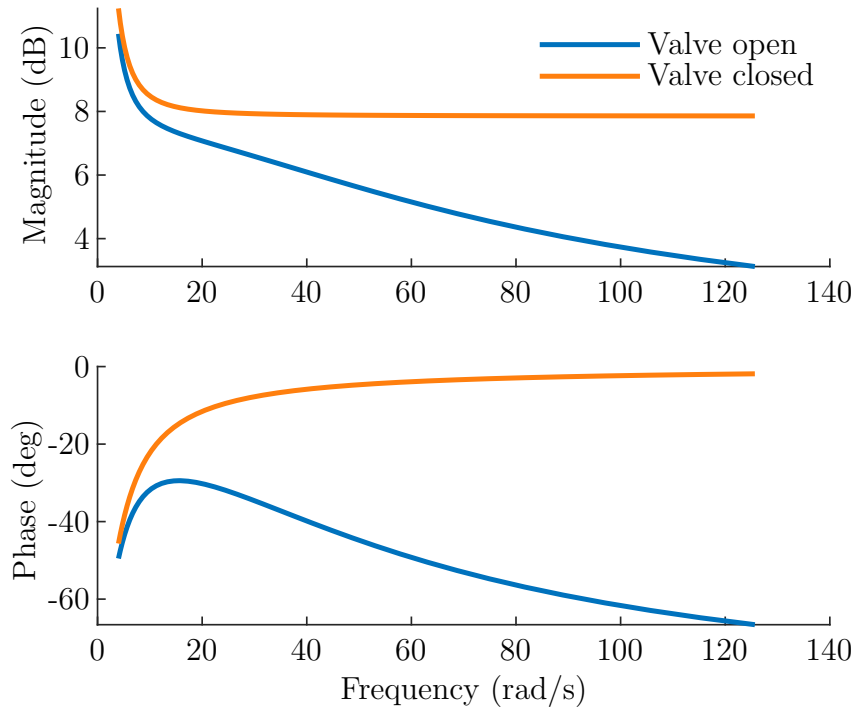$$AQ_h + B\,\text{sgn}(Q_h)Q_h^2 + I\dot{Q}_h = C(Q_0 - Q_h) \tag{4.58}$$

99

Figure 4.23: Bode diagrams of accelerance of the linear system with the valve open and closed.

corresponding to the hydraulic network diagram in Figure 4.26. Here the piecewise behaviour of the system, previously captured by a pair of equations in Equation 4.20 is represented by the signum function, for compactness, The system behaviour can be analysed by solving the ODE

$$\dot{Q}_h = \frac{C}{I}Q_0 - \frac{A+C}{I}Q_h - \frac{B}{I}\operatorname{sgn}(Q_h)Q_h^2. \tag{4.59}$$

Clearly, while using this model could be expected to more accurately capture the physics involved, it precludes the use of any linear analysis. Instead, the ode45 solver was used in Matlab to simulate the system at a number of frequencies. The coefficients used were $A = 9.04 \times 10^7$ Pas/m^3 and $B = 7.04 \times 10^8$Pas^2/m^6 , representative of the oil-based inerter in Chapter 5.

Equation 4.59 was used to simulate the behaviour of the inerter with the valve open at 1000 frequencies from 1-100rad/s. Unit amplitude was used for the input displacement. The effective Bode diagram of the system is shown in Figure 4.27. This data for the quadratic system is compared with that for the linear approximation, both calculated using Equation 4.54 and using the `bodeplot` function.
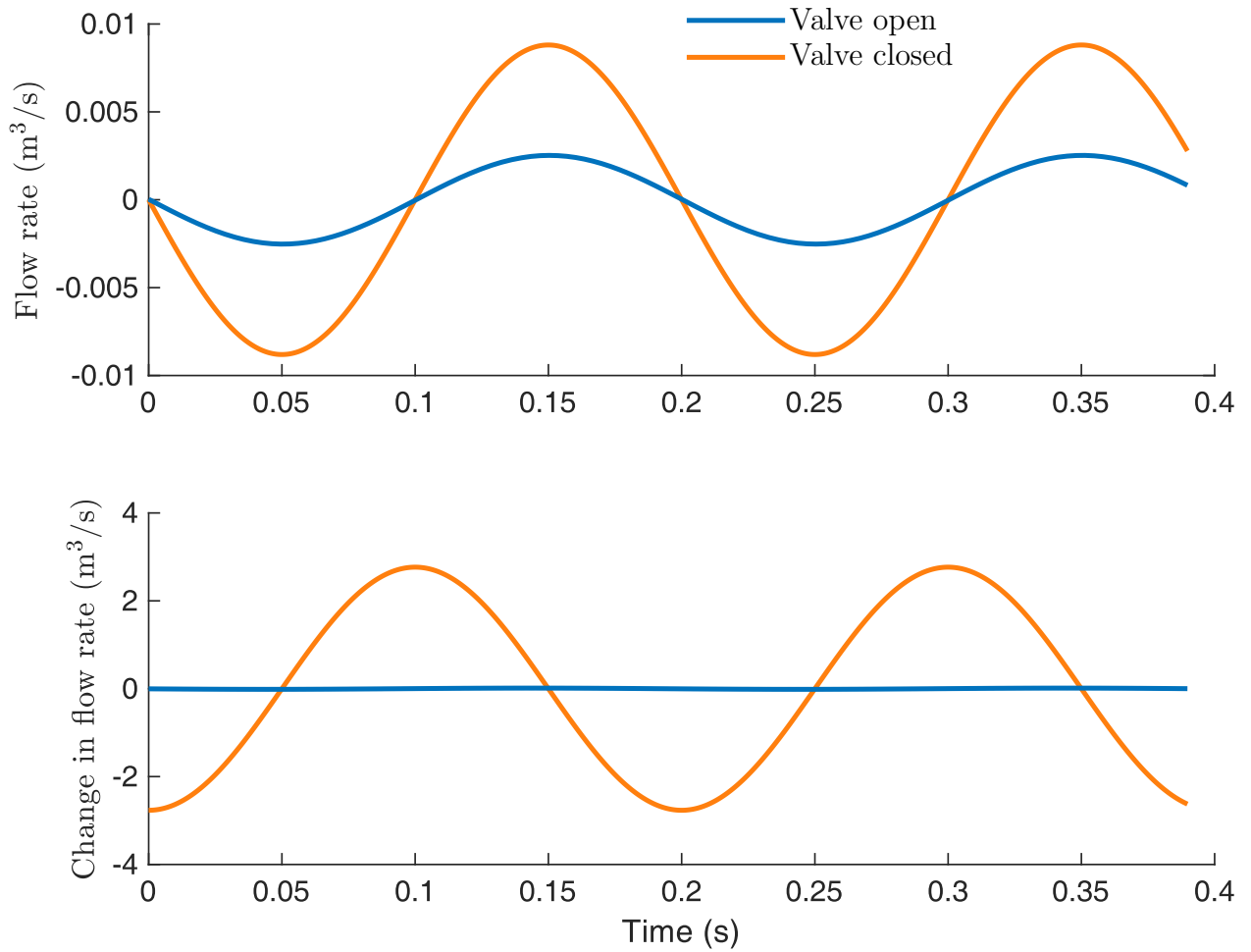
Figure 4.24: Variation of flow rates and change in flow rates for a sinusoidal input varying at 5Hz.

The log scale in Figure 4.27 makes it difficult to distinguish the data. To aid clarity, the percentage error of the linear approximation compared to the quadratic model is shown in Figure 4.29. It can be seen that the error is greatest when the phase increases and is lower at high frequencies, where the inertance component of the force dominates.

Overall, with these reasonably representative values, the linear approximation remains within ±5% of the expected value for the quadratic model. This implies that the linear approximation may have value, which would aid in control of the MR inerter and characterisation of the device. This assumption can be expected to be stronger away from the peak. As shown in Figure 4.29, this is a conservative estimate. If the displacement amplitude is reduced to a 0.1m (more representative of the work in the
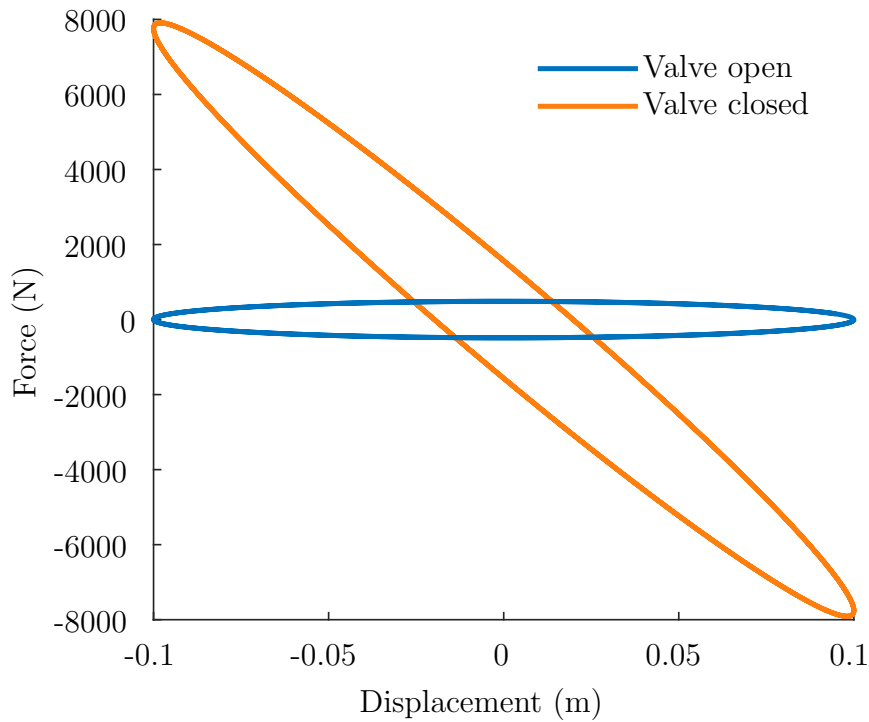
Figure 4.25: Force-displacement diagram for a sinusoidal input varying at 5Hz, for the inerter with and without a bypass valve.
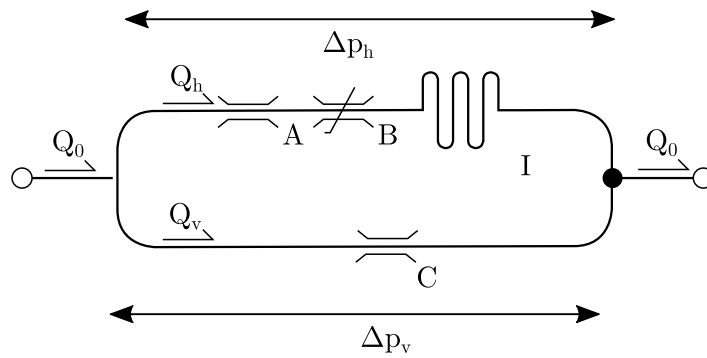

Figure 4.26: Hydraulic network diagram of the quadratic model. Note the symbol $\neq$ denotes non-linear hydraulic resistance.

rest of this thesis) then the agreement of the linear model increases significantly.

4.4.3 Full quasi-dynamic model

Up until this point, only two extremes have been considered - the valve could either be fully open or fully closed. This fails to capture a fundamental characteristic of the MR valve. The strength of the magnetic field allows the yield pressure to be
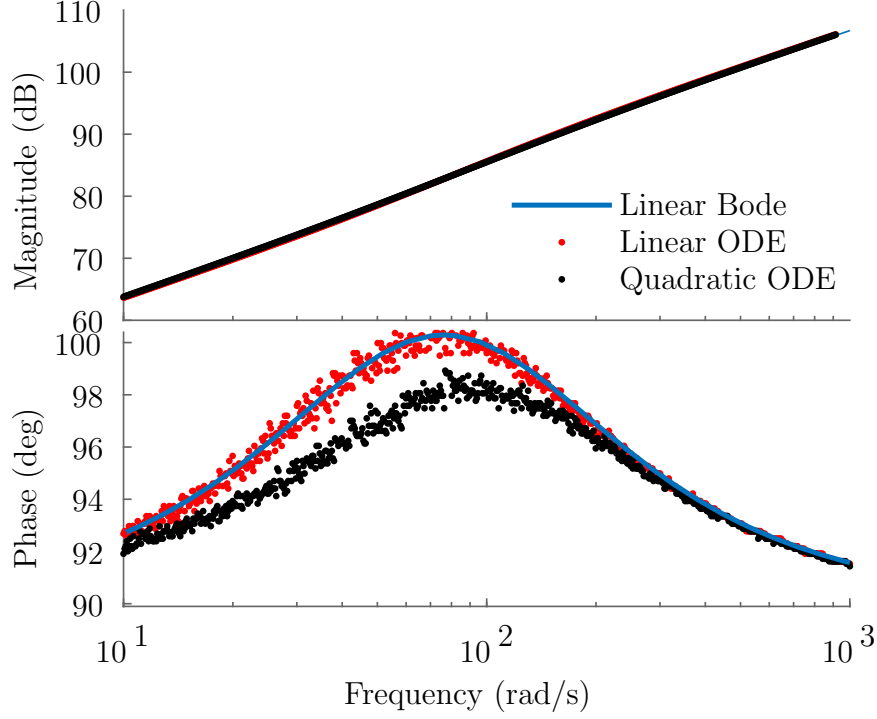
Figure 4.27: Effective Bode diagram of the quadratic model. Top figure plots $|\frac{\hat{F}}{\hat{x}}|$ in decibels.

top be continuously varied between zero and some maximum value. This means that the inertance can, theoretically, also be set at any value between the minimum and maximum, in a controllable way. Modelling this behaviour is fundamental to designing any potential control scheme in the future.

The semi-active inerter can be considered to exhibit a form of switching behaviour. The system behaviour has two distinct regions, in which the behaviour is described by a different system of equations. Which region the device is in depends on the ratio of the absolute pressure drop across the helix to the yield stress, $\frac{\Delta p_h}{\tau_y}$. The flow rate in the helix can be described by

$$\text{S1:}\ Q_h = Q_0,\ \dot{Q}_h = \dot{Q}_0 \qquad\qquad\qquad \text{if}\ \left|\frac{\Delta p_h}{\tau_y}\right| \leq 1 \tag{4.60}$$

$$\text{S2:}\ Q_h = \int \dot{Q}_h \mathrm{d}t,\ \dot{Q}_h = \frac{1}{I}\left[\tau_y + CQ_0 - (A+C)Q_h - BQ_h^2 \operatorname{sgn}(Q_h)\right]\ \ \text{if}\ \left|\frac{\Delta p_h}{\tau_y}\right| > 1, \tag{4.61}$$

When the pressure drop across the helix is less than the yield stress, (i.e $\frac{\Delta p_h}{\tau_y} \leq 1$) there is no flow in the bypass valve. This means the device will be working as a
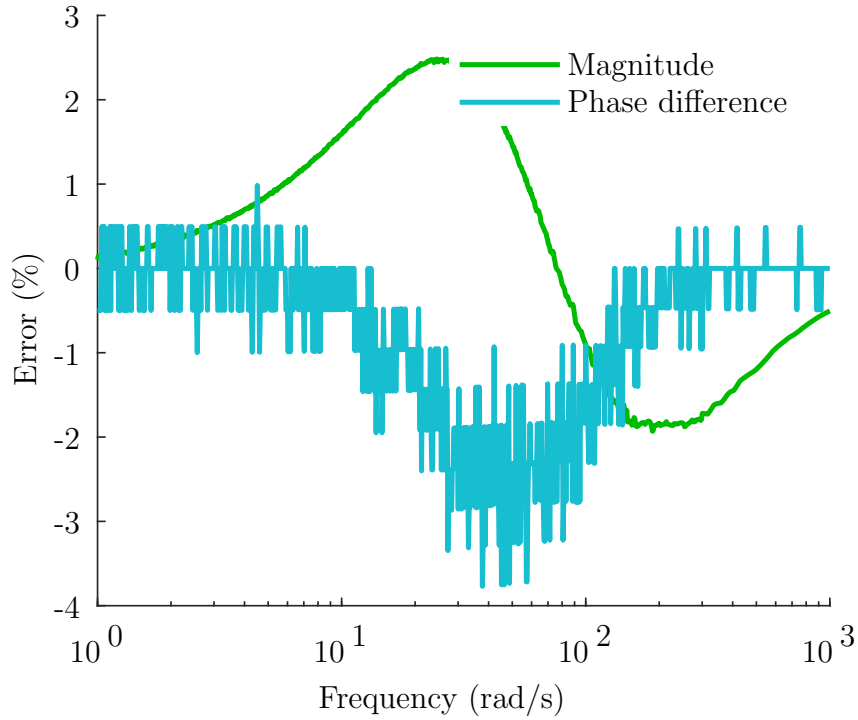
103

Figure 4.28: Error of the linear approximation as a percentage of the values calculated for the quadratic model.

conventional helical inerter and so can be modeled using Equation 4.1. Continuity of flow implies S1, Equations 4.60.

If, instead, the pressure drop in the helix exceeds the yield stress, then there will be flow in both the valve and the helix. From continuity of pressure and Equation 4.51,

$$I\dot{Q}_h + AQ_h + BQ_h^2\,\mathrm{sgn}(Q_h) = \tau_y + C(Q_0 - Q_h). \tag{4.62}$$

Thus the ODE of the system is as described by S2, Equations 4.61.

By setting Q_h and $\dot{Q}_h$ to zero, independently, the points of intersection with the opposite axis on the phase plane can be found. With $Q_h = 0$, the switching point is at $\dot{Q}_h = \pm\frac{\tau_y}{I}$. Conversely, if $\dot{Q}_h = 0$, the intercept would be at $\frac{1}{2}(\sqrt{\frac{A^2}{B^2} + 4\frac{\tau_y}{B}} - \frac{A}{B})$. The switching points for an indicative system were found numerically and are plotted in Figure 4.30.

4.5   Conclusion

This chapter presents an overview of the design issues considered in the creation of a semi-active inerter. Through this work, objectives 2 and 3 were achieved, with a
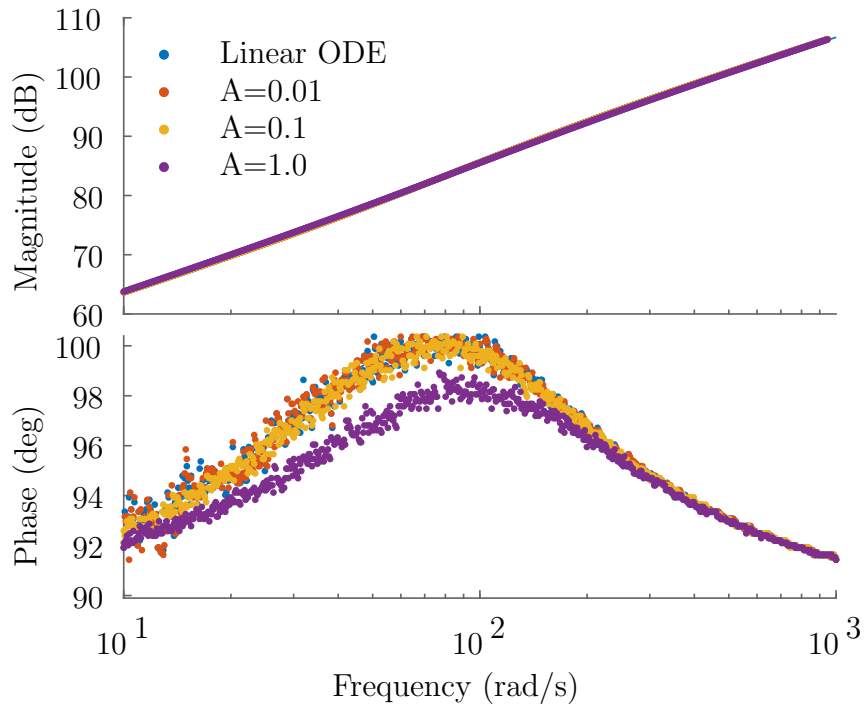
Figure 4.29: Effective bode diagrams of the linear system and quadratic system with amplitudes of 0.01m, 0.1m and 1.0m, respectively.
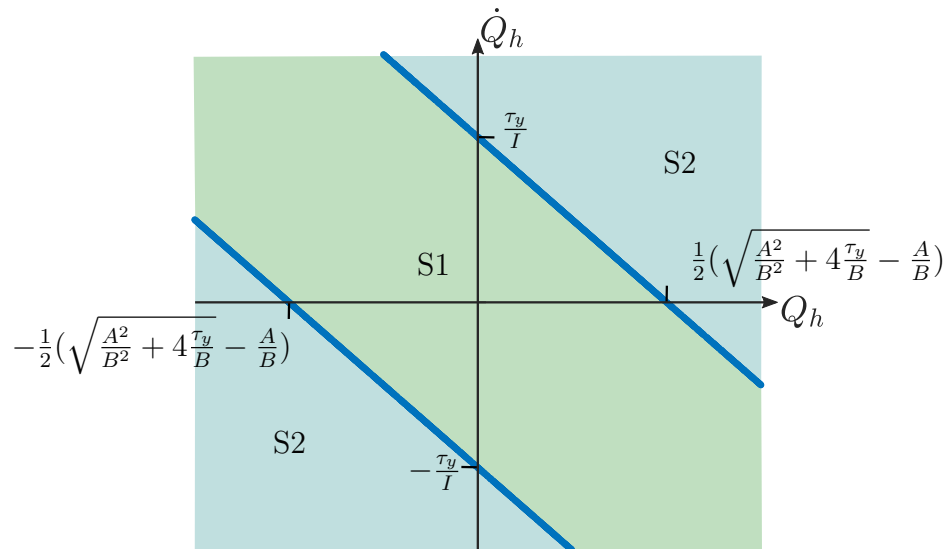

Figure 4.30: Within the green region of the phase plane, the inerter can be modeled using S1. Outside of these bounds, the inerter can be modeled using S2.

model of a semi-active inerter being developed and used to investigate a practical design.

In Section 4.2, three different layouts were presented. These were the series layout, I1; the dual-helix layout, I2; and the bypass valve layout, I3. A general model of the

helical inerter, as set out by Ref. [103], was described and used to analyse all three layouts. It was shown that design I1 could more strictly be thought of as a passive inerter with semi-active damping. It was shown how such a design could have some use, as part of a semi-active PVID. It was also shown that design I3 was effectively a subset of design I1, with both being true semi-active inerters. Example control envelopes were created for both designs and the benefits of both were discussed. Design I2 allows a specific control envelope to be designed for, by setting upper and lower bounds on inertance. However, design I3 offers the largest control envelope and requires less space, at the cost of the off-state inertance limit.

Section 4.3 covered the design of an annular MR valve. The constrained optimisation scheme for MR dampers, as presented in Ref. [202] was detailed. A new optimisation scheme was then presented, which aimed to maximise the control envelope of a semi-active inerter. This was used to design an example valve, which was compared against a valve designed using the damping optimisation method. It was shown that using the new method increased the area of the control envelope by around 16.9%. The limitations of the bypass valve optimisation scheme and some possible avenues for future enquiry were discussed.

Through the analysis in this chapter, design I3 was shown to have the greatest control range. This would aid in characterising its parameters. For this reason, design I3 was selected as the basis for an experimental prototype. The goal of this would be to validate the models developed in this chapter. Chapter 5 describes the development and testing of this rig.

Chapter 5

Designing and testing a prototype semi-active inerter

5.1 Introduction

In Chapter 4 various designs for a semi-active helical inerter were discussed. The designs were compared and the bypass valve design selected as the most likely to be successful. Quasi-static and quasi-dynamic models were developed to model the behaviour of this type of inerter.

The current chapter describes the experimental work undertaken to create a physical realisation of the semi-active inerter. The iterative design approach used is described, as well as the software and hardware used to test the rig. The ways in which the results ultimately fall short of being able to validate the models created in Chapter 4 are also discussed.

Section 5.4 then describes the design and testing of an oil-based inerter. The goal with of this was to ensure the operation of the test set-up and to identify any potential issues before using the expensive MRF. This approach also offered a higher level of predictability, being more similar to previous helical inerters. The design of the rig is detailed, as is the test methodology. The data is presented and then discussed.

Following on from this, Section 5.5 details the development and testing of the MR fluid-based semi-active helical inerter in a similar way. The changes in design which were made based on the testing of the oil-based inerter are discussed, including the design of he valve and the update to the filling methodology. The methodology is stated and the data presented and discussed.

5.2   Experimental approach

An iterative design approach was used. Initially a rig would be designed to use hydraulic oil as the working fluid. This was to create a cheap prototype which could be used to explore appropriate experimental protocols. The oil-based prototype also offered an opportunity to identify general design issues which could be considered when deigning the MR-based system.

Multiple rounds of testing were planned using the oil-based prototype. The goal of this was, at each stage, to use the data collected from the previous round of testing to update the design, data collection methodology, and system identification method. In this way, the aim was to only implement the MR fluid-based inerter once the best pathway for success was identified.

Unfortunately, constraints on time, staffing and facilities, exacerbated by the COVID-19 pandemic, meant that this plan was only partially realised. Two rounds of experiments were completed with the oil-based rig. At this point, the experimental timelines were reassessed, which identified that there was either time for one more design iteration with the oil-based system or a single design cycle with the MRF-based rig. It was decided that, despite the fact that the oil-based rig was still not performing as expected, there was better potential for knowledge gain in commissioning and testing the MRF-based inerter.

The designs and results presented in this chapter do not represent a final design of a semi-active inerter. Ultimately, they fall short of being able to either validate or disprove the models presented in Chapter 4. Nevertheless, both the results and designs are presented here with the goal of informing any future research. Potential ways in which both could be improved upon are discussed briefly here and, in more detail, in Chapter 6.

5.3   Test facility

A sketch of the test facility is shown in Figure ??, accompanied by an annotated in Figure 5.2. The rig was actuated by an Instron PLL25K servo-hydraulic actuator, fitted with a load cell. The actuator was actuated by controlled by a pair of Moog servo valves. The system allowed for loads of up to 25kN to be delivered across a 100mm range, at velocities of up to $\pm 1\mathrm{ms}^{-1}$. The actuator was situated next to a steel pillar, which acted as ground. A steel mount was manufactured and attached to the pillar. The mount featured a central hole, to allow passage for the piston.
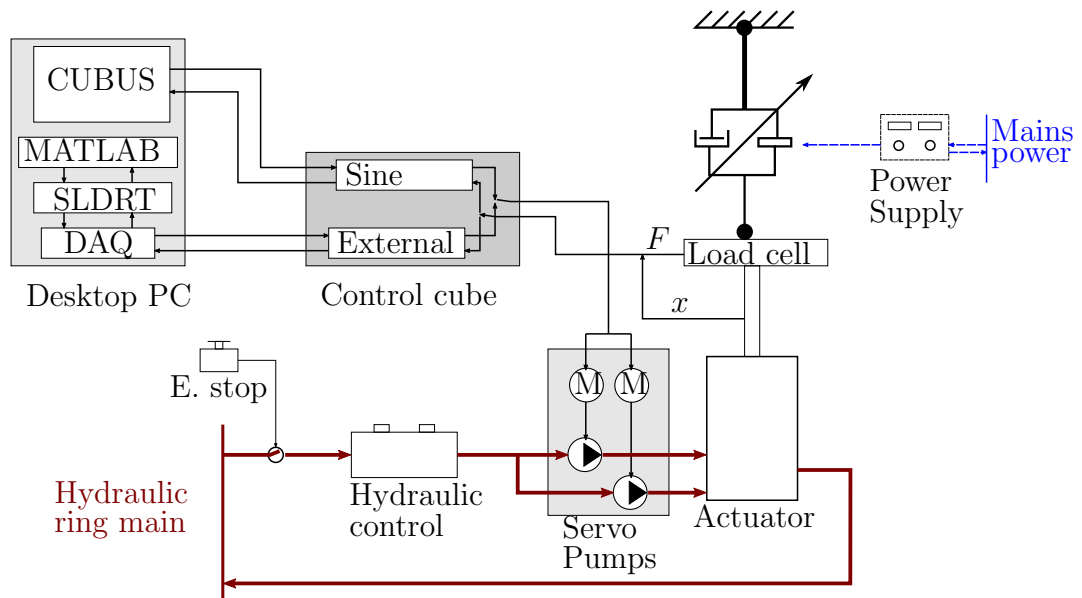
Figure 5.1: A schematic of the test facility. The path of the hydraulic supply is shown by the thicker, maroon arrows, while the dashed blue arrows indicate the voltage supply to the MR valve. Note this is simplified for clarity and is not intended as a formal circuit diagram.
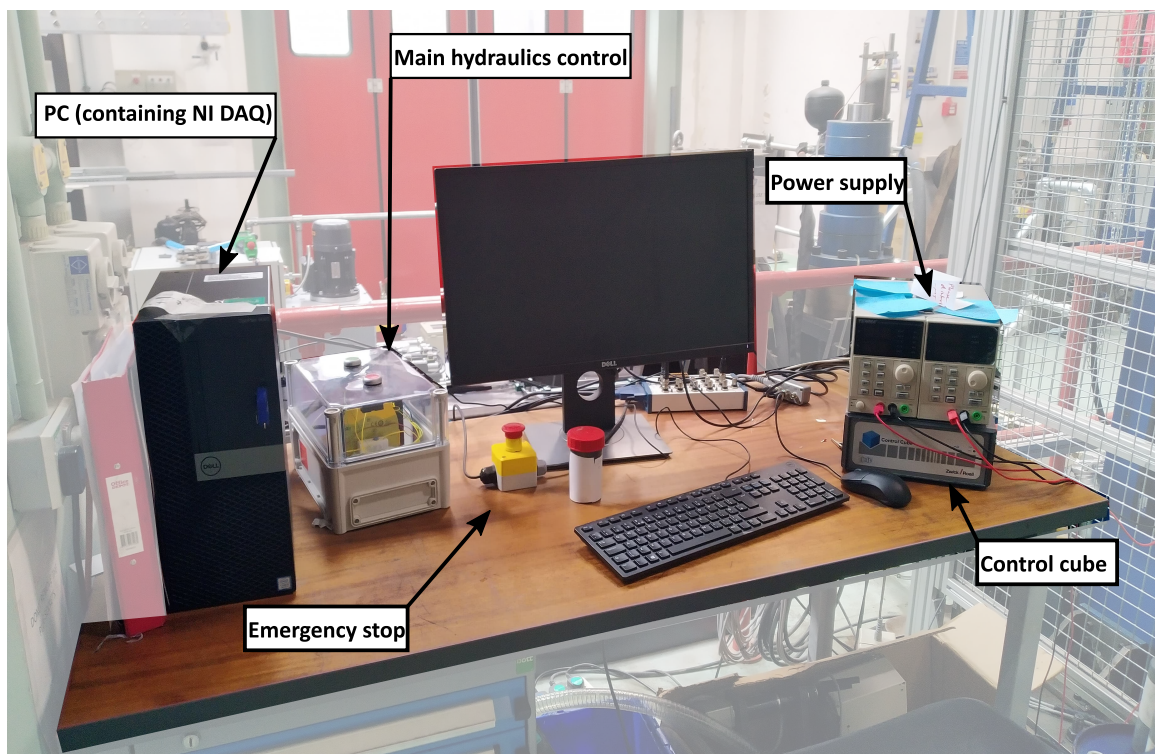

Figure 5.2: An annotated photo of the controllers used.

The control signal to the servo valves was provided by a CATS[3] control cube. The signal from the load cell was also routed through the cube. The cube was connected to a desktop PC through a National Instruments PCIe-6321 multifunction input/output (I/O) device.

Control signals could be generated in two ways. The first method was to use CUBUS/CATS[3] control software. The software allows sinusoidal signals to be generated at specified frequencies, midpoint and amplitudes. Data logging was also provided through the software, allowing force, displacement and target signal to be recorded. The software could be run in either force or displacement driven modes.

The second method used to generate signals was to run the CUBUS/CATS[3] in external signal mode. Signals could then be created using Simulink, a package within `Matlab`. Simulink Desktop Real-time (SLDRT) was then used to provide a real-time kernel and I/O blocks. Voltage signals were passed through the I/O device, to the control cube. The measured voltage signal from the load cell was then passed back through the I/O device into Simulink, to be logged. This setup up allowed for arbitrary signals to be generated.

Current control for the MR valve was provided using a TENMA 72-10495 Digital-Control DC power supply. This could supply up a current of up to 5A (or up to 30V) out of each of its two ports. The supply had a resolution of 1mA and an accuracy of 99.5%.

For safety reasons, the hydraulic actuator was contained within a cage. An electronic interlock on the door prevented high pressure supply to the cylinder with the cage door open.

5.4 Oil-based inerter

5.4.1 Design

An Aventics double-acting, through-rod, pneumatic cylinder was sourced to act as the main body of the inerter. A through-rod cylinder was required to avoid a volume difference between up and down strokes. A pneumatic cylinder was selected instead of a hydraulic cylinder with the goal of minimising friction between the piston head and the cylinder wall. The expected loads and pressures during operation were significantly lower than for a conventional hydraulic system and within the range the component is rated for (up to 10bar). The cylinder stroke was 100mm.

Figure 5.3 shows the inerter schematically and in situ, respectively. The cylinder (A) was fixed to a bracket at the top using four bolts. The plate had a central hole

to allow passage of the piston and was bolted to the central pillar. The other end of the piston attached to the actuator with a spherical eye joint.

The helix was created from 3.1m of polyvinyl chloride hose. The hose (B) was wrapped around a 0.2m diameter central core to maintain its helical shape and fastened in place using cable ties. The core itself was attached to the protective cage. A bypass (C) was constructed from rubber hose on the opposite side of the cylinder.

Three-way ball valves (D, E) were included at the top and bottom of the cylinder. The valves allowed for flow to be isolated either in the helix, in the valve, or in both. A filling port (F) was included at the bottom of the rig. A bleed valve (G) was connected at the top of the rig to allow air to escape during the filling process (see Section 5.4.1.2).
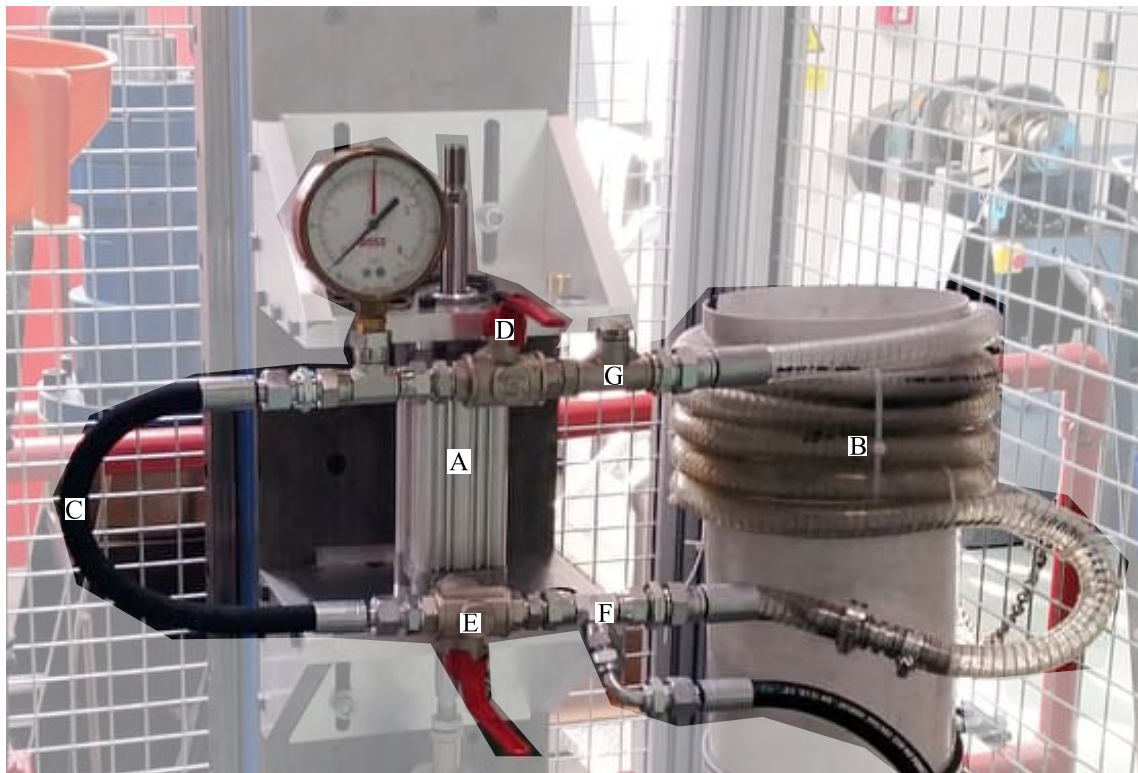

Figure 5.3: The inerter in situ, annotated as referenced in text

The inerter dimensions are given in Table 5.1.

Table 5.1: Dimensions (m) of the inerter.

r_1	r_2	r_3	r_4	L
0.0315	0.01	0.025	0.01	3.14

5.4.1.1 Working fluid

MANNOL 7408 mineral engine oil was used as the working fluid. According to the manufacturer the oil has a density of 892kg/m^3 at 20°C and a kinematic viscosity of 282mm^2/s at 40°C. This translates to a dynamic viscosity of 0.251Pas.

5.4.1.2 Filling strategy

An earlier design of the inerter was filled from the top. While this simplified the design significantly, it created difficulties in removing all the air contained within the system. Despite best efforts, a significant (c.a. 10-15ml) air pocket was observed at the top of the helix. The compressibility effects of this were also very apparent in the early tests. Based on these early tests, the filling strategy underwent a major redesign.

With the ball valves (parts (D and E) in Figure 5.4) fully open and the piston head at its full downward stroke, the fluid was fed in through a hand pump (H). It entered the inerter through the filling port (F) at the lowest point. The fluid was continuously pumped until it visibly reached the top of the inerter and the pressure gauge (I) reported a positive pressure in the system. The entry valve (J) was then closed and the system left for 10 minutes to rest, allowing air to escape from the bleed valve (G).
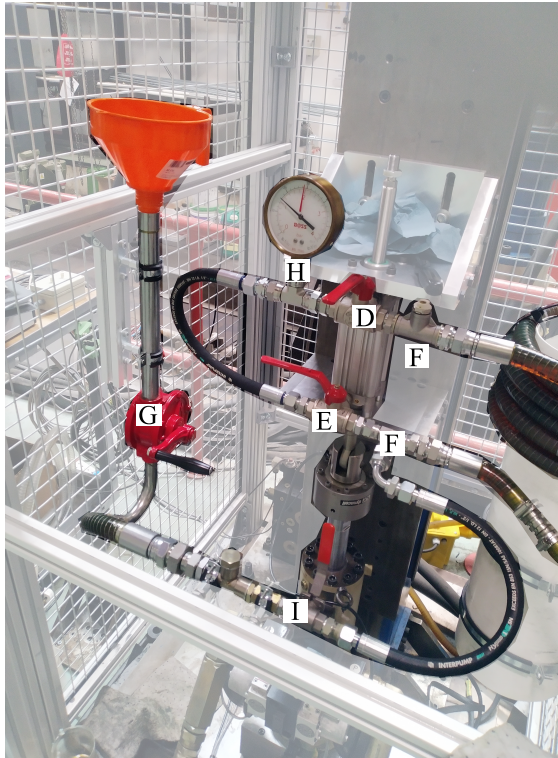
Figure 5.4: The inerter rig, with the elements used in the filling process labelled.

After resting, the piston was slowly cycled and the process repeated until no air exited the bleed valve.

Based on visual estimates of the size of the remaining air bubble, this process resulted in a 90% reduction in entrapped air. Unfortunately, small local high points around the connections, as shown in Figure 5.5, prevented further reduction.
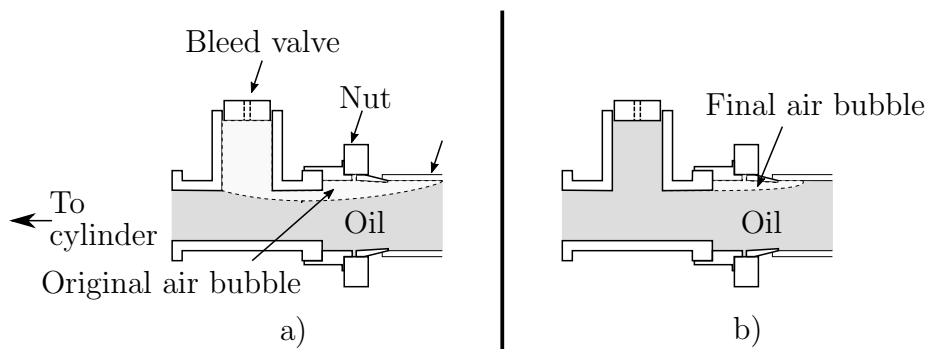

Figure 5.5: a) Initially a large amount of air was trapped at the highest point of the system. Even after a rigorous filling protocol, b) some of this air remained at local high points.

Figure 5.6 gives a qualitative demonstration of the effect of the filling protocol. It can be seen that the non-linearity in the south east corner is greatly reduced in the

second test, which followed the filing protocol. Note that, due to changes in the test protocol[1], the two data sets aren't directly comparable. For ease of comparison, both datasets have been normalised by their own maximum force and displacement values. Experimental differences between the two datasets mean it cannot be concluded that this difference was definitely due to the improved filling protocol. This figure is meant as a qualitative example only.
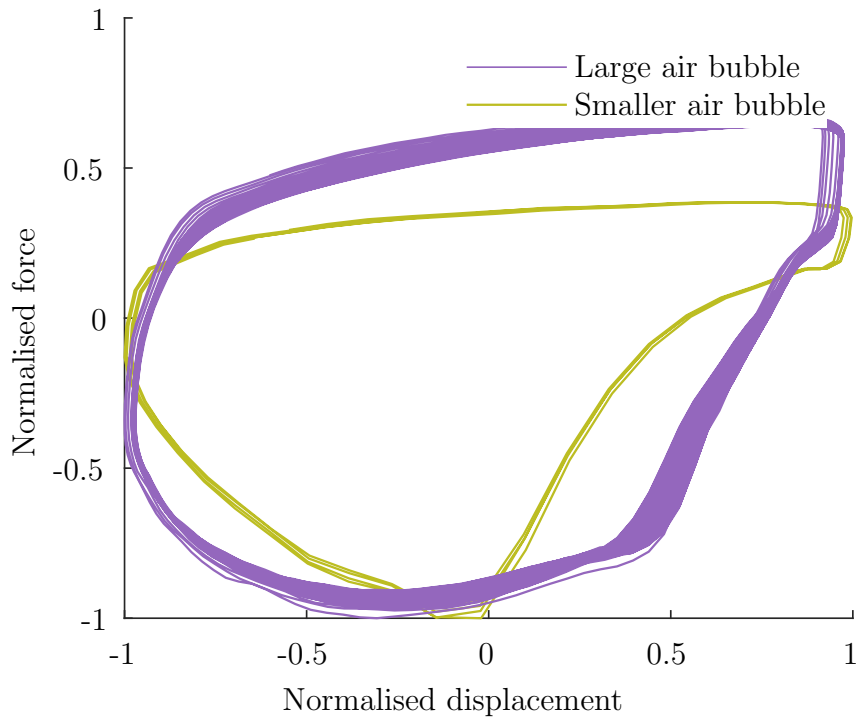

Figure 5.6: The lower part of the hysteris loop became more regular with the updated filling protocol. The earlier test (labelled 'large air bubble') was conducted at an amplitude of 10mm, while the later was at 4mm. Both tests were conducted at 4Hz.

5.4.2 Predicted behaviour

The inertance and damping ratios for the rig with the bypass valve locked off (i.e. acting as a conventional helical inerter) were calculated using the model developed by Swift et al. [103]. This model predicted $b = 11.2$kg of inertance, a linear damping coefficient of $c_l = 44.4$Nm/s and a quadratic damping coefficient of $c_q = 15.5$kg/m.

---

[1]Both were tested using sinusoidal displacement at 4Hz, the earlier test was conducted at an amplitude of 10mm, while the later one was conducted at 10mm. Reducing the air in the system reduced the relaxation, as desired, but this meant that the force safety limits were reached at lower amplitudes

In Chapter 4, it was shown that a linearised quasi-dynamic model had a 97% agreement with a full non-linear quasi-dynamic model, with the benefit of greater simplicity and speed. Using a modified version linear model, the expected behaviour of the inerter with its valve open and closed were compared assuming a forcing amplitude of 10mm. Equation 5.1 was modified to account for the greater mass of the fluid in the bypass valve. The inertia of the fluid in the valve was approximated as $I_v = \frac{\rho l_v}{A_v}$. The transfer function was then found to be

$$G(s) = \frac{\Delta \hat{p}_h}{\hat{Q}_0} = \frac{II_v s^2 + (CI + DI_v)s + CD}{(I + I_v)s + (C + D)}. \tag{5.1}$$

The remainder of the analysis remained as described in Section 4.4.1.

This predicted behaviour is shown in Figure 5.7 and the coefficients used in the model are presented in Table 5.2.
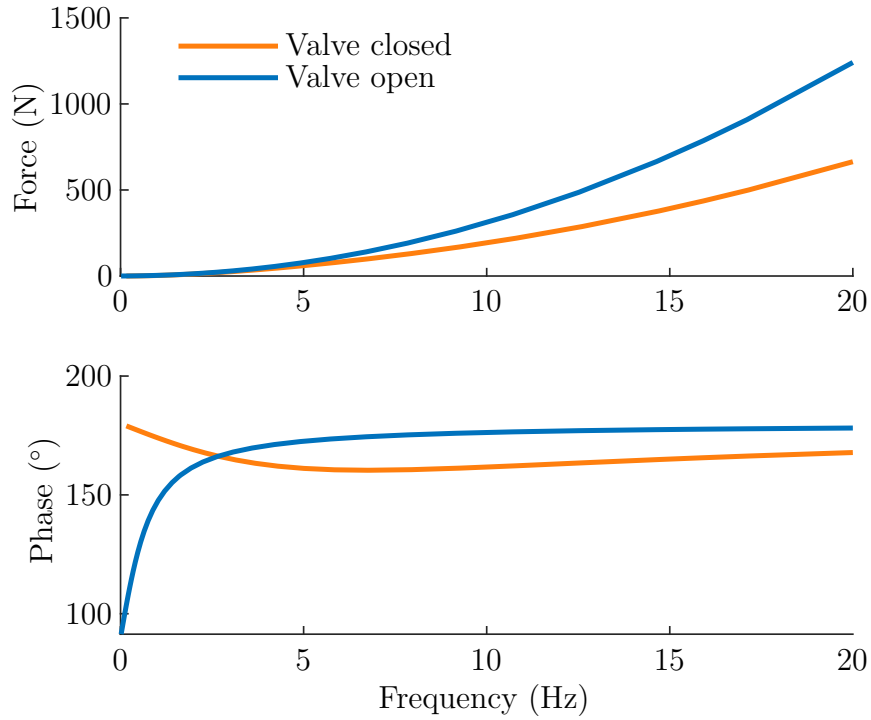

Figure 5.7: Comparison of the expected maximum force and phase of the oil-based inerter with the valve open and closed between 0-20hz, at 10mm amplitude forcing.

Table 5.2: Dimensions (m) of the inerter.

I	I_v	C	D
1.43×10^6	7.88×10^7	1.43×10^6	5.84×10^6

5.4.3 Methodology

The prototyping process was used as an opportunity to trial different parameter combinations. The sinusoidal signals were generated within CUBUS, which allowed the amplitude and frequency, as well as number of cycles to be specified. All tests were conducted in displacement control mode.

Sinusoidal tests were conducted with flow in the helix only, the bypass valve only, and in both. An exploratory approach was taken to find a suitable combination of amplitude and frequency for the forcing signal. Table 5.3 summarises which tests were conducted with each combination. For this series of tests, 10 cycles per test were deemed to be sufficient.

Table 5.3: Combinations of test parameters used in sinusoidal tests. V means the test was done with the flow in the valve only, H means flow in the helix, and B means flow in both.

	Amplitude (mm)		
Frequency (Hz)	4	5	8
1	H	B,H	H
1.5	H	B,H	H
2	H	B,H	H
2.5	H	B,H	-
3	H	B,H	-
3.5	H	B,H	-
4	H	B,H	-
4.5	H	-	-

The majority of the tests were conducted sequentially from lowest to highest frequency. A test would be conducted at 4mm amplitude, then 5mm amplitude and finally at 8mm amplitude. The maximum frequency studied each time was reduced as the system hit the maximum allowed force. Tests were conducted in pairs at each frequency, with the helix only test being conducted before the valve and helix test. Finally, a 3mm amplitude, 8Hz test was conducted ad hoc., with flow in the helix only.

5.4.4 Data

Figure 5.8 compares the data collected from the rig with the valve closed with the modelled data. The modelled data was generated in Matlab using the theory de-

116

scribed by Swift et al. [103]. The comparisons are done at 1Hz and 4Hz, respectively, both at 5mm amplitude.
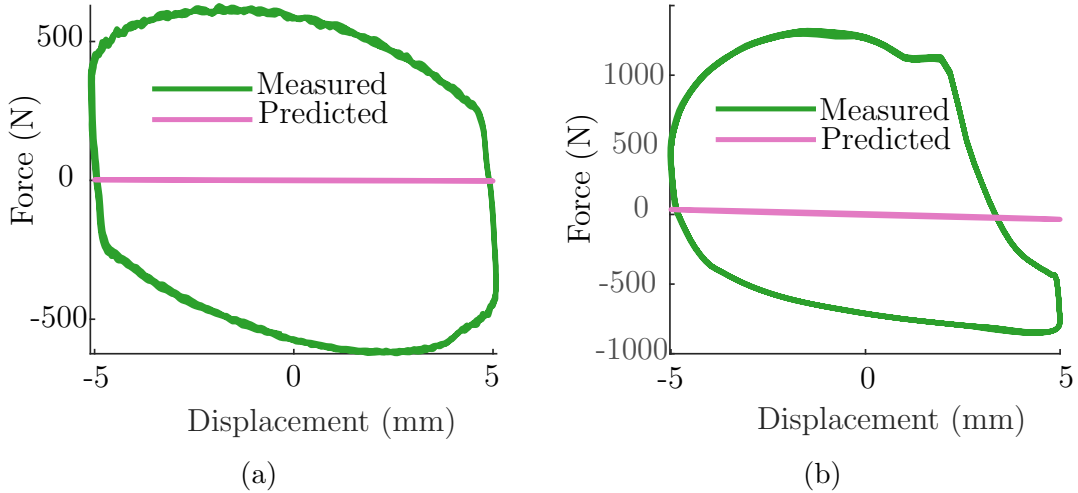

Figure 5.8: Comparison of modeled force-displacement with measured data at a) 1Hz and b) 4Hz. Both tests at 5mm amplitude.

Figure 5.9 compares the behaviour of the rig with the valve open and closed. The eight tests were conducted at 1, 2, 3 and 4Hz respectively. All tests were conducted at 5mm amplitude.

Figures 5.10 and 5.11 shows the data with flow in the helix only. In Figure 5.10 the tests conducted at the same frequency with different amplitudes. In Figure 5.11 the tests at the same amplitudes but with different frequencies are compared. The aim of these tests was to gain a sense of which combinations of parameters would be useful to test, as well as to get a sense for any non-linearities in the inerter.

5.4.5 Discussion

Figure 5.9 compares the behaviour of the inerter with the quasi-steady model. It can be seen that the measured force was several orders of magnitude greater than predicted. For the 1Hz test, a maximum force of 2.6N was expected but 629N was measured. For the 4Hz test a maximum of 35N was predicted and 1322N was measured. At least part of this discrepancy can be attributed to friction, possibly between the seal and cylinder body.

From Figure 5.9 it can be seen that opening the valve had a clear effect on the force. With the valve open, there is a reduction in the peak force generated of around 80N. This reduction was generally not dependent on the frequency or the size of
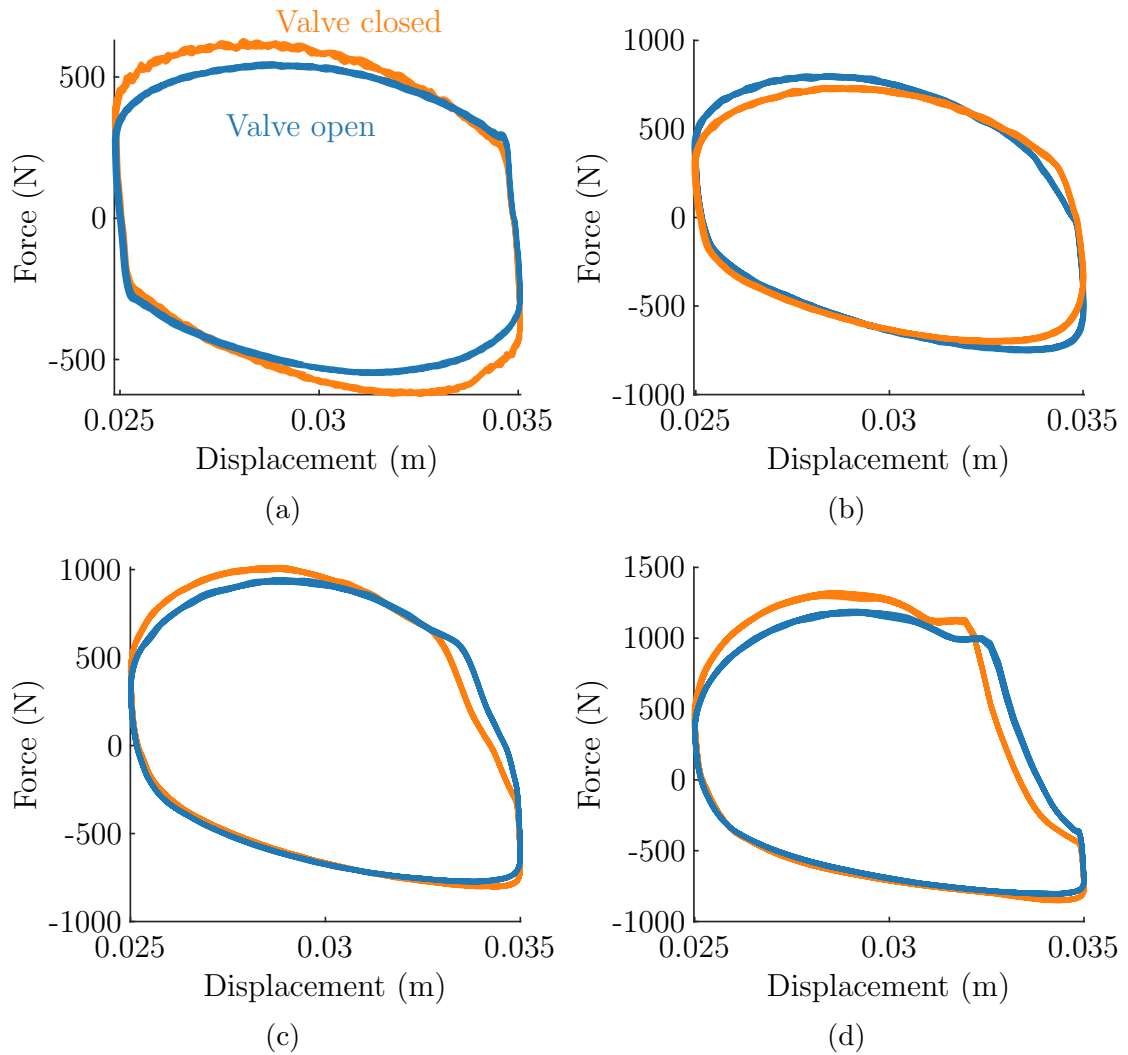
Figure 5.9: Comparison of the inerter with the valve open and closed at a) 1Hz, b) 2Hz, c) 3Hz and d) 4Hz. All tests at 5mm amplitude.

relative size of the underlying force, with the exception of the 4Hz test. In the 4hz test, the difference between peak forces was approximately 200N. However this test also displayed additional non-linearities, visible in the rightmost portion of the data, discussed more below.

Some attempt was made to apply a non-linear evolutionary optimiser to fit a parametric model to this data, with the goal of identifying the inertance and non-linear damping components. Unfortunately, the discrepancies between the different data sets meant consistent values for these could not be identified.

Figures 5.10 and 5.11 show the data for the helix-only tests, grouped together by frequency and amplitude, respectively. Plotted in this way, two major features become apparent. The first feature is the step type forcing, most clearly visible in
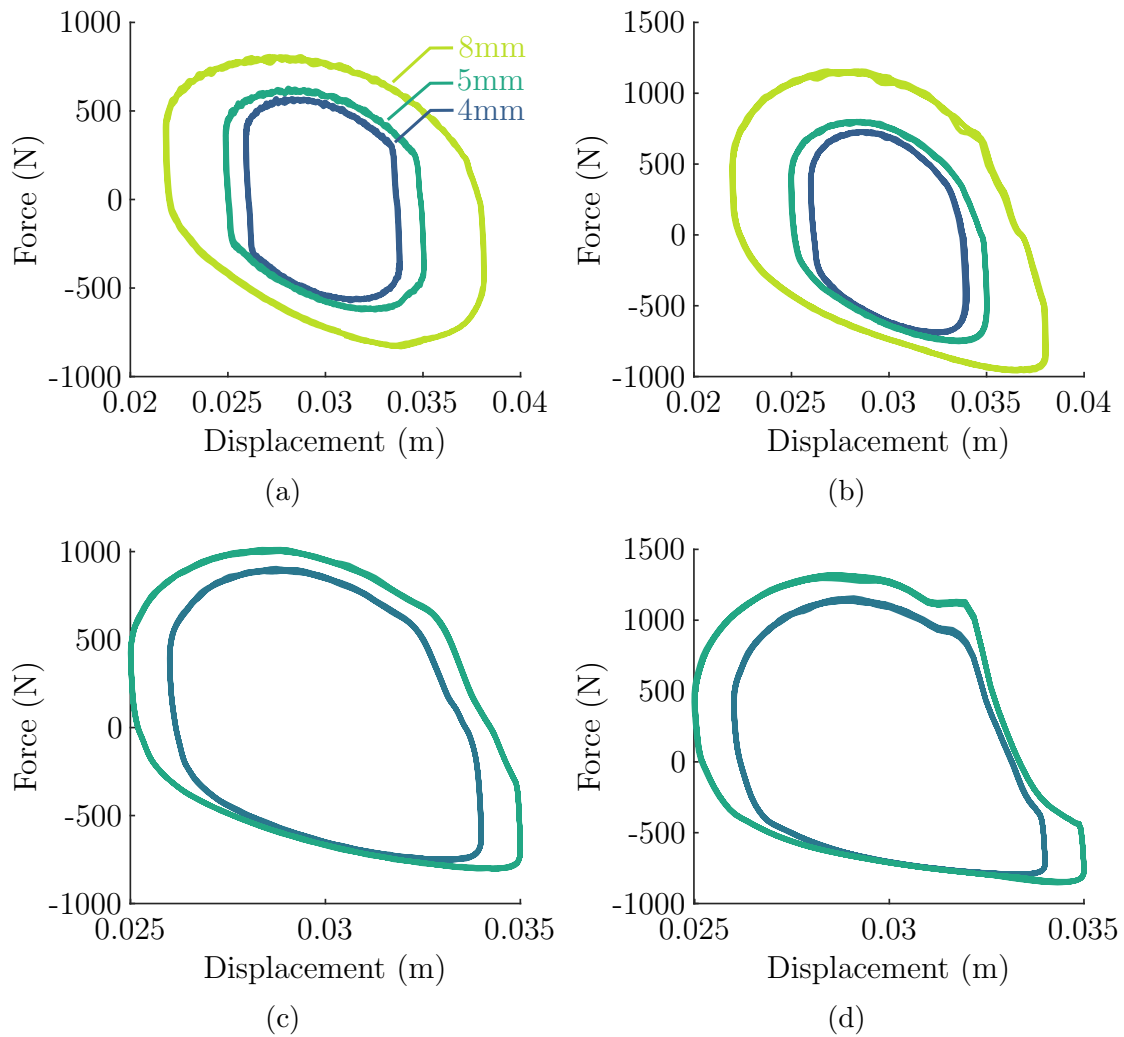
Figure 5.10: Data collected from helix only tests at a) 1Hz, b) 2Hz, c) 3Hz and d) 4Hz.

Figure 5.10a. It can be seen that at maximum and minimum displacement, the force jumps from c. -400N to 500N (and vice versa). This behaviour would be consistent with friction effects, as these points correspond to the piston changing its direction of movement. The fact that this friction component is of a similar or greater size to any of the other forces involved make characterising the inerter extremely difficult.

The second apparent feature is the concave nature of the right hand side of the force-displacement loop at higher frequencies. This behaviour is seen most clearly in Figures 5.11a and 5.11b. The exact reason for this behaviour is unknown but one possibility is that it has to do with trapped air, which the filling process was unable to remove. The feature clearly becomes more apparant at higher frequencies and so is likely at least partially acceleration dependent.
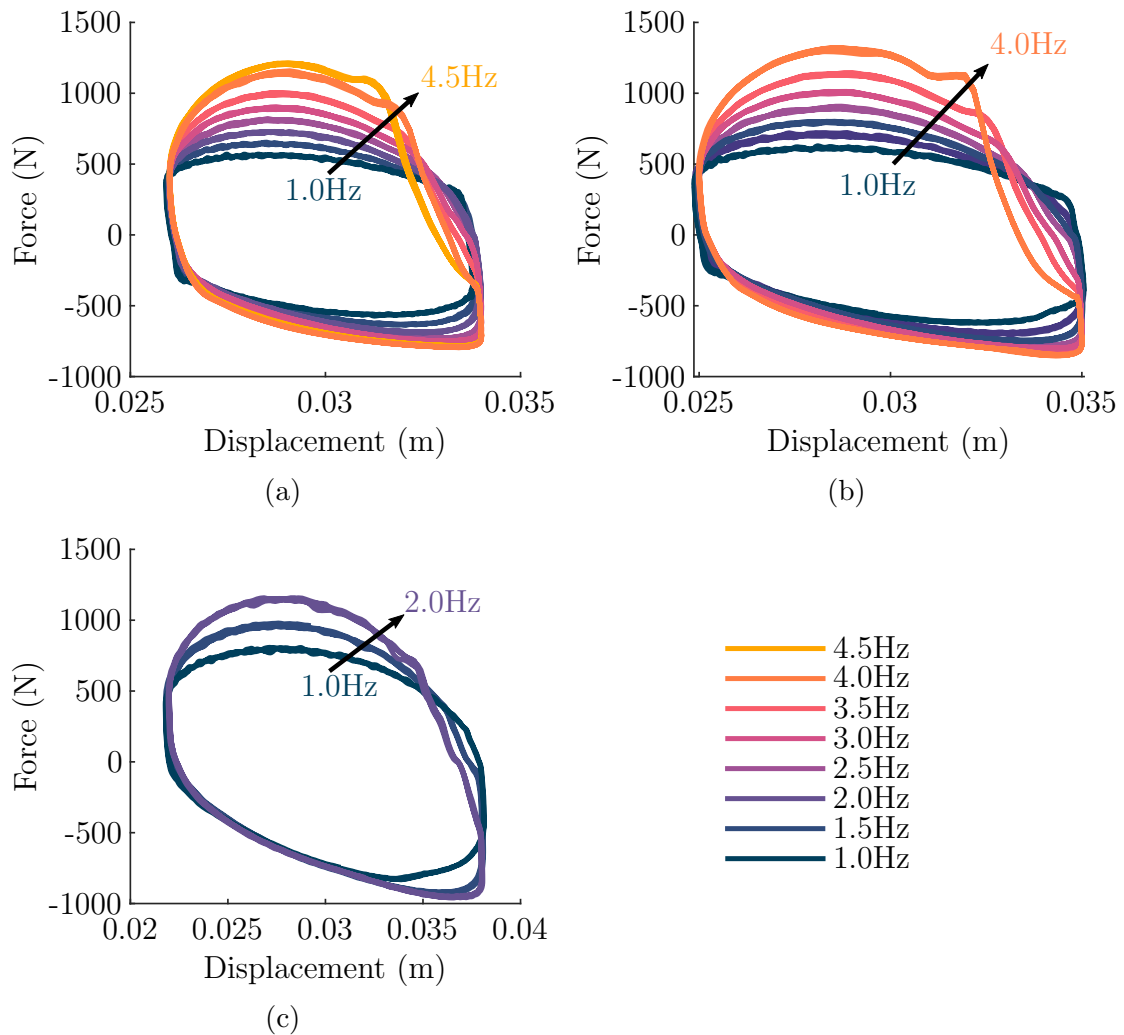
Figure 5.11: Data from the helix only tests collected at a) 4mm amplitude b) 5mm amplitude and c) 8mm amplitude.

The asymmetric nature of the force is unusual. It might be the case that an air bubble at the top of the system was moving between the cylinder and the helix. When in the cylinder, compression of the air bubble against the top of the cylinder would cause an additional force. However, once the air moved into the helix, there would simultaneously be less compression of the air and a decrease in the mass of the rotating fluid. This would lead to less inertance and a reduction in the quadratic damping term. Combined with the reduced compression force, this could lead to the observed dramatic drop in force at the right hand side of the loop. This speculation was not able to be experimentally verified.

Overall, the data from these tests was inconclusive. Friction was identified to be a major issue, and some interesting non-linearities were found. Additionally, the

inertance of the inerter could not be consistently verified. Nevertheless, it was decided that it was nessecary to test the MR-based inerter, even given the likely possibility that the inerter component of the rig was not working as expected.

5.5 MR-based inerter

5.5.1 Valve Design

The annular valve was designed using the damping valve design methodology [202], as the design preceded the optimisation work described in Chapter 4. A gap height of $h = 0.5$mm was used, to be consistent with the previous work. The valve was designed to provide a magnetic field intensity of $H_f = 190$kAm^{-1} with a current of $I = 2.5$A. The valve material was mild steel (1008). A design with four wraps and 27 turns (N=108) was chosen, as it was judged that using a higher number of turns risked magnetic saturation in the steel. The dimensions of the valve are given in Table 5.4.

Table 5.4: Dimensions (mm) of the valve, as labelled in Figure 4.13b (repeated below). The wire diameter is d_w and the total number of coils is N.

t_a	w_c	h	r_v	t_b	h_c	l_v	d_w	N
5.67	2.06	0.50	10.00	2.84	14.30	20	0.51	112

The design was verified using the finite element analysis software package `Finite Element Method Magnetics` [222]. The results of this verification are shown in figures 5.12a and 5.12b. It can be seen that the targeted field intensity is achieved across the active length of the valve.
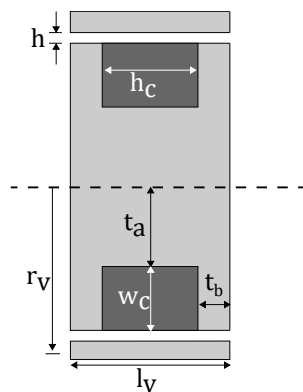
Figure 4.13b, repeated.
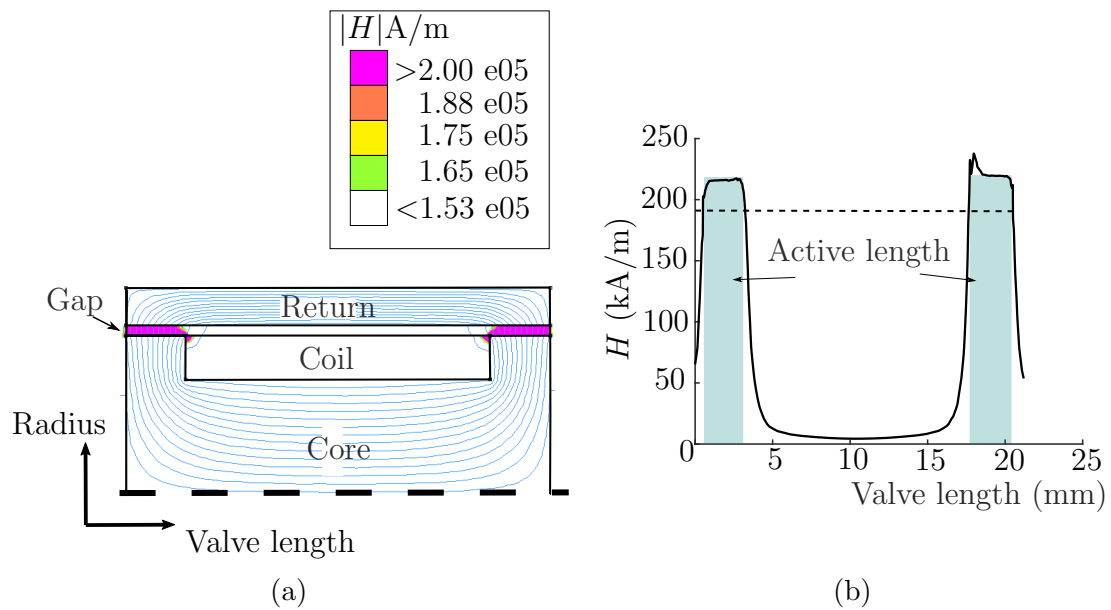
Figure 5.12: Verification of the valve design in `Finite Element Method Magnetics`. a) shows the finite element analysis, while b) shows the plot of H along the length of the channel.

The valve was fitted with spokes to keep the core in place. These spokes were fastened to the core using cones. These cones also served the purpose of smoothly channelling the fluid into the narrow channel, avoiding areas of recirculation which would otherwise occur at the flat faces. An exploded assembly diagram of the valve is shown in Figure 5.13, to illustrate the construction.
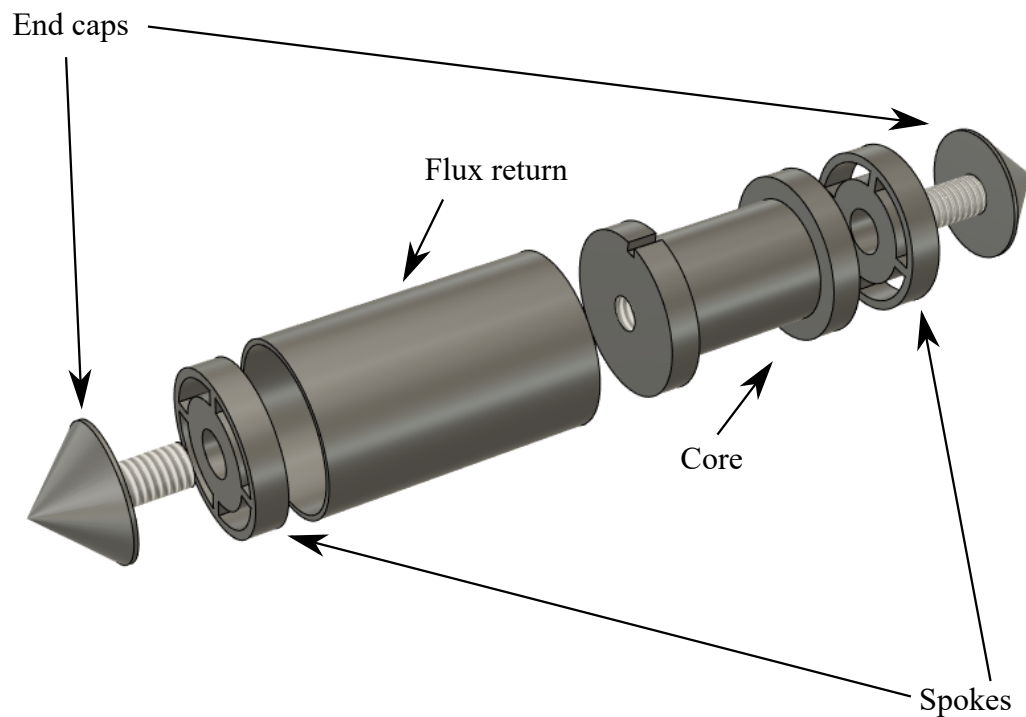
Figure 5.13: Exploded diagram of the annular valve.

In order to hold the valve in position, a cradle was designed. This cradle consisted of three parts:

- a valve holder which went around the valve;

- a connector, through which the wire ran; and

- a valve cap to help plug the gap made for the wire.

These components were made of non-magnetic stainless steel and fitted on either end with 3/8" threads, to attach them to the standard connections. An exploded diagram of the valve cradle is shown in Figure 5.14.
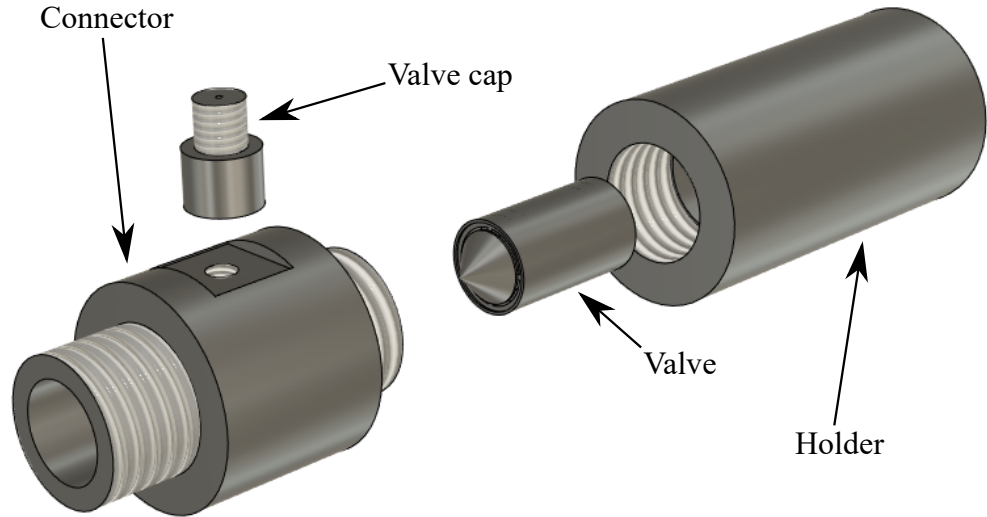
Figure 5.14: Exploded diagram of the valve cradle.

5.5.2 Rig Design

Other than the inclusion of the MR valve, the inerter was kept substantially the same. The only other change made from the oil-based rig was to move the filling system, to shorten the length of the pipe between the pump and the inerter.

5.5.3 Fluid characterisation

The viscosity of the MR fluid was measured at a range of temperatures from 18-51°C. The fluid was shaken thoroughly by hand for 20 minutes to mix. A sample of fluid was placed in a Brookfield DV-II+ Pro viscometer, attached to a Brookfield TC-650 water bath. While being constantly mixed by the viscometer at 50 rpm, the nominal temperature was targeted with the water bath. Once reached, a reading was taken over approximately 30s. The results of these tests are shown in Figure 5.15, with a quadratic best fit calculated using the `Matlab polyfit` function. The calculated fit is

$$\mu = -4.045 \times 10^4 - 992.3T + 8.8T^2, \tag{5.2}$$

where T is the temperature in °C.
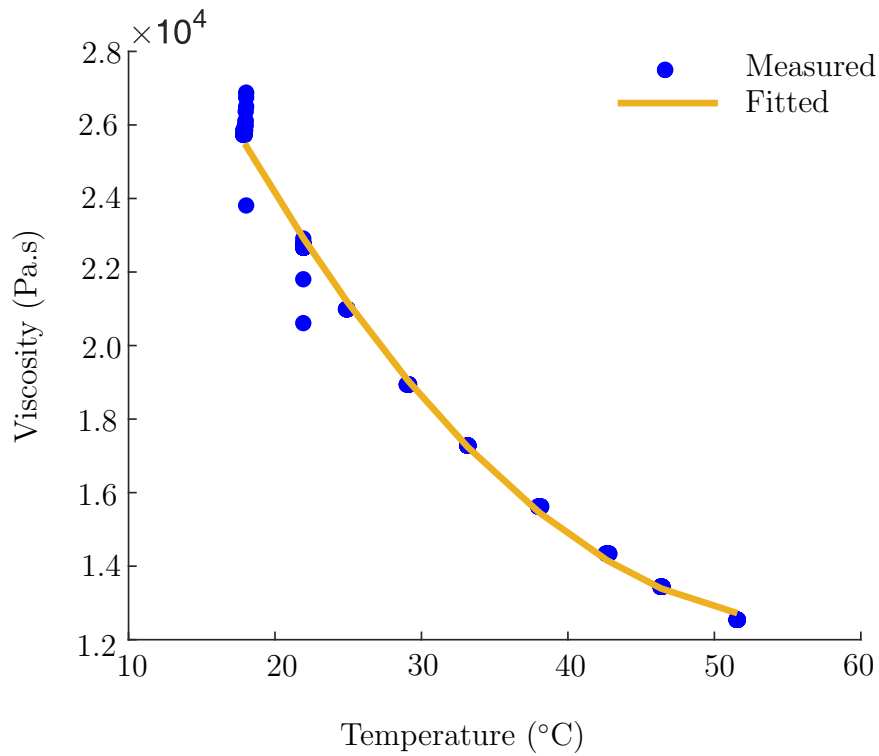
Figure 5.15: Measured dynamic viscosity data for the MR fluid.

Density was measured by heating 50ml of fluid in a kiln to 45°C. The fluid was then set on scales and allowed to cool. Temperature and mass readings were taken every five minutes. This data is plotted in Figure 5.16, along with a linear fit calculated using `polyfit`. This fit is

$$\rho = 2.25 \times 10^3 - 0.06T. \tag{5.3}$$

Due to imprecision in measuring the volume of the fluid, and the small range of measured density, it is more reasonable to describe the density as $2248\text{kgm}^{-3}\pm2\%$.
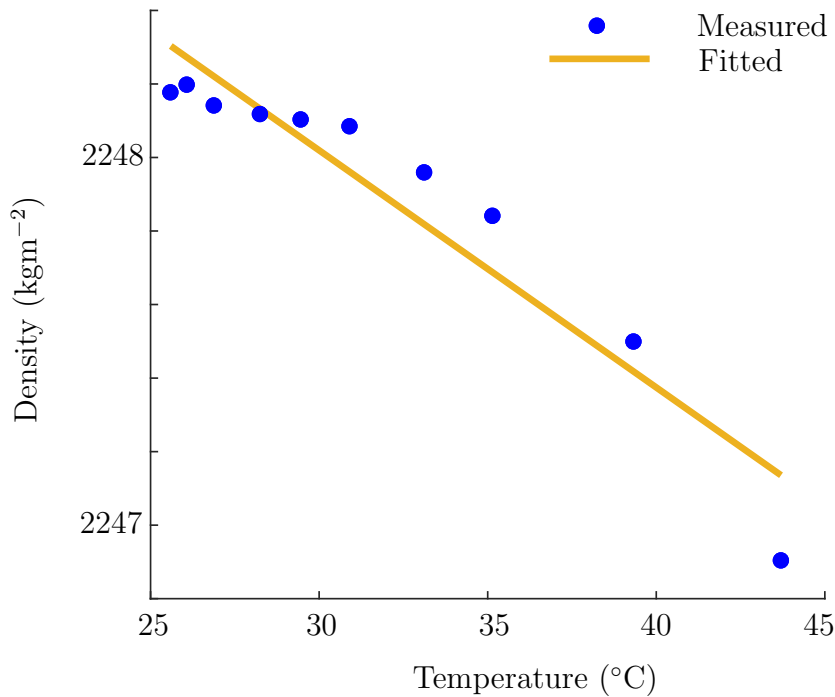
Figure 5.16: Measured density of the fluid from 25-40°.

5.5.4 Methodology

Before testing, the rig was run for 20 minutes at its maximum stroke of 60mm, with flow in both the valve and the helix. This process was to mix the fluid, which has a tendency to sediment over time. The resistance of the valve was checked with a multimeter, to check there was neither a short nor an issue with the contact surfaces. The CUBUS software was set to displacement control mode, cyclic testing, and high pressure hydraulics was supplied to the actuator.

Based on initial experiments and the oil-based rig, two issues were identified which had the potential to make the experimental results time-dependant. The first issue was sedimentation of the fluid. It was observerved that the iron particles would collect on the outer wall of the helix, turning the MR fluid into a two-phase mix. While this was only observed over longer periods of time (i.e. over multiple days without excitation), without further study it could not be guaranteed that this wouldn't cause an observable change in fluid properties over multiple tests.

The second issue was a small amount of fluid leakage observed around the joints. This persisted even when the joints were tightened multiple times. This leakage would mean that the amount of air trapped within the fluid would increase over time.

Depending on the locations of these air pockets, they could have a significant effect on the behaviour of either the valve, the helix or both.

The time-dependent nature of these issues meant that the ordering of the tests needed to be considered, to reduce the effects on the data. The ramp tests, designed to characterise the valve, and the full-inerter cyclical tests are different in nature and so are considered separately here.

Additionally, based on the data from the oil-test, the decision was made to design the test protocol to target higher frequencies. This would proportionally increase the acceleration content of the force signal compared to the displacement. The force safety limit was also increased to account for the fact that c.500N of force was being contributed by friction and not by pressure in the circuit. The goal was to increase the amount of inertance in the signal compared to the frictional contribution. It was also decided that varying the signal amplitude did not have any value and that 5mm displacement was sufficient. A range of frequencies from 7.5Hz to 10.0Hz was selected for study, in 0.5Hz increments. Seven values of current were selected between 0A and 2.4A.

The experimental protocol was designed to cover each combination of parameters twice. Firstly, the flow was isolated to the valve. 0A was supplied to the valve and the rig forced with a 20 cycle, 5mm amplitude, 7.5Hz frequency force signal. Once completed, the current was increased to 0.25A and the test repeated. Once all the current values had been tested, the frequency was increased to 8.0Hz, current set to 0A and the series of tests repeated. Once all the current/frequency combinations had been tested, the sequence was then repeated in reverse, starting with 2.4A, 10.0Hz and lowering to 0A, 7.5Hz. For clarity, this process is shown in Figure 5.17.
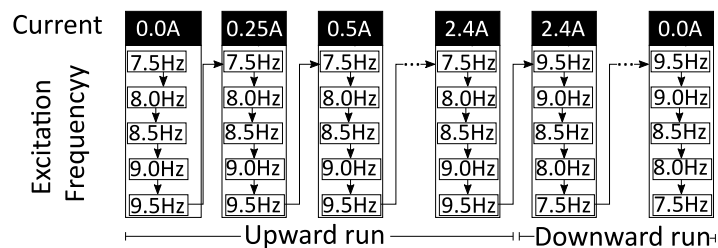
Figure 5.17: Order of experiments for the valve only and valve and helix tests.

After the valve only tests were completed, the flow was isolated to the helix and a series of tests were completed, again starting at 7.5Hz, increasing up to 10.0Hz and then descending to 7.5Hz. Finally, both ball valves (D and E in Figure 5.3) were opened to allow flow in both valve and helix and the test sequence from the valve-only tests was repeated.

5.5.5 Data processing

For the valve only tests, force and displacement data was collected following the order described above. The displacement data was then filtered in `Matlab` using a Savitsky-Golay filter [223], [224]. This filter preserves higher order terms and allows the displacement data to be differentiated to find the velocity (and again for the acceleration). The force was reduced by linear interpolation to retain the phase with the calculated velocity values.

5.5.6 Data

5.5.6.1 Valve-only tests

In Figure 5.18 the data collected on the downward set of tests are plotted over one another for comparison purposes. While the overall shape of the loop is comparable to that observed in other tests of MR valves (eg. Ref. [225]), the friction component described in Section 5.4 is also observed here. Additonally, the loop displays some asymmetric behaviour. The differences between the two tests are small, to the point of almost being indistinguishable.
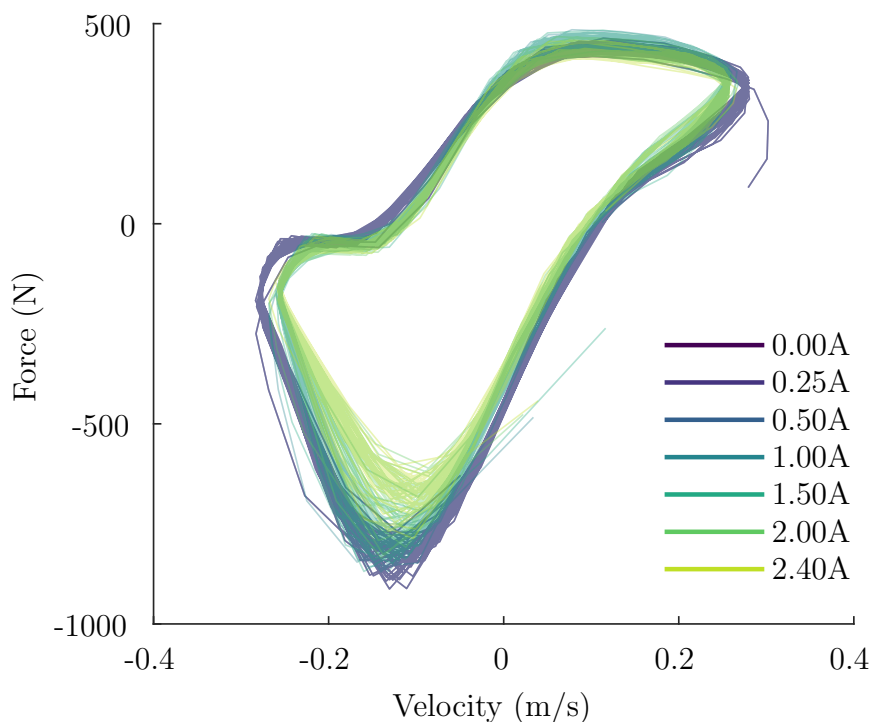
Figure 5.18: Valve only test data collected on the downward set of tests.

In Figure 5.19 a cross-section of the results for the valve-only tests is shown. These figures show the force-velocity data from the test conducted on the upwards run to that in the downwards run. Notable features include the overall asymmetry around the x axis, the inconsistent variance from cycle to cycle, and the large non-linearity in the south-west quadrant of the figures. This last feature is markedly less apparent in the later tests and those on the downwards run.

5.5.6.2 Inerter tests

In Figure 5.20, the data from the helix-only tests at 9.0Hz and 9.5Hz are compared to the modelled force. As in other tests, the measured data contains a significant frictional component. Additionally, clear non-linearities are visible, especially in the North-East area of the figures. However, in as much as the slope of the measured data can be interpreted, it is qualitatively consistent with that of the predicted data.

Figure 5.21 shows the test data collected at 9.5Hz, with flow in both the valve and the helix. The data collected with the valve isolated so that flow was only possible through the helix is also included. A similar non-linearity to that observed in the high frequency data of Figure 5.11 is observable. As Figure 5.18 the valve-only tests, there no clear distinction can be observed between the tests with different current values applied to the valve.
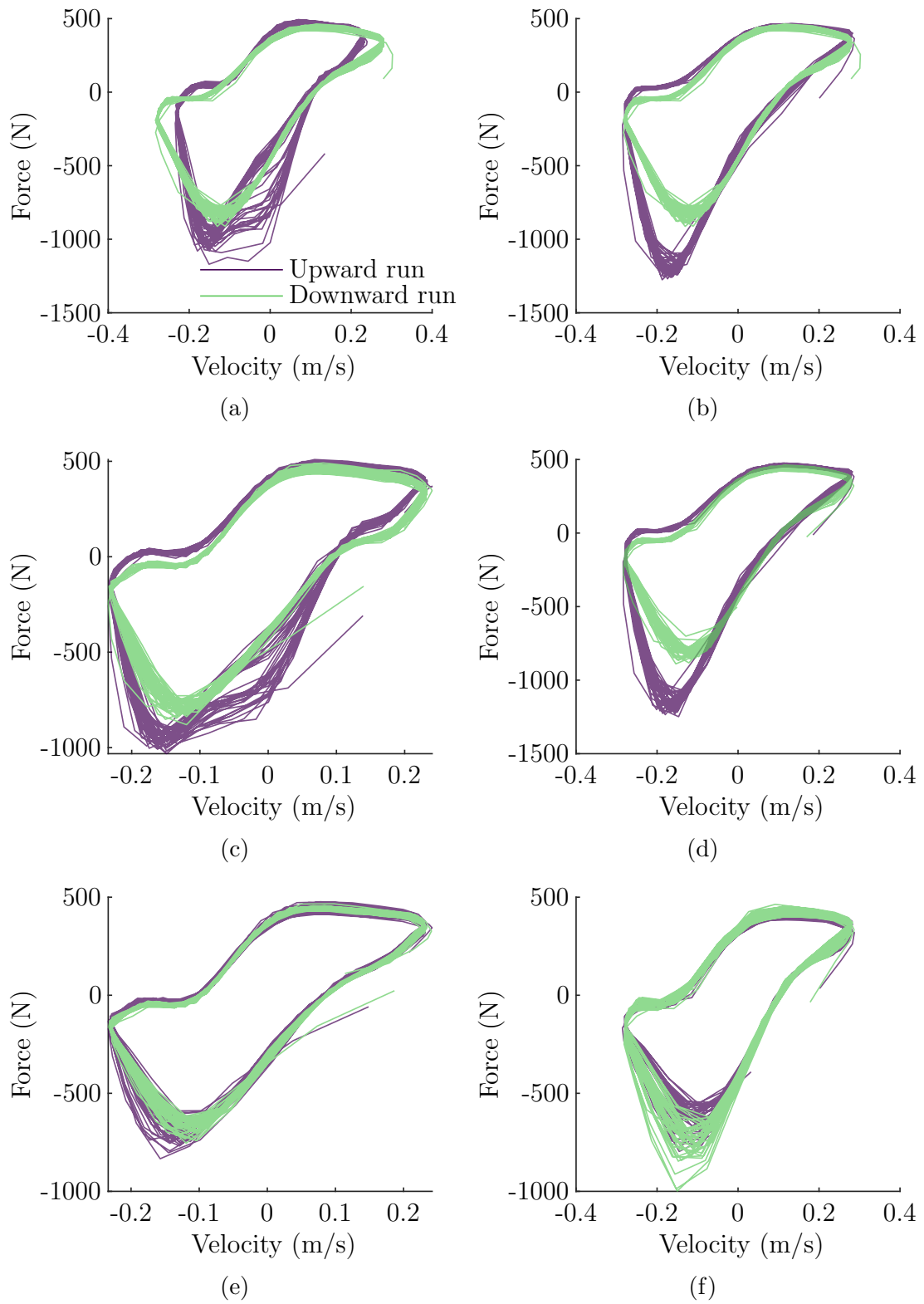
Figure 5.19: Representative selection of results showing the difference between data collected with the same parameters on the upward (purple) and downward (green) passes. The parameters were a) 7.5hz & 0A. b) 9.5hz & 0A, c) 7.5hz & 1.0A, d) 9.5hz & 1.0A, e) 7.5hz & 2.4A, and f) 9.5hz & 2.4A

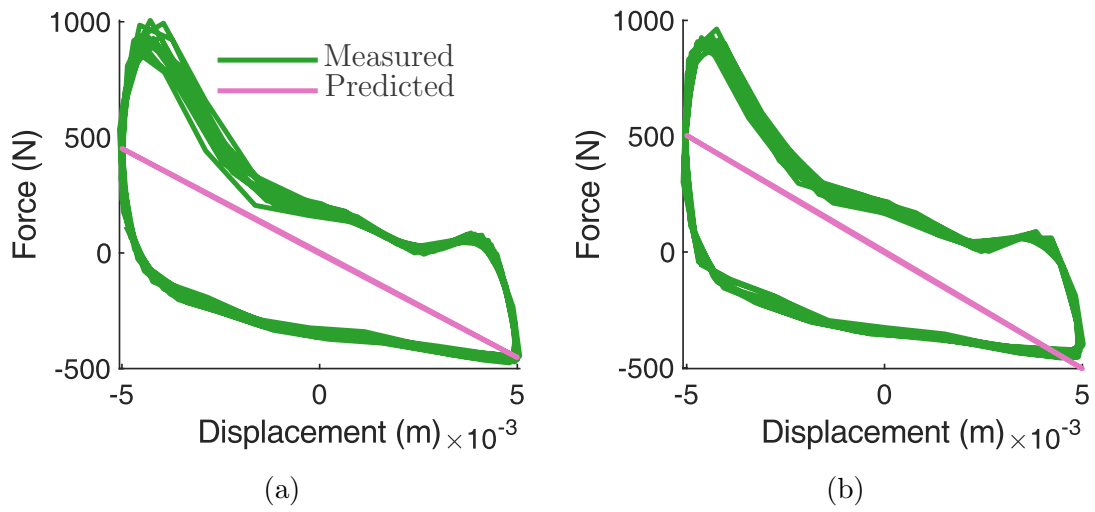Figure 5.20: Helix only test data at a) 9Hz, 5mm and b) 9.5Hz, 5mm compared to the model.
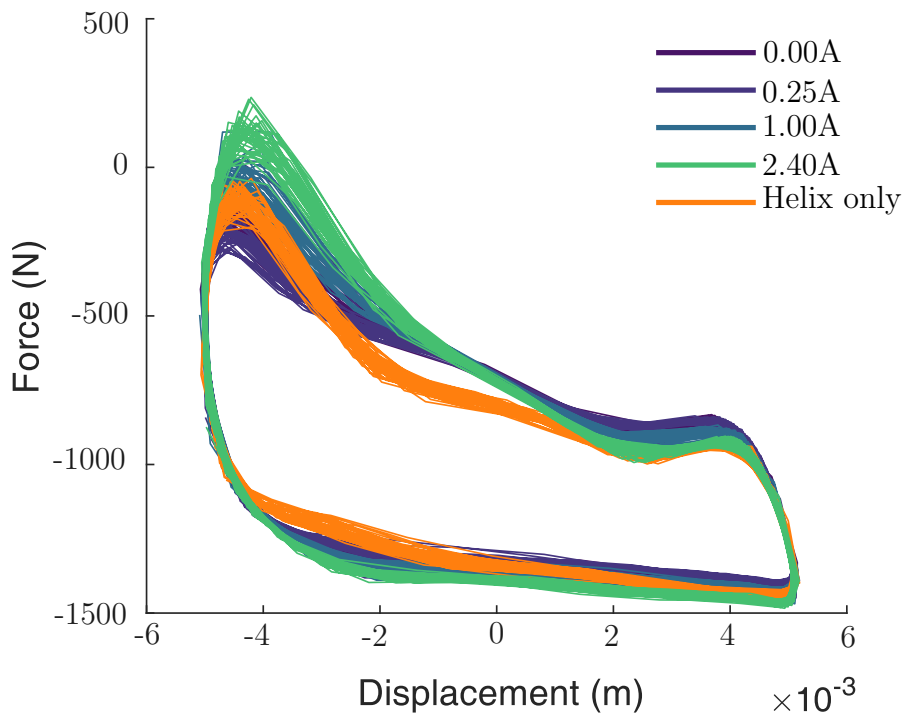

Figure 5.21: Full rig and helix only tests at 9.5hz, 5mm.

5.5.7 Discussion

As with the data presented in Section 5.4, complicating effects in the data make a proper characterisation of the rig impossible. Similar issues to those observed with the oil-filled rig are also observed in the MR fluid rig, confirming that the issues are inherent to the rig as designed and not simply an artifact of the fluid used.

The behaviour of the valve, observed in Figure 5.18, is surprising. A conventional design process was followed and the design was verified as much as possible using FEM, as discussed in Section 5.5.1. Electrical failure was considered as a possibility. However, the resistance of the wires was checked at regular intervals and remained consistent at 5.8Ω and 6.4Ω. These values are slightly lower than the expected 7Ω, possibly due to fewer wraps being used than designed. Although this might lead to some reduction in the upper value of the valve, this variation should be observable. Additionally, the voltage and current supplied drawn by the valve were monitored throughout testing and no difference was observed between the upwards and downwards runs. Any short in the circuit could be expected to be apparent in the voltage draw. If the non-operation of the valve is caused by the electrical circuit, it is neither caused by a short nor by faulty connection.

One additional factor that must be accounted for is the discrepancy between the data from upward run of tests and that from the downward, seen in Figure 5.19. Overall, the data on the upward run displayed a greater distribution. It was also qualitatively more dissimilar to data in previous studies off MR dampers (eg. Figure 13 in Ref. [225]), with a large non-linearity visible in the South-East portion of the loops. The data from later tests on the downward run is distinctly more symmetric.

A possible cause for both these issues is again trapped air. If the fluid in the valve gap contained a substantial proportion of air, then this would break the magnetic circuit. This failure of the magnetic - rather than the electrical - circuit would explain the lack of distinction between the data from tests with different current values, especially when the data is further complicated by a significant frictional components. Additionally, a compressing and decompressing air bubble would explain the asymmetry in earlier tests. Speculatively, the repeated motion of the fluid may have either caused the air bubble to dissolve as testing continued, or to have moved further around the hydraulic circuit, to a point where it could move freely without compressing.

The measured data displayed in Figures 5.20 and 5.21 is similar in nature to. that in Figure 5.9, describing the oil-based inerter. The concave non-linearity which was observed in the high frequency oil tests is also visible. The cause of this is, again, likely to be due to compression of trapped air. With the valve not working as expected

when isolated, it is unlikely that it had any observable effect on the behaviour of the fluid in the helix.

The combination of the denser fluid with the higher frequency tests means that the inertance component of the force can be expected to be greater than that in the oil-based tests. This might also be visible in the measured data, although the complications make it difficult to be certain. If the issues with friction and trapped air can be solved, then this test regime should be appropriate for identifying the inertance.

5.5.8   Friction quantification

An attempt was made to quantify the frictional force in the measured data using the self adaptive differential evolution algorithm (SADE) to fit the parameters of

$$F = \begin{cases} b\ddot{x} + c_{quad}\dot{x}^2 + c_{lin}\dot{x} + kx + F_{\text{fc}}x, & \text{if } \dot{x} \geq 0 \\ b\ddot{x} - c_{quad}\dot{x}^2 + c_{lin}\dot{x} + kx - F_{\text{fc}}x & \text{otherwise} \end{cases} \tag{5.4}$$

to the measured data from the tests with the valve closed. Equation 5.4 should be familiar as being Equation 4.11, with the MR term removed and with the addition of a Coulomb friction term, F_{fc}.

SADE [226] is a modified version of the differential evolution [227] algorithm. In brief, SADE operates by generating trial vectors, mutating and combining them, before discarding the worse vectors and repeating over a number of generations, in an analogue to evolution. A more complete description of this algorithm is included in Appendix C. The implementation used here made use of the `FreeLunch` [228] and `Toybox` [229] packages in `Python`, which operate as described in Ref. [230]. The aim was to fully identify the system.

The results were inconsistent. As an example, Table 5.5 shows the parameters calculated from two independent runs of the algorithm on the same measured data (10 cycles, 15mm amplitude, 1Hz, oil-based rig). The calculated fits are plotted over the measured data in Figure 5.22. Both sets of parameters are, on their face, reasonable, with normalised mean square errors (NMSE) of 1.02 and 1.14 and plausible hysteris loops. However, it can be seen that both the c_{quad} and F_{fc} differ substantially. Additionally, the predicted inertance value of 600kg is substantially higher than the 160.4kg calculated using Equation 4.6 (in fact 600kg corresponds to the upper bound set on the inertance value during implementation).

The inconsistency of these results, along with a lack of opportunity for verification meant that this approach was eventually discontinued. It might be that the model

Table 5.5: Best fit and calculated parameters from SADE. NMSE refers to normalised mean square error.

Trial	NMSE	b (kg)	c_{lin} (kgs^{-1})	c_{quad} (kgm^{-1})	k (Nm^{-1})	F_{fc}(N)
a)	1.14	600	1,540	16.5	69,381	594
b)	1.02	600	1,494	1.2	69,000	41.58
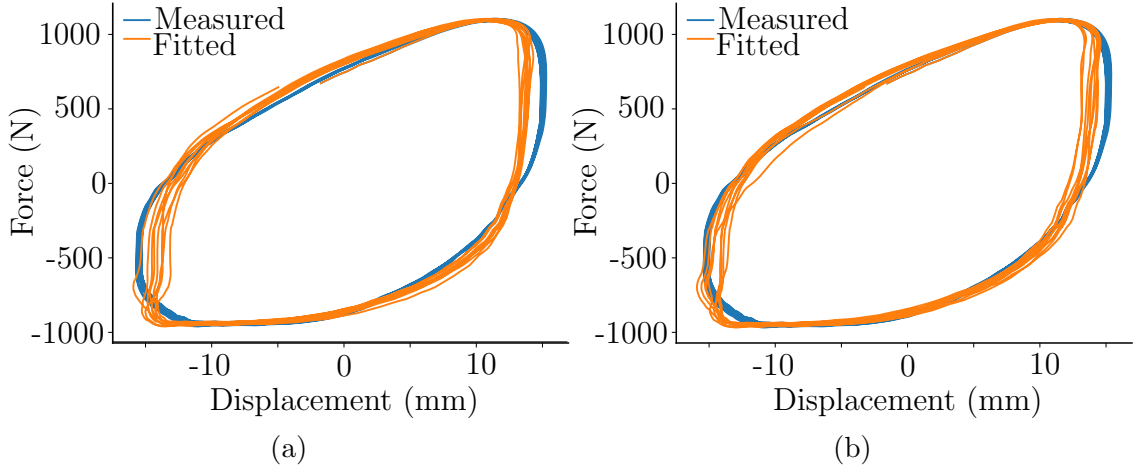
Figure 5.22: Measured data (blue) from a 10 cycles at 15mm amplitude, 1Hz and simulated data using the parameters calculated by SADE (orange) in two separate runs.

used lacks a global optima, without some of the possible variables being fixed. Equally, the model might also be insufficient - for example, trapped air might mean that a constant stiffness term is not an accurate assumption. Finally, it may just be that the data collected was insufficiently large for the algorithm, and so running the rig for c. 100 or 1000 cycles, rather than 10 might be required.

A more straightforward approach is shown in Figure 5.23. Here, measured data is shown from a single cycle from 80 different tests with the same amplitude (5mm), collected from the MR rig on the same day. 70 of these tests were conducted with the valve open, 10 with the valve closed, and all tests were conducted from 7.5-9.0 Hz. The maximum and minimum force at the extreme displacements (defined as being outside the range $[-3.5, 3.5]$ mm) were found. Calculating the difference of these lead to a values of $F_{fc} = 950$-$1,440$N (mean value of $1,170$N) at minimum displacement, and 430-630N (mean value of 510N) at the maximum displacement.

The discrepancy between these values, along with the low confidence at minimum displacement further emphasises the difficulty of calculating a meaningful value for F_{fc}. The available data is simply insufficient to disentangle the effects of friction with those of trapped air with any degree of confidence.
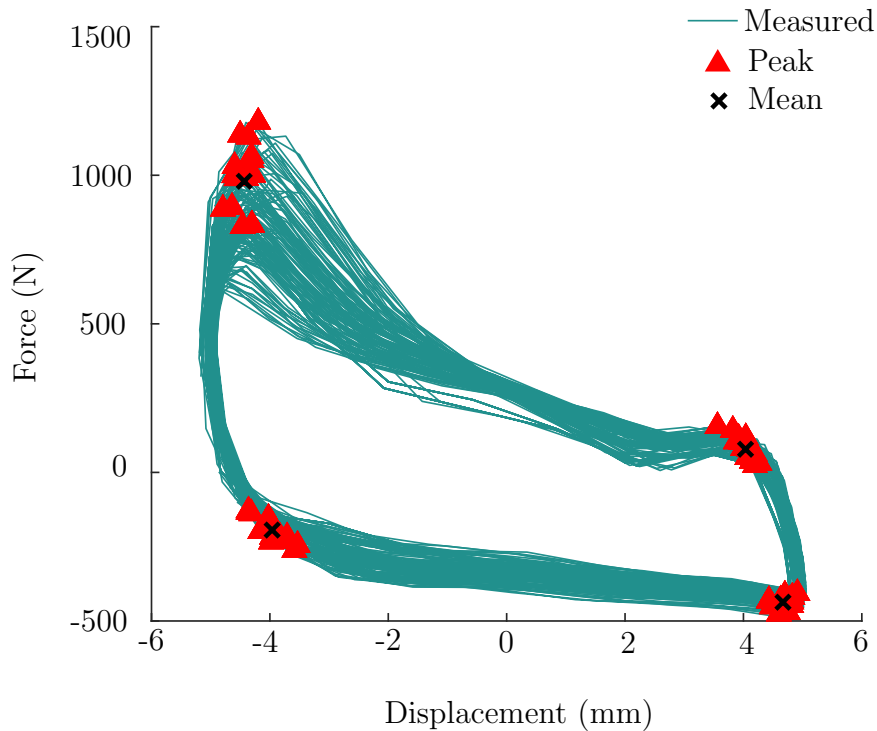
Figure 5.23: Force displacement data from 80 different tests, with the maximum and minimum force values at the displacement extremes marked, along with their average values.

5.6   Conclusion

This chapter built on the theoretical work in Chapter 4 and described the practical design and testing of a prototype semi-active inerter rig. Some discussion was given to the iterative design approach, which saw initial work being done on an oil-based design before moving onto using the MR fluid. While constraints on both time and facilities meant that this process could not be followed in full, it did lead to substantial progress.

Much discussion was given to the practicalities of the rig. The filling strategy, developed with the goal of minimising air within the system, is detailed. The practical design of an external MR bypass valve - a novel use for MR valves - is also discussed. Finite element verification of the valve design is also given.

Experimental data from both the oil-based and MRF-based inerter rigs has been presented. Overall, these results are less than conclusive. Both friction and trapped air caused substantial complexity in the measured force data. These issues hampered the characterisation of the inerter and the operation of the MR valve.

While there has been some very recent investigation into using MR fluid for flow

control in soft robotics [231], the work presented here is unique in terms of the scale of MR fluid used. Filling such a complex geometry with around 2.5 litres of dense, viscous fluid was undeniably an ambitious task. Given the growing popularity of MR fluid for semi-active control, it is likely that future researchers will have similar ambitions. With this in mind, Chapter 6 discusses the issues encountered in more detail, along with some proposed improvements to overcome them. The chapter also discusses some of the practical ways in which semi-active inerters could be employed in machining operations.

Chapter 6

Discussion and recommendations

6.1 Introduction

This chapter has two parts. In Section 6.2, the limitations of the experimental work presented in Chapter 5 are discussed. Some recommendations are made for modifications to the design to aid in future testing. Additionally, some more significant redesigns are also proposed, as alternative directions for research.

Section 6.3 builds and expands on the work presented in Chapter 3. Ways in which semi-active inerters might be employed to suppress chatter in different machining systems are proposed. Three different areas are looked at: conventional machine tools, adaptive fixturing, and robotic machining. In each case, the focus is on practical implementations, looking at the potential benefits and research challenges in each area.

6.2 The semi-active inerter using MR fluid: limitations and future directions

In Chapter 5, various limitations of the prototype design were noted. In this section, potential improvements which might be made to fix these immediate issues are presented. These improvements could form the next iteration of the design process, beyond the scope of the current work. Further, some larger redesigns are presented. These redesigns offer alternative avenues of investigation but would require more significant effort to implement.

6.2.1 Minor design iterations

In the short term, the issues experienced with the semi-active inerter as tested in Chapter 5 can be divided into two main categories:

1. issues concerning air bubbles; and

2. issues with system identification.

In this section, both of these issues are explored and some proposals are made to deal with them. These proposals are made with the iterative design process in mind. In any hypothetical continuation of this projects, these proposals woulds be sensible initial options with which to improve the prototype.

Air trapped in the system, due to an insufficiently rigorous filling process, led to both fluid compressibility and to gaps in the magnetic circuit. This impacted both the operation of MR valve and the inertance of the device. Two avenues of attack present themselves here: further improvements to the design in aid of the filling process; and methods of identifying trapped air before testing. Cavitation might be a complicating factor but it is hoped that reducing the total air in the system will also reduce the risk of cavitation.

An obvious first step in this process might be to check that the issues with the valve were indeed due to trapped air, rather than other sources. While it is considered a likely candidate, if there are further, unidentified issues with the valve then it would be important to explore them at this stage of the process.

Assuming that the only substantial change to the fluid is the introduction of the air,[1] then this could be estimated using the bulk modulus of the fluid. A method for establishing the bulk modulus using three pressure transducers along a length of straight pipe was presented by Johnstoe and Edge [232]. This might be appropriate for establishing the modulus of the fluid immediately above and below the valve, as shown in Figure 6.1 , and so identifying if an air bubble was passing through the valve. However, it is not clear that the method would be practical for characterising the fluid within the valve itself, given the complex geometry. If there were an air bubble contained entirely within the valve itself, this method might fail to identify it. Even restricting the pressure transducers to either side of the valve, the flexible pipe material may be an issue.

---

[1]n.b. this assumption would not hold if there was evidence of substantial settling or sedimentation of the fluid
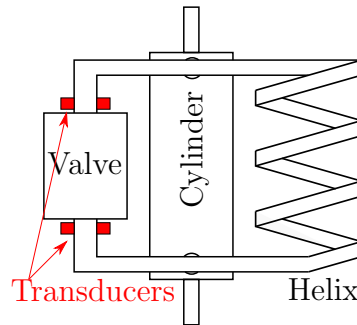
Figure 6.1: Diagram showing transducers placed above and below the valve, which might allow the bulk modulus of the fluid to be measured.

Ultrasonic methods may be more appropriate in this case, as they might allow measurement of the fluid in the valve itself. The measurement of a reflected ultrasonic pulse to identify phase boundaries in a fluid is a well-established technique [233]. More complex arrays of sensors can allow for the measurement of the size [234]. Leighton et al. [235] present a combined method, using multiple frequencies of signal. One major uncertainty that would need to be dealt with for any ultrasonic method selected, however, is the effect of the presence of the iron particles. It is not immediately clear how well ultrasonic techniques would deal with the three-phase mixture - in fact Leighton et al. [235] note that conventional ultrasonic measurement can confuse gas bubbles with similarly sized solid particles. A further complication which would need to be considered is the annular shape of the valve. Additionally, it might be desirable to conduct this testing with the valve switched on. Any confounding interactions between air bubbles and the magnetic fields would need to be considered in this case.

This work to convincingly establish that air bubbles were the cause of the valve issues would be costly in both time and equipment. It would also be of questionable value - establishing the presence of air bubbles would give no additional insight in how to improve the design. The time required for this might be better spent on improving the filling of the rig. Three immediate options, which might all be employed together, are presented here in order of increasing difficulty.

The simplest fix to the system would be to reduce leakage at the fastenings. While this would be unlikely to fix the issue in its entirety, reducing the visible leakage at the joints would be important for preventing air from entering the system during testing. From observation, leakage was a more significant problem for the device when filled with MR fluid than with hydraulic oil. With the device remaining as in Figure **??**, each fastening could be checked with a digital torque meter and then tightened with a torque wrench. A series of tests could be conducted, designed to

create higher pressures than would be required in testing the MR inerter. If leakage were still an issue at this point, then either a redesign or re-specification of the threaded components might be required.

A more involved modification of the rig would be the introduction of a fluid reservoir at the highest point. It might be that the bleed valve in its current form would be ineffective at allowing air to leave the system. Introducing a small head of fluid around the bleed valve, as shown in Figure 6.2, would allow air to escape but not fluid. This could allow for the system to be cycled with the valve open, without an associated loss of fluid. This might allow the air trapped at the joints to be driven out of the system. The valve could then be sealed to keep the system pressurised during testing.
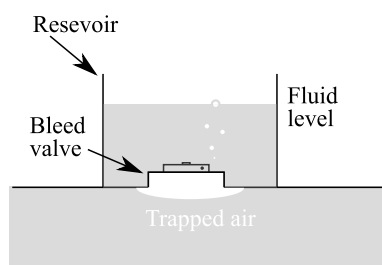
Figure 6.2: Diagram of a fluid reservoir placed around the bleed valve, allowing air to escape the system without a loss of fluid.

A third approach to reducing the appearance of air bubbles would be to introduce multiple ports and air traps throughout the system. Allowing for filling at multiple locations would increase confidence that the fluid was reaching all parts of the system. For example, a port below the valve and an air trap above it would increase confidence that air had been purged from the valve. However, adding extra ports would require substantial modification of the design. This solution would work best when paired with the addition of pressure gauges, as discussed below.

One alternative which has been suggested [236] is the use of a vacuum pump to degas the MR fluid. Significantly reducing the pressure around the fluid to allow the gas phase to more easily escape. Whether this would be practical in situ would be a matter for future investigation. It is unclear whether this process would have any effects on the properties of the MR fluid. One study on an MR elastomer in vacuum conditions showed reduced but still acceptable performance [237]. However,

the study is not nessicarily generalisable: MR elastomers are structurally different to fluids. Nevertheless, this option would merit further investigation.

The main issue with system identification was a lack of direct pressure signals. Having data from only a single force response meant that the pressure drops across the valve and helix could only be inferred. Identifying a non-linear system from a single signal, with uncertainty in the damping, stiffness, and friction terms, was difficult to do with any certainty.

A relatively straightforward change would be to include pressure sensors. Four digital sensors could be inserted in the system, immediately above and below the valve and helix, as shown in Figure 6.3. Being able to independently measure the pressure drop across both valve and helix would allow the models developed in to be validated in a more systematic manner. In addition, the sensor data would aid in identifying the location of any air bubbles in the system, as well as removing the issue of the friction term. Redesigning the rig to include these sensors and calibrating the pressure to the force signal would take some work but should not prove too complex.
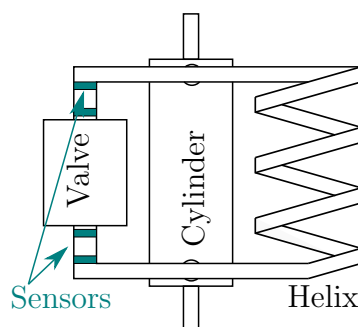
Figure 6.3: Proposed locations of the digital pressure sensors.

6.2.2 Major redesigns

The changes discussed in the previous section are pragmatic improvements, progressively iterating on the previous work. Some additional ideas present themselves, however, which would take more time and resources to implement. Three such ideas are discussed here. Each of these represents a major departure from the design as presented in Chapter 5, to the extent that they could be substantial new research projects in themselves.

One avenue of research would be investigating the possibility of using an orifice MR valve. An example of an orifice MR valve is shown in Figure 6.4. Olabi and Grünewald [156] showed that this valve layout offers less damping per unit length than the annular design. As such, the orifice valve has generally been neglected as

a topic of research. However, as noted in Chapter 4, the requirements of the bypass valve are different to those of the MR damper. More space is available and the focus is on the ratio of fluid resistance in the on-state to that in the off-state. The orifice valve might allow for a simpler design, which is easier to work with, adjust and make leak proof than the annular design. As such, it merits investigation. As with the annular valve, an investigation of the optimization of the design orifice bypass valve should be conducted. Simplicity of design should be prioritised.
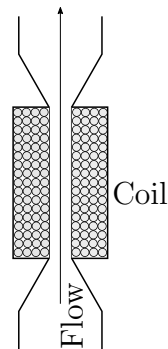
Figure 6.4: A sketch of an orifice valve.

A key issue with the inerter design as presented in this thesis is the use of the MR fluid. The fluid is expensive (costing 985 US dollars per litre before tax as of December 2022) and extremely viscous and dense. These latter two characteristics hampered the filling process. With these issues in mind, developing a design which only requires a minimal amount of MR fluid would have substantial value. Cheaper hydraulic oil could then be used to provide the inertance required.

Two potential designs which could meet the goal of minimal MR fluid use are shown in Figure 6.5a and 6.5b. In Figure 6.5a, the MR fluid is kept in a u-bend shaped chamber, which contains the valve. As the MR fluid is significantly denser than hydraulic oil, the two fluids should remain unmixed. This design does present some issues, in that the U-bend would need to be kept in a specific orientation. This clearly limits the use cases, as well as meaning the design would fail to meet all the requirements of an inerter as laid out by Smith [99].

The second design, Figure 6.5b, makes use of a second hydraulic cylinder. This would contain a valve within the piston, so that the second cylinder would operate in the same way as an MR damper. The hydraulic oil in the bypass channel would actuate this second damper. As the two fluids never make contact, there is no risk of them mixing. However, the additional cylinder would most likely increase the mechanical losses in the system.
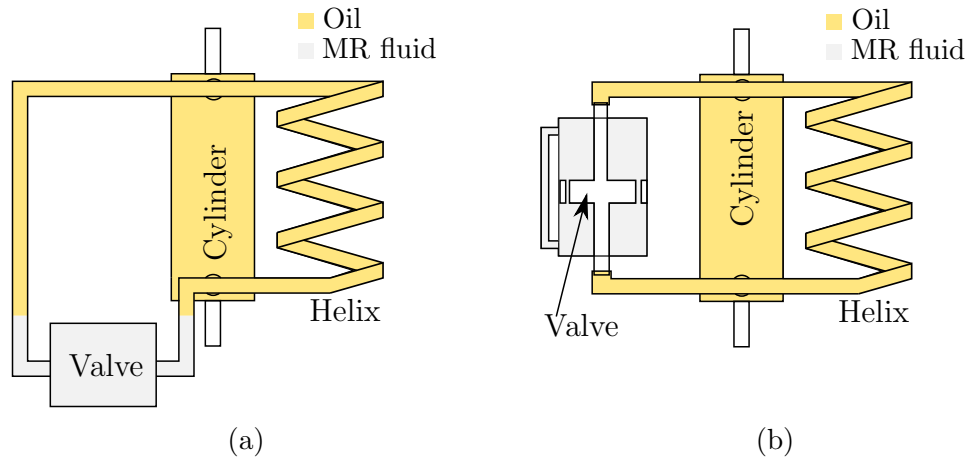
Figure 6.5: Two alternative designs of semi-active helical inerter, designed to reduce the use of MR fluid.

The final proposal presented here is also the most radical departure from the rest of the work. While the helical inerter has much potential, it also presents many issues, as documented in this thesis. It is important not to neglect the other designs of inerter available. Hu et al. [125] have previously presented a design of semi-active inerter using a linear actuator. However, this design operates too slowly for the needs of machining. For low latency control, the clear candidate is electromagnetism.

Thus, the proposal is that focus should be given to the development of rotating masses, the inertia of which can be controlled by electromagnets. This could then form the flywheel in either a rack-and-pinion or ball-screw inerter. Two potential methods are presented in Figures 6.6a and 6.6b. These are only initial concepts - feasibility studies would be required before developing these designs further.

The design in Figure 6.6a is inspired by magnetic clutches. It consists of a set of magnetisable discs, separated from one another by a lubricating fluid. The lowest disc would be directly attached to the rotating element. This lowest disc would contain an electromagnet. When subject to the magnetic field, these discs would contact and, bound by friction, rotate with the lowest disc. By fine control of the magnetic field, the number of discs - and so the mass - can be controlled. This would mean that the inerter would not provide continuously variable inertance, but instead a kind of step-wise change, defined by the mass of the individual discs. Additionally, the fine control of the magnetic field required might present some design issues.

A second design, shown in Figure 6.6b, is more similar to that of Hu et al. [72] in operation. A hollow rotating flywheel would contain steel ball-bearings in individual channels. Electromagnetic circuits would be contained in the centre and outer
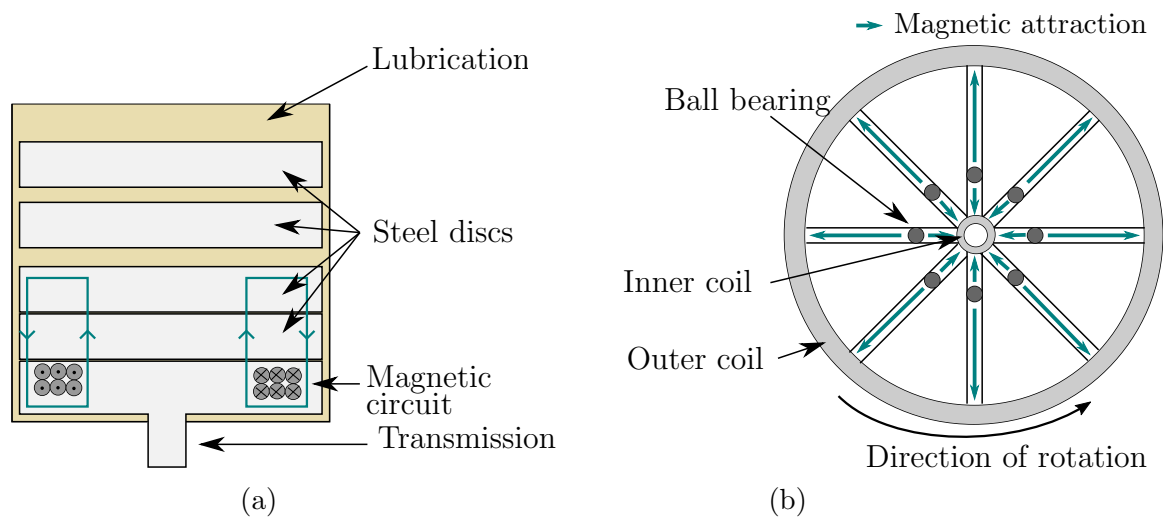
Figure 6.6: Two designs of magnetic flywheel.

perimeter[2] of the flywheel. A sensor (possibly a rotary encoder or accelerometer) would form part of a control loop with the magnets, to detect the speed of rotation. Through controlling the magnetic fields, the radial location of the ball bearings could be controlled. This would allow the inertia of the flywheel to be controlled. As a matter of first impression, this design presents a more complicated control problem compared to that in Figure 6.6a but would allow for continuously variable inertia. Whether one of these designs would be preferable to the other is a matter for future research.

6.3 Potential uses for the semi-active inerter in chatter mitigation

In Chapter 1, the current and ongoing importance of chatter as an area of study was discussed. Five reasons, identified by Munoa et al., [21] that chatter will remain an area of concern despite - if not because of - improvements in other areas of machining were discussed. These reasons included increasing machine power, flexible parts and machine tools, and reductions in friction. The importance of chatter as an issue is underscored by the host of research on the topic, a small selection of which was discussed in Chapter 2.

---

[2]This outer circuit wouldn't strictly be needed, as the ball bearings would be subject to a centrifugal force outwards. The outer magnet might allow for greater control compared to a single magnet, although whether it would in reality would be a matter for investigation.

A more detailed description of chatter can be found in Chapter 3. Here, the possibility of the semi-active inerter to offer productivity improvements was explored. This exploration was conducted with a focus on two possible techniques: discrete inertance variation, and continuous inertance variation. These techniques were developed by way of analogy with existing spindle speed variation methods.

These two methods were chosen as potential areas to explore due to limitations with spindle speed variation. For discrete spindle speed variation, the need to pause the operation while a new speed is selected inherently limits productivity. Continuous spindle speed variation, meanwhile, is limited by the ability of the motor or gearing system to vary at high frequencies.

The analysis conducted in Chapter 3 was limited in scope to an idealised inerter model and to an SDoF system model. While these assumptions were justified in the context of a feasibility study, they do not represent the actual requirements of machinists or machining systems. In Section 6.3.1, these needs and their implications will be considered will be considered in terms of the design of semi-active inerters for machining systems.

While DIV and CIV represent two promising applications for a semi-active inerter in machining, they are not the only possible options. In Sections 6.3.2 and 6.3.3, the opportunity will be taken to briefly discuss two other possible areas of investigation. These areas are robotic machining and semi-active fixturing, respectively.

6.3.1 Semi-active inerter design within conventional machine tools

Munoa et al. [21] list three challenges faced by the development of vibration absorbers for chatter mitigation:

1. large space required at critical locations;

2. poor ability to deal with varying dynamic properties; and

3. the tuning techniques being unfamiliar to those working in industry.

The semi-active inerter clearly has potential in solving these second and third issues. Inherently, the ability to vary inertance makes the device suitable for tackling varying dynamic properties. Likewise, the methods of discrete or continuous inertance variation, as laid out in Chapter 3, would not require manual tuning. However, the

issue of spacing and placement is non-trivial and merits some discussion. This section will focus on these issues, discussing the range of machine tools which might be considered.

The semi-active inerter has two general use cases in this context. The first is as a part of a tuned mass inerter damper, providing a controllable inertance in conjunction with a mass element. In this use case, the TMID would be external to the vibrating element, as shown in Figure 6.7b. This type of device has been previously investigated for vibration control of buildings [238]. However, work has already been conducted in this area using piezoelectric actuators [239]. While a TMID could potentially offer a larger control force, the small space requirements of the piezo-electric transducer would be hard to match. Therefore, the focus of this section will be on the developmemt of the inerter for use as part of a tuned inerter damper.
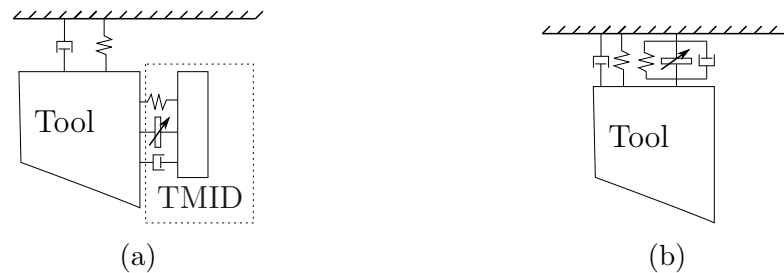
Figure 6.7: Sketches of a) a tuned mass inerter damper attached to a tool and b) a tuned inerter damper in situ.

As a tuned inerter damper, the inerter would sit (alongside spring and damping elements as needed) between the machine tool and ground. This is shown in Figure 6.7. It would not contribute an additional degree of freedom to the tool, as with a TMID, but instead act to change the effective mass of the tool. This would allow for the kinds of control strategies discussed in Chapter 4.

Of all the machine tools, boring bars might be the most approachable for this kind of project. As long, slender members they are inherently extremely susceptible to vibrations. They also provide a lot of space in which an inerter could be situated and they can be well approximated by a relatively simple dynamic model [240]. Figure 6.8 shows a potential design of a tuned inerter damper, built into the base of a boring bar. Such a design would be a natural progression, once a working semi-active inerter is designed. Designing a semi-active tuned inerter damper for a boring bar would allow the control strategies presented in Chapter 3 to be tested, as well as providing an opportunity to investigate the issues of practical design, without the need for to focus on sizing to a significant extent.
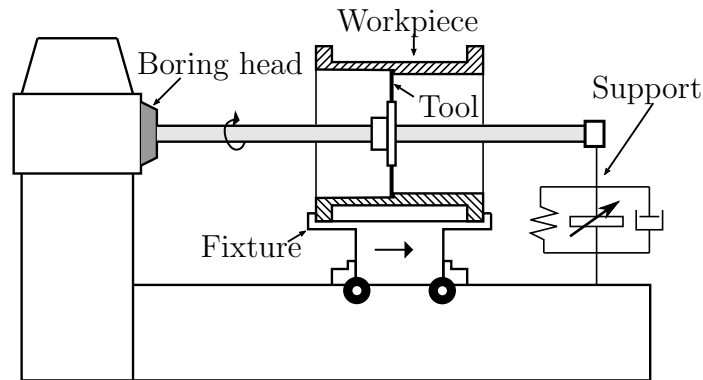
Figure 6.8: Design of a tuned inerter damper built into the support of a boring bar.

Lathes offer an increase in challenge, due to the greater restriction in space available. Designing semi-active inerters for use in these small spaces will require first ascertaining the limits of the design and models. With a helical design for example, there will be a practical lower limit to the radius of hose used for the helix, which will in turn limit the bend radius. The design of MRF-based helical inerter would also have constraints imposed on the design of the valve - a further reason to investigate the possibility of a orifice valve. A fruitful avenue of research may be to focus on the miniaturisation of a passive inerter as a matter of first resort. A study into the practical size limits of inerters (of any type) could lead to interesting applications in other areas.

In addition to the issues discussed for lathes, designing a tuned inerter damper for milling (or for modern multitool computer numerical controlled machines) presents a further issue. As discussed in Chapter 2, chatter in milling is at least an MDoF problem. From a practical standpoint, fitting multiple tuned inerter dampers into the workspace will require an even greater level of miniaturisation. The minimum practical size of a helical inerter is unknown. t seems likely that efficiency would be reduced due to a greater proportion of losses, for example, but this has not yet been studied. In addition, the control of the semi-active inerters will necessarily differ from those developed for boring and turning. While not directly applicable, a recent paper by Ma, Yang and Jin [241] conveys the scale of the analysis required for a passive device in the 2DoF case. Developing a control scheme which can deal with the complexities will require the development of accurate, verified and validated models of the semi-active inerters employed.

6.3.2 Semi-active inerters for fixturing

Fixture design is a key, but complicated, task within machining [242]. Fixtures are required to hold a workpiece in the desired position and orientation with respect to the tool, and to provide support during machining. The time-consuming nature of fixture design means that it can annul the increased productivity offered by computer numerical controlled machine cells [77]. As such, active fixturing[3] has been an area of much research in recent years. Much of the focus has been on reconfigurability and on the control of the clamping force, both areas in which active control is required. However, there some research surrounding semi-active fixturing for chatter suppression, and it is in this niche that the potential for semi-active inerter merits investigation.

Chatter where the workpiece, instead of the tool, is the critical element is often a feature of thin-walled parts, for example aerospace components [21]. The fixturing of such parts is an attractive avenue of investigation for the semi-active inerter as the space restrictions are less onerous than with tool vibrations. Two classes of design will be discussed here: designs which absorb vibration in the base and those which attach to the workpiece directly.

An example of an active base was presented by Rashid and Cornel [243]. This design made use of piezoelectric actuators which could move the base by up to 5μm. Such a design would likely form the benchmark for any semi-active inerter based design. Another benchmark would be the passive inerter based design presented by Wang, Li and Zheng [244]. In general, a semi-active inerter based design would look similar in layout to both, with a similar control loop to that in the active base. Practically, it would likely consist of multiple semi-active inerters combined with passive elements, in order to manage vibration from any angle. The semi-active design should aim to improve on the active design through decreased power draw or improved range of force for the amount of space used, while offering similar levels of performance and greater adaptability to the passive design.
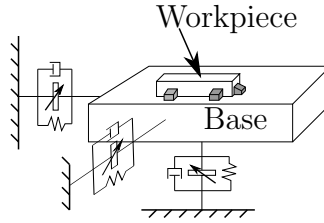
---

[3]also known as adaptive fixturing

Figure 6.9: General layout of a base for chatter supression, based on a semi-active inerter.

A second approach to chatter mitigation is attaching vibration absorbers to the workpiece directly. An example of this approach include the use of piezoelectric patches by Zhang and Sims [245]. The researchers noted the difficulty of removing the bonding material used to attach the transducers after use with this approach. A more recent approach is the flexture-based design by Picavea et al. [246]. Here, flexible beams are designed to form part of an adaptive system, such that they form a vibration absorber between the workpiece and the active fixture. This approach requires fixtures to be designed for each workpiece of any specific geometry and material. A semi-active element could instead allow the same fixture to be automatically reconfigured.

6.3.3 Semi-active inerters for industrial robots

The increasing needs of manufacturers for reprogrammable, customisable tools and processes has led to much research into industrial robotics [247]. Within high MRR, contact based operations (eg. milling), robots can and have been used as tool holders, as workpiece fixtures, or as auxiliary units. However, compared to computer numerical controlled machines, industrial robots have a low stiffness, leading to issues with both accuracy and vibration. Industrial robots tend to be large structures, with relatively easy access for modification. As such the potential for designing inerters for industrial robotics without the need to tackle the issues with miniaturisation is clear.

Chatter as it relates to industrial robots is different to that in conventional machining [248]. The dynamics of the robot depend on its pose. As such, an operation at previously stable parameters can become unstable, just through the change in angle of a joint. This complicates the process of creating stability lobe diagrams, to the point of uselessness. Additionally, industrial robots are more prone to mode coupling chatter than to the regenerative kind which is more common in conventional processes. Mode coupling chatter occurs when vibration in two or more directions interacts to cause the tool to follow an elliptical path. While regenerative chatter

is local to the vibrating element, mode coupling chatter occurs at the fundamental mode and involves the entire structure [25].

The initial focus of any semi-active inerter design for industrial robots should be on the placement. The goal would be to be able to adjust the natural frequencies of limbs in different directions, to avoid the coupling of their vibration modes. Sketches of two different possible schema are shown in Figure 6.10. In Figure 6.10a, a single inerter is positioned between the base of the robot and ground allows the principle resonance in that direction. This solution would be attractive due to the simplicity of using a single inerter, although it might be insufficient to deal with the complex, multidirectional modes possible. In Figure 6.10b, multiple inerters situated between each limb at the joints would be better placed to target the specific modes of issue. However, this would become costly and require a more complex control system.
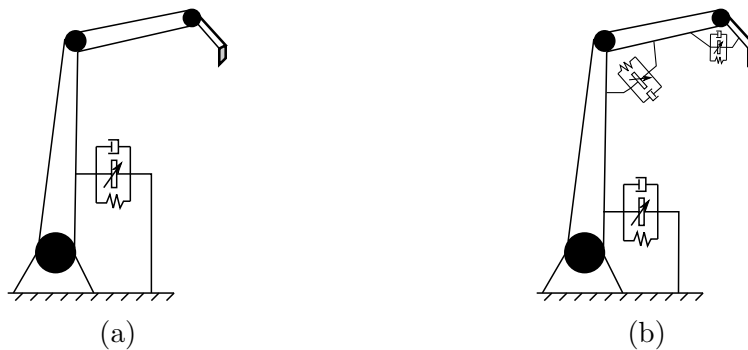
Figure 6.10: Two different schema for placing semi-active inerters in an industrial robot, with a) a single inerter at the base and b) multiple inerters at each joint.

The two examples in Figure 6.10 represent the extremes of a continuum of potential solutions. Developing models, with suitable levels of fidelity, of inerter, robot, and tool-workpiece interaction would allow for further investigation. A lot of this work could be validated using passive inerters, allowing for work to progress in parallel with the development of semi-active inerters. Equally, the rate of change of inertance might be low enough that the existing solution developed by Hu et al. [72] might be appropriate.

6.4 Conclusion

The first part of this chapter discussed the limitations of the work presented in Chapter 5. Some specific ways in which the prototype semi-active inerter could be improved

for future tests were presented. In the short term, the main focus would be on reducing the air trapped in the system and on simplifying the parameter estimation process. Additionally, some more radical alternatives to the current design were proposed. These proposals included using an orifice MR valve, designs for inerters using two different fluids, and designs for mechanical semi-active inerters using magnetic fields in different ways.

The second part of this chapter focused on the ways in which semi-active inerters could be employed in machining processes in future. Within conventional machining, the need for miniaturisation presents a difficulty, especially if the goal is to produce effective designs to work within modern multitool computer numerical control machines. Two potential avenues of research present themselves for fixturing solutions: placing the semi-active inerters in the base or placing one within an active fixturing system. Finally, the initial focus of semi-active inerters for robotic machining would be using models to identify the appropriate amount and placement needed to handle mode coupling chatter.

These avenues of research will be briefly revisited in Chapter 7. This final chapter will conclude the thesis as a whole, and discuss some possibilities for future research.

Chapter 7

Conclusions and future work

7.1   Conclusion

This thesis has explored the potential role of the semi-active inerter within semi-active machining. This research took the form of both model-based analytical work and experimental investigation of a prototype device. A clear case for the potential value of the semi-active inerter was presented.

Four objectives for this research were presented at the outset of this thesis:

O1. Explore the case for semi-active inerters in chatter mitigation, focusing on conventional machining operations.

O2. Design a new semi-active inerter which uses magnetorheological fluid.

O3. Create models of the semi-active inerter, to both aid in design and to support future exploration of control schemes.

O4. Build and test a semi-active inerter, with the goal of validating the models.

Objectives O1-3 were met in full. Objective O4 was partially fulfilled, with a prototype device being designed and tested but with the data collected being insufficient for meaningful system identification.

The case for semi-active inerters in chatter mitigation, objective O1., was explored using various methods. A single degree of freedom machining system with an ideal inerter inserted between the vibrating tool and ground was assumed. Two different use cases were explored:

- Discrete inertance variation uses the inerter to shift the natural frequency of the vibrating element, to move the machining operation into a stable lobe. This

method was explored using linear chatter analysis. A new type of stability lobe diagram was presented to help visualise the system. It was shown that the required change in inertance to would depend on the tooth passing frequency, mass of the vibrating element, and depth of cut. It was proposed that this method be restricted to high speed machining operations, due to the difficulty of finding stable lobes at low tooth passing frequencies.

- Continuous inertance variation can mitigate chatter by varying the effective mass of the vibrating element cyclically, so as to disrupt the regenerative effect. This method was explored using semi-discretisation and time-domain simulations. The effects were found to be additive with chatter. It was also found that the ratio of change-in-inertance to mass was the important characteristic. No benefit was found in increasing the ratio of inertia variation to spindle speed.

- In both cases, the need for a semi-active inerter with a large range of inertance was noted. It was also noted that this change would need to be rapid, especially in the case of continuous inertance variation.

Objective O2 was met by the investigating three potential designs of helical inerter using magnetorheological fluid.

- It was shown that placing a valve in series with the helix would only allow the damping to be controlled. Using two helices, one containing a valve, was found to allow a minimum inertance value to be enforced. However, removing the second helix and using a design with a single helix and valve in parallel was shown to offer the greatest range of inertance.

- The valve design was also considered. It was shown that a previous optimisation scheme for MR dampers would not lead to optimal design for the bypass valve. A new, more appropriate scheme was devised by relaxing the constraint on valve gap height and requiring a maximum ratio of on- to off-state pressure drop, instead of maximum total damping. Results from this scheme were verified using finite element software.

- Some potential other designs of semi-active inerter with rapid controllability were also presented and discussed in brief.

In meeting objective O3, a number of models of the semi-active inerter were devised. These modelled behaviour in both the mechanical and fluid domains

- A quasi-dynamic model was devised. This model was based on an existing model of the helical inerter, combined with a Bingham fluid model of the MR valve. This model was used to investigate design options.

- In order to account for the varying inertance, a quasi-dynamic model was developed. It was shown that, when only considering a valve which could be fully on or fully off, neglecting the quadratic damping term could still return a reasonably accurate solution, with the benefit that the resulting linear model could be assessed using conventional linear control methods. A further model was also devised to account for the fact that the valve could be partially open.

Finally, objective O4 was met through the design and testing of two prototype semi-active inerters.

- An initial design filled with hydraulic oil was built to check the filling process and experimental setup. The oil-based inerter exhibits a large friction force. Additionally, the existence of air bubbles within the fluid meant neither the inertance nor damping could be identified.

- An MR fluid inerter was also designed and tested. The issues experienced with th oil-based design persisted. In addition, the MR valve failed to work as expected. Electrical failure was rejected as the cause, with air bubbles causing a gap in the magnetic circuit being considered a more probable caused of this issue.

- Various methods were proposed to deal with these issues in any future designs. These methods included reducing the leakage of the joints, including a fluid reservoir around the bleed valve, and including multiple filling points. The idea of including digital pressure sensors to aid in system identification was also discussed.

7.2   Future work

The role of the semi-active inerter in machining science is still very much an open question. In many ways, this reflects the nature of the inerter itself, as a recently synthesised device. The big questions remain:

1. how best to design practical implementations of the inerter; and

2. how best to employ the inerter to control vibrations.

At its broadest, these questions are the same for the semi-active inerter, although this work has raised some more specific issues which merit investigation.

In terms of practical implementation, the difficulties of designing a semi-active helical inerter should by now be clear to the reader. These difficulties are not, however, insurmountable, given sufficient time and resources. The bones of a roadmap for this can be found in Chapter 6, should any researcher wish to continue the practical work detailed in this thesis. For those pursuing different implementations, Bonello's five principles for adaptive vibration absorbers, found in Section 2.3.4 are a good place to start.

In terms of implementations within machining operations, the issue of miniaturisation will inevitably need to be tackled at some point. This would seem to be a fruitful area of design for inerters in general, and should lead to greater understanding of their limitations. The possibilities for robotic machining also seem exciting - this is an area of research with a large amount of potential for big gains in productivity.

Outside of machining science, the semi-active inerter has potential uses for other vibration control. The most obvious of these would be areas in which inerters are already employed: civil structures and automotives. However, there are likely to be others which have been overlooked here. The possibility for using semi-active inerters as re-tunable vibration absorbers for structures which have a natural frequency which changes over time is intriguing. One such example would be vibration absorbers for freight vehicles which adapt to the increased mass when loaded.

One final area of future research which has been largely overlooked in this thesis is control system design. At present, all implementations of the inerter are imperfect, involving non-linearities of various kinds. It is unlikely that a semi-active inerter with perfectly linear behaviour will be developed in the near future. As with other areas of non-linear control, the issue of designing strategies for the behaviour of any given semi-active inerter which may be developed will provide an interesting research challenge.

Appendices

Appendix A

Derivation of Equation 3.23

Beginning with Equation 3.22

$$(m_0 + m_1 \sin(\omega_M t + \phi))\ddot{x}(t) + c\dot{x}(t) + kx(t) = wK_s(x(t - \tau) - x(t)), \quad \text{(3.22 revisited)}$$

define the amplitude ratio, $R_A = \frac{m_1}{m_0}$, and modulation ratio, $R_M = \frac{\tau_M}{\tau} = \frac{\tilde{\tau_M}}{\tilde{\tau}}$, where $\tau_M = \frac{2\pi}{\omega_M}$ is the modulation period. The coefficient of $\ddot{x}(t)$ now becomes $m_0(1 + R_A \sin(\frac{2\pi t}{R_M \tau}))$.

Making this substitution, by k and defining the non-dimensional depth of cut to be $\tilde{w} = \frac{wK_s}{k}$, dividing both sides of Equation 3.22 leads to

$$\frac{m}{k}\left(1 + R_A \sin\left(\frac{2\pi t}{R_M \tau}\right)\right)\ddot{x}(t) + \frac{c}{k}\dot{x}(t) + x(t) = \tilde{w}(x(t - \tau) - x(t)). \quad \text{(A.1)}$$

Define non-dimensional time as $\tilde{t} = \omega_0 t$, where $\omega_0 = \sqrt{\frac{k}{m}}$ is the natural frequency of the unmodulated system. Assuming sinusoidal motion, $x(t) = X\sin(\omega t) \implies x(\tilde{t}) = X\sin\left(\frac{\omega}{\omega_0}\tilde{t}\right) = X\sin(\omega\tilde{t})$, so that $\dot{x}(t) = \omega_0\dot{x}(\tilde{t})$ and $\ddot{x}(t) = \omega_0^2\ddot{x}(\tilde{t})$,

$$\frac{m\omega_0^2}{k}\left(1 + R_A \sin\left(\frac{2\pi\tilde{t}}{R_M\tilde{\tau}}\right)\right)\ddot{x}(\tilde{t}) + \frac{c\omega_0}{k}\dot{x}(\tilde{t}) + x(\tilde{t}) = \tilde{w}(x(\tilde{t} - \tilde{\tau}]) - x(\tilde{t})), \quad \text{(A.2)}$$

where $\tilde{\tau} = \omega_0\tau$ is the non-dimensional time delay. As $\frac{m\omega_0^2}{k} = 1$ and $\frac{c\omega_0}{k} = 2\zeta$, where $\zeta = \frac{c}{2\sqrt{km}}$ is the damping ratio, if we define the modulation parameter to be $\chi(\tilde{t}) = \frac{1}{1+R_A \sin\left(\frac{2\pi}{R_M\tilde{\tau}}\tilde{t}\right)}$ then we reach

$$\frac{1}{\chi}(\tilde{t})\ddot{x}(\tilde{t}) + 2\zeta\dot{x}(\tilde{t}) + x(\tilde{t}) = \tilde{w}(x(\tilde{t} - \tilde{\tau}) - x(\tilde{t})), \quad \text{(3.23 revisited)}$$

which is Equation 3.23, as required.

Appendix B

Derivation of Equation 4.14

The volumetric flow rate in helix $_B$ is

$$Q_B = A_B u_B = Q_0 - Q_A = A_1 \dot{x} - A_A u_A. \tag{B.1}$$

The pressure drop across both helixes must be equivalent so

$$\frac{\alpha_B}{r_{3,B}^2} u_B + \frac{\beta_B}{r_{3,B}^0 .5} u_B^2 + \frac{C}{A_v} u_B + \tau_y = \frac{\alpha_A}{r_{3,A}^2} u_A + \frac{\beta_A}{r_{3,A}^0 .5} u_A^2. \tag{B.2}$$

By substituting Equation B.1 into B.2,

$$\frac{\alpha_B}{r_{3,B}^2} \left[\frac{A_1}{A_B} \dot{x} - \frac{A_A}{A_B} u_A \right] + \frac{\beta_B}{r_{3,B}^0 .5} \left[\left(\frac{A_1}{A_B} \right)^2 \dot{x}^2 + \left(\frac{A_A}{A_B} \right)^2 u_A^2 - 2 \frac{A_1}{A_B} \dot{x} \frac{A_A}{A_B} u_A \right] + \frac{C}{A_v} u_B + \tau_y$$

$$= \frac{\alpha_A}{r_{3,A}^2} u_A + \frac{\beta_A}{r_{3,A}^0 .5} u_A^2, \tag{B.3}$$

can be formed. Equation B.3 can be rearranged to the form

$$\left[\frac{\beta_B A_A^2}{r_{3,B}^0 .5 A_B^2} - \frac{\beta_A}{r_{3,A}^0 .5} \right] u_A^2 - \left[\frac{\alpha_B A_A}{r_{3,B}^2 A_B} + \alpha_A r_{3,A}^2 + 2 \frac{\beta_B}{r_{3,B}^0 .5} \frac{A_1}{A_B} \dot{x} \frac{A_A}{A_B} \right] u_A$$

$$+ \left[(\frac{\alpha_B A_1}{r_{3,B}^2 A_B} \dot{x} + \frac{\beta_B A_1^{2}}{r^{0}}_{3,B} .5 A_B^2) \dot{x}^2 + \tau_y \right] = 0. \tag{B.4}$$

Appendix C

The SADE algorithm 4.14

SADE is a modified version of the differential evolution (DE) algorithm. What follows is a very brief description. The interested reader is directed to Refs. [227] and [226] for more complete descriptions of DE and SADE, respectively.

DE is based on the idea of the survival of the fittest. It commences with the creation of a number of candidate vectors, consisting of potential values of the model parameters, known as a *generation* of size N. For each vector in the generation, a *mutated* vector is created through the addition and subtraction of the parameter values in three of the other vectors in the generation. A *trial* vector is then created by combining the mutated vector with the original, choosing a random number of parameters from each. This is done through a series of binomial trials on a per parameter basis. Both the original and trial vectors are then used to simulate the system under investigation. The vector that creates the best fit is selected for the next generation, while the other is eliminated. This is iterated across a number of generations, G. This process is shown for a linear SDOF mass-spring-damper system in Figure C.1, as reference.

The DE algorithm relies on four main hyperparameters. The size of population, N, and number of generations, G, have already been discussed. Additionally, the creation of the mutated vector is controlled by a *scaling factor*, f, while the chance of a parameter being selected from either the original or the mutated vector is controlled by the *crossover parameter*, C_r. DE can be sensitive to these hyperparameters.

SADE is a version of DE in which f and C_r adapt themselves over the run time of the algorithm. Initially, these two hyperparameters are selected from a Gaussian distribution about the mean. After a number of generations, known as the *training period*, the algorithm then recalculates a new mean and distribution from the values which resulted in surviving vectors. This process iterates throughout the run time

of the cycle. Additionally, the mutation method is also adapted in similar, from a cohort of four candidate methods as detailed in Ref. [226].

In the work presented in Chapter 5, SADE was implemented in python using the `FreeLunch` [228] and `Toybox` [229] packages. The algorithm operates as described in Ref. [230]. The hyperparameters used are given in Table C.1. Goodness of fit was assessed using by calculating the normalised mean-square error (NMSE). This cost function returns a value of 100 if the simulated data is the mean of the measured data, and 0 if the two are perfectly correlated. A value of NMSE< 5 is considered a good fit and NMSE< 1 is considered excellent [230].

Table C.1: Hyperparameters of the Differential Evolution algorithm

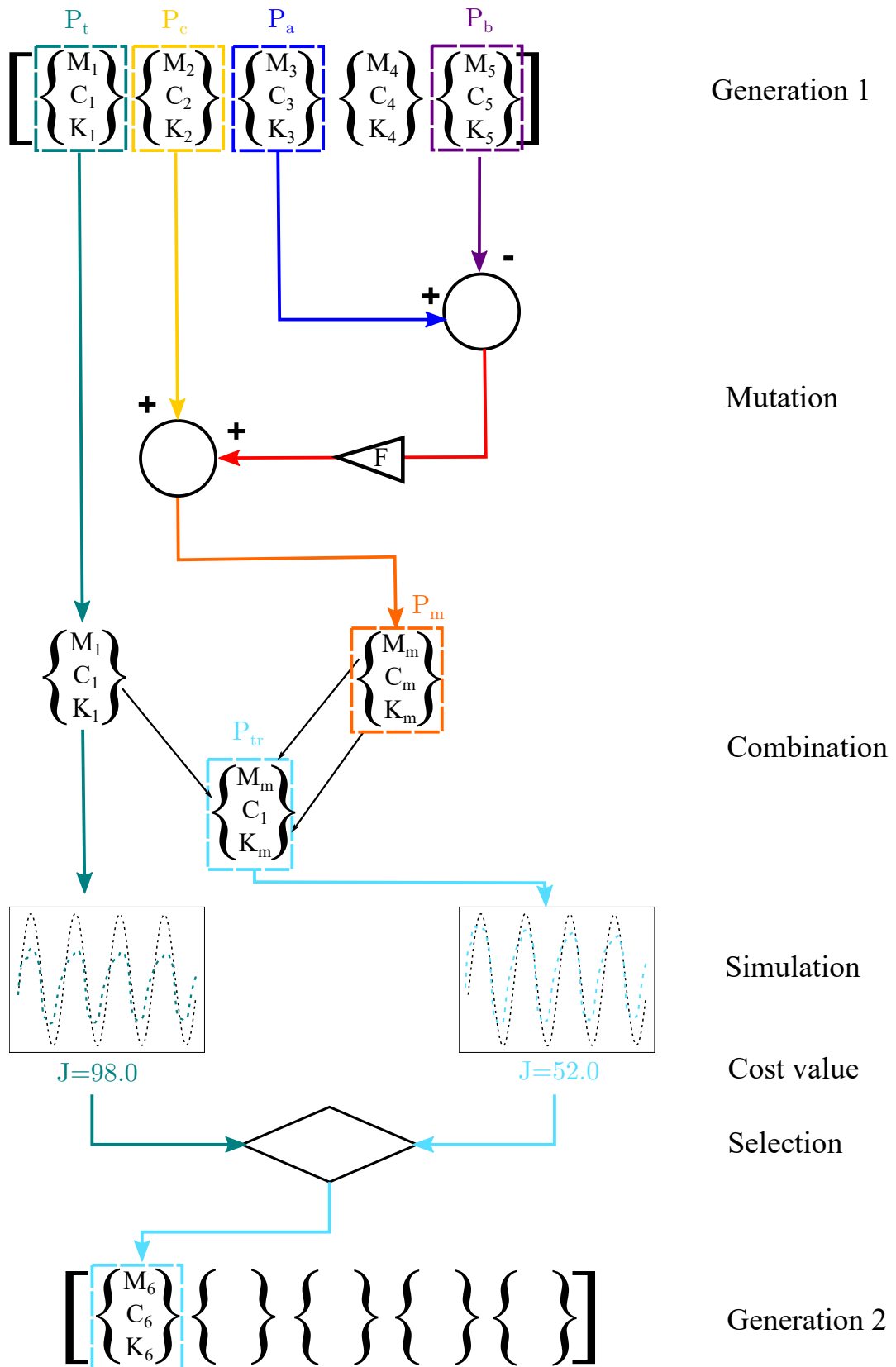| N	G	Integration method	Tolerance
20	20	Runge-Kutta 4(5)	1×10^{-3}

Figure C.1: Differential evolution works through a process of mutating, combing and selecting a stronger population over a number of generations.

References

[1] F. A. Firestone, "A new analogy between mechanical and electrical systems," The Journal of the Acoustical Society of America, vol. 4, no. 3, pp. 249–267, 1933.

[2] M. C. Smith, "Synthesis of mechanical networks: the inerter," IEEE Transactions on Automatic Control, vol. 47, pp. 1648–1662, Oct 2002.

[3] J. C. Schönfeld, "Analogy of hydraulic, mechanical, acoustic and electric systems," Applied Scientific Research, Section B, vol. 3, pp. 417–450, Dec 1954.

[4] W. M. Kuhnert, P. J. P. Gonçalves, D. F. Ledezma-Ramirez, and M. J. Brennan, "Inerter-like devices used for vibration isolation: A historical perspective," Journal of the Franklin Institute, vol. 358, no. 1, pp. 1070–1086, 2021.

[5] S. Nakaminami, H. Kida, K. Ikago, and N. Inoue, "Dynamic testing of a full-scale hydraulic inerter-damper for the seismic protection of civil structures," in Proceedings of the 7th International Conference on Advances in Experimental Structural Engineering, AESE 2017 (M. Furinghetti, D. Bolognini, and A. Pavese, eds.), International Conference on Advances in Experimental Structural Engineering, pp. 41–54, EUCENTRE, Jan. 2017.

[6] Y. Sugimura, W. Goto, H. Tanizawa, T. Nagasaku, K. Saito, and T. Ninomiya, "Response control effect of hi-rised steel building structure using tuned viscous mass dampers," AIJ Journal of Technology and Design, vol. 18, no. 39, pp. 441–446, 2012.

[7] S. Kawamata, "Liquid type mass damper with elongated discharge tube." U.S. patent 8881876 B2, Oct. 1989.

[8] M. C. Smith, N. E. Houghton, P. J. G. Long, and A. R. Glover, "Force-controlling hydraulic device." U.S. patent 8881876 B2, Nov. 2014.

[9] R. Tuluie, "Fluid inerter." U.S. patent 0032442 A1, Feb. 2013.

[10] B. Gartner and M. Smith, "Damping and inertial hydraulic device." U.S. patent 0037362 A1, Feb. 2011.

[11] K. Xu, K. Bi, Q. Han, X. Li, and X. Du, "Using tuned mass damper inerter to mitigate vortex-induced vibration of long-span bridges: Analytical study," Engineering Structures, vol. 182, pp. 101 – 111, 2019.

[12] R. Ma, K. Bi, and H. Hao, "Mitigation of heave response of semi-submersible platform (SSP) using tuned heave plate inerter (THPI)," Engineering Structures, vol. 177, pp. 357 – 373, 2018.

[13] F. Scheibe and M. Smith, "Analytical solutions for optimal ride comfort and tyre grip for passive vehicle suspensions," Vehicle System Dynamics, vol. 47, no. 10, pp. 1229–1252, 2009.

[14] F.-C. Wang and M.-K. Liao, "The lateral stability of train suspension systems employing inerters," Vehicle System Dynamics, vol. 48, no. 5, pp. 619–643, 2010.

[15] J. Jiang, M. Smith, and N. Houghton, "Experimental testing and modelling of a mechanical steering compensator," in 2008 3rd International Symposium on Communications, Control and Signal Processing, pp. 249–254, IEEE, 2008.

[16] H. Frahm, "Improved means for damping the vibrations of bodies." G.B. patent 190923828A, 1909.

[17] D. Karnopp, M. J. Crosby, and R. A. Harwood, "Vibration control using semi-active force generators," Journal of Engineering for Industry, vol. 96, no. 2, pp. 619–626, 1974.

[18] N. R. Fisco and H. Adeli, "Smart structures: Part I - Active and semi-active control," Scientia Iranica. Transaction A, Civil engineering, vol. 18, no. 3, p. 275, 2011.

[19] G. Tlusty, Manufacturing processes and equipment. Prentice Hall, 1999.

[20] F. Taylor, "On the art of cutting tools," Trans. ASME, vol. 28, 1907.

[21] J. Muñoa, X. Beudaert, Z. Dombovari, Y. Altintas, E. Budak, C. Brecher, and G. Stepan, "Chatter suppression techniques in metal cutting," <u>CIRP Annals</u>, vol. 65, no. 2, pp. 785–808, 2016.

[22] H. Dogan, N. Sims, and D. Wagg, "Investigation of the inerter-based dynamic vibration absorber for machining chatter suppression," <u>Journal of Physics. Conference Series</u>, vol. 1264, no. 1, 2019.

[23] G. Quintana and J. Ciurana, "Chatter in machining processes: A review," <u>International Journal of Machine Tools and Manufacture</u>, vol. 51, no. 5, pp. 363–376, 2011.

[24] M. Wiercigroch and E. Budak, "Sources of nonlinearities, chatter generation and suppression in metal cutting," <u>Philosophical Transactions of the Royal Society of London. Series A: Mathematical, Physical, and Engineering Sciences</u>, vol. 359, no. 1781, pp. 663–693, 2001.

[25] Z. Pan, H. Zhang, Z. Zhu, and J. Wang, "Chatter analysis of robotic machining process," <u>Journal of Materials Processing Technology</u>, vol. 173, no. 3, pp. 301–309, 2006.

[26] M. Siddhpura and R. Paurobally, "A review of chatter vibration research in turning," <u>International Journal of Machine Tools & Manufacture</u>, vol. 61, pp. 27–47, 2012.

[27] R. N. Arnold, "Cutting tools research: Report of subcommittee on carbide tools: The mechanism of tool vibration in the cutting of steel," <u>Proceedings / Institution of Mechanical Engineers</u>, vol. 154, no. 1, pp. 261–284, 1946.

[28] B. Stone, <u>Chatter and machine tools</u>. Cham: Springer, 2014.

[29] S. A. Tobias and W. Fishwick, "Theory of regenerative machine tool chatter," <u>The Engineer</u>, vol. 205, no. 7, pp. 199–203, 1958.

[30] J. Tlusty and M. Polacek, <u>Beispiele der behandlung der selbsterregten Schwingung der Werkzeugmaschinen FoKoMa</u>. Hanser Verlag, Munchen, 1957.

[31] M. Eynian, <u>Prediction of vibration frequencies in milling using modified Nyquist method</u>, vol. 11. 2015.

[32] P. V. Bayly, J. E. Halley, B. P. Mann, and M. A. Davies, "Stability of interrupted cutting by temporal finite element analysis," Journal of Manufacturing Science and Engineering, vol. 125, no. 2, pp. 220–225, 2003.

[33] T. Insperger and G. Stépán, "Stability analysis of turning with periodic spindle speed modulation via semidiscretization," Journal of Vibration and Control, vol. 10, no. 12, pp. 1835–1855, 2004.

[34] Y. Altintas and M. Weck, "Chatter stability of metal cutting and grinding," CIRP Annals, vol. 53, no. 2, pp. 619 – 642, 2004.

[35] J. Tlusty, W. Zaton, and F. Ismail, "Stability lobes in milling," CIRP Annals, vol. 32, no. 1, pp. 309 – 313, 1983.

[36] Y. Altintas, "Analytical prediction of three dimensional chatter stability in milling," JSME International Journal Series C Mechanical Systems, Machine Elements and Manufacturing, vol. 44, no. 3, pp. 717–723, 2001.

[37] W. Tang, Q. Song, S. Yu, S. Sun, B. Li, B. Du, and X. Ai, "Prediction of chatter stability in high-speed finishing end milling considering multi-mode dynamics," Journal of Materials Processing Technology, vol. 209, no. 5, pp. 2585–2591, 2009.

[38] C. Yue, H. Gao, X. Liu, S. Y. Liang, and L. Wang, "A review of chatter vibration research in milling," Chinese Journal of Aeronautics, vol. 32, no. 2, pp. 215–242, 2019.

[39] Z. Dombovari, D. A. Barton, R. Eddie Wilson, and G. Stepan, "On the global dynamics of chatter in the orthogonal cutting model," International Journal of Non-linear Mechanics, vol. 46, no. 1, p. 330, 2010.

[40] T. Kalmár-Nagy, G. Stépán, and F. C. Moon, "Subcritical Hopf bifurcation in the delay equation model for machine tool vibrations," Nonlinear Dynamics, vol. 26, no. 2, pp. 121–142, 2001.

[41] G. Stepan, R. Szalai, B. P. Mann, P. V. Bayly, T. Insperger, J. Gradisek, and E. Govekar, "Nonlinear dynamics of high-speed milling—analyses, numerics, and experiments," Journal of Vibration and Acoustics, vol. 127, no. 2, pp. 197–203, 2005.

[42] V. Sellmeier and B. Denkena, "Stable islands in the stability chart of milling processes due to unequal tooth pitch," International Journal of Machine Tools & Manufacture, vol. 51, no. 2, pp. 152–164, 2011.

[43] S. H. Gao and G. Meng, "Unstable islands and bifurcation analysis in a spindle milling system supported by ball bearings," Proceedings of the Institution of Mechanical Engineers. Part K, Journal of Multi-body Dynamics, vol. 225, no. 3, pp. 235–251, 2011.

[44] T. L. Schmitz, Machining dynamics : frequency response to improved productivity. New York: Springer, 2009.

[45] S. Smith and J. Tlusty, "Stabilizing chatter by automatic spindle speed regulation," CIRP Annals, vol. 41, no. 1, pp. 433–436, 1992.

[46] J. Muñoa, A. Iglesias, A. Olarra, Z. Dombovari, M. Zatarain, and G. Stepan, "Design of self-tuneable mass damper for modular fixturing systems," CIRP Annals, vol. 65, no. 1, pp. 389–392, 2016.

[47] E. Budak, L. Tunç, S. Alan, and H. N. Özgüven, "Prediction of workpiece dynamics and its effects on chatter stability in milling," CIRP Annals, vol. 61, no. 1, pp. 339–342, 2012.

[48] M. Wang, T. Zan, and X. Gao, "Modeling and optimization of a friction damper for boring chatter control," Advances in Mechanical Engineering, vol. 6, pp. 690768–690768, 2015.

[49] N. D. Sims, "Vibration absorbers for chatter suppression: A new analytical tuning methodology," Journal of Sound and Vibration, vol. 301, no. 3, pp. 592–607, 2007.

[50] S. Zeng, X. Wan, W. Li, Z. Yin, and Y. Xiong, "A novel approach to fixture design on suppressing machining vibration of flexible workpiece," International Journal of Machine Tools and Manufacture, vol. 58, pp. 29–43, 2012.

[51] S. Smith, R. Wilhelm, B. Dutterer, H. Cherukuri, and G. Goel, "Sacrificial structure preforms for thin part machining," CIRP Annals, vol. 61, no. 1, pp. 379–382, 2012.

[52] H. Takeyama, N. Iijima, N. Nishiwaki, and K. Komoto, "Improvement of dynamic rigidity of tool holder by applying high-damping material," CIRP Annals, vol. 33, no. 1, pp. 249–252, 1984.

[53] M. Zatarain, J. Muñoa, G. Peigné, and T. Insperger, "Analysis of the influence of mill helix angle on chatter stability," CIRP Annals, vol. 55, no. 1, pp. 365–368, 2006.

[54] M. Zatarain and Z. Dombovari, "Stability analysis of milling with irregular pitch tools by the implicit subspace iteration method," International Journal of Dynamics and Control, vol. 2, no. 1, pp. 26–34, 2014.

[55] P. Bari, M. Law, and P. Wahi, "Geometric models of non-standard serrated end mills," International Journal of Advanced Manufacturing Technology, vol. 111, no. 11-12, pp. 3319–3342, 2020.

[56] M. Rahman and Y. Ito, "Detection of the onset of chatter vibration," Journal of Sound and Vibration, vol. 109, no. 2, pp. 193–205, 1986.

[57] T. L. Schmitz, K. Medicus, and B. Dutterer, "Exploring once-per-revolution audio signal variance as a chatter indicator," Machining Science and Technology, vol. 6, no. 2, pp. 215–233, 2002.

[58] N.-C. Tsai, D.-C. Chen, and R.-M. Lee, "Chatter prevention for milling process by acoustic signal feedback," International Journal of Advanced Manufacturing Technology, vol. 47, no. 9-12, pp. 1013–1021, 2010.

[59] I. N. Tansel, M. Li, M. Demetgul, K. Bickraj, B. Kaya, and B. Ozcelik, "Detecting chatter and estimating wear from the torque of end milling signals by using index based reasoner (IBR)," International Journal of Advanced Manufacturing Technology, vol. 58, no. 1, pp. 109–118, 2012.

[60] J. Tlusty and G. Andrews, "A critical review of sensors for unmanned machining," CIRP Annals, vol. 32, no. 2, pp. 563–572, 1983.

[61] S. S. Rao, Mechanical vibrations. Singapore ; London: Prentice Hall, 4th ed. in SI units / SI conversion by yap fook fah. ed., 2011.

[62] R. Hahn, "Analysis and optimisation for inerter-based isolators via fixed-point theory and algebraic solution," Transactions of the ASME, pp. 331–335, 1951.

[63] M. Wang, T. Zan, Y. Yang, and R. Fei, "Design and implementation of non-linear TMD for chatter suppression: An application in turning processes," International Journal of Machine Tools & Manufacture, vol. 50, no. 5, pp. 474–479, 2010.

[64] Y. Yang, W. Dai, and Q. Liu, "Design and machining application of a two-DOF magnetic tuned mass damper," The International Journal of Advanced Manufacturing Technology, vol. 89, no. 5, pp. 1635–1643, 2017.

[65] "Mode coupling chatter suppression for robotic machining using semi-active magnetorheological elastomers absorber," Mechanical Systems and Signal Processing, vol. 117, pp. 221–237, 2019.

[66] J. Pena-Barrio, M. Sanz-Calle, G. Aguirre, A. Iglesias, G. Stepan, L. N. López de Lacalle, J. Muñoa, and Z. Dombovari, "Optimal tuning strategy for chatter avoidance in thin-walled part milling by means of tuneable clamping table," in Proceedings of ISMA, ISMA, 2020.

[67] J. P. Den Hartog, Mechanical vibrations. New York: McGraw-Hill, 1934.

[68] E. Rivin and H. Kang, "Enhancement of dynamic stability of cantilever tooling structures," International Journal ofMachine Tools & Manufacture, vol. 32, no. 4, pp. 539–561, 1992.

[69] Y. Yang, J. Muñoa, and Y. Altintas, "Optimization of multiple tuned mass dampers to suppress machine tool chatter," International Journal of Machine Tools & Manufacture, vol. 50, no. 9, pp. 834–842, 2010.

[70] J. Burtscher and J. Fleischer, "Adaptive tuned mass damper with variable mass for chatter avoidance," CIRP Annals, vol. 66, no. 1, pp. 397–400, 2017.

[71] I. Lazar, S. Neild, and D. Wagg, "Using an inerter-based device for structural vibration suppression," Earthquake Engineering & Structural Dynamics, vol. 43, no. 8, pp. 1129–1147, 2014.

[72] M. Z. Hu, Y.and Chen, Z. Shu, and L. Huang, "Analysis and optimisation for inerter-based isolators via fixed-point theory and algebraic solution," Journal of Sound and Vibration, vol. 346, no. 1, pp. 17–36, 2015.

[73] H. Dogan, N. D. Sims, and D. J. Wagg, "Design and implementation of TID for vibration suppression," in Proceedings of ISMA, ISMA, 2020.

[74] A. Bilbao-Guillerna, I. Azpeitia, S. Luyckx, N. Loix, and J. Muñoa, "Low frequency chatter suppression using an inertial actuator," pp. 1–6, Mar 2012.

[75] N. Sims and Y. Zhang, "Piezoelectric active control for workpiece chatter reduction during milling," in Proceedings of SPIE, vol. 5390, (Bellingham WA), pp. 335–346, SPIE, 2004.

[76] M. Chen and C. Knospe, "Control approaches to the suppression of machining chatter using active magnetic bearings," IEEE Transactions on Control Systems Technology, vol. 15, no. 2, pp. 220–232, 2007.

[77] O. Bakker, T. Papastathis, A. Popov, and S. Ratchev, "Active fixturing: literature review and future research directions," International Journal of Production Research, vol. 51, no. 11, pp. 3171–3190, 2013.

[78] M. Wang and R. Fei, "Chatter suppression based on nonlinear vibration characteristic of electrorheological fluids," International Journal of Machine Tools & Manufacture, vol. 39, no. 12, pp. 1925–1934, 1999.

[79] D. Mei, T. Kong, A. Shih, and Z. Chen, "Magnetorheological fluid-controlled boring bar for chatter suppression," Journal of Materials Pprocessing Technology, vol. 209, no. 4, pp. 1861–1870, 2009.

[80] C. Biju and M. Shunmugam, "Performance of magnetorheological fluid based tunable frequency boring bar in chatter control," Measurement : Journal of the International Measurement Confederation, vol. 140, pp. 407–415, 2019.

[81] "Chatter suppression in boring operation using magnetorheological fluid damper," Materials and Manufacturing Processes, vol. 23, no. 4, pp. 329–335, 2008.

[82] D. Sajedi Pour and S. Behbahani, "Semi-active fuzzy control of machine tool chatter vibration using smart MR dampers," International Journal of Advanced Manufacturing Technology, vol. 83, no. 1, pp. 421–428, 2016.

[83] "Study on the influence of magnetorheological fluid on tool vibration during end milling process," International Journal of Dynamics and Control, vol. 5, no. 3, pp. 696–703, 2017.

[84] E. Dìaz-Tena, L. L. de Lacalle Marcaide, F. C. Gómez, and D. C. Bocanegra, "Use of magnetorheological fluids for vibration reduction on the milling of thin floor parts," Procedia Engineering, vol. 63, pp. 835–842, 2013. The Manufacturing Engineering Society International Conference, MESIC 2013.

[85] J. Ma, D. Zhang, M. Wu, B.and Luo, and Y. Liu, "Stability improvement and vibration suppression of the thin-walled workpiece in milling process via magnetorheological fluid flexible fixture," International journal of Advanced Manufacturing Technology, vol. 88, no. 5, pp. 1231–1242, 2017.

[86] "Semi-active magnetorheological damper device for chatter mitigation during milling of thin-floor components," Applied Sciences, vol. 10, no. 15, p. 5313, 2020.

[87] J. Sexton, R. Milne, and B. Stone, "A stability analysis of single-point machining with varying spindle speed," Applied Mathematical Modelling, vol. 1, no. 6, pp. 310–318, 1977.

[88] T. Inamura and T. Sata, "Stability analysis of cutting under varying spindle speed," Journal of the Japan Society of Precision Engineering, vol. 43, no. 505, pp. 80–85, 1977.

[89] T. Insperger and G. Stépán, Semi-discretization method for delayed systems, vol. 55. Chichester, UK: John Wiley & Sons, Ltd, 2002.

[90] M. Zatarain, I. Bediaga, J. Muñoa, and R. Lizarralde, "Stability of milling processes with continuous spindle speed variation: Analysis in the frequency and time domains, and experimental correlation," CIRP Annals, vol. 57, no. 1, pp. 379–384, 2008.

[91] I. Bediaga, M. Zatarain, J. Muñoa, and R. Lizarralde, "Application of continuous spindle speed variation for chatter avoidance in roughing milling," Proceedings of the Institution of Mechanical Engineers. Part B, Journal of Engineering Manufacture, vol. 225, no. 5, pp. 631–640, 2011.

[92] D. Segalman and J. Redmond, "Chatter supression through variable impedance and smart fluids," in Proceedings of SPIE, vol. 2721, pp. 353–363, SPIE, 1996.

[93] D. Segalman and E. Butcher, "Suppression of regenerative chatter via impedance modulation," Journal of Vibration and Control, vol. 6, no. 2, pp. 243–256, 2000.

[94] F. Defant and P. Albertelli, "A novel harmonic solution for chatter stability of time periodic systems," Journal of Sound and Vibration, vol. 490, p. 115719, 2021.

[95] D. J. Wagg, "A review of the mechanical inerter: historical context, physical realisations and nonlinear applications," Mechanical Systems and Structures, vol. 104, no. 1, pp. 13–34, 2021.

[96] W. G. Flannelly, "Dynamic antiresonant vibration isolator." U.S. patent 33223379A, May 1967.

[97] W. C. Flower, "Understanding hydraulic mounts for improved vehicle noise, vibration and ride qualities," SAE Technical Paper Series, 1985.

[98] Z. Chen and Y. Hu, Inerter and Its Application in Vibration Control Systems. Singapore: Springer, 2019.

[99] M. Smith, "The inerter: A retrospective," Annual Review of Control, Robotics, and Autonomous Systems, vol. 3, no. 1, pp. 361–391, 2020.

[100] C. Papageorgiou, N. Houghton, and M. Smith, "Experimental testing and analysis of inerter devices," Journal of Dynamic Systems, Measurement, and Control, vol. 131, no. 1, pp. 1–11, 2009.

[101] W.-J. Wang, F.-C.and Su, "Impact of inerter nonlinearities on vehicle suspension control," Vehicle System Dynamics, vol. 46, no. 7, pp. 575–595, 2008.

[102] Y. Li, S. Li, and Z. Wang, J.and Chen, "A new type of damper combining eddy current damping with rack and gear," Journal of Vibration and Control, vol. 27, no. 9-10, pp. 1087–1097, 2021.

[103] S. J. Swift, M. C. Smith, A. R. Glover, C. Papageorgiou, B. Gartner, and N. E. Houghton, "Design and modelling of a fluid inerter," International Journal of Control, vol. 86, no. 11, pp. 2035–2051, 2013.

[104] M. Germano, "On the effect of torsion on a helical pipe flow," Journal of Fluid Mechanics, vol. 125, no. 7, pp. 1–8, 1982.

[105] B. Titurus, "Generalized liquid-based damping device for passive vibration control," AIAA journal, vol. 56, no. 10, pp. 4134–4145, 2018.

[106] J.-S. Hwang, J. Kim, and Y.-M. Kim, "Rotational inertia dampers with toggle bracing for vibration control of a building structure," Engineering Structures, vol. 29, no. 6, pp. 1201–1208, 2007.

[107] R. Ma, K. Bi, and H. Hao, "A novel rotational inertia damper for amplifying fluid resistance: Experiment and mechanical model," Mechanical Systems and Signal Processing, vol. 149, 2021.

[108] C. Scarborough, "Technical insights: Renault's J-damper," Autosport, 2008.

[109] M. Z. Q. Chen, C. Papageorgiou, F. Scheibe, F. Wang, and M. C. Smith, "The missing mechanical circuit element," IEEE Circuits and Systems Magazine, vol. 9, no. 1, pp. 10–26, 2009.

[110] M. Smith and F.-C. Wang, "Performance benefits in passive vehicle suspensions employing inerters," Vehicle System Dynamics, vol. 42, no. 4, pp. 235–257, 2004.

[111] S. Zhang, M. Zhu, Y. Li, J. Jiang, R. Ficca, M. Czechowicz, R. Neilson, S. Neild, and G. Herrmann, "Ride comfort enhancement for passenger vehicles using the structure-immittance approach," Vehicle System Dynamics, vol. 59, no. 4, pp. 504–525, 2021.

[112] S. Zhang, J. Jiang, and S. Neild, "Passive vibration control: A structure-immittance approach," Proceedings of the Royal Society. A, Mathematical, Physical, and Engineering Sciences, vol. 473, no. 2201, pp. 20170011–20170011, 2017.

[113] F.-C. Wang and H.-J. Hsieh, M.-R.and Chen, "Stability and performance analysis of a full-train system with inerters," Vehicle System Dynamics, vol. 50, no. 4, pp. 545–571, 2012.

[114] T. Lewis, J. Jiang, S. Neild, C. Gong, and S. Iwnicki, "Using an inerter-based suspension to improve both passenger comfort and track wear in railway vehicles," Vehicle System Dynamics, vol. 58, no. 3, pp. 472–493, 2020.

[115] S. Evangelou, D. J. Limebeer, R. Sharp, and M. Smith, "Control of motorcycle steering instabilities: Passive mechanical compensators incorporating inerters," IEEE Control Systems Magazine, vol. 26, no. 5, pp. 78–88, 2006.

[116] M. Fox, J. Roach, and H. E.A., "Dual rack and pinion rotational inerter system and method for damping movement of a flight control surface of an aircraft." U.S. patent 10107347 B2, 2018.

[117] M. Fox and J. Roach, "Rotational inerter and method for damping an actuator." U.S. patent 10088006 B2, Oct. 2018.

[118] L. Marian and A. Giaralis, "Optimal design of a novel tuned mass-damper–inerter (TMDI) passive vibration control configuration for stochastically support-excited structural systems," Probabilistic Engineering Mechanics, vol. 38, pp. 156–164, 2014.

[119] A. Javidialesaadi and N. Wierschem, "Design and performance evaluation of inerter-based tuned mass dampers for a ground acceleration excited structure," Soil dynamics and Earthquake Engineering (1984), vol. 140, 2021.

[120] I. Lazar, S. Neild, and D. Wagg, "Vibration suppression of cables using tuned inerter dampers," Engineering Structures, vol. 122, pp. 62–71, 2016.

[121] R. Ma, K. Bi, and H. Hao, "Heave motion mitigation of semi-submersible platform using inerter-based vibration isolation system (IVIS)," Engineering Structures, vol. 219, p. 110833, 2020.

[122] N. Smith and W. D.J., "A fluid inerter with variable inertance properties," in 6th European Conference on Structural Control, no. 199, (Sheffield), pp. 1–8, EACS, 2016.

[123] C. Liu, L. Chen, X. Zhang, Y. Yang, and J. Nie, "Design and tests of a controllable inerter with fluid-air mixture condition," IEEE Access, vol. 8, pp. 125620–125629, 2020.

[124] Y. Wang, H. Meng, B. Zhang, and R. Wang, "Analytical research on the dynamic performance of semi-active inerter-based vibration isolator with acceleration–velocity-based control strategy," Structural Control and Health Monitoring, vol. 26, no. 4, pp. e2336–n/a, 2019.

[125] Y. Hu, M. Z. Q. Chen, S. Xu, and Y. Liu, "Semiactive inerter and its application in adaptive tuned vibration absorbers," IEEE Transactions on Control Systems Technology, vol. 25, no. 1, pp. 294–300, 2017.

[126] M.-C. Tsai and C.-C. Huang, "Development of a variable-inertia device with a magnetic planetary gearbox," IEEE/ASME Transactions on Mechatronics, vol. 16, no. 6, pp. 1120–1128, 2011.

[127] P. Brzeski, T. Kapitaniak, and P. Perlikowski, "Novel type of tuned mass damper with inerter which enables changes of inertance," Journal of Sound and Vibration, vol. 349, pp. 56–66, 2015.

[128] P. Brzeski, M. Lazarek, and P. Perlikowski, "Experimental study of the novel tuned mass damper with inerter which enables changes of inertance," Journal of Sound and Vibration, vol. 404, pp. 47–57, 2017.

[129] X.-L. Zhang, T. Zhang, J. Nie, and L. Chen, "A semiactive skyhook-inertance control strategy based on continuously adjustable inerter," Shock and Vibration, vol. 2018, pp. 1–8, 2018.

[130] W.-M. Zhong, X.-X. Bai, C. Tang, and A.-D. Zhu, "Principle study of a semi-active inerter featuring magnetorheological effect," Frontiers in Materials, vol. 6, 2019.

[131] P. Bonello, "Adaptive tuned vibration absorbers: Design principles, concepts and physical implementation," in Vibration Analysis and Control (F. Beltran-Carbajal, ed.), ch. 1, Rijeka: IntechOpen, 2011.

[132] D. Pietrosanti, M. De Angelis, and M. Basili, "Optimal design and performance evaluation of systems with tuned mass damper inerter (tmdi)," Earthquake Engineering & Structural Dynamics, vol. 46, no. 8, pp. 1367–1388, 2017.

[133] Y. Wang, H. Ding, and L.-Q. Chen, "Averaging analysis on a semi-active inerter–based suspension system with relative-acceleration–relative-velocity control," Journal of Vibration and Control, vol. 26, no. 13-14, pp. 1199–1215, 2020.

[134] J. Carlson and M. R. Jolly, "MR fluid, foam and elastomer devices," Mechatronics (Oxford), vol. 10, no. 4, pp. 555–569, 2000.

[135] M. J. Wilson, A. Fuchs, and F. Gordaninejad, "Development and characterization of magnetorheological polymer gels," Journal of Applied Polymer Science, vol. 84, no. 14, pp. 2733–2742, 2002.

[136] X. Liu, P. Wong, W. Wang, and W. Bullough, "Feasibility study on the storage of magnetorheological fluid using metal foams," Journal of Intelligent Material Systems and Structures, vol. 21, no. 12, pp. 1193–1200, 2010.

[137] J. Rabinow, "The magnetic fluid clutch," Transactions of the American Institute of Electrical Engineers, vol. 67, no. 2, pp. 1308–1315, 1948.

[138] W. Wimslow, "Method and means for translating electrical impulses into mechanical force." U.S. patent 2,417,850, Mar. 1947.

[139] X. Zhao, Electrorheological material and device design and preparation [electronic resource]. New York: Nova Science Publishers, 2008.

[140] A. Olabi and A. Grünewald, "Design and application of magneto-rheological fluid," Materials in Engineering, vol. 28, no. 10, pp. 2658–2664, 2007.

[141] W. Lu, Y. Luo, L. Kang, and D. Wei, "Characteristics of magnetorheological fluids under new formulation," Journal of Testing and Evaluation, vol. 47, no. 4, pp. 3123–3137, 2019.

[142] J. R. Morillas and J. de Vicente, "Magnetorheology: a review," Soft Matter, vol. 16, pp. 9614–9642, 2020.

[143] J. Berasategi, A. Gomez, M. M. Bou-Ali, J. Gutiérrez, J. M. Barandiarán, I. V. Beketov, A. P. Safronov, and G. V. Kurlyandskaya, "Fe nanoparticles produced by electric explosion of wire for new generation of magneto-rheological fluids," Smart Materials and Structures, vol. 27, no. 4, p. 45011, 2018.

[144] I. Arief and P. Mukhopadhyay, "Magnetorheology in CoNi nanoplatelet-based MRFs: Effect of platelet orientation and oscillatory shear," Journal of Magnetism and Magnetic Materials, vol. 479, pp. 326–331, 2019.

[145] Z. Xia, X. Wu, G. Peng, L. Wang, W. Li, and W. Wen, "A novel nickel nanowire based magnetorheological material," Smart Materials and Structures, vol. 26, no. 5, p. 54006, 2017.

[146] S. Lee, K.-Y. Shin, and J. Jang, "Enhanced magnetorheological performance of highly uniform magnetic carbon nanoparticles," Nanoscale, vol. 7, no. 21, pp. 9646–9654, 2015.

[147] J.-P. Lucking Bigué, A. Landry-Blais, A. Pin, R. Pilon, J.-S. Plante, X. Chen, and M. Andrews, "On the relation between the mason number and the durability of MR fluids," <u>Smart Materials and Structures</u>, vol. 28, no. 9, p. 94003, 2019.

[148] S. G. Sherman, A. C. Becnel, and N. M. Wereley, "Relating Mason number to Bingham number in magnetorheological fluids," <u>Journal of Magnetism and Magnetic Materials</u>, vol. 380, pp. 98–104, 2015.

[149] M. Ashtiani, S. Hashemabadi, and A. Ghaffari, "A review on the magnetorheological fluid preparation and stabilization," <u>Journal of Magnetism and Magnetic Materials</u>, vol. 374, pp. 716–730, 2015.

[150] D. Bica, L. Vékás, M. V. Avdeev, O. Marinică, V. Socoliuc, M. Bălăsoiu, and V. M. Garamus, "Sterically stabilized water based magnetic fluids: Synthesis, structure and properties," <u>Journal of Magnetism and Magnetic Materials</u>, vol. 311, no. 1, pp. 17–21, 2007.

[151] J. Viota, A. Delgado, J. Arias, and J. Durán, "Study of the magnetorheological response of aqueous magnetite suspensions stabilized by acrylic acid polymers," <u>Journal of Colloid and Interface Science</u>, vol. 324, no. 1, pp. 199–204, 2008.

[152] A. Lebedev and S. Lysenko, "Magnetic fluids stabilized by polypropylene glycol," <u>Journal of Magnetism and Magnetic Materials</u>, vol. 323, no. 10, pp. 1198–1202, 2011. Proceedings of 12th International Conference on Magnetic Fluid.

[153] R. Stanway, J. L. Sproston, and A. K. El-Wahed, "Applications of electrorheological fluids in vibration control: a survey," <u>Smart Materials and Structures</u>, vol. 5, no. 4, pp. 464–482, 1996.

[154] N. M. Wereley and L. Pang, "Nondimensional analysis of semi-active electrorheological and magnetorheological dampers using approximate parallel plate models," <u>Smart Materials and Structures</u>, vol. 7, no. 5, pp. 732–743, 1998.

[155] E. Cook, W. Hu, and N. M. Wereley, "Magnetorheological bypass damper exploiting flow through a porous channel," <u>Journal of Intelligent Material Systems and Structures</u>, vol. 18, no. 12, pp. 1197–1203, 2007.

[156] A. Grünewald and A. Olabi, "Design of magneto-rheological (MR) valve," <u>Sensors and Actuators. A. Physical.</u>, vol. 148, no. 1, pp. 211–223, 2008.

[157] W. H. Kim, J. H. Park, J. Park, G.-W. Kim, Y.-S. Lee, and S.-B. Choi, "Comparative study on wear characteristics between flow mode and shear mode magnetorheological dampers," Tribology Transactions, vol. 61, no. 3, pp. 459–473, 2018.

[158] W. Kordonski and S. Gorodkin, "The behavior of a magnetorheological (MR) fluid under compressive deformation," Journal of Rheology (New York : 1978), vol. 60, no. 1, pp. 129–139, 2016.

[159] J. A. Ruiz-López, R. Hidalgo-Alvarez, and J. de Vicente, "A micromechanical model for magnetorheological fluids under slow compression," Rheologica Acta, vol. 55, no. 3, pp. 215–221, 2016.

[160] P. Chen, X.-X. Bai, and L.-J. Qian, "Magnetorheological fluid behavior in high-frequency oscillatory squeeze mode: Experimental tests and modelling," Journal of Applied Physics, vol. 119, no. 10, p. 105101, 2016.

[161] R. H. Ewoldt, P. Tourkine, G. H. McKinley, and A. E. Hosoi, "Controllable adhesion using field-activated fluids," vol. 23, no. 7, pp. 073104–073104–13, 2011.

[162] I. I. M. Yazid, S. A. Mazlan, F. Imaduddin, H. Zamzuri, S. B. Choi, and T. Kikuchi, "An investigation on the mitigation of end-stop impacts in a magnetorheological damper operated by the mixed mode," Smart Materials and Structures, vol. 25, no. 12, p. 125005, 2016.

[163] C. Yang, J. Fu, M. Yu, X. Zheng, and B. Ju, "A new magnetorheological elastomer isolator in shear–compression mixed mode," Journal of Intelligent Material Systems and Structures, vol. 26, no. 10, pp. 1290–1300, 2015.

[164] W. K. Yi, "What in the world are magnetic dampers?." https://www.torque.com.sg/features/what-are-magnetorheological-dampers/, 2019. (accessed: 07-06-2021).

[165] D. Hua, X. Liu, Z. Li, P. Fracz, A. Hnydiuk-Stefan, and Z. Li, "A review on structural configurations of magnetorheological fluid based devices reported in 2018-2020," Frontiers in Materials, vol. 8, 2021.

[166] S.-H. Choi, S. Kim, P. Kim, J. Park, and S.-B. Choi, "A new visual feedback-based magnetorheological haptic master for robot-assisted minimally invasive surgery," Smart Materials and Structures, vol. 24, no. 6, p. 65015, 2015.

[167] S. Guo, Y. Song, X. Yin, L. Zhang, T. Tamiya, H. Hirata, and H. Ishihara, "A novel robot-assisted endovascular catheterization system with haptic force feedback," IEEE Transactions on Robotics, vol. 35, no. 3, pp. 685–696, 2019.

[168] M. Waga, Y. Aita, J. Noma, T. Kikuchi, and Y. Nonomura, "Scissors-type haptic device using magnetorheological fluid containing iron nanoparticles," Technologies (Basel), vol. 7, no. 1, p. 26, 2019.

[169] T. Kikuchi, J. Noma, S. Akaiwa, and Y. Ueshima, "Response time of magnetorheological fluid–based haptic device," Journal of Intelligent Material Systems and Structures, vol. 27, no. 7, pp. 859–865, 2016.

[170] A. K. El Wahed and L. B. Balkhoyor, "The performance of a smart ball-and-socket actuator applied to upper limb rehabilitation," Journal of Intelligent Material Systems and Structures, vol. 29, no. 13, pp. 2811–2822, 2018.

[171] J. L. Zite, F. Ahmadkhanlou, V. A. Neelakantan, and G. N. Washington, "A magnetorheological fluid based orthopedic active knee brace," in Smart Structures and Materials 2006: Industrial and Commercial Applications of Smart Structures Technologies (E. V. White, ed.), vol. 6171, pp. 148 – 156, International Society for Optics and Photonics, SPIE, 2006.

[172] F. Jonsdottir, E. Thorarinsson, H. Palsson, and K. Gudmundsson, "Influence of parameter variations on the braking torque of a magnetorheological prosthetic knee," Journal of Intelligent Material Systems and Structures, vol. 20, no. 6, pp. 659–667, 2009.

[173] A. Zahedi, B. Zhang, A. Yi, and D. Zhang, "A soft exoskeleton for tremor suppression equipped with flexible semiactive actuator," Soft Robotics, 2020.

[174] J. Rabinow, "Magnetic fluid torque and force transmitting device." U.S. patent 2575360 A, Nov. 1951.

[175] R. Rizzo, A. Musolino, F. Bucchi, P. Forte, and F. Frendo, "A multi-gap magnetorheological clutch with permanent magnet," Smart Materials and Structures, vol. 24, no. 7, p. 75012, 2015.

[176] S. B. Lokhande and S. R. Patil, "Experimental characterization and evaluation of magnetorheological clutch for an electric two-wheeler application," Measurement : Journal of the International Measurement Confederation, vol. 175, p. 109150, 2021.

[177] W. Li and H. Du, "Design and experimental evaluation of a magnetorheological brake," International Journal of Advanced Manufacturing Technology, vol. 21, no. 7, pp. 508–515, 2003.

[178] E. J. Park, D. Stoikov, L. Falcao da Luz, and A. Suleman, "A performance evaluation of an automotive magnetorheological brake design with a sliding mode controller," Mechatronics (Oxford), vol. 16, no. 7, pp. 405–416, 2006.

[179] K. Karakoc, E. J. Park, and A. Suleman, "Design considerations for an automotive magnetorheological brake," Mechatronics (Oxford), vol. 18, no. 8, pp. 434–447, 2008.

[180] Q. H. Nguyen and S. B. Choi, "Optimal design of an automotive magnetorheological brake considering geometric dimensions and zero-field friction heat," Smart Materials and Structures, vol. 19, no. 11, p. 115024, 2010.

[181] S. M. Kalikate, S. R. Patil, and S. M. Sawant, "Simulation-based estimation of an automotive magnetorheological brake system performance," Journal of Advanced Research, vol. 14, pp. 43–51, 2018.

[182] J. Dai, H. Chang, R. Zhao, J. Huang, K. Li, and S. Xie, "Investigation of the relationship among the microstructure, rheological properties of MR grease and the speed reduction performance of a rotary micro-brake," Mechanical Systems and Signal Processing, vol. 116, pp. 741–750, 2019.

[183] M. R. Jolly, J. W. Bender, and J. D. Carlson, "Properties and applications of commercial magnetorheological fluids," Journal of Intelligent Material Systems and Structures, vol. 10, no. 1, pp. 5–13, 1999.

[184] J. Goldasz and B. Sapinski, "Nondimensional characterization of flow-mode magnetorheological/electrorheological fluid dampers," Journal of Intelligent Material Systems and Structures, vol. 23, no. 14, pp. 1545–1562, 2012.

[185] N. D. Sims, R. Stanway, A. R. Johnson, and P. Mellor, "Design, testing, and model validation of an MR squeeze-flow vibration damper," in Proceedings of SPIE, vol. 4331, (Bellingham WA), pp. 111–120, SPIE, 2001.

[186] "Magnetorheological damper behaviour in accordance with flow mode," European Physical Journal. Applied Physics, vol. 84, no. 2, p. 21101, 2018.

[187] X. Zhu, X. Jing, and L. Cheng, "Magnetorheological fluid dampers: A review on structure design and analysis," vol. 23, no. 8, pp. 839–873, 2012.

[188] S. YOKOTA, K. YOSHIDA, and Y. KONDOH, "A pressure control valve using MR fluid," Proceedings of the JFPS International Symposium on Fluid Power, vol. 1999, no. 4, pp. 377–380, 1999.

[189] M. Y. Salloom and Z. Samad, "Design and modeling magnetorheological directional control valve," Journal of Intelligent Material Systems and Structures, vol. 23, no. 2, pp. 155–167, 2012.

[190] J.-H. Yoo and N. M. Wereley, "Performance of a magnetorheological hydraulic power actuation system," Journal of Intelligent Material Systems and Structures, vol. 15, no. 11, pp. 847–858, 2004.

[191] W. L. Wilkinson, Non-Newtonian fluids : fluid mechanics, mixing and heat transfer. International series of monographs on chemcial engineering ; vol.1, Pergamon Press, 1960.

[192] A. Rossi, F. Orsini, A. Scorza, F. Botta, N. P. Belfiore, and S. A. Sciuto, "A review on parametric dynamic models of magnetorheological dampers and their characterization methods," Actuators, vol. 7, no. 2, p. 16, 2018.

[193] X. Wang and F. Gordaninejad, "Flow analysis of field-controllable, electro- and magneto-rheological fluids using herschel-bulkley model," Journal of Intelligent Material Systems and Structures, vol. 10, no. 8, pp. 601–608, 1999.

[194] B. F. Spencer, S. J. Dyke, M. K. Sain, and J. D. Carlson, "Phenomenological model for magnetorheological dampers," Journal of Engineering Mechanics, vol. 123, no. 3, pp. 230–238, 1997.

[195] M.-G. Yang, C.-Y. Li, and Z.-Q. Chen, "A new simple non-linear hysteretic model for MR damper and verification of seismic response reduction experiment," Engineering Structures, vol. 52, pp. 434–445, 2013.

[196] D. H. Wang and W. H. Liao, "Modeling and control of magnetorheological fluid dampers using neural networks," Smart Materials and Structures, vol. 14, no. 1, pp. 111–126, 2005.

[197] H. Tsang, R. Su, and A. Chandler, "Simplified inverse dynamics models for MR fluid dampers," Engineering Structures, vol. 28, no. 3, pp. 327–341, 2006.

[198] S.-B. Choi, S.-K. Lee, and Y.-P. Park, "A hysteresis model for the field-dependent damping force of a magnetorheological damper," Journal of Sound and Vibration, vol. 245, no. 2, pp. 375–383, 2001.

[199] M. Zeinali, A. Y. Abd Fatah, H. Zamzuri, and S. A. Mazlan, "A GA-weighted adaptive neuro-fuzzy model to predict the behaviour of magnetorheological damper," Applied Mechanics and Materials, vol. 663, pp. 203–207, 2014.

[200] G. Jin, M. Sain, K. Pham, F. Billie, and J. Ramallo, "Modeling MR-dampers: a nonlinear blackbox approach," in Proceedings of the 2001 American Control Conference. (Cat. No.01CH37148), vol. 1, pp. 429–434 vol.1, IEEE, 2001.

[201] C.-C. Chang and P. Roschke, "Neural network modeling of a magnetorheological damper," Journal of Intelligent Material Systems and Structures, vol. 9, no. 9, pp. 755–764, 1998.

[202] N. C. Rosenfeld and N. M. Wereley, "Volume-constrained optimization of magnetorheological and electrorheological valves and dampers," Smart Materials and Structures, vol. 13, no. 6, pp. 1303–1313, 2004.

[203] M. M. Naserimojarad, M. Moallem, and S. Arzanpour, "A comprehensive approach for optimal design of magnetorheological dampers," Journal of Intelligent Material Systems and Structures, vol. 29, no. 18, pp. 3648–3655, 2018.

[204] E. J. Park, L. F. da Luz, and A. Suleman, "Multidisciplinary design optimization of an automotive magnetorheological brake design," Computers & Structures, vol. 86, no. 3, pp. 207–216, 2008.

[205] A. Younis, K. Karakoc, Z. Dong, E. Park, and A. Suleman, "Application of SE-UMRE global optimization algorithm in automotive magnetorheological brake design," Structural and Multidisciplinary Optimization, vol. 44, no. 6, pp. 761–772, 2011.

[206] S. Smith and J. Tlusty, "Stabilizing chatter by automatic spindle speed regulation," CIRP Annals, vol. 41, no. 1, pp. 433–436, 1992.

[207] L. Vela-Martínez, J. Jauregui-Correa, E. Rodriguez, and J. Alvarez-Ramirez, "Using detrended fluctuation analysis to monitor chattering in cutter tool machines," International Journal of Machine Tools and Manufacture, vol. 50, no. 7, pp. 651–657, 2010.

[208] T. Takemura, T. Kitamura, and T. Hoshi, "Active suppression of chatter by programed variation of spindle speed," Journal of the Japan Society of Precision Engineering, vol. 41, no. 484, pp. 489–494, 1975.

[209] S. Seguy, T. Insperger, L. Arnaud, G. Dessein, and G. Peigné, "On the stability of high-speed milling with spindle speed variation," The International Journal of Advanced Manufacturing Technology, vol. 48, no. 9-12, pp. 883–895, 2010.

[210] X. Liu, J. Z. Jiang, B. Titurus, and A. Harrison, "Model identification methodology for fluid-based inerters," Mechanical Systems and Signal Processing, vol. 106, pp. 479–494, 2018.

[211] M. Tipuric, P. Deastra, D. Wagg, and N. Sims, "Semi-active inerters using magnetorheological fluid: a feasibility study," in Proceedings of SPIE - The International Society for Optical Engineering, vol. 10595, SPIE, 2018.

[212] M. Tipuric, D. Wagg, and N. Sims, "Magnetorheological bypass valve design for a semi-active inerter," vol. 10967, SPIE, 2019.

[213] M. Tipuric, P. Deastra, D. Wagg, and N. Sims, "Vibration suppression using the concept of a semi-active magnetorheological inerter device," in Proceedings of ISMA, ISMA, 2018.

[214] M. Mao, Y.-T. Hu, W.and Choi, and N. Wereley, "A magnetorheological damper with bifold valves for shock and vibration mitigation," Journal of Intelligent Material Systems and Structures, vol. 18, no. 12, pp. 1227–1232, 2007.

[215] W.-M. Zhong, X.-X. Bai, C. Tang, and A.-D. Zhu, "Principle study of a semi-active inerter featuring magnetorheological effect," Frontiers in Materials, vol. 6, 2019.

[216] C. Pan, R. Zhang, H. Luo, C. Li, and H. Shen, "Demand-based optimal design of oscillator with parallel-layout viscous inerter damper," Structural Control and Health Monitoring, vol. 25, no. 1, pp. e2051–n/a, 2018.

[217] J. O. Wilkes, Fluid Mechanics for Chemical Engineers with Microfluidics and CFD, Second Edition. Pearson, 2005.

[218] MagWeb, "Free B(H) & core loss curves." `https://magweb.us/free-bh-curves/`. (accessed: 2021-06-22).

[219] L. Corp, "Magneto-rheological (MR) fluid." `https://www.lord.com/products-and-solutions/active-vibration-control/industrial-suspension-systems/magneto-rheological-mr-fluid`. (accessed: 2021-06-22).

[220] S. Bordoloi and H. H. Guerrero, "Design for control: A new perspective on process and product innovation," International Journal of Production Economics, vol. 113, no. 1, pp. 346–358, 2008. Research and Applications in E-Commerce and Third-Party Logistics Management Special Section on Meta-standards in Operations Management: Cross-disciplinary perspectives.

[221] P. Deastra, "Tuned-inerter-based-dampers with linear hysteretic damping for earthquake protection of building structures," 2021.

[222] D. Meeker, "Finite Element Method Magnetics, v.8." `https://www.femm.info/wiki/HomePage/`, 2008. (accessed: 2022-12-03).

[223] A. Savitzky and M. J. E. Golay, "Smoothing and differentiation of data by simplified least squares procedures," Analytical Chemistry (Washington), vol. 36, no. 8, pp. 1627–1639, 1964.

[224] S. R. Krishnan and C. S. Seelamantula, "On the Selection of Optimum Savitzky-Golay Filters," IEEE Transactions on Signal Processing, vol. 61, no. 2, pp. 380–391, 2013.

[225] D. C. Batterbee, N. D. Sims, R. Stanway, and M. Rennison, "Magnetorheological landing gear: 2. validation using experimental data," Smart Materials and Structures, vol. 16, no. 6, pp. 2441–2452, 2007.

[226] A. Qin and P. Suganthan, "Self-adaptive differential evolution algorithm for numerical optimization," in 2005 IEEE Congress on Evolutionary Computation, vol. 2, pp. 1785–1791 Vol. 2, IEEE, 2005.

[227] R. Storn and K. Price, "Differential evolution – a simple and efficient heuristic for global optimization over continuous spaces," Journal of Global Optimization, vol. 11, no. 4, pp. 341–359, 1997.

[228] M. Champneys, "Freelunch0.1.0." `https://github.com/MDCHAMP/FreeLunch`. (accessed: 2021-09-21).

[229] M. Champneys, "Toybox v.0.2.0." `https://github.com/MDCHAMP/Toybox`. (ccessed: 2021-09-21).

[230] K. Worden and G. Manson, "On the identification of hysteretic systems. part I: Fitness landscapes and evolutionary identification," <u>Mechanical Systems and Signal Processing</u>, vol. 29, pp. 201–212, 2012.

[231] K. McDonald, A. Rendos, S. Woodman, K. A. Brown, and T. Ranzani, "Magnetorheological fluid-based flow control for soft robots," <u>Advanced Intelligent Systems</u>, vol. 2, no. 11, pp. 2000139–n/a, 2020.

[232] D. N. Johnston and K. A. Edge, "In-situ measurement of the wavespeed and bulk modulus in hydraulic lines," <u>Proceedings of the Institution of Mechanical Engineers, Part I: Journal of Systems and Control Engineering</u>, vol. 205, no. 3, pp. 191–197, 1991.

[233] S. L. Morriss and A. D. Hill, "Ultrasonic imaging and velocimetry in two-phase pipe flow," vol. 115, no. 2, pp. 108–116, 1993.

[234] W. F. Kolbe, B. T. Turko, and B. Leskovar, "Fast ultrasonic imaging in a liquid filled pipe," <u>IEEE Transactions on Nuclear Science</u>, vol. 33, no. 1, pp. 715–722, 1986.

[235] T. Leighton, D. Ramble, A. Phelps, C. Morfey, and P. Harris, "Acoustic detection of gas bubbles in a pipe," <u>Acta Acustica united with Acustica</u>, vol. 84, no. 5, pp. 801–814, 1998.

[236] P. Keogh. Personal communication, Nov. 2022.

[237] Y. Shida, Y. Kakinuma, T. Aoyama, H. Minami, and H. Anzai, "Basic performance evaluation of electrorheological gel in vacuum condition," <u>Journal of Intelligent Material Systems and Structures</u>, vol. 22, no. 15, pp. 1699–1705, 2011.

[238] A. Giaralis and A. Taflanidis, "Optimal tuned mass-damper-inerter (TMDI) design for seismically excited MDOF structures with model uncertainties based on reliability criteria," <u>Structural Control and Health Monitoring</u>, vol. 25, no. 2, pp. e2082–n/a, 2018.

[239] Y. Tarng, J. Kao, and E. Lee, "Chatter suppression in turning operations with a tuned vibration absorber," Journal of Materials Processing Technology, vol. 105, no. 1, pp. 55–60, 2000.

[240] M. Miguélez, L. Rubio, J. Loya, and J. Fernández-Sáez, "Improvement of chatter stability in boring operations with passive vibration absorbers," Journal of Energy Resources Technology, vol. 52, no. 10, pp. 1376–1384, 2010.

[241] W. Ma, Y. Yang, and X. Jin, "Chatter suppression in micro-milling using shank-mounted two-DOF tuned mass damper," Precision Engineering, vol. 72, pp. 144–157, 2021.

[242] J. Leopold and L. Hong, "Clamping modelling: state-of-the-art and future trends," Industrial Robot, vol. 36, no. 3, pp. 249–254, 2009.

[243] A. Rashid and C. Mihai Nicolescu, "Active vibration control in palletised workholding system for milling," International Journal of Machine Tools and Manufacture, vol. 46, no. 12, pp. 1626–1636, 2006.

[244] F.-C. Wang, C.-H. Lee, and R.-Q. Zheng, "Benefits of the inerter in vibration suppression of a milling machine," Journal of the Franklin Institute, vol. 356, no. 14, pp. 7689–7703, 2019.

[245] Y. Zhang and N. D. Sims, "Milling workpiece chatter avoidance using piezoelectric active damping: a feasibility study," Smart Materials and Structures, vol. 14, no. 6, pp. N65–N70, 2005.

[246] J. Picavea, A. Gameros, J. Yang, and D. Axinte, "Vibration suppression using tuneable flexures acting as vibration absorbers," International Journal of Mechanical Sciences, vol. 222, 2022.

[247] W. Ji and L. Wang, "Industrial robotic machining: a review," International Journal of Advanced Manufacturing Technology, vol. 103, no. 1-4, pp. 1239–1255, 2019.

[248] Z. Yuan, L.and Pan, D. Ding, S. Sun, and W. Li, "A review on chatter in robotic machining process regarding both regenerative and mode coupling mechanism," IEEE/ASME Transactions on Mechatronics, vol. 23, no. 5, pp. 2240–2251, 2018.